Active tectonics in the Kenya Rift.

Implications for continental rifting and paleodrainage systems.

Kumulative Dissertation

zur Erlangung des akademischen Grades „doctor rerum naturalium“ (Dr. rer. nat.)
in der Wissenschaftsdisziplin „Geologie”

eingereicht an der
Mathematisch-Naturwissenschaftlichen Fakultät
der Universität Potsdam

vorgelegt von

Dipl.-Geol. Simon Riedl

Ort und Tag der Disputation: Potsdam, 21.01.2022

Betreuer: Prof. Manfred Strecker, PhD
Institut für Geowissenschaften
Universität Potsdam

Prof. Dr. Bodo Bookhagen
Institut für Geowissenschaften
Universität Potsdam

Gutachter: Prof. Manfred Strecker, PhD
Institut für Geowissenschaften
Universität Potsdam
Deutschland

Prof. Dr. Giacomo Corti
National Research Council of Italy
Institute of Geosciences and Earth Resources
Florenz, Italien

PD Dr. Sascha Brune
Geoforschungszentrum Potsdam

Published online on the
Publication Server of the University of Potsdam:
https://doi.org/10.25932/publishup-53855
https://nbn-resolving.org/urn:nbn:de:kobv:517-opus4-538552

Erklärung zur Eigenständigkeit

Hiermit erkläre ich, Simon Riedl, an Eides statt, dass ich die Dissertation *„Active tectonics in the Kenya Rift. Implications for continental rifting and paleodrainage systems.“* selbst verfasst und keine anderen als die angegebenen Quellen und Hilfsmittel verwendet habe.

Alle wörtlich oder inhaltlich übernommenen Stellen habe ich als solche gekennzeichnet und durch Angaben der Herkunft kenntlich gemacht. Bereits in einer Fachzeitschrift publizierte oder zur Publikation eingereichte Kapitel sind eindeutig gekennzeichnet.

Ich erkläre weiterhin, dass die Dissertation bisher nicht in dieser oder anderer Form in einem anderen Prüfungsverfahren vorgelegt wurde.

Potsdam, am 22.09.2021

Allgemeinverständliche Zusammenfassung

Die Oberfläche der Erde besteht aus ozeanischen und kontinentalen Platten. Diese Platten bewegen sich sehr langsam – entweder aufeinander zu, aneinander vorbei oder voneinander weg. An den Plattengrenzen kommt es dadurch zu Erdbeben, Vulkanismus, und über Jahrmillionen zur Entstehung von Gebirgen oder Ozeanen. In Ostafrika befindet sich eine solche Grenze, entlang der sich zwei benachbarte Kontinentalplatten auseinanderbewegen und als Folge ein breiter Grabenbruch entsteht, der sich in ferner Zukunft in ein Ozeanbecken entwickeln wird, das über den Golf von Aden mit dem Indischen Ozean verbunden sein wird.

Diese Arbeit beschäftigt sich mit der jüngeren Geschichte des Ostafrikanischen Grabenbruchs in Kenia und der damit zusammenhängenden stufenartigen Zerschneidung der Landschaft durch Brüche während der letzten 500.000 Jahre. Die Höhen der einzelnen Bruchstufen im Graben werden untersucht. Dabei nutze ich die Daten von Vermessungssatelliten und von Luftbildern. Durch Gesteinsproben von Vulkanen und radiometrischen Datierungen lässt sich zudem das Alter der dortigen Gesteine bestimmen. Zusammengenommen kann daraus die Entstehungsgeschichte des Grabens der letzten 500 tausend Jahre abgeleitet werden und bestimmt werden, dass sich in diesem Zeitraum die Kontinentalplatten von Ostafrika mit einer Geschwindigkeit von mindestens 1,6 mm pro Jahr auseinanderbewegt haben. Diese Bewegung findet größtenteils in einem schmalen Bereich der Mitte des Ostafrikanischen Grabens statt, nicht aber an dessen Rändern. Dies zeigt, dass die Bildung dieser Plattengrenze bereits in einem fortgeschrittenen Stadium ist.

Durch diese stetige Plattenbewegung entstehen im Grabenbruch Senken, in denen sich Seen bilden. Diese Arbeit untersucht neben der Entwicklung der Grabenstrukturen, wie diese einzelnen Seebecken in der Vergangenheit durch Flüsse miteinander verbunden waren, als Klimaschwankungen feuchtere Umweltbedingungen hervorriefen und somit höhere Seespiegelstände und eine Verbindung der Becken durch einen Überlauf der Seen ermöglichten. Entlang der Flüsse konnten sich vor etwa 10 tausend Jahren bestimmte Fischarten ausbreiten, was die heutige Verbreitung Arten in voneinander getrennten Seebecken erklärt. Überreste dieser Wasserverbindung sind tief eingeschnittene Schluchten, Ablagerungen von ehemaligen Seen, und Fischfossilien. Aufgrund zyklisch auftretender Klimaänderungen kann davon ausgegangen werden, dass sich solche feuchten Umweltbedingungen in der jüngeren geologischen Vergangenheit immer wieder ereigneten und das Ökosystem beeinflussten.

Im Verlauf der letzten 1 Million Jahren hat sich daher nicht nur die Oberflächenform des Ostafrikanischen Grabens durch Bruchbildung und vulkanische Aktivität stetig verändert, sondern auch die Umweltbedingungen. In diesem Zusammenhang zeigt die Untersuchung eines 160 m langen Bohrkerns aus dem Südbereich des Grabenbruchs, dass es wiederholt feuchte Zeiträume mit Seen und Waldbedeckung im Wechsel mit trockeneren Phasen und savannenartiger Landschaft gab. Meine Arbeit untersucht daher, wie sich durch die Auseinanderbewegung der Kontinentalplatten die Oberfläche und die Topographie des Grabenbruchs langfristig verändert. Zugleich zeigt sie die Konsequenzen dieser immer noch andauernden Zergliederung der Erdoberfläche für den Wasserhaushalt und das Ökosystem auf.

Zusammenfassung

Magmatische und tektonisch aktive Grabenzonen (Rifts) stellen die Vorstufen entstehender Plattengrenzen dar. Diese sich spreizenden tektonischen Provinzen zeichnen sich durch allgegenwärtige Abschiebungen aus, und die räumliche Verteilung, die Geometrie, und das Alter dieser Abschiebungen lässt Rückschlüsse auf die räumlichen und zeitlichen Zusammenhänge zwischen tektonischer Deformation, Magmatismus und langwelliger Krustendeformation in Rifts zu. Diese Arbeit konzentriert sich auf die Störungsaktivität im Kenia-Rift des känozoischen Ostafrikanischen Grabensystems im Zeitraum zwischen dem mittleren Pleistozän und dem Holozän.

Um die frühen Stadien der Entstehung kontinentaler Plattengrenzen zu untersuchen, wird in dieser Arbeit eine zeitlich gemittelte minimale Extensionsrate für den inneren Graben des Nördlichen Kenia-Rifts (NKR) für die letzten 0,5 Mio Jahre abgeleitet. Die Analyse beruht auf Messungen mit Hilfe des digitalen TanDEM-X-Höhenmodells, um die Abschiebungen entlang der vulkanisch-tektonischen Achse des inneren Grabens des NKR zu kartieren und deren Versatzbeträge zu bestimmen. Mithilfe von vorhandenen Geochronologiedaten der deformierten vulkanischen Einheiten sowie in dieser Arbeit erstellten $^{40}Ar/^{39}Ar$-Datierungen werden zeitlich gemittelte Extensionsraten berechnet. Die Auswertungen zeigen, dass im inneren Graben des NKR die langfristige Extensionsrate für mittelpleistozäne bis rezente Störungen Mindestwerte von 1,0 bis 1,6 mm yr^{-1} aufweist und lokal allerdings auch Werte bis zu 2,0 mm yr^{-1} existieren. In Anbetracht der nahezu inaktiven Randstörungen des NKR zeigt sich somit, dass sich die Extension auf die Region der aktiven vulkanisch-tektonischen Achse im inneren Graben konzentriert und somit ein fortgeschrittenes Stadium kontinentaler Extensionsprozesse im NKR vorliegt.

In dieser Arbeit wird diese räumlich fokussierte Extension zudem im Rahmen einer Störungsanalyse der jüngsten vulkanischen Erscheinungen des Kenia-Rifts betrachtet. Die Arbeit analysiert mithilfe von Geländekartierungen und eines auf Luftbildern basierenden Geländemodells die Störungscharakteristika der etwa 36 tausend Jahre alten Menengai-Kaldera und der umliegenden Gebiete im zentralen Kenia-Rift. Im Allgemeinen sind die holozänen Störungen innerhalb des Rifts reine, NNO-streichende Abschiebungen, die somit das gegenwärtige tektonische Spannungsfeld wiederspiegeln; innerhalb der Menengai-Kaldera sind die jungen Strukturen jedoch von andauernder magmatischer Aktivität und von Aufdomung überprägt. Die Kaldera befindet sich im Zentrum eines sich aktiv dehnenden Riftsegments und zusammen mit den anderen quartären Vulkanen des Kenia-Rifts lassen sich diese Bereiche als Kernpunkte der extensionalen Störungsaktivität verstehen, die letztlich zu einer weiter entwickelten Phase magmengestützter Kontinentalseparation führen werden.

Die bereits seit dem Tertiär andauernde Störungsaktivität im Kenia-Rift führt zur Zergliederung der größeren Rift-Senken in kleinere Segmente und beeinflusst die Sedimentologie und die Hydrologie dieser Riftbecken. Gegenwärtig sind die meisten, durch Störungen begrenzten Becken des Kenia-Rifts hydrologisch isoliert, sie waren aber während feuchter Klimaphasen hydrologisch miteinander verbunden; in dieser Arbeit untersuche ich deshalb auch diese hydro-

logische Verbindung der Rift-Becken für die Zeit der Afrikanischen Feuchteperiode des frühen Holozäns. Mithilfe der Analyse von digitalen Geländemodellen, unter Berücksichtigung von geomorphologischen Anzeigern für Seespiegelhochstände, Radiokarbondatierungen und einer Übersicht über Fossiliendaten konnten zwei kaskadierende Flusssysteme aus diesen Daten abgeleitet werden: eine Flusskaskade in Richtung Süden und eine in Richtung Norden. Beide Kaskaden haben die derzeit isolierten Becken während des frühen Holozäns durch überlaufende Seen und eingeschnittene Schluchten miteinander verbunden. Diese hydrologische Verbindung führte zu der Ausbreitung aquatischer Fauna entlang des Rifts, und gleichzeitig stellte die Wasserscheide zwischen den beiden Flusssystemen den einzigen terrestrischen Ausbreitungskorridor dar, der eine Überquerung des Kenia-Rifts ermöglichte. Diese tektonisch-geomorphologische Rekonstruktion erklärt die heute isolierten Vorkommen nilotischer Fischarten in den Riftseen Kenias sowie die isolierten Vorkommen Guineo-Congolischer Säugetiere in Wäldern östlich des Kenia-Rifts, die sich über die Wasserscheide im Kenia-Rift ausbreiten konnten.

Auf längeren Zeitskalen sind solche Phasen hydrologischer Verbindung und Phasen der Isolation wiederholt aufgetreten und zeigen sich in wechselnden paläoökologischen Indikatoren in Sedimentbohrkernen. Hier stelle ich einen Sedimentbohrkern aus dem Koora-Becken des Südlichen Kenia-Rifts vor, der einen Datensatz der Paläo-Umweltbedingungen der letzten 1 Million Jahre beinhaltet. Dieser Datensatz zeigt, dass etwa vor 400 tausend Jahren die zuvor relativ stabilen Umweltbedingungen zum Erliegen kamen und tektonische, hydrologische und ökologische Veränderungen dazu führten, dass die Wasserverfügbarkeit, die Grasland-Vergesellschaftungen und die Bedeckung durch Baumvegetation zunehmend stärkeren und häufigeren Schwankungen unterlagen. Diese großen Veränderungen fallen zeitlich mit Phasen zusammen, in denen das südliche Becken des Kenia-Rifts von vulkanischer und tektonischer Aktivität besonders betroffen war. Die vorliegende Arbeit zeigt deshalb deutlich, inwiefern die tektonischen und geomorphologischen Gegebenheiten im Zuge einer zeitlich langanhaltenden Extension die Hydrologie, die Paläo-Umweltbedingungen sowie die Biodiversität einer Riftzone beeinflussen können.

Abstract

Magmatic continental rifts often constitute the earliest stage of nascent plate boundaries. These extensional tectonic provinces are characterized by ubiquitous normal faulting and volcanic activity; the spatial pattern, the geometry, and the age of these normal faults can help to unravel the spatiotemporal relationships between extensional deformation, magmatism, and long-wavelength crustal deformation of continental rift provinces. This study focuses on the active faulting in the Kenya Rift of the Cenozoic East African Rift System (EARS) with a focus on the mid-Pleistocene to the present-day.

To examine the early stages of continental break-up in the EARS, this thesis presents a time-averaged minimum extension rate for the inner graben of the Northern Kenya Rift (NKR) for the last 0.5 m.y. Using the TanDEM-X digital elevation model, fault-scarp geometries and associated throws are determined across the volcano-tectonic axis of the inner graben of the NKR. By integrating existing geochronology of faulted units with new $^{40}Ar/^{39}Ar$ radioisotopic dates, time-averaged extension rates are calculated. This study reveals that in the inner graben of the NKR, the long-term extension rate based on mid-Pleistocene to recent brittle deformation has minimum values of 1.0 to 1.6 mm yr^{-1}, locally with values up to 2.0 mm yr^{-1}. In light of virtually inactive border faults of the NKR, we show that extension is focused in the region of the active volcano-tectonic axis in the inner graben, thus highlighting the maturing of continental rifting in the NKR.

The phenomenon of focused extension is further investigated with a structural analysis of the youngest volcanic manifestations of the Kenya Rift, their relationship with extensional structures, and their overprint by Holocene faulting. In this context I analyzed the fault characteristics at the ~36 ka old Menengai Caldera and adjacent areas in the Central Kenya Rift using detailed field mapping and a structure-from-motion-based DEM generated from UAV data. In general, the Holocene intra-rift normal faults are dip-slip faults which strike NNE and thus reflect the present-day tectonic stress field; however, inside Menengai caldera persistent magmatic activity and magmatic resurgence overprints these young structures significantly. The caldera is located at the center of an actively extending rift segment and this and the other volcanic edifices of the Kenya Rift may constitute nucleation points of faulting an magmatic extensional processes that ultimately lead into a future stage of magma-assisted rifting.

When viewed at the scale of the entire Kenya Rift the protracted normal faulting in this region compartmentalizes the larger rift depressions, and influences the sedimentology and the hydrology of the intra-rift basins at a scale of less than 100 km. In the present day, most of the fault-bounded sub-basins of the Kenya Rift are hydrologically isolated due to this combination of faulting and magmatic activity that has generated efficient hydrological barriers that maintain these basins as semi-independent geomorphic entities. This isolation, however, was overcome during wetter climatic conditions during the past when the basins were transiently connected. I therefore also investigated the hydrological connectivity of the rift basins during the African Humid Period of the early Holocene, when climate was wetter. With the help of DEM analysis, lake-highstand indicators, radiocarbon dating, and a review of the fossil record, two lake-river-

cascades could be identified: one directed southward, and one directed northward. Both cascades connected presently isolated rift basins during the early Holocene via spillovers of lakes and incised river gorges. This hydrological connection fostered the dispersal of aquatic faunas along the rift, and in addition, the water divide between the two river systems represented the only terrestrial dispersal corridor across the Kenya Rift. The reconstruction explains isolated distributions of Nilotic fish species in Kenya Rift lakes and of Guineo-Congolian mammal species in forests east of the Kenya Rift. On longer timescales, repeated episodes of connectivity and isolation must have occurred. To address this problem I participated in research to analyze a sediment drill core from the Koora basin of the Southern Kenya Rift, which provides a paleo-environmental record of the last 1 Ma. Based on this record it can be concluded that at ~400 ka relatively stable environmental conditions were disrupted by tectonic, hydrological, and ecological changes, resulting in increasingly large and frequent fluctuations in water availability, grassland communities, and woody plant cover. The major environmental shifts reflected in the drill core data coincide with phases where volcano-tectonic activity affected the basin. This thesis therefore shows how protracted extensional tectonic processes and the resulting geomorphologic conditions can affect the hydrology, the paleo-environment and the biodiversity of extensional zones in Kenya and elsewhere.

Table of Contents

List of Figures and Tables

List of Figures

List of tables

List of Abbreviations

AHP African Humid Period
BP Before present
CA Correspondence analysis
cal BP Calibrated years before present
CI Confidence interval
CKR Central Kenya Rift
CPD Cumulative probability distribution
D/P Phytolith tree cover density index (high/low values indicate dominant tree/grass cover)
DEM Digital elevation model (bare-earth topography)
dGPS Differential Global Positioning System
DLR German Aerospace Center
DSM Digital surface model
EARS East African Rift System
EGM96 Earth Gravitational Model, version from 1996
GDC Geothermal Development Company of Kenya
GNSS Global navigation satellite system
GPS Global positioning system
IGS International GNSS Service
Iph Phytolith index (high/low values indicate short/tall grasses)
LCT Large Cutting Tools (Artifacts used to typify Achulean technology)
MSA Middle Stone Age
NKR Northern Kenya Rift
NOAA National Oceanic and Atmospheric Administration
SfM Structure-from-Motion
S_{Hmax} Maximum horizontal stress
S_{hmin} Minimum horizontal stress
SKR Southern Kenya Rift
SRTM Shuttle Radar Topography Mission
TanDEM-X TerraSAR-X add-on for Digital Elevation Measurement (satellite mission)
UAS Unmanned aircraft system
UAV Unmanned aerial vehicle
WGS84 World Geodetic System, version from 1984
XRD X-ray diffraction
XRF X-ray fluorescence

Chapter 1

Introduction

1.1 State of the art and principal research questions to be addressed

Continental magmatic rifts occur in areas of reduced lithospheric thickness and are associated with strong gravity anomalies, volcanic fissure systems and eruptive centers, and extensive lava flows (e.g., Buck, 2006; Burke and Dewey, 1973; Ebinger and Sleep, 1998; Hansen et al., 2012; Simiyu and Keller, 1997; Wright et al., 2016). These are generally areas of long-wavelength crustal upwarping (e.g., Moucha and Forte, 2011; Smith, 1994; Wichura et al., 2015), horizontal deviatoric tensional stresses, and low-magnitude seismogenic faulting that result in extension zones of variable width (e.g., Buck, 2004; Parsons and Thompson, 1991). If extensional processes are sustained, such extensional zones eventually result in continental separation and the formation of ocean basins (e.g., Brune et al., 2016; Corti, 2009; Wilson, 1968).

Extensional processes have led to the formation of many rift zones during the course of Earth's history, but it is the Cenozoic rift zones that now provide snapshots of the early evolutionary stages of continental separation, prior to the formation of ocean basins. These tectonic processes appear to have generally operated rather slowly over geological timescales involving millions of years (e.g., Corti, 2009), but when considered over shorter time scales there appears to have been far greater variability in the rates at which tectonic and the accompanying magmatic processes have operated (e.g., Ebinger et al., 2010). These aspects can be observed and analyzed in the Cenozoic East African Rift System (EARS).

Uplift, volcanism, and normal faulting in the EARS are hallmarks of one of the largest magmatic extensional zones on Earth (Burke, 1996). Comprised of the largely amagmatic western and the magmatic eastern branch, extension processes in the ~5000-km-long EARS have generated a series of transiently linked and isolated rift basins (e.g., Ebinger and Scholz, 2011; Tiercelin and Lezzar, 2002). These basins constitute strategic locations for a variety of natural resources, including hydrocarbons and geothermal energy (e.g., Kombe and Muguthu, 2019; Omenda and Simiyu, 2015; Riaroh and Okoth, 1994), but they have also played a pivotal role in the dispersal of species, particularly in the evolution of hominins (Behrensmeyer et al., 2002; Cohen et al., 2016; Isaac, 1978; Potts, 2013; Scholz et al., 2007; Shackleton, 1955).

1 Introduction

An areally extensive, low-density mantle anomaly under the EARS (e.g., Achauer and Masson, 2002; Ebinger and Sleep, 1998; Simiyu and Keller, 1997) helps support average elevations of >1000 m (Moucha and Forte, 2011) that started developing between 17 and 13 Ma (Wichura et al., 2015). As such, understanding the first-order mechanisms of rifting and the more regional spatiotemporal evolution of normal faults and individual sedimentary basins in East Africa are critical aspects for exploring how geodynamic and surface processes are potentially linked with topographic development, magmatic evolution, and long-term environmental and biotic impacts. In the EARS tectonically created changes in topography and relief have had far-reaching consequences, including impacts on atmospheric circulation patterns that in turn influenced rainfall patterns, drainage systems, and surface processes (e.g., Ebinger and Scholz, 2011; Levin et al., 2009; Sepulchre et al., 2006; Wichura et al., 2015, 2010). Changes in each of these aspects throughout the EARS over time have been difficult to quantify, but valuable information has been obtained from limited exposures of sedimentary and volcanic rift-basin strata (e.g., Ebinger and Scholz, 2011; Frostick and Reid, 1990; Morley et al., 1992; Odada et al., 2003; Renaut et al., 1999; Roberts et al., 2012; Saneyoshi et al., 2006; Tiercelin et al., 2012). In most sectors of the EARS, however, a direct inspection of such deposits is difficult, because old strata either lie below thick volcano-sedimentary sequences or areally extensive lakes (e.g., Cohen et al., 1993; Scholz and Finney, 1994) or because differential faulting, uplift, and erosion along the rift flanks have been insufficient to expose such deposits.

Cenozoic extension accompanied by rift-shoulder uplift and volcanism has created a complex patchwork of high basin-bounding fault scarps in the EARS (Baker and Wohlenberg, 1971; Ebinger et al., 2000; Tiercelin and Lezzar, 2002). Unlike the larger basins of the humid western branch of the EARS, the eastern branch hosts largely exposed basins that allow an assessment of depositional environments through time (e.g., Ebinger and Scholz, 2011; Tiercelin and Lezzar, 2002). In Kenya, Cenozoic rifting began in the Turkana depression and in the region of the Elgeyo escarpment during the Paleogene (Morley et al., 1992; Torres Acosta et al., 2015a), whereas the present-day rift configuration, characterized by the asymmetric northern, central and southern Kenya rift basins, was established after <15 Ma during E-W-oriented extension (e.g., Baker et al., 1988; Strecker et al., 1990). After a Pleistocene change in extension direction to the neotectonic NW-SE-orientation, internal rift segmentation by oblique normal faulting and continued formation of volcanic edifices and fault-bounded barriers ultimately compartmentalized the larger asymmetric basins into a series of distinct, transiently isolated, and partially connected small-scale sedimentary depozones (e.g., Bosworth et al., 1992; Strecker et al., 1990). Similar changes of fault kinematics in the western rift have led to oblique normal and strike-slip faulting along the rift center and border faults (Mortimer et al., 2007; Ring et al., 2005). These young zones of extension display complex geometries and fault patterns, often with pronounced impacts on drainage networks and the formation of lakes (Bergner et al., 2009).

These young zones of extension are the current manifestations of ongoing magmatic and extensional tectonic processes, that are focused on an approximately 40-km-wide volcano-tectonic axis in the inner graben of the Kenya Rift. As such, this region affords insight into the style, rate, and timing of closely-spaced extensional zones that are intimately associated with large volcanic eruptive centers, magmatic extrusions, hydrothermal activity and geophysical anomalies (e.g.,

Baker, 1986; Baker et al., 1971; Macdonald, 2002; Renaut et al., 2017; Roecker et al., 2017; Rooney, 2020; Simiyu and Keller, 1997; Tarits et al., 2006; Williams et al., 1984).

In this thesis, I will analyze the mid-Pleistocene to recent extension zones and their spatial and temporal patterns in the southern and central parts of the Northern Kenya Rift (NKR), in the Central Kenya Rift (CKR), and in parts of the Southern Kenya Rift (SKR). This analysis provides important information on the amount of vertical offsets, the amount of extension, and the character of kinematic linkage between differently oriented fault zones within the inner graben. These young structural depressions can be viewed as magmatic centers with intervening zones of extension in a nascent continental rift and they are the harbingers of a more evolved rifting stage, where magmatic centers may constitute nucleation points for future magma-assisted rifting stages.

More specifically, I will focus on a number of timely research topics and analytical tasks that form the foundation for this research and that will help to understand the structural and geomorphic signals of advanced rifting recorded in the landscape:

- Morphometric analysis of the 12-m-resolution TanDEM-X science DEM, first with the aim to identify active fault zones in the context of the overall East African Rift evolution and second, to document their impact on the fluvial network in the Kenya Rift (addressed in the manuscripts presented in chapters 2 and 5).
- Structural mapping using the TanDEM-X science DEM and structure-from-motion generated DEM complemented by field inspection and validation, including description of fault-scarp morphology and variability in vertical offsets, as well as an analysis of the youngest manifestations of caldera volcanism and faulting to elucidate the youngest history of faulting during the late Pleistocene and Holocene (addressed in the manuscripts of chapters 2 and 3).
- Compilation of geochronologic information from previous studies and sampling for Ar/Ar-dating of key lava flows within the inner graben aimed at developing a robust chronostratigraphy of Pleistocene to Holocene volcanic units. The goal is to derive a tectonic subsidence history and and an extension rate that can be compared with geodetically determined deformation rates (addressed in the manuscript presented in chapter 2).
- Geomorphic, structural and sedimentological analysis of Quaternary fault-bounded basins in the SKR in the context of structurally and magmatically controlled basin compartmentalization and its impact on fluvial network evolution and long-term paleoenvironmental conditions (addressed in the manuscripts of chapters 4 and 5).

1.2 Brief geological history of the Northern and Central Kenya rifts

In the Cenozoic EARS (Fig. 1.1), magmatism has been a major feature since the Paleogene, and it has been accompanied by tectonic deformation (Boone et al., 2018; Chapman et al., 1978; Morley et al., 1992; Rooney, 2017; Torres Acosta et al., 2015a). The present-day morphology of the Kenya Rift, however, is a phenomenon that has mainly evolved during the Neogene, but older rift structures and volcano-tectonic strata have been imaged by seismic reflection profiling (e.g., Dunkelman et al., 1989; Mugisha et al., 1997) or they have been inferred from other geophysical observations (e.g., Hautot et al., 2000; Plasman et al., 2017). Since the Miocene, the uplift of the East African Plateau between 17 and 13.5 Ma (Wichura et al., 2015) and ubiquitous volcanism in the greater Kenya Rift region have formed an up to 2000 to 3000-m-high elevated dome-shaped area that hosts widespread lava flows and volcanic edifices (e.g., Baker et al., 1971; Chapman et al., 1978; Chapman and Brook, 1978; Crossley and Knight, 1981; Dunkley et al., 1993; King et al., 1972). Angular unconformities and lateral pinch-outs in the oldest volcanic units reflect the early development of a central sag area and help to define the onset of extensional deformation during that time (Chapman et al., 1978; Jones and Lippard, 1979; Pickford, 1982). The widespread Middle Miocene flood phonolites of central Kenya (Fig 1.1b) document the earliest faulting and the development of large rift-bounding faults in the NKR and CKR that influenced subsequent volcanic and sedimentary deposition in the region of the present-day rift. For example, the Elgeyo fault on the western boundary of the NKR is the oldest structure of the Kenya Rift and younger strata were banked against it (Chapman et al., 1978; Mugisha et al., 1997). In general, extension and faulting in the Miocene generated an approximately north-south oriented halfgraben system that approximately follows the suture between the Archean Tanzania Craton and the Proterozoic Mozambique Belt (Hetzel and Strecker, 1994; McConnell, 1972; Smith and Mosley, 1993). The principal faults of this early Kenya Rift halfgraben dip to the east (Chapman et al., 1978; Crossley, 1979; Dunkley et al., 1993; Morley et al., 1992; Smith, 1994). During the late Miocene to early Pliocene, however, the Kenya Rift transitioned to a full-graben system and antithetic normal faults were generated along the present-day eastern rift margin (e.g., Baker et al., 1988; Dunkley et al., 1993). At that time, the Kenya Rift was bounded to the west by the east-dipping Elgeyo fault, and the faults that bound the Kamasia Range (southern NKR), the Mau escarpment (CKR), and the Nguruman escarpment (SKR) (Chapman et al., 1978; Crossley, 1979; Jones and Lippard, 1979). To the east, the Sattima Fault (CKR) and the faults defining the Ngong-Turoka-escarpment (SKR) developed subsequently (e.g., Baker, 1986; Fig. 1.1) The area was covered with a trachytic volcanic series (the >2.5 to 3 Ma old “Plateau Trachytes”), which are the latest effusive volcanic rocks that occur on the present-day rift horst areas.

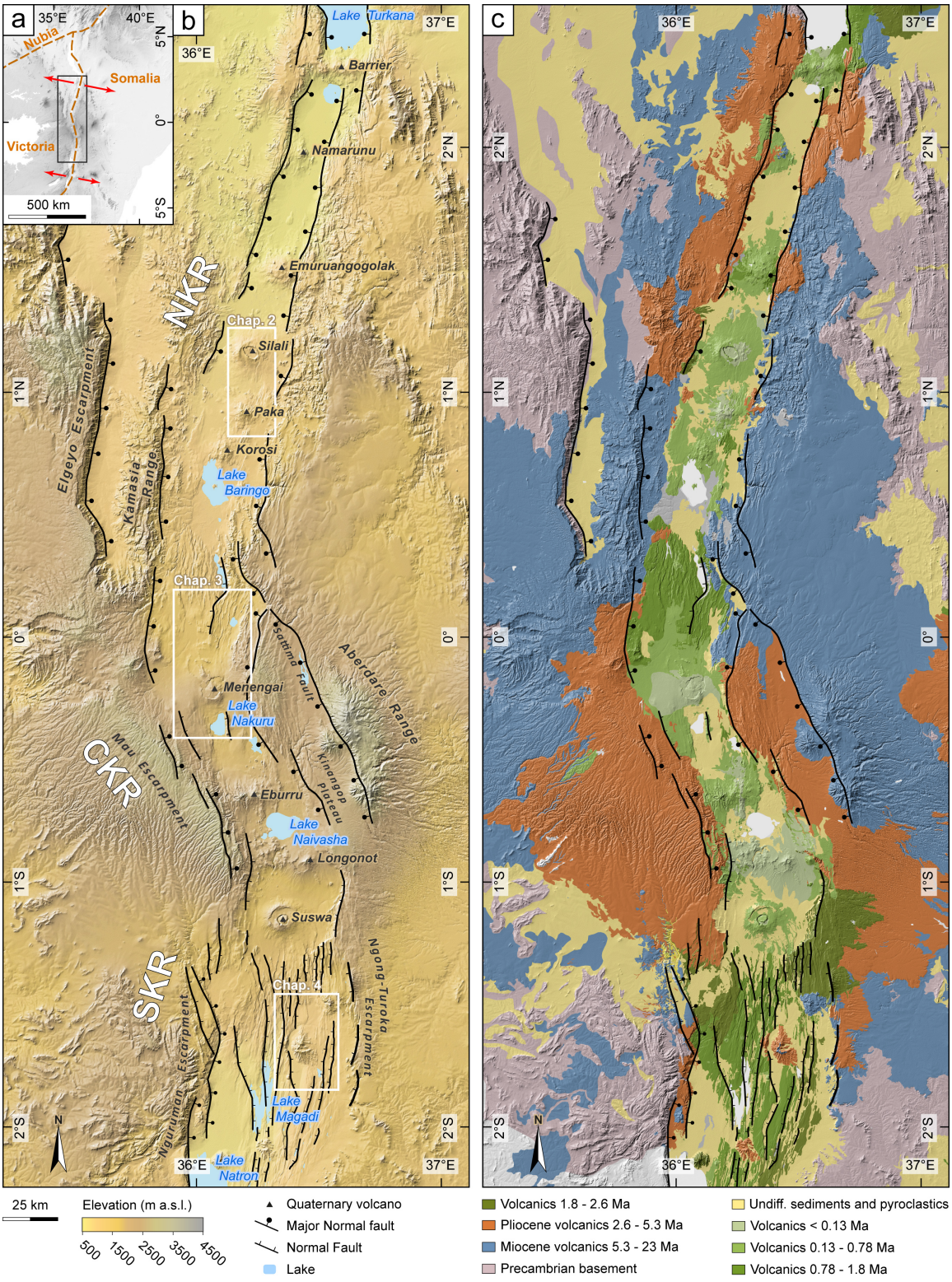

Figure 1.1. Overview map of the Kenya Rift.

(a) *Plate tectonic configuration showing plate boundaries (orange) and present-day extension direction (red arrows).* ***(b)*** *Topographic map of the Kenya Rift, subdivided into the Northern (NKR), Central (CKR) and Southern (SKR) Kenya Rift. White boxes denote the study areas of chapters 2 to 4 (chapter 5 covers the entire Kenya Rift).* ***(c)*** *Geological map of the Kenya Rift (from Guth, 2014; Ministry of Energy of Kenya, 1987).*

East-West-directed extension during the early rift evolution shaped the first-order, rift-bounding structures, and hence the Kenya Rift can be subdivided into the NNE-SSW-striking SKR and NKR, and the NNW-SSE-oriented CKR. Subsequently, tectonic subsidence was focused in the inner graben (e.g., Baker et al., 1988; Dunkley et al., 1993; Strecker et al., 1990); this neotectonic depression also limits the areal extent of all subsequently deposited Quaternary volcanic and sedimentary units (Fig. 1.1c shows the age of the volcanic units of the Kenya Rift, which highlights how the areal extent of the younger volcanic units of the Kenya Rift is more limited than the extent of older units).

Within the inner graben, areally extensive sequences of early to mid-Pleistocene flood volcanics are confined by the bounding fault scarps on the west and east, respectively. In the SKR, these units are represented by the Magadi trachytes (e.g., Baker, 1958); in the CKR, they are represented by the Gilgil, Naivasha, and Mbaruk trachytes (e.g., Leat, 1991) as well as the Hannington Trachyphonolites (e.g., Clément et al., 2003; McCall, 1967) and Baringo Trachytes farther north (e.g., Deino and McBrearty, 2002). These units are pervasively faulted by North to NNE-striking normal faults and these areas comprise a small-scale horst-and-graben topography on the floor of the rift valley that is responsible for the compartmentalization of the inner graben. Within the inner graben, a series of Quaternary volcanic centers exist (Williams et al., 1984) and consist of trachyte-basalt shields that have been affected by caldera collapse (e.g., Baker et al., 1971; Dunkley et al., 1993; Hackman, 1988; Leat, 1984; Williams, 1978). From north to south these volcanic centers are the Barrier, Namarunu, Emuruangogolak, Silali, Paka, and Korosi volcanoes in the NKR, the Menengai, Eburru, Longonot volcanoes in the CKR, and Mt. Suswa in the SKR (e.g., Macdonald and Bagiński, 2009; Williams et al., 1984; Fig. 1.1b). Of these volcanic edifices Menengai caldera, which is located in the transition between the southern sector of the NKR and the northern part of the CKR, constitutes the youngest large-volume volcano collapse site in in the Kenya Rift, because it was formed after 36 ka (Blegen et al., 2016). This eruptive center is responsible for the current hydrological isolation between the central and northern areas of the Kenya Rift, but well-developed lacustrine shorelines indicate that this barrier was overtopped during wetter climatic conditions during the Holocene, when fluvial connectivity existed between the Northern and Central Kenya rifts.

The volcanic edifices are aligned along the volcano-tectonic axis of the rift. This volcano-tectonic axis is also characterized by high heat flow, hydrothermal activity, seismicity, active normal faulting, and dike intrusion (e.g., Dunkley et al., 1993; Sturchio et al., 1993; Tongue et al., 1994). This is a unifying character of all three major rift sectors. For example, in the Central and Southern Kenya Rift sectors, seismicity and young extensional deformation is dominant and characterizes the inner graben areas, including the Lake Magadi (Atmaoui and Hollnack, 2003; Ebinger et al., 2017; Ibs-von Seht et al., 2001), Olorgesailie, Lake Naivasha, Lake Elmentaita areas, as well as the Lake Baringo area and regions farther north (e.g., Tongue et al., 1994, 1992).

1.3 Statement regarding author contributions

This cumulative dissertation comprises two published, and one submitted manuscript: an additional manuscript is in the review stage by the co-authors and will be submitted in due course. Chapter 2 and chapter 3 correspond to manuscripts where I was the first author, chapters 4 and 5 are studies where I significantly contributed. The four manuscripts are referenced throughout the text and the numbering of the individual chapters, figures, and tables was adjusted to the cumulative style of this thesis. The bibliography and all supplementary material for the four manuscripts are also presented at the end of the dissertation.

After this introduction to the research topics and to the geodynamic and structural setting of the EARS, I present the four research chapters which are followed by a brief discussion and conclusion of my studies. Each research chapter is introduced by the relevant research question and research hypothesis to be tested, a brief geological introduction to the study area, and the specific methodology used to answer the research questions. The study areas presented in the different contributions are shown on figure 1.1b.

Below, I briefly review the different author contributions.

- Chapter 2: "Mid-Pleistocene to recent crustal extension in the inner graben of the Northern Kenya Rift", in review at *Geochemistry, Geophysics, Geosystems* of the American Geophysical Union, is authored by S. Riedl, D. Melnick, L. Njue, M. Sudo, and M. R. Strecker.

  Author contributions: SR and MS developed the research design. SR developed the analysis code, performed the study of the long-term extension rates, did the radioisotopic dating and produced all figures. SR wrote the paper supported by MS. All co-authors contributed to the discussion of the research results.

- Chapter 3: "Continental rifting at magmatic centres: structural implications from the Late Quaternary Menengai Caldera, central Kenya Rift", published 2020 in the *Journal of the Geological Society* 177, 153–169, https://doi.org/10.1144/jgs2019-021, is authored by S. Riedl, D. Melnick, G. K. Mibei, L. Njue, and M. R. Strecker.

  Author contributions: SR, DM and MS designed the study. SR did the structural analysis of the Menengai caldera. SR produced all figures. SR wrote the paper supported by DM and MS. All co-authors contributed to the discussion of the research results.

- Chapter 4: "Increased ecological resource variability during a critical transition in hominin evolution", published 2020 in *Science Advances* 6, eabc8975, https://doi.org/10.1126/sciadv.abc8975, is authored by R. Potts, R. Dommain, J. W. Moerman, A. K. Behrensmeyer, A.L. Deino, S. Riedl, E. J. Beverly, E. T. Brown, D. Deocampo, R. Kinyanjui, R. Lupien, R. B. Owen, N. Rabideaux, J. M. Russell, M. Stockhecke, P. deMenocal, J. T. Faith, Y. Garcin, A. Noren, J. J. Scott, D. Western, J. Bright, J. B. Clark, A. S. Cohen, C. B. Keller, J. King, N. E. Levin, K. B. Shannon, V. Muiruri, R. W. Renaut, S.M. Rucina, and K. Uno.

Author contributions: RP conceived the study. RP and AKB selected the drilling location. DD, RK, JWM, RBO, JMR, NR and MS contributed data. SR and YG did the age and proxy uncertainty analysis of the drill core data. SR and PdM did the time-series analysis of the dataset. RP and RD wrote the manuscript, with support from SR, JWM and AKB. All authors contributed to methods, analyses, and discussion of the data interpretations. SR, RD, YG, JWM, JBC, AKB, PdM, JTF and RP developed the figures. Specifically, SR created figures 4.3 and 4.4, and figures C.2, C.3, C.4, C.5, C.7, C.9. KBS, RD, AN, and JBC provided field and laboratory support.

- Chapter 5: "An early Holocene river system along the Kenya Rift valley and its influence on faunal exchange and longitudinal diversity gradients in East Africa", to be submitted to the *Proceedings of the National Academy of Sciences*, is authored by R. Dommain, S. Riedl, L. Olaka, P. deMenocal, A. Deino, R. B. Owen, V. Muiruri, J. Müller, R. Potts, and M. R. Strecker.

  Author contributions: RD designed the study. RD, SR, LO, AD, RP, and MS performed field sampling. SR did UAV surveys and generated a structure-from-motion digital elevation model of the Koora basin. RD, SR, PdM, AD, BO, and VM performed lab analyses. RD, SR, AD, and BO analyzed the data. RD and SR integrated the data. SR did the spatial analysis of the digital elevation models, the reconstruction of the paleo-catchments and reconstruction of the river network. RD and SR wrote the manuscript, with support from RP and MS. All co-authors contributed to the discussion of the research results. SR created figures 5.1 and 5.3. RD created figure 5.2 with contributions from SR.

  An updated version of chapter 5 is in revision at PNAS as of February 01, 2022.

Chapter 2

Mid-Pleistocene to recent crustal extension in the inner graben of the Northern Kenya Rift

Simon Riedl[1], Daniel Melnick[2], Lucy Njue[3], Masafumi Sudo[1], Manfred R. Strecker[1]

1. University of Potsdam, Institute of Geosciences, Germany
2. Instituto de Ciencias de la Tierra, Universidad Austral de Chile
3. Geothermal Development Company, Kenya

This chapter has been submitted to *Geochemistry, Geophysics, Geosystems* and is awaiting minor revisions.
Riedl, S., Melnick, D., Njue, L., Sudo, M. and Strecker, M.R. Mid-Pleistocene to recent crustal extension in the inner graben of the Northern Kenya Rift. *In review at Geochemistry, Geophysics, Geosystems*.
Supporting information is available in Appendix A.

Abstract

Magmatic continental rifts often constitute nascent plate boundaries, yet long-term extension rates and transient rate changes associated with these early stages of continental breakup remain difficult to determine. Here, we derive a time-averaged minimum extension rate for the inner graben of the Northern Kenya Rift (NKR) of the East African Rift System for the last 0.5 m.y. We use the TanDEM-X science digital elevation model to evaluate fault-scarp geometries and determine fault throws across the volcano-tectonic axis of the inner graben of the NKR. Along rift-perpendicular profiles, amounts of cumulative extension are determined, and by integrating four new $^{40}Ar/^{39}Ar$ radiometric dates for the Silali volcano into the existing geochronology of the faulted volcanic units, time-averaged extension rates are calculated. This study reveals that in the inner graben of the NKR, the long-term extension rate based on mid-Pleistocene to recent brittle deformation has minimum values of 1.0 to 1.6 mm yr^{-1}, locally with values up to 2.0 mm yr^{-1}. A comparison with the decadal, geodetically determined extension rate reveals that at least 65% of the extension must be accommodated within a narrow, 20-km-wide zone of the inner rift. If additional magmatic diking is considered, a minimum of 78% of the total rift extension may occur within the inner graben. In light of virtually inactive border faults of the NKR, we show that extension is focused in the region of the active volcano-tectonic axis in the inner graben, thus highlighting the maturing of continental rifting in the NKR.

2.1 Introduction

Continental rifts give an insight in the early stages of divergence and breakup of the continental lithosphere. The extension in active rift zones is accommodated by brittle deformation, i.e. normal faulting, and by magmatic processes such as dike intrusions (e.g., Abbey and Niemi, 2020; Muirhead et al., 2016, 2015; Oliva et al., 2019; Weinstein et al., 2017; Wright et al., 2016). On decadal timescales, these processes can be quantified by geodetic and geophysical methods, such as GPS measurements (e.g., Saria et al., 2014) InSAR analyses (e.g., Keir et al., 2009; Wright et al., 2006) or recordings of local seismicity (e.g., Ebinger et al., 2017; Wilks et al., 2017). The long-term character of extension rates on geologic timescales, however, remains difficult to determine, especially within nascent plate boundaries, where the crust is entirely continental, and rate determinations that involve the analysis of the ocean-floor (e.g., DeMets and Merkouriev, 2019, 2016) cannot be applied. However, if well-preserved normal-fault scarps in chronologically constrained rock exposures exist, the horizontal component of fault motion can be used to determine extension rates on longer timescales (e.g., Mouslopoulou et al., 2012; Muirhead et al., 2016; Shmela et al., 2021; Siegburg et al., 2020). This study takes advantage of such tectonic archives in the Northern Kenya Rift (NKR) with the aim to derive a robust long-term extension rate for the eastern branch of the East African Rift System (EARS) during the last 0.5 m.y.

The EARS comprises a magmatic eastern branch and a western branch that exhibits localized magmatic activity (e.g., Baker and Wohlenberg, 1971; Ebinger, 1989). Plate tectonic reconstructions for East Africa suggest a stable extension rate of 4.2 – 5.0 mm yr^{-1} for the entire EARS over a multi-million-year timescale based on reconstructions of seafloor spreading data (DeMets and Merkouriev, 2016). However, such data does not allow to distinguish between the extension at the western and at the eastern branch of the EARS. Therefore, long-term extension rates of exclusively the eastern branch have remained difficult to resolve. On the contrary, short-term extension rates are available; geodetic plate kinematic models have yielded decadal-scale extension rates of 2 – 3 mm yr^{-1} for the eastern branch (Saria et al., 2014). However, it is not known whether extensional processes have operated at similar rates over intermediate timescales involving several 10^3 to 10^5 years. In other areas of the EARS, such as the Northern Main Ethiopian Rift, periods of higher and lower extension rates on such timescales have been reported (e.g., Siegburg et al., 2020). In addition, more mature continental rifts such as the Afar region are affected by extension characterized by magmatic cycles lasting between 20 and 40 kyrs (Medynski et al., 2016, 2013), but shorter pulses of high magmatic and tectonic activity have been documented as well (Ayele et al., 2007; Ebinger et al., 2010; Wright et al., 2006). Such episodes can contribute significantly to the long-term extension record of the corresponding plate margins.

The Kenya Rift is younger than the Main Ethiopian Rift to the north, and although it has lower spreading rates and less magmatic activity, a more active rifting phase involving dike intrusion is reported to have occurred in 2007 in the Natron Basin of northern Tanzania and southern Kenya (Biggs et al., 2009a; Calais et al., 2008). It is therefore reasonable to expect that continental rifts during the early stages of tectonic evolution could also be subject to varying extensional activity

over time. Consequently, to understand the processes which shape a continental rift in its initial phase, it is necessary to complement geodetic data with geologic long-term rates.

However, active tectonism in rifts is also accompanied by simultaneous erosion and degradation of fault scarps and rift-shoulder areas, with the subsiding graben providing accommodation space for the resulting sedimentary and volcanic deposits. If volcanic activity is intense and the rates of erosion and sedimentation high, or if the rate of extension is very low, the manifestations of extensional processes can be masked by erosion of fault scarps and by draping of the sedimentary and volcanic units over the various fault generations (Kübler et al., 2018; McCalpin, 2005; Vanneste et al., 2001). Examples of the masking of long-term tectonic processes are the Rio Grande Rift, which has a very low extension rate of ~0.12 mm yr^{-1} (Ricketts et al., 2014) and Iceland, which has a relatively high extension rate (~2 cm yr^{-1}), but is affected by glacial overprint. In contrast to either of the above examples, the semiarid to arid NKR has both exceptionally low erosion rates (between 0.0015 and 0.0130 mm yr^{-1} denudation; Torres Acosta et al., 2015b), and an extension rate of ~2.5 mm yr^{-1} (Saria et al., 2014). Importantly, surface offsets in this environment are large enough to overcome the effects of scarp modification and the very low volumes moved by erosion and deposition, resulting in a good preservation of fault-scarp morphology. Fault scarps within the tectonically active inner graben along the volcano-tectonic axis of the NKR are mainly developed in volcanic rocks, which furthermore provide an excellent opportunity to derive a chronology of faulting. This unique combination of sufficiently high deformation rates with low rates of erosion thus results in a generally high preservation potential for fault scarps with a broad age spectrum and good dating potential, which makes the NKR an ideal location for studying the faulting history within a continental rift over timescales of up to 10^6 years.

In this study we investigated the extension rate during rifting over the last 0.5 m.y. We focused on the ~40-km-wide, magmatically active inner graben of the NKR, where closely spaced normal faults mainly affect syntectonic volcanic units associated with the Pleistocene Paka (0.90° N 36.20° E) and Silali (1.15° N 36.20° E) volcanoes. This region is also characterized by pronounced aridity, low fluvial connectivity with other rift sectors, and some of the lowest erosion and sedimentation rates in the Kenya Rift (Garcin et al., 2017; Torres Acosta et al., 2015b, 2015a).

To decipher the faulting history in this rift sector we first used satellite-derived digital elevation models (DEMs; i.e., the TanDEM-X science DEM) to determine the apparent throw along normal faults that have affected the volcanic rocks of the Pleistocene Paka and Silali caldera volcanoes and their immediate surroundings in the inner graben. We then used the individual fault geometries to establish east-west cross-sections over the full width of the inner graben and plotted cumulative vertical offsets across these individual faults. Finally, we used $^{40}Ar/^{39}Ar$ geochronology on the faulted volcanic units and synthesized existing geochronological data to refine the Quaternary chronological framework and derive estimates of long-term extension-rates for the inner graben.

2.2 Regional geodynamic and geological setting

2.2.1 Plate tectonic setting and history of the NKR

The EARS is a nascent divergent plate boundary located between the Nubian plate and the Somalian plate, and surrounds the Victoria microplate (e.g., Calais et al., 2006; Saria et al., 2014; Stamps et al., 2008). A long-term divergent motion between the Nubian and Somalian plates since at least 16 Ma has been determined based on the geometry of nearby ocean ridges (SW India Ridge, Red Sea, Gulf of Aden; DeMets and Merkouriev, 2016) and sustained, steady extensional processes have been inferred for at least the last 5.2 m.y. (DeMets and Merkouriev, 2016). The northern part of the EARS comprises the Afar and Ethiopian rifts, while farther south it consists of two branches: a generally low-magmatic western branch and a magmatically very active eastern branch. The Kenya Rift is part of the eastern branch, separating the Somalian plate to the east from the Victoria microplate to the west (Fig. 2.1a).

In Kenya, Paleogene magmatism preceded the development of large-scale rift faults in the northernmost sector of the rift (Morley et al., 1992). Volcanism has, however, been ubiquitous along the entire length of the present-day Kenya Rift since the Miocene (e.g., Baker et al., 1971; Chapman et al., 1978; Chapman and Brook, 1978; Crossley and Knight, 1981) and the associated volcanic units are currently exposed along the rift shoulders (Fig. 2.1b-c). The onset of faulting in the NKR post-dates the regional emplacement of the Middle Miocene flood phonolites that covered this part of central Kenya (op. cit.). The relationship between volcanism and extensional processes is illustrated at latitude 1° N by the history of the east-dipping Elgeyo Fault that forms the western boundary of the NKR; the units affected by this fault are also exposed in the footwall of an east-dipping fault that delimits the Kamasia Range within the NKR (Chapman et al., 1978; Mugisha et al., 1997). Miocene faulting generated a generally north-south oriented half-graben array in northern Kenya, with east-dipping principal faults (Chapman et al., 1978; Crossley, 1979; Dunkley et al., 1993; Morley et al., 1992; Smith, 1994). This was followed in the Late Miocene to Early Pliocene by west-dipping, antithetic normal faulting along the present-day eastern margin of the rift, which resulted in the development of the Kenya Rift into a full-graben system (e.g., Baker et al., 1988; Dunkley et al., 1993). This full-graben system continued to develop into the Pliocene, accompanied by a relatively narrow zone of tectonic subsidence, known as the inner graben (e.g., Baker et al., 1988; Dunkley et al., 1993; Strecker et al., 1990). Whereas volcanic units still outside of the inner graben are not younger than ~2.5 to 3 Ma (e.g. the Orus Trachyte and Emuruagiring Lavas on the Eastern rift shoulders; Dunkley et al., 1993), the Quaternary volcanic processes have been restricted to this inner graben (e.g., Baker et al., 1988; Dunkley et al., 1993). The inner graben accommodates and spatially restricts an areally extensive series of flood trachyphonolites and trachytes that span the region between Lake Magadi and Lake Turkana (e.g., Baker, 1958; McCall, 1967). In the NKR these units are largely represented by the Hannington Trachyphonolite (~0.89 Ma; Clément et al., 2003), the Baringo Trachyte (0.545 ± 0.003 Ma; Deino and McBrearty, 2002), and the Loyamarok Trachytes/Phonolites (0.57 Ma; e.g., Carney, 1972; Hackman, 1988). In the western part of the NKR's inner graben these units belong to the ~0.6 to ~0.3 m.y. old Kapthurin Formation (e.g., Deino and McBrearty, 2002). The trachyphonolitic and

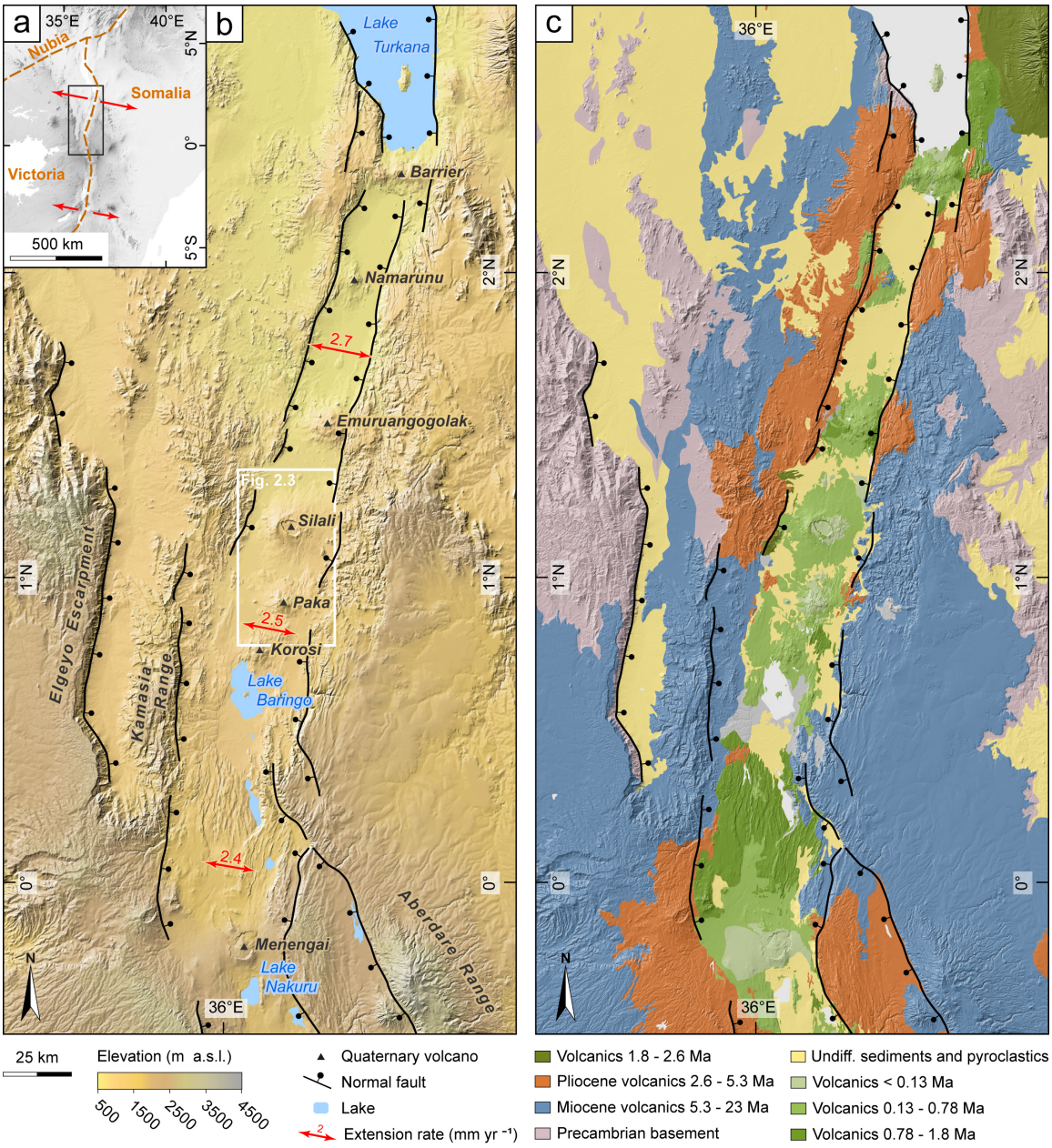

Figure 2.1. Study area of Chapter 2.

(a) *Overview map shows plate boundaries of the East African Rift. Red arrows represent present-day extension rate, after Saria et al. (2014). The divergent movement of the Somalia and Victoria plates shapes the Kenya Rift (black box).* ***(b)*** *Topographic map of the NKR, showing the location of rift border faults and quaternary volcanoes. Present-day extension (red arrows) is based on the plate kinematic model by Saria et al. (2014). White box shows the location of the study area.* ***(c)*** *Geological overview of the NKR. Colors indicate ages of volcanic units. As the rift developed during time, the increasing topographic gradient restrict younger volcanic rocks to a spatially narrow zone of the rift. Quaternary volcanic rocks (green) are therefore only exposed in the inner graben, where volcano-tectonic activity is focused.*

trachytic flows form the basal strata of the inner graben; they are cut by north to north-northeast striking normal faults that are less than 0.5 m.y. old. This youngest phase of extensional tectonism was accompanied by trachyte-basalt shield volcanism (e.g., Baker et al., 1971; Dunkley et al., 1993; Hackman, 1988; Williams, 1978) and the formation of isolated silicic domes (Macdonald et al., 1987; Thompson and Dodson, 1963). In the NKR the Korosi, Paka, Silali, and Emuruangogolak caldera volcanoes are all located within the inner graben; they are aligned along the volcano-tectonic axis of the rift, which is also characterized by numerous sites with ongoing hydrothermal activity, active normal faults, seismicity, and dike intrusion (Dunkley et al., 1993; Sturchio et al., 1993; Tongue et al., 1994). In the southern Kenya Rift, seismicity is common and young zones of extensional deformation are clearly evident in the Lake Magadi area (Atmaoui and Hollnack, 2003; Ebinger et al., 2017; Ibs-von Seht et al., 2001).

2.2.2 Geology of the Paka and Silali inner graben volcanoes

The basin floor of the inner graben of the NKR has an elevation of about 870 m in the south and about 650 m in the north. Our study area covers a 60 km long and 20 km wide section of the inner graben (Fig. 2.1b). It includes the Paka volcano in the south and the Silali volcano in the north, and a brief history of these Pleistocene volcanoes is therefore appropriate (Fig. A.1 shows a geological map of these two volcanoes). The basal volcanic deposit associated with the Paka volcano has been dated to 0.390 ± 0.006 Ma (Dunkley et al., 1993); this unit is overlain by a series of younger trachytic and basaltic lavas (mapped as “Lower Trachytes”, “Lower Basalts”, “Upper Trachytes”, and “Upper Basalts” by Dunkley et al., 1993) and pyroclastic deposits, which combine to form a volcanic feature that rises to ~650 m above the rift floor. Its summit caldera formed about 0.01 m.y. ago (Dunkley et al., 1993). Similarly, the basal deposit associated with the ~750 m high Silali volcano, some 28 km to the north of the Paka volcano, has been dated to 0.224 ± 0.009 Ma and is overlain by younger volcanic strata (mapped as “Kapedo Tuffs”, “Summit trachytes”, “Katenmening lavas” and a “post-caldera lava sequence” by Dunkley et al., 1993) that were erupted during multiple phases of high activity (Dunkley et al., 1993; Macdonald et al., 1995; Smith et al., 1995). The Silali caldera has been interpreted to be younger than 0.063 ± 0.010 Ma (Smith et al., 1995) and the most recent volcanic activity (a series of faulted basaltic lava flows on the eastern and northern flanks of the volcano) is as young as 0.004 ± 0.002 Ma (Dunkley et al., 1993; Smith et al., 1995). No eruptions are known to have been witnessed by humans at either of the two volcanoes, but they are both associated with pronounced geothermal activity and InSAR studies indicate that they are both affected by inflation and deflation events (Biggs et al., 2016, 2009b; Friese, 2015).

Both the Paka and Silali volcanoes are traversed by a ~10 to 15 km wide, north to north-northeast striking zone of closely spaced normal faulting. This zone comprises a series of horst-and-graben structures on the Paka volcano’s eastern flanks, bounded to the west by a fault that runs 1 km to the west of the summit caldera. The fault zone traverses the central and eastern parts of the shield volcano but does not affect its western flanks. The fault zone is wider at the Silali volcano than at the Paka volcano; it comprises horst-and-graben structures on Silali’s southern, eastern and northern flanks. This fault zone corresponds to the volcano-tectonic axis of the NKR; it rep-

resents the youngest fault activity in the NKR, which has continued from the time of formation of the central volcanoes right up to the present, and it is the main focus of this study.

2.3 Materials and Methods

2.3.1 Analysis of the digital elevation model

We used the satellite-derived TanDEM-X Science DEM (12 m spatial resolution) to map and describe the fault geometries within the NKR. Since the normal fault scarps in the study area are usually close to vertical, fault heaves - and therefore the amount of extension - cannot be easily determined in the field. However, the hanging-walls and footwalls of the faulted volcanic rocks show little degradation and have little sedimentary cover, which means that fault throws can be measured using the vertical offsets at the fault scarps. Extension can then be calculated on the basis of the throw and a range of dips (e.g., Melnick et al., 2012).

We first mapped fault-scarp locations and created apparent displacement-length profiles for the mapped fault scarps. The vertical offsets for each fault scarp was determined using a six-stage workflow. (a) DEM strips were extracted from the TanDEM-X Science DEM along zones that extended a maximum distance of 500 m either side of each fault scarp. The extracted fault-related DEM strips were detrended along the strikes of the faults in order to avoid overestimation of vertical fault offsets on hillslopes. (b) Each fault was then divided into 96 m (8 DEM pixel) long segments and each segment analyzed to determine the apparent vertical offset (Fig. 2.2a). (c) An across-scarp swath profile was then created for each fault segment. The corresponding footwall and hanging-wall areas of each profile were determined using an assisted-manual approach and planes were fitted to these footwall and hanging-wall surfaces. The elevation difference between the two planes was then extracted at each scarp location to obtain the apparent vertical displacement of the fault segment (Fig. 2.2b). (d) The 1-sigma uncertainty in the apparent displacement was determined for each fault segment (using Gauss' error propagation principles) as the square root of the sum of the squares of the uncertainties in hanging-wall and footwall elevations. (e) In order to take into account the effect of possible surface erosion we assumed a maximum denudation rate of 1.3 m per 100 kyr, this being the average maximum erosion rate in the NKR determined using cosmogenic nuclides (Garcin et al., 2017; Torres Acosta et al., 2015b). (f) These throws determined for each fault segment were then projected back on the map (Fig. 2.2c) and also combined into displacement-length plots along each of the faults. The analysis was done using TopoToolbox (Schwanghart and Scherler, 2014) and MATLAB (Mathworks, 2020), the code is available in Riedl et al. (2021a).

In order to determine the cumulative throw across the whole volcano-tectonic axis of the NKR's inner graben we compiled representative east-west cross-sections across the rift floor and added the individual fault throws obtained for the whole cross-section. The rift-wide extension was then calculated by determining fault heaves based on fault throw at a range of different dips (e.g., Bell et al., 2011; Lamarche et al., 2006; Melnick et al., 2012). Representative fault planes are rarely exposed in the NKR but fault dips of between 55° and 65° have been reported from seismic reflection profiles from Lake Turkana (Dunkelman et al., 1989, 1988; Morley et al., 1992) and also from

field observations in the southern part of the Kenya Rift (Strecker, 1991). We therefore used a dip of 1.80 ± 0.35 m·m^{-1} (equal to 55° to 65°) to calculate the amount of extension for the mapped faults. Similar dips were applied in fault displacement-length studies of the Kenya Rift (60° by Muirhead et al., 2016; 65° by Shmela et al., 2021). The derived extension values were then combined with radioisotopic dates to estimate minimum long-term extension rates for each of the east-west profiles (see next section).

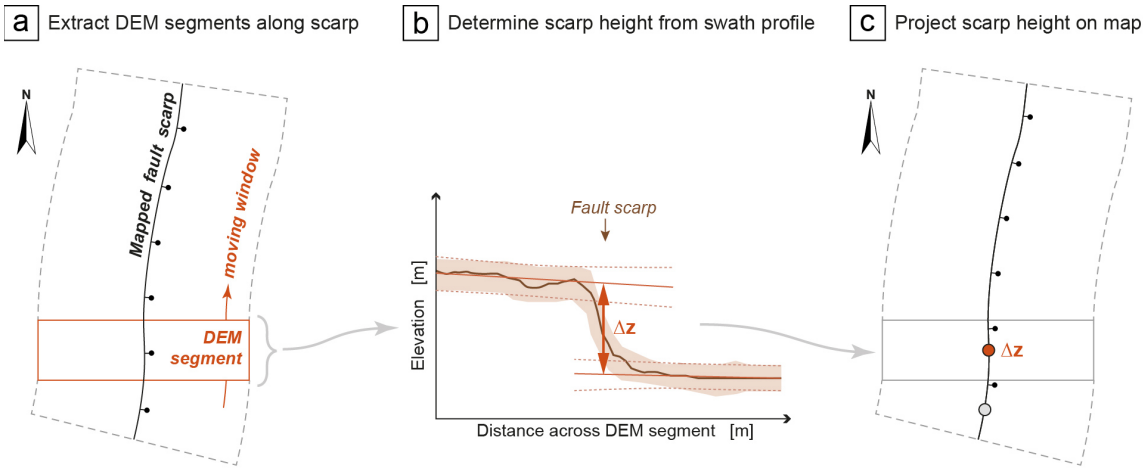

Figure 2.2. Schematic workflow for scarp height detection and measurement.
(a) *The TanDEM-X Science DEM was extracted along each of the mapped fault scarps and detrended along strike. These DEM strips were then partitioned into 96 m long segments along the length of each fault.* ***(b)*** *A swath profile was then created across each such DEM segment, with each profile representing a cross-section across the fault scarp at a specific distance along the fault. In each such segment of the fault, planes were fitted to the hanging wall and foot-wall surfaces and the scarp height for each profile extracted as the elevation difference between the two at the scarp location.* ***(c)*** *The extracted scarp heights for each DEM strip were then saved on the map as data points along the fault.*

2.3.2 Geochronology

To obtain age constraints for the faulted volcanic rocks we used $^{40}Ar/^{39}Ar$ geochronology, integrating previously published radioisotopic ages for rock units in the NKR with new results from our own $^{40}Ar/^{39}Ar$ analyses of samples from the Silali volcano. We compiled the radioisotopic ages reported by Smith et al. (1995), the published chronology of the Quaternary rift volcanoes (Dunkley et al., 1993), and 12 of the $^{40}Ar/^{39}Ar$ ages from the Paka volcano obtained by Potsdam University through a consulting contract with the German Federal Institute for Geosciences and Natural Resources (Friese, 2015) (Table A.1), with new $^{40}Ar/^{39}Ar$ geochronology data for four samples from the Silali volcano, which were analysed at the geochronology laboratory of the University of Potsdam (Table A.2). These new samples were two groundmass and one multi-crystal feldspar separate of massive lava flows, and one feldspar separate of a tephra layer. All the samples were irradiated for four hours at the Oregon State University Reactor, in two charges, with the neutron flux during irradiation monitored using Fish Canyon Tuff sanidine (FC3S: age

of 27.5 ± 0.2 Ma; Ishizuka, 1998; Uto et al., 1997) for samples S04-01 and S01-01 in 2015, and Alder Creek sanidine (ACs-2: age of 1.193 ± 0.001 Ma; Nomade et al., 2005) for samples S06-03 and S07-01 in 2019. The argon isotope analyses and age calculation for S04-01 and S01-01 followed the methodology of Uto et al. (1997), and those for S06-03 and S07-01 were conducted using MassSpec software (developed by A. Deino of Berkeley Geochronology Center, USA). All samples were heated using a 50 W CO_2 laser (10.6 μm wavelength) and analysed with a Micromass 5400 noble gas mass spectrometer equipped with an electron multiplier. The ages of the three rock samples were determined using multi-grain incremental heating methodology, and plateau ages in each analysis were evaluated using the criteria described in Fleck et al. (1977). The tephra sample was analysed using total fusion analyses of individual feldspar crystals, and a weighted average age was calculated from the measurements with overlapping 2σ age error and similar Ca/K ratios. All radioisotopic ages were calculated using the decay constants and atmospheric $^{40}Ar/^{36}Ar$ ratio from Steiger and Jäger (1977). The radioisotopic ages of faulted volcanic units were considered to be maximum ages for the normal faults that cut through them. The ages were then combined with the fault geometry data and used to calculate minimum long-term extension rates across the study area.

2.4 Results

2.4.1 Overview

The Paka and Silali volcanoes of the inner graben of the NKR are cut by numerous normal faults (Fig. 2.3a), which strike NNE (between 10° and 20°), have lengths between several 100 m up to ~10 km and apparent throws ranging from < 4 m up to 130 m (Fig. 2.3b). In the south, at Paka volcano, faults with scarp heights >20 m mainly occur in a narrow zone of approximately 5 km width to the east of the volcano. Where the faulted units are oldest, fault scarps exhibit heights of above 100 m. In the lowlands to the north and to the southwest of Paka, faulted sectors also occur, but the fault scarps are smaller and rarely exceed heights of 15 m. North of Paka volcano, the zone of faulting continues in a spatially more even distribution, and affects the southern, eastern and western parts of the shield of Silali volcano in a 10 to 15 km wide zone of semi-parallel, intervening grabens, which have individual scarp heights of mostly below 30 m.

2.4.2 Radioisotopic dating results for Silali volcano

At Silali volcano, our study has provided new $^{40}Ar/^{39}Ar$-geochronological data (Fig. 2.3a) that complements the existing dates from Dunkley et al. (1993) and Smith et al. (1995). The south-eastern flanks of Silali are mainly covered by the “flank fissure basalts” (Dunkley et al., 1993), which are cut by a series of small grabens (geological map shown in Fig. A.1). Close to such a ~9 km long graben system, a groundmass sample of this unit was dated to 180 ± 70 ka (sample S06-03; Fig. 2.4a). This date confirms that the widespread lava flows exposed at the south-eastern flanks of the volcanic edifice pre-date the ≤63 ka caldera collapse, and constitute a maximum age of the normal fault scarps in this area. One of these fault scarps is sealed by a small, unfaulted eruptive center, located directly on top of the scarp. The groundmass of this eruptive cen-

ter was dated to 80 ± 60 ka (sample S07-01; Fig 2.4b), constituting the minimum age of the corresponding fault.

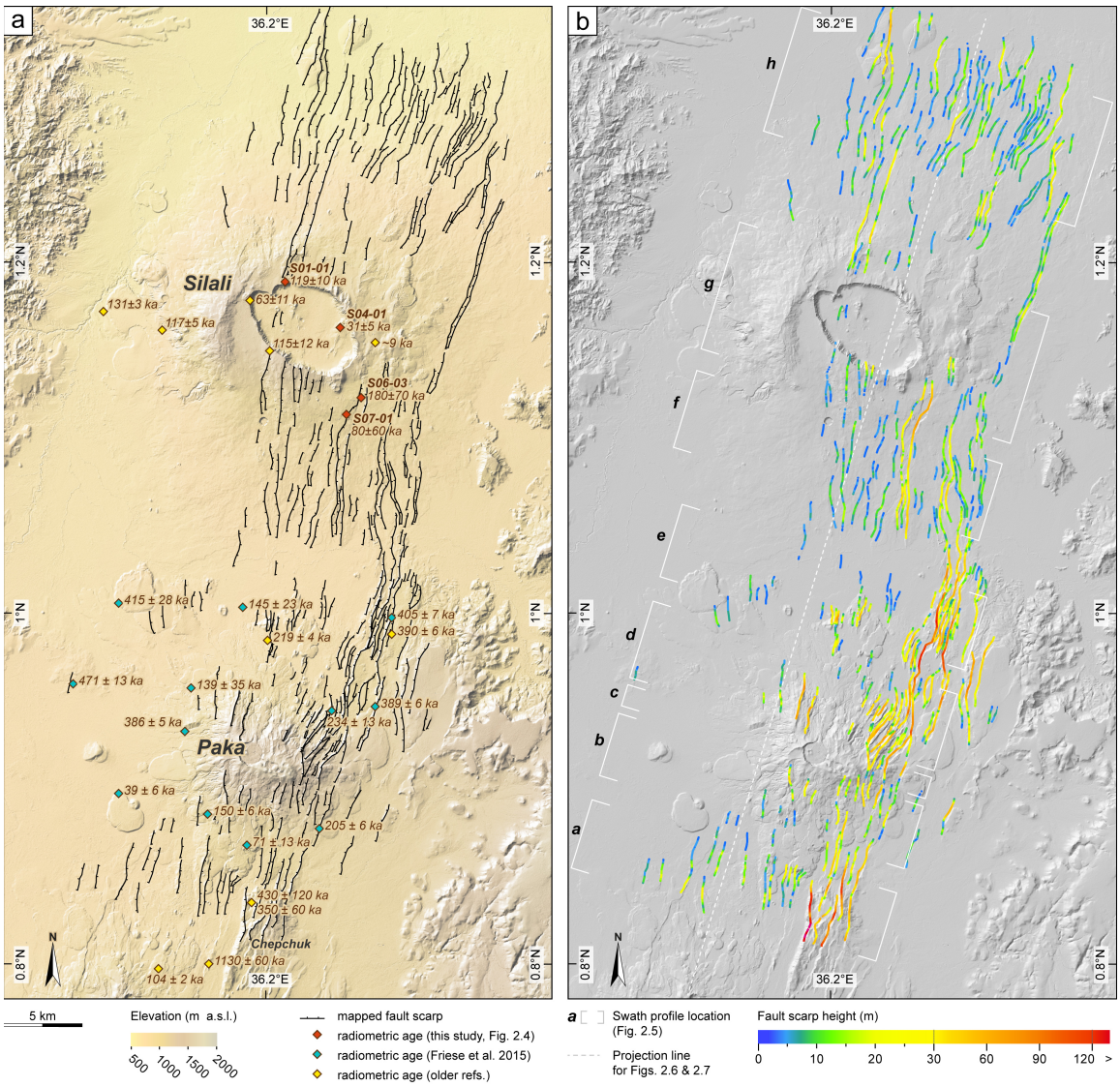

Figure 2.3. Map of results at the Paka and Silali volcanoes.
(a) *Topographic map of Paka and Silali volcanoes in the inner graben of the NKR, showing the mapped fault scarps and the radioisotopic age data that was used in this study. Red diamonds mark new ages from this study, turquoise diamonds show dates from the German Federal Institute for Geosciences and Natural Resources dating campaign (2015), yellow diamonds denote radioisotopic dates from Dunkley et al. (1993), Smith et al. (1995) and Sturchio et al. (1993) (see Table A.1 for a sample list, and Fig. A.1 for a geological map).* ***(b)*** *Map of the normal fault scarp heights in the inner graben as determined in this study (data available in Riedl et al., 2021b). The boxes a-h denote eight zones from south to north that are individually described in this section and shown as cross-sections in figure 2.5. The white dashed line represents the projected line along the rift, which was used in figures 2.6-2.7 and to calculate the minimum long-term extension rate along the rift.*

Inside the caldera of Silali volcano, the caldera floor is partly covered by a trachytic lava flow, whose feldspars were dated by us to 31 ± 5 ka (sample S04-01; Fig. 2.4c). Based on the local outcrop patterns and temporal relationships between volcanic units we consider this age to be the maximum age of the normal faults which occur inside Silali caldera.

On the northern flanks of Silali, close to the caldera rim, a tephra layer was sampled and the analysis of its feldspar crystals provided an age of 119 ± 10 ka (sample S01-01; Fig 2.4d). This tephra was overlain by lava flows of the northern flanks of the volcano. We therefore use this age as an upper age limit for the faults that occur to the north of Silali caldera.

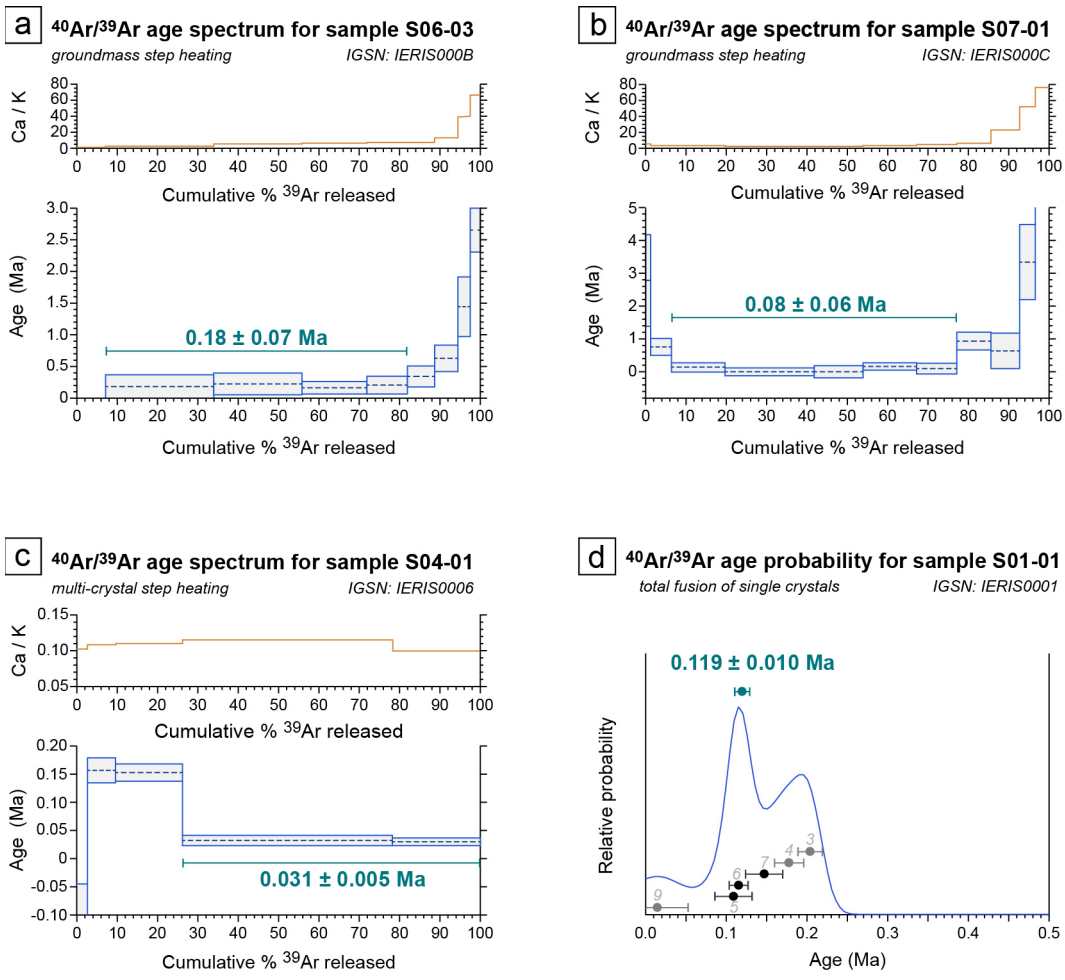

Figure 2.4. $^{40}Ar/^{39}Ar$ analytical results of volcanic rocks from Silali volcano.
(a,b,c) *show age spectra and Ca/K plots of multi-grain step-heating analyses from lava flow samples. All ages from individual steps are shown with 1σ error. The final radioisotopic age plateaus are highlighted in green, the plateau criteria are described in the methodology section;* ***(d)*** *shows the age-probability of the total-fusion analysis from individual crystals from the tephra sample S01-01. A final weighted average age of this sample was determined using analyses #5, #6, #7. The analytical data of all samples are available in the Geochron database (Riedl et al., 2021c) (Table A.2).*

2.4.3 Fault geometries and extension rates

The study area can be divided into eight zones from south to north covering the Paka and Silali areas and the intervening lowlands, each with their own distinctive and characteristic fault patterns (zones a-h in Fig. 2.3b; Fig. 2.5). The geometries of the normal faults within these zones are described below.

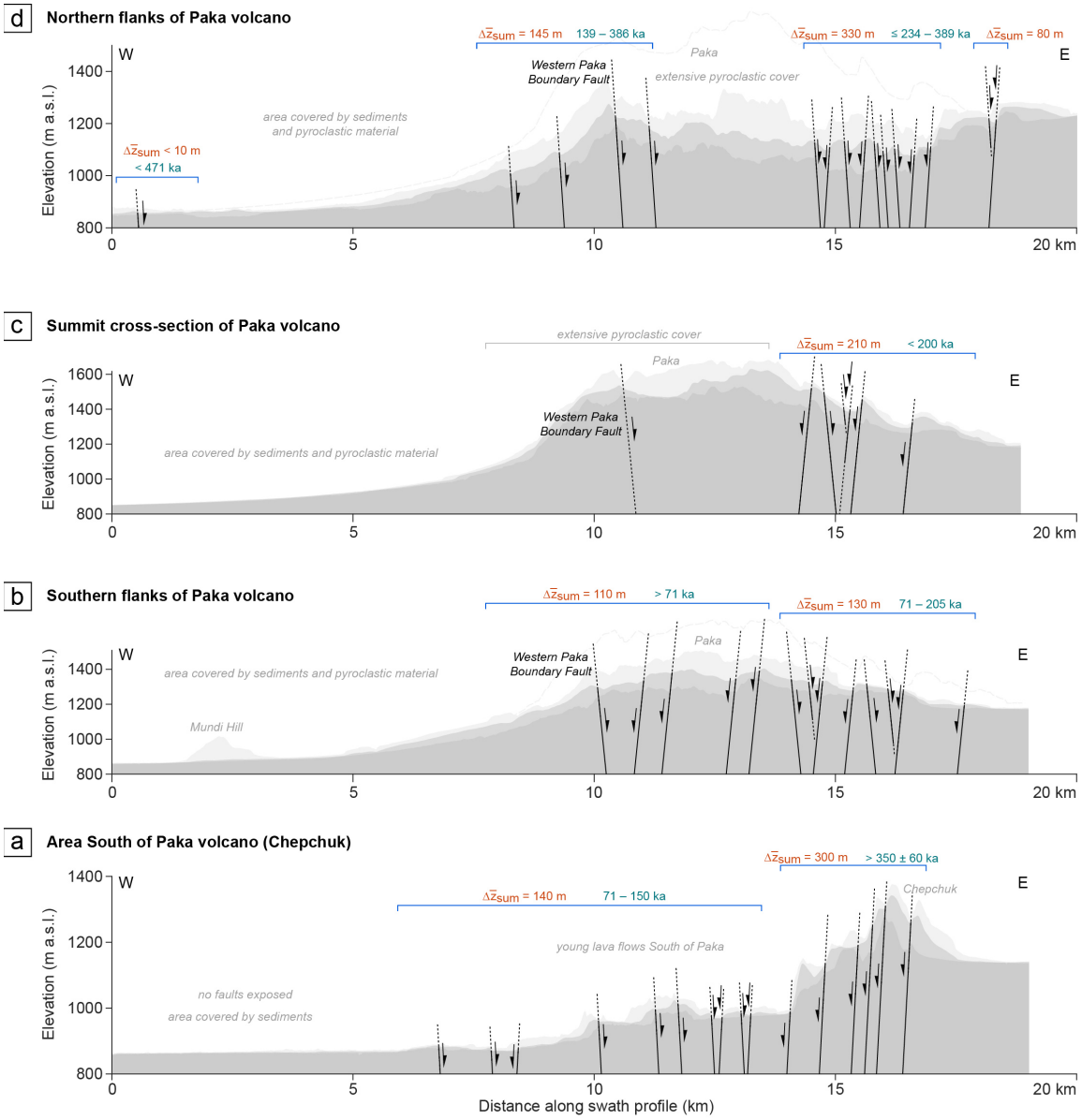

Figure 2.5. East-west cross-sections of the inner graben zones as shown in Fig. 2.3.
(a to d) *cross-sections of the Paka area. Profiles are sorted from south (bottom) to north (top). Normal faults are extrapolated to depth. Faults with similar age are grouped with brackets and shown with their cumulative throw* $\Delta\bar{z}_{sum}$*. Ages indicate oldest possible times when the fault scarps could have been established.*
(continued on next page)

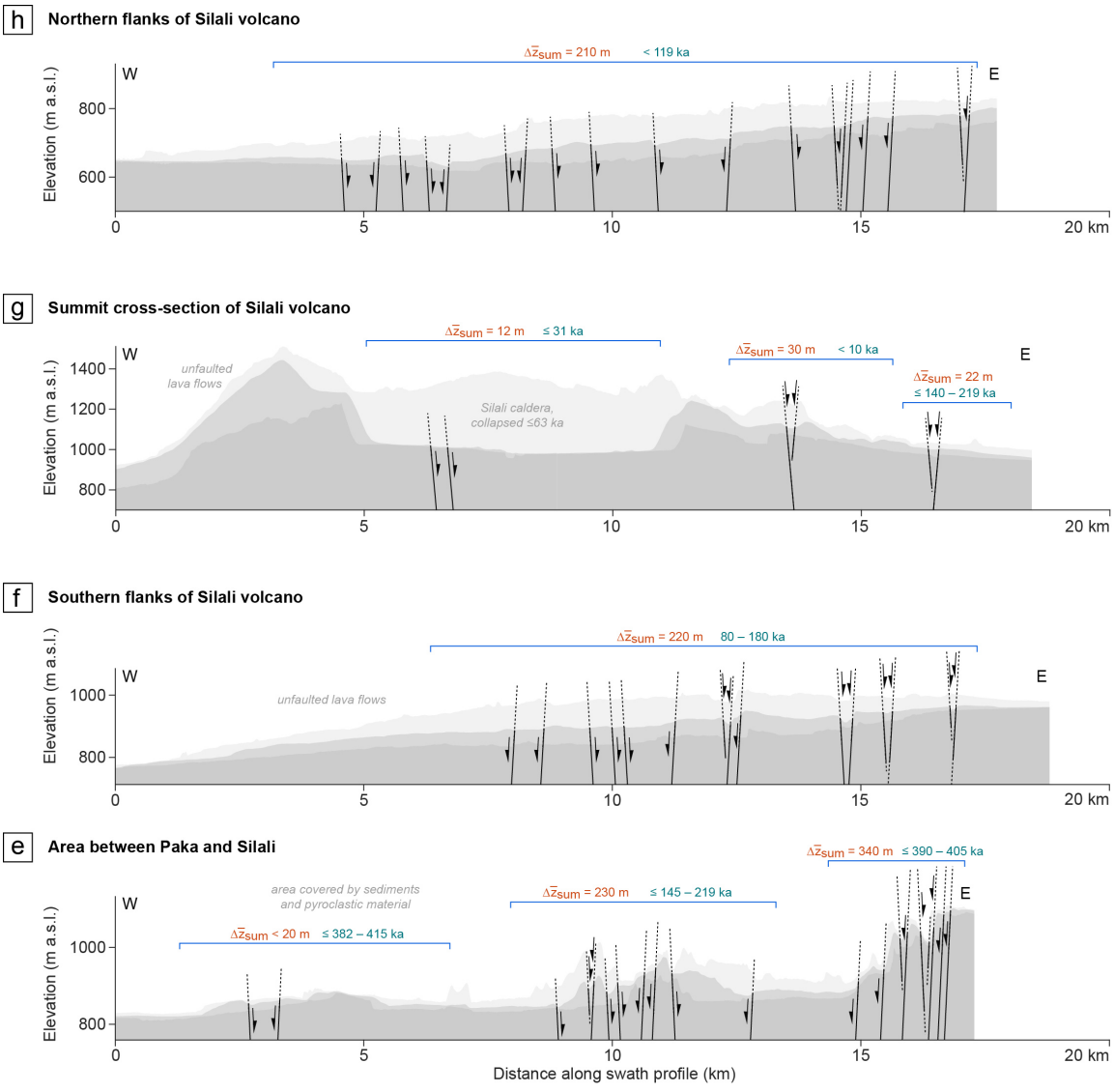

Figure 2.5 (continued)

(e to h) *cross-sections of the Silali area. Profiles are sorted from south (bottom) to north (top). Normal faults are extrapolated to depth. Faults with similar age are grouped with brackets and shown with their cumulative throw* $\Delta\bar{z}_{sum}$*. Ages indicate possible maximum ages of fault scarp formation.*

Lowlands to the south of the Paka volcano; Chepchuk cross-section

Our southernmost cross-section traverses the low-elevation area to the south of the Paka volcano (Fig. 2.5a). In this section, 70% of the cumulative throw is accommodated in the east, where the oldest Middle Pleistocene volcanic rocks of the inner graben are exposed. These "Chepchuk volcanics" (Carney, 1972) are cut by six semi-parallel, north-south striking normal faults, all with downthrows to the west, separations between 300 and 600 m, and scarp heights that range from 30 to 200 m, with the westernmost scarp being the most prominent. The cumulative throw of this group of faults is 340 m. The Chepchuk volcanics in this area are considered to be remnants of an old rift volcano whose base has been dated to 1.13 ± 0.06 and 1.22 ± 0.06 Ma (Carney, 1972). None of the rest of the sequence has been dated radiometrically, but the Chepchuk volcanics have been correlated with other units that are older than 0.5 m.y. (Dunkley et al., 1993), and sinter deposits associated with geothermal activity along these faults have been dated to 430 ± 120 ka and 350 ± 60 ka (Sturchio et al., 1993). Farther west along the cross-section, the low-elevation region to the south of the Paka volcano is covered by younger (Upper Pleistocene) basalt flows. Normal faulting in this area has generated 300 to 600 m wide symmetric graben structures with average scarp heights of less than 20 m, and a cumulative throw of 140 m. These basalts have not been dated radiometrically in this area but farther to the north a stratigraphically low section of the same basaltic flows has been dated to 150 ± 6 ka (PK-26 in Friese, 2015). In places, faulted flows of these basalts are overlain by trachytes that have been dated to 71 ± 13 ka in the north of the section (PK-27 in Friese, 2015), and to 104 ± 2 ka to the south of the section (the "Upper Trachytes" of Korosi; Dunkley et al., 1993). The observed vertical offsets across the normal faults are therefore interpreted to have maximum ages ranging between 71 ka and 150 ka. The fault scarps of the Chepchuk cross-section therefore represent a minimum long-term extension rate of 1.4 ± 0.2 mm yr^{-1} up to 1.6 ± 0.2 mm yr^{-1} where scarps are highest (Fig. 2.6).

Southern flanks of the Paka volcano

On the southern flanks of the Paka volcano (Fig. 2.5b), the exposed rocks are mostly faulted trachytic lava flows (the "Lower Trachytes" and "Upper Trachytes" of Dunkley et al., 1993) and volcaniclastic deposits. The scarp heights of the individual normal faults in this area (generally between 5 and 30 m) are more uniform across the width of the cross-section compared to the southernmost cross-section, with a fault spacing of 350 m to 500 m. The cumulative vertical offset along this cross-section is up to 260 m. The trachytes that are widespread in the eastern part of this cross-section have been dated to 205 ± 6 ka (PK-8 in Friese, 2015; mapped by Dunkley et al., 1993, as "Upper Trachytes", but herein reinterpreted as "Lower Trachytes"), indicating a younger age of faulting. The summit area and western slopes of the Paka volcano are, however, mainly covered by volcaniclastic deposits, including poorly consolidated scoria and pumice deposits, which tend to conceal any fault scarps. Gullies incised into the volcaniclastic sediments and the steep fronts of lava-flow stacks add to the complexity of this area over an approximately 4 km wide portion of the cross-section. The lower age limit of the faulting is determined by a trachyte flow that covers some of the faults and that has been dated to 71 ± 13 ka (PK-27 in Friese, 2015). Farther west along the cross-section, the faulted area terminates at the "Western Paka Boundary Fault" (Dunkley et al., 1993). The rift valley floor to the west of the Paka volcano is covered with alluvium, concealing any possible fault scarps. Young trachytic pumice cones that

partly cover the alluvial deposits on the valley floor and show no evidence of any faulting have been dated to 39 ± 6 ka (PK-29 in Friese, 2015). We therefore derive a minimum long-term extension rate for this zone of 1.1 ± 0.3 mm yr^{-1}, and up to 2.0 ± 0.3 mm yr^{-1} closer to the summit of Paka (Fig. 2.6, section b).

Summit area of the Paka volcano

At the summit of the Paka volcano (Fig. 2.5c), the extensive pyroclastic cover would have concealed any faults cutting this part of the volcano. However, trachytes on its eastern flanks that are of Middle to Late Pleistocene age are cut by north-south striking normal faults. The faults are more closely spaced than farther south, with separations of between 150 and 250 m; average scarp heights range up to 25 m, with restricted scarp sectors reaching up to 70 m. The faulted units displace the approximately 200 ka old trachyte sequence, indicating a younger age for the faulting. The summit caldera, however, which is stratigraphically bracketed to have collapsed at approximately 10 ka (Dunkley et al., 1993), does not record any vertical offsets in the caldera walls. We derive a minimum long-term extension rate of below 0.7 to 1.0 ± 0.2 mm yr^{-1}, which most likely underestimates the extension occurring in the areas with extensive pyroclastic cover (Fig. 2.6, section c).

Northern flanks of the Paka volcano

The cross-section on the northern flanks of Paka volcano (Fig. 2.5d) is characterized by two distinct areas that show different styles of normal faulting. Firstly, the central and western parts of the cross-section is very sparsely faulted. The cumulative throw of 150 m from a total of five fault scarps across the 14 km wide section of the northwest flank of the Paka volcano and the lowlands farther west account for <30% of the throw in this cross-section. The faulted Lower Trachytes and Lower Basalts in this part of the cross-section are associated with an early eruptive phase of the Paka volcano (Dunkley et al., 1993; Sceal, 1974; ages between approximately 139 ka and 386 ka of samples PK-15 and PK-16 confirmed in Friese, 2015) indicating that there has been only a limited amount of faulting since their extrusion. Only two major normal faults occur in this area, which run to the west of the summit caldera; these are the north-south striking Western Paka Boundary Fault, and a parallel fault about 800 m farther east. Both have downthrows to the east and scarp heights of about 50-70 m. There are only three more fault scarps farther to the east along the cross-section, each with average offsets of less than 10 m. One small fault scarp with a throw <10 m occurs in the far west of the cross-section, in an 471 ± 13 ka old volcanic unit (PK-22 of Friese, 2015). Close to the summit, however, any existing fault scarps may have been masked by young pyroclastic deposits. The second area, in the eastern part of this cross-section is characterized by a 2.5 km wide, densely faulted area that accommodates >70% of the total throw in this cross section. The faults in this area strike north-south at their northern and southern ends, but strike NNE in their central segments, resembling an en-échelon array of normal faults within a sigmoidally shaped pull-apart structure. The faults have an average separation of 250 m and have average scarp heights of approximately 40 m, resulting in a cumulative throw of ~330 m. The rocks affected by these faults are mostly “Lower Trachytes” and “Lower Basalts” from the older units of the Paka volcanic sequence. These units have been dated to between 389 ± 6 ka and 234 ± 13 ka (PK-6 and PK-5 from Friese, 2015), indicating a younger age of faulting. This

area is bounded to the east by two north-south striking normal faults with downthrows to the west and a scarp height of up to 80 m, which continue farther north into a major extension zone to the north of the Paka volcano. The calculated long-term extension rate represented by the faults in this zone is 1.3 ± 0.2 mm yr^{-1}, with values up to 2.3 ± 0.3 mm yr^{-1} where the fault scarps are highest (Fig. 2.6, section d).

Area between the Paka and Silali volcanoes

The low-elevation area between the Paka volcano in the south and the Silali volcano in the north (Fig. 2.5e) is characterized by a distinct, narrow zone of normal faulting with large vertical offsets in the eastern part of the cross-section, where 60% of the cumulative throw are accommodated, and a relatively sparse distribution of normal faults with small vertical offsets in the central and western parts of the cross-section, which only account for 40% of the cumulative throw. The westernmost part of the cross-section is characterized by Middle to Late Pleistocene volcanic series of the Paka and Silali shields and a narrow area covered with alluvium. Trachyte lava flows exposed in this area have a maximum age of 415 ± 28 ka (PK-19 of Friese, 2015) and have been little affected by faulting; only a few, minor fault scarps are present, with a cumulative throw of only 20 m, suggesting that this area has seen little tectonic activity since that time. Lava flows exposed in the central part of the cross-section have been dated to 219 ± 4 ka (Dunkley et al., 1993) and to 145 ± 23 ka (PK-13 of Friese, 2015). In these units, north-south striking normal faults with an average separation of less than 300 m and an average height of less than 20 m occur. Farther north these faults are probably concealed beneath a cover of alluvium until they reach the southern flanks of the Silali volcano. The majority of the vertical offset, however, is accommodated within a fault zone approximately 3.5 km wide along the eastern margin of the inner graben, which contains normal faults with separations of between 60 and 200 m. These faults strike NNE-SSW; their downthrows are mostly to the west and the average scarp height is 42 m. Two scarps have maximum apparent throws that exceed 100 m (one of 114 m and the other of 130 m). Together with occasional, smaller-scale antithetic faults, this zone forms a down-to-the-west staircase morphology with small horst and graben structures. The area consists mainly of basalts from the Paka volcanic series and the Middle Pleistocene “Secuminus Trachytes” that have been dated to 390 ± 6 ka (Dunkley et al., 1993) and to 405 ± 7 ka (PK-10 of Friese, 2015), and which must pre-date the observed fault scarps. Interestingly, a series of aligned monogenetic cones occurs within the basalts, running parallel to the faults. This narrow fault zone continues northward as far as the southern flanks of the Silali volcano. The fault-derived extension rate in this cross-section is 1.2 to 1.6 mm yr^{-1}, with peak values up to 2.3 ± 0.6 mm yr^{-1} where fault scarps are highest (Fig. 2.6, section e).

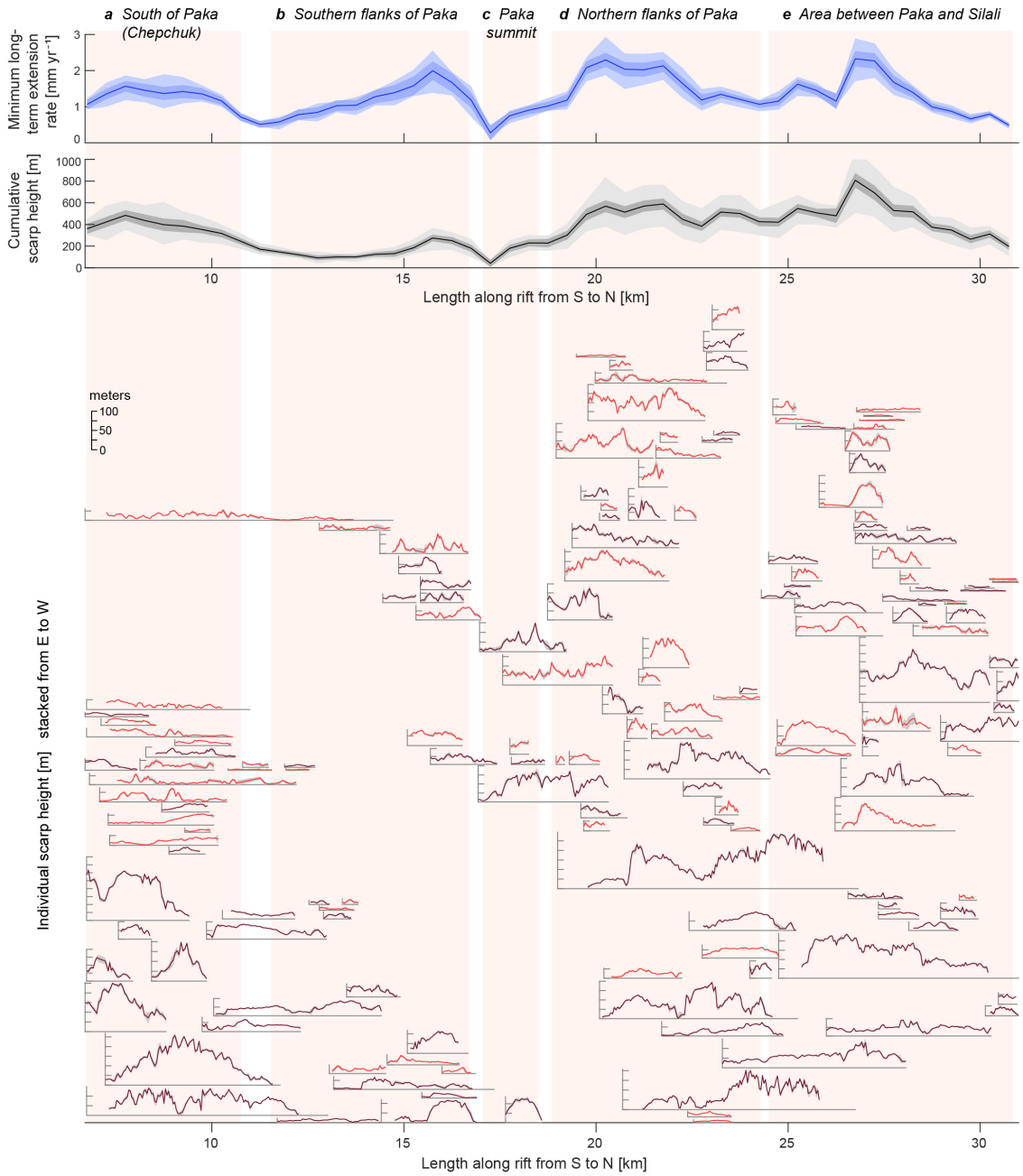

Figure 2.6. Scarp height and long-term extension rate of the Paka zones of the study area.
The lower part of the figure shows the individual scarp-height-along-length diagrams for the mapped faults. These diagrams are arranged from south (left) to north (right), and stacked from east (bottom) to west (top); color denote dip direction (dark red: to the west; bright red: to the east); vertical background bars mark the rift zones that are described in the text (Fig. 2.3b). The black curve on the upper part shows the cumulative scarp height for the entire inner graben, from south (left) to north (right); grey envelopes denote 1-sigma-uncertainties (dark grey) and absolute minimum/maximum values of the analysis (light grey). The blue curve on top shows the calculated minimum long-term extension rate along the rift based on the scarp heights and the geochronology of the faulted units.

Southern flanks of the Silali volcano

The fault zones of the inner graben described above continue northward to the volcanic edifice of the Silali shield. There, they constitute a 12 to 16 km wide zone of normal-faulted terrain that cut the central and eastern flanks of the volcano and strike north-northeast. The western flanks of the volcano are, however, not affected by any faulting.

The most southerly of the Silali cross-sections (Fig. 2.5f) reveals an unfaulted western section and a zone of normal faults in the central and eastern parts of the cross-section. This zone is a continuation of the fault zones farther south, but here it is about 12 km wide and the average separation is in excess of 600 m. This zone comprises sub-parallel graben structures in which downthrows to the west and to the east contribute equally to a cumulative throw of 220 m. The majority of the faults have vertical offsets of less than 12 m; only those faults in two particular graben systems that are 2.5 km apart have larger vertical offsets, with maxima of 36 m and 62 m. The exposed rocks are mainly basalts of the Silali pre-caldera sequence, which were previously undated but for which we present herein two new Ar-Ar ages (Fig. 2.4a-b). The older of the two ages obtained (180 ± 70 ka) constrains the age of the footwall of the largest graben, while the younger age (80 ± 60 ka) is from an unfaulted basaltic cone that covers one of the scarps of the graben and must therefore be younger than the faulting. With these age constraints we calculated a minimum long-term extension rate of 0.9 ± 0.1 mm yr^{-1}, for the southern flanks of the Silali volcano, up to 1.2 ± 0.2 mm yr^{-1} where fault scarps are highest (Fig. 2.7, section f).

Silali volcano summit cross-section

The recorded cumulative offset in the Silali summit cross-section is 64 m and thus significantly less than in the cross-sections farther south. Once again, the western flanks of the volcano are unaffected by faulting; the corresponding units have been dated to 117 ± 5 ka (Dunkley et al., 1993), and to 123 ka (Smith et al., 1995), indicating that no faulting has occurred in this area since that time. The summit is dominated by a 7 km wide and 200 to 300 m deep caldera that collapsed shortly after about 63 ± 11 ka (Smith et al., 1995). Since a caldera collapse is a gravitational process, the distinct ring fault of the caldera itself has not been included in calculations of cumulative scarp heights. However, the zone of north-south striking normal faults on the southern flanks of the volcano continues into the summit area, cutting through the southern and northern caldera walls. The fault zone is evident within the caldera where it is mainly represented by a series of aligned monogenetic volcanic cones and small lava flows that cover the caldera floor; two normal-fault scarps were identified within the caldera, with average vertical offsets of 2 m and 9 m. Some intra-caldera effusive rocks have yielded dates as young as 9 ka (Smith et al., 1995), and new radioisotopic date obtained for this study indicates an age of 31 ± 5 ka (Fig. 2.4c) for one of the larger intra-caldera trachyte lava flows, which we considered the maximum age for the fault scarps observed inside the caldera. To the north of the caldera the same fault zone continues directly from the rim as a full graben, with average scarp heights of 12 m and 20 m, on units that we dated to have a maximum age of 119 ± 10 ka (Fig. 2.4d). In contrast, the eastern flanks of the summit region are mainly covered by young lavas (e.g. “Black Hill Trachytes”), which post-date the caldera collapse and have been dated between 7 ± 2 ka and 9 ± 2 ka (Smith et al., 1995). Only two < 20 m high faults scarps affect this otherwise mostly unfault-

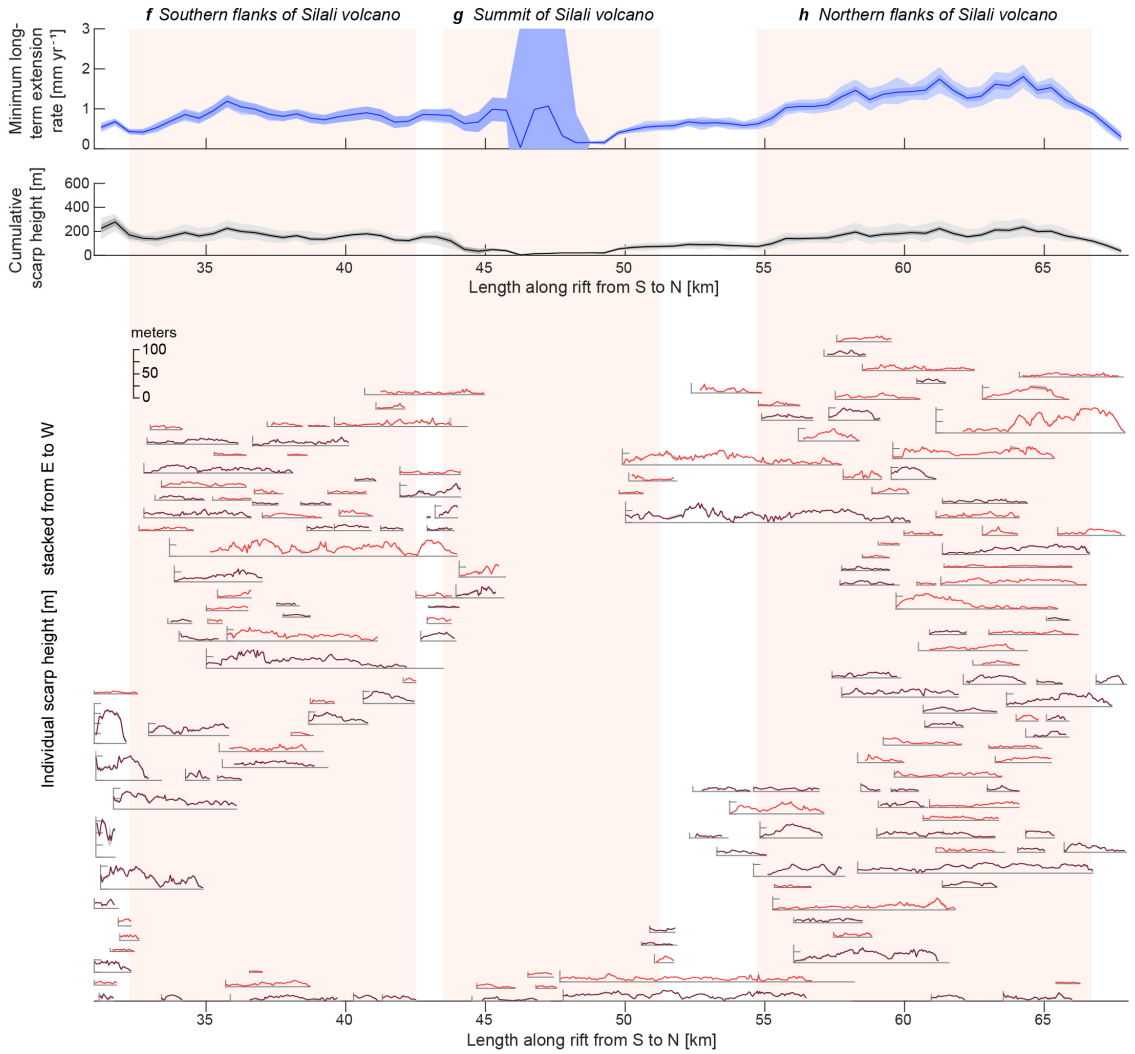

Figure 2.7. Scarp height and long-term extension rate of the Silali zones of the study area.
The lower part of the figure shows the individual scarp-height-along-length diagrams for the mapped faults. The scarp-height-along-length diagrams are arranged from south (left) to north (right), and stacked from east (bottom) to west (top); color denote dip direction (dark red: to the west; bright red: to the east); vertical background bars mark the rift zones that are described in the text (Fig. 2.3b). The black curve on the upper part shows the cumulative scarp height for the entire inner graben, from south (left) to north (right); grey envelopes denote 1-sigma uncertainties (dark grey) and absolute minimum/maximum values of the analysis (light grey). The blue curve on top shows the calculated minimum long-term extension rate along the rift based on the scarp heights and the geochronology of the faulted units.

ed area, but once again there are volcanic cones present along a linear, north-northeastward trend parallel to the fault zones. Farther east, on the lowermost slopes of the eastern flanks of the Silali volcano, one graben cuts pre-caldera basalts. This full graben is about 120 m wide and bounded by 5 to 22 m high fault scarps. The total fault-based extension rate on this cross-section is 1.1 ± 4.3 mm yr^{-1}. As some of the faulted units are very young, the error of this calculated value is much higher than for the other cross-sections (Fig. 2.7, section g).

Northern flanks of the Silali volcano

As with the southern flanks, the northern flanks of the Silali volcano are affected by an approximately 16 km wide zone of approximately 30 NNE-striking normal faults with strikes of between 10° and 20°. The separation between individual faults ranges between 350 and 900 m in the western half of the cross-section, and between 200 and 500 m in the eastern part of the cross-section. The average scarp heights range from 5 m to 12 m and the maximum scarp height rarely exceeds 20 m. The cumulative throw of these faults is 210 m. The surface of the northern flank consists entirely of pre-caldera basalts, which have been estimated to be more than 100 ka old (Dunkley et al., 1993). Based on our dating of a stratigraphically lower unit close to the summit area to the north of the caldera, we infer that the basalt flows on these northern flanks must be younger than 119 ± 10 ka (Fig. 2.4d). We use this as a maximum age estimation for the fault scarps in this cross-section, resulting in a long-term average extension rate of 1.5 ± 0.3 mm yr^{-1} to up to 1.8 ± 0.3 mm yr^{-1} (Fig. 2.7, section h).

2.5 Discussion

In this study we have made use of the widely distributed Quaternary fault scarps in the volcanic units of the inner graben of the NKR and exploited their good potential for radioisotopic dating, in combination with previously published age determinations, to derive extension rates for the NKR over the last 0.5 m.y. Below, we discuss the methodological robustness and the implications that our findings have with regard to extension processes in the NKR and elsewhere.

2.5.1 Analytical robustness and caveats

To provide a robust calculation of a minimum long-term extension rate, our methodology is conservatively designed to avoid an over-estimation of rates. Our results are based on (a) a geochronology, which is focused on maximum age constraints; (b) the fault throws that are derived from our scarp-height detection method; these are only taken into account where the fault-scarp morphology is unequivocal. Areas where faults might be present but fault scarps are masked due to unconsolidated sedimentary cover are not considered in the calculation. In addition, the DEM used in this study allows for the recognition of small fault scarps, but the quantification is limited where faults have short lengths or sub-meter throws.

To assess the oldest possible time of faulting for each fault scarp, we use the age of the faulted units as upper age limits. Although in some cases faulting and volcanism might occur simultaneously, based on our field inspection and published accounts it is most likely that most of the observed deformation occurred later than the emplacement of the volcanic units (e.g., Dunkley et al., 1993; Mibei et al., 2021b). The use of radioisotopic dating can only bracket the timing of deformation, but not directly date when the faulting occurred. We therefore describe all our calculated extension rates as “minimum long-term rates”, which are time-averaged extension rates, as we cannot resolve if individual fault scarps were formed during shorter intervals of time or if they formed over the entire time since the effusion of the dated units. In addition, despite the coverage with radioisotopic dates, not all detected fault scarps are located close to sampling

points of dated units. We therefore also rely on the mapping of the stratigraphy of the Paka and Silali volcanoes and the correlatability of the dated units. Some of the spatially more widespread volcanic units are likely to have been extruded over longer periods of volcanic activity (e.g., Dunkley et al., 1993), which cannot be fully represented using a single age. At the Silali volcano, for example, the "Upper Basalts" that cover extensive areas of the southern and northern flanks are widespread and might actually represent a longer eruption phase (Dunkley et al., 1993; Smith et al., 1995); this may explain the slightly lower extension rates calculated for faults at the flanks of the Silali volcano, as some of its areas might be younger than our age correlations with the sparsely available radioisotopic dating suggest. Moreover, the uncertainties of some of the used radioisotopic dates are high. The dates for the S06-03 and S07-01 samples (Fig. 2.4) were obtained from a young basaltic groundmass, which has low contents of both potassium (due to the composition) and radiogenic argon (due to the young age), which limited analytical precision. These age uncertainties are propagated into the calculated extension rates and result in wider error margins, especially where most of the faulted units are very young (e.g., Fig. 2.7 at Silali summit).

In general, the quantification of fault offsets is affected by a detection bias and a natural bias (e.g., Muirhead et al., 2016; Schultz et al., 2009). On the one hand, the spatial resolution of the DEM limits the detectability of small faults; on the other hand, fault scarps may not be fully preserved due to erosion, colluvial cover or sedimentary burial. The minimum length of detectable fault scarps is confined by the 12 m spatial resolution of the TanDEM-X DEM. This study uses eight-pixel-wide (96 meter) windows along each fault trace to determine vertical offset values; therefore, the shortest individual scarp that we could describe is 300 m long. As our study does not analyze the lengths of individual faults, but aims for summing the measured throws to a total amount of across-rift extension (rate), sectors with small-scale fault segmentation along strike were grouped together and further analyzed as merged fault scarps. The absolute vertical precision of the used TanDEM-X DEM has been described to be approximately 2 m (Purinton and Bookhagen, 2017); however, the vertical offsets that our study can determine are as low as 5 m. To minimize the natural bias our study corrects for erosion of the lava flows (chapter 2.3.1), and to prevent an under-estimation of fault throws due to colluvial cover in the vicinity of the scarp (e.g., Cartwright et al., 1995), the vertical offset of a wider area of both hanging walls and footwalls is considered (Fig. 2.2). However, in unconsolidated sedimentary deposits and volcaniclastic cover strata, faults are not preserved. Especially in the summit region of the Paka volcano and on its western flanks, deep fault-parallel gully erosion suggests that in the area of the "Western Paka boundary fault" (Fig. 2.5c), normal faulting exists but the preservation of fault scarps is exceptionally low, resulting in an underestimation of extension (segment c in Fig. 2.6). We also cannot exclude that faults masked by sediment exist beneath alluvium in the topographically low-lying areas in the western part of the study area, but both the western flanks of the Silali volcano are not faulted, and to the far west of Paka, the isolated, >400-ka-old volcanic units record a total throw of less than 10 m. Most of the faulted lava flows at the Paka and Silali volcanoes do not show significant sedimentary covers on the downthrown hanging walls, and the original units are well exposed; we therefore consider our analysis to yield representative minimum long-term extension rates for the study area.

2.5.2 Apparent extension rates in time and space and implications for the NKR

Our analysis has provided minimum estimations for long-term extension rates of the inner graben of the NKR that range between approximately 1.0 mm yr^{-1} and 1.6 mm yr^{-1}, locally values of 2.0 mm yr^{-1} exist. Together, these values are significantly lower than the geodetically derived decadal extension rate of the Victoria-Somalia plate boundary, which is reported to be between 2.5 mm yr^{-1} and 2.6 mm yr^{-1} at the latitude of the study area (Saria et al., 2014). Long-term rates based on plate-tectonic reconstructions exist for East Africa and predict total rates between 4 and 5 mm yr^{-1} (DeMets and Merkouriev, 2016), but these values define the motion between the Nubia and Somalia plates and do not resolve motion for plates with an intermediate position, such as the Victoria plate. Our analysis will therefore focus on the disparity between the middle Pleistocene and decadal extension rates between the Victoria and Somalia plates.

Our data reveals the amount of extension that is manifested by brittle surface deformation in the inner graben of the Kenya Rift since approximately 0.4 Ma. The responsible structures are broadly distributed throughout the inner graben, and the amount of extension accommodated by these structures is concentrated on the eastern margin of the inner graben (Fig. 2.8a). For example, east of the Paka volcano there is a well-developed fault zone, where total throws of more than 600 m are attained. However, the extension rate in this region is more evenly distributed in space (Fig. 2.8b), suggesting that extensional processes between the middle Pleistocene and the present-day have been active over the entire width of the inner graben. Interestingly, at Silali, some of the youngest faults generate nearly all of the overall extension rate in the center of the inner graben (Fig. 2.8a and b, areas marked by the star symbol). This suggests a spatial focus of rifting on timescales of about 10 kyr. In contrast, our overall temporal resolution is not accurate enough to test the hypothesis of pulsed tectono-magmatic activity on 10^5 yr timescales, as observed by Siegburg et al. (2020) in the more advanced Northern Main Ethiopian Rift.

North of the study area Melnick et al. (2012) derived extension rates between 3.5 and 6 mm yr^{-1} based on deformed Holocene shorelines in the Suguta Valley of the Northern Kenya Rift that are even higher than the geodetic rates by Saria et al. (2014), which suggests that such pulses may also exist in Kenya. This may be supported by phases of pronounced magmatic activity and the generation of the caldera volcanoes in the Northern Kenya Rift (Dunkley et al., 1993; McCall, 1999; Mibei et al., 2021b; Smith et al., 1995). In light of our mid-Pleistocene to recent extension rates these pulses must be averaged out due to episodes of intervening reduced rifting. Such lower long-term rates are also supported by other extension-rate calculations; for example, profile-balancing techniques applied to the faulted and subsided Mio-Pliocene Plateau Trachytes of the Central Kenya Rift amount to extension values between 1.4 and 1.7 mm yr^{-1} (Strecker, 1991). Similarly, in the Magadi basin of the Southern Kenya Rift, a time-averaged extension rate based on the throws of intra-rift faults is reported to be 1.63 ± 0.10 mm yr^{-1} (Muirhead et al., 2016).

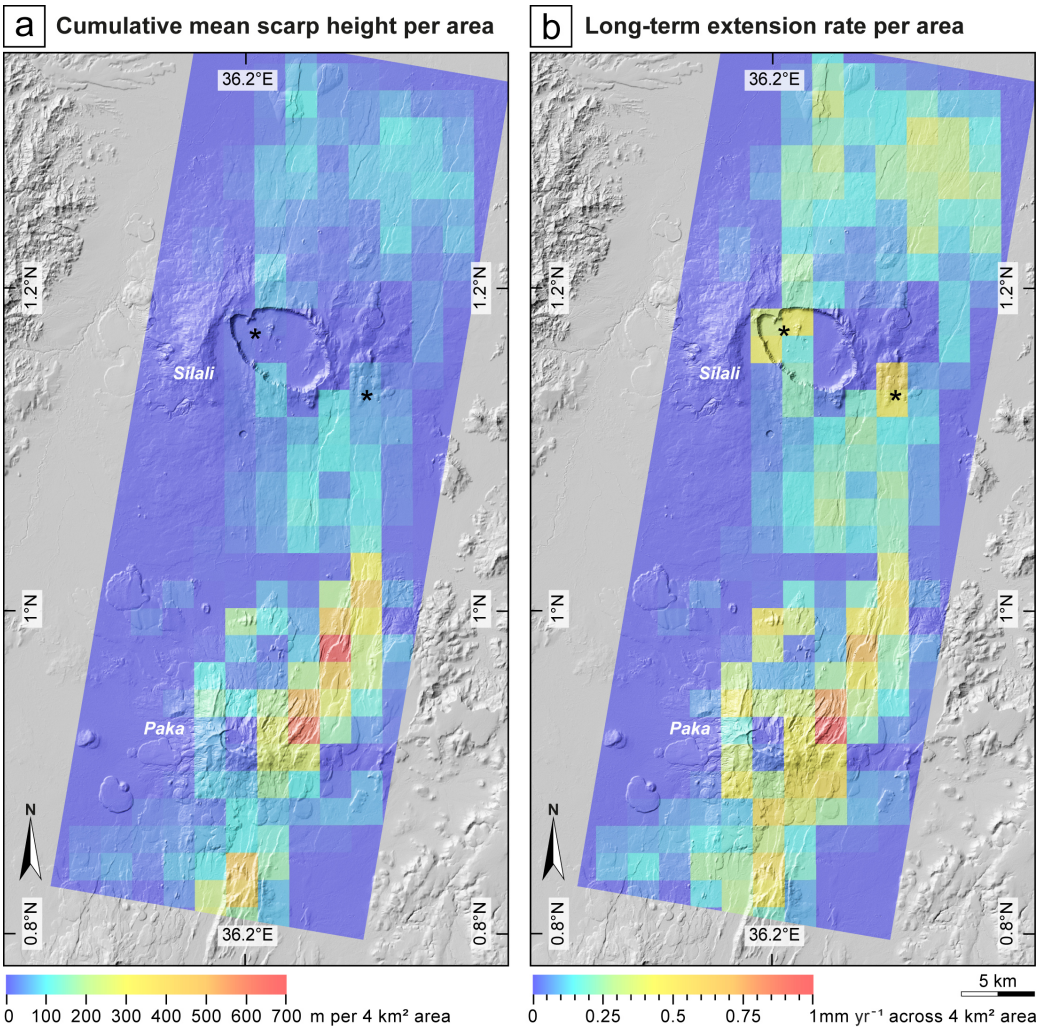

Figure 2.8. Map of cumulative scarp height and extension rate per area

Distribution of ***(a)*** *cumulative scarp height per 4 km² grid cell and* ***(b)*** *long-term minimum extension rate across each 2-km-wide grid cell. Whereas cumulative scarp height per area is highest in a narrow zone between the SE and the NE of the Paka volcano, the calculated long-term extension rate is more evenly distributed across the inner graben, although the sector east of Paka still accommodates most of the extension; Farther north, at the Silali volcano, close to the caldera a group of fault scarps with relatively low scarp heights (below 10 and 20 m; marked *) yield localized high long-term extension rates of up to ~0.5 mm yr^{-1} across a 2 km wide grid cell. Because the associated fault scarps are located in the youngest units (~10 ka) of the study area, this emphasizes that during shorter time intervals, almost the entire rift extension can be accommodated in a narrow zone by few faults.*

2.5.3 Amount of mid-Pleistocene to recent extension and magmatism

Our data shows that most of the current extension is taking place within the inner graben and that this process has been going since the mid-Pleistocene. However, the extension rate derived from surface-deformation features does not take into account the contribution by magmatic diking. Exhumed magmatic rifts such as the Proterozoic Zimbabwe dike (e.g., Mukasa et al., 1998; Wilson, 1996; Worst, 1960) emphasize the influence of crustal-scale magmatic intrusions on extension. In Kenya, volume estimates of plutonic rocks associated with the widespread extrusive units suggest a total volume of 111.2 $\times 10^3$ km^3 of added gabbroic rocks in the crust of the Kenya Rift between 0° and 2°N (Karson and Curtis, 1989); as this estimate is only based on units that are preserved at the surface, the actual intrusive volume might be even higher (e.g., Guth, 2015; Prodehl et al., 1997). The existence of intrusive material in the crust is also supported by an axial positive gravity anomaly (Lichoro et al., 2019; Mariita and Keller, 2007; Swain, 1992), which suggests dike intrusions that account for 20% (Ebinger et al., 2017) and up to 22 to 26% of the crustal volume over the width of the inner graben (Swain, 1992). At surface, mafic magmatic extrusions sourced from deep crustal levels are aligned with young fault scarps at the central volcanoes (Mibei et al., 2021a), indicating that the emplacement of dikes extends to the shallow crust. In addition, frequent, low-magnitude earthquakes along the volcano-tectonic axis at Baringo at about 5 to less than 12 km depth that indicate WNW-ESE-oriented extension (Ebinger et al., 2017; Tongue et al., 1994), and the parallelism between the youngest faults and hydrothermal manifestations (Dunkley et al., 1993; Mibei et al., 2021b; Sturchio et al., 1993) also lend support to this notion.

The derived volume by Karson and Curtis (1989) corresponds to the formation of a 10-km-wide intrusion since the onset of rifting, and the Quaternary contribution to this intrusion with at least 4800 km^3 of intrusive material would relate to dikes with a total width of 0.43 km. Although small, the emplacement of such a magmatic body in the shallow crust would increase the extension rate by at least 0.36 mm yr^{-1}. Although this is an oversimplification as the inner graben probably comprises multiple, parallel mafic dikes at depth, this consideration of the magmatic contribution to the extension process helps to reconcile the disparate geologic and geodetic extension rates. Despite located in a different setting, the process of dike emplacement in the Snake River Plain of Idaho with dikes striking parallel to Basin-and-Range normal faults to the northeast and southeast of the Yellowstone hotspot trail emphasizes that in areas of high heat flow and active magmatism dike intrusions accommodate the lack of brittle faulting and extension (Kuntz et al., 1992).

2.5.4 Focused extension in the inner graben and rift maturity

Currently, the overall subsidence and extension in the Northern Kenya Rift reflects deformation processes within the inner graben; this area corresponds to the youngest manifestation of extensional faulting that transitioned from a pronounced asymmetry with major faults associated with an east-dipping master fault in the west and subsequently established antithetic, west-dipping normal faults to the formation of the magmatically and tectonically inner graben (Bosworth and Maurin, 1993; Dunkley et al., 1993; Saneyoshi et al., 2006). This transition to a more symmetric rift and localized subsidence and extension can be observed in all sectors of the Kenya Rift (e.g.,

Baker et al., 1988; Dunkley et al., 1993; Strecker et al., 1990) and appears to be the consequence of protracted extensional faulting along listric master faults and subsequent hanging-wall segmentation by antithetic faulting (Baker et al., 1988; Hautot et al., 2000; Mugisha et al., 1997; Torres Acosta et al., 2015a), a sequence of events that is also predicted by numerical models of strain localization (e.g., Richter et al., 2021). Geological mapping of the major east-dipping normal faults in the Northern Kenya Rift documents that despite their major offsets during the Tertiary, these structures are no longer tectonically active (e.g., Carney, 1972; Chapman et al., 1978; Lippard, 1972; Mugisha et al., 1997).

Moreover, geological field data from outside the inner graben in the Central Kenya Rift do not support the notion of sustained neotectonic normal faulting along older rift structures. Isolated instances of fault reactivation along rift-bounding structures outside the inner graben, appear to have involved a significant component of lateral motion rather than dip-slip normal faulting (Bosworth and Strecker, 1997; Strecker et al., 1990). This suggests that the amount of extension accrued across these structures must be minimal (Doser and Yarwood, 1991; Zielke and Strecker, 2009) and the ongoing extension is taking place in the inner graben. Indeed, the faults associated with the inner graben have been active since the late Pliocene until the present day (e.g., Baker et al., 1988; Clarke et al., 1990; Deino and McBrearty, 2002; Dunkley et al., 1993; Wilson et al., 2014) and define the active volcano-tectonic axis (Atmaoui and Hollnack, 2003; Ibs-von Seht et al., 2001; Kanda et al., 2019; Muirhead et al., 2016, 2015; Oliva et al., 2019; Riedl et al., 2020; Robertson et al., 2015; Simiyu and Keller, 2001; Sturchio et al., 1993; Tongue et al., 1994; Wamalwa and Serpa, 2013; Weinstein et al., 2017).

In conclusion, the comparison between the geologically determined extension rate with the geodetic extension rate clearly documents that at least 65% of the total extension is accommodated within intra-rift normal faults of the NKR. Incorporating the extension by magmatic diking, at least 78% of the total extension of the NKR is accommodated in the inner graben. These values are similar to what has been reported for the Magadi basin of the Southern Kenya Rift (Muirhead et al., 2016). The bulk of extension between the Victoria and Somalia plates is thus rather localized within this nascent plate boundary and represents a more advanced stage of continental break-up than previously thought.

2.6 Conclusions

The structural inventory of fault scarps in the inner graben of the Northern Kenya Rift provides valuable insight into the mode of continental rifting between the Victoria and Somalia plates during the last 0.5 m.y. Our comprehensive analysis of normal-fault scarps using the TanDEM-X digital elevation model (12 m spatial resolution) in the area of the Paka and Silali volcanoes has resulted in a detailed record of vertical offsets across a total of 328 fault zones. We integrated the fault throws along rift-perpendicular cross-sections, and by using both published and new radioisotopic dates of the faulted units, we derived time-averaged minimum extension rates of 1.0 to 1.6 mm yr^{-1}, locally reaching 2.0 mm yr^{-1}. The derived rates solely represent the amount of extension accommodated by brittle deformation in the NKR, and are compatible with published long-term rates obtained from other studies of the Central and Southern Kenya Rift

sectors, which applied a related methodology. In areas where the age of faulting is 10 ka and less, we observed that only few faults accommodate almost all of the extension across the rift, indicating that fault activity may be localized on 10-kyr-timescales. We suggest that an additional average rate of 0.36 mm yr^{-1} is accommodated by the emplacement of mafic dikes in the crust as suggested by seismicity, gravity, and seismic refraction data. Comparing the mid-Pleistocene to recent extension rate derived in our study with published present-day geodetic extension rates of 2.5 to 2.6 mm yr^{-1}, we show that in the NKR at least 65% of the extension, or, including dike activity, at least 78% of the extension, is accommodated in the ~20-km-wide zone of the inner graben. Such focused extension in a narrow zone within the greater rifted region of east Africa suggests that the location of the Kenya Rift coincides with a nascent plate boundary in an advanced stage of continental break-up, with an active volcano-tectonic-axis and virtually no activity along structures that were generated during earlier stages of rifting at the rift margins.

2.7 Acknowledgments and Open Research

The authors thank the management of the Geothermal Development Company of Kenya (GDC) and M. Frei (BGR - Federal Institute for Geosciences and Natural Resources, Hannover, Germany) for the management of our joint project among BGR, GDC, and the University of Potsdam (UP). Funds for fieldwork, analysis of structural data and radioisotopic dating were subcontracted to M. Strecker of UP as part of the GEOTHERM program, project no. BGR 05-2343, BMZ PN 2009.2222.9. Additional financial support was provided by funds of the graduate program “Shaping Earth’s Surface in a Variable Environment” (GK 1364) of the German Science Foundation (Deutsche Forschungsgemeinschaft, DFG) granted to M. Strecker (grant number STR 373/19-1). We appreciate the continued support of Dr. P. Omenda (GDC) throughout the project. The GDC team in Nakuru contributed during fieldwork and did the logistical preparation for a sampling campaign at the Silali volcano; we particularly thank T. Lopeyok, G. Mibei, Dr. A. Wamalwa and J. Lagat. The use of the TanDEM-X science DEM (© DLR 2017) was authorized by the German Aerospace Center (DLR).

The software and datasets for this research are available at the following sources: The MATLAB script to extract fault scarp heights from DEM is available at Figshare via https://dx.doi.org/10.6084/m9.figshare.15156954 under the GPL 3.0 license (Riedl et al., 2021a). Geochronological data from Silali volcano (Fig. 2.4; Table A.2) is available in the Geochron database at https://doi.org/10.26022/IEDA/111911 (Riedl et al., 2021c). The fault scarp heights at Paka and Silali are available as a GIS dataset at Figshare via https://dx.doi.org/10.6084/m9.figshare.15156834 under the CC-BY-CA 4.0 license (Riedl et al., 2021b). The TanDEM-X science DEM can be obtained for research purposes at https://tandemx-science.dlr.de/ by the DLR. Sample metadata are registered at https://www.geosamples.org/ with their IGSN. Appendix A of this thesis contains supporting tables and figures.

Chapter 3

Continental rifting at magmatic centres: structural implications from the Late Quaternary Menengai Caldera, central Kenya Rift

Simon Riedl[1], Daniel Melnick[1,2], Geoffrey K. Mibei[3], Lucy Njue[3], Manfred R. Strecker[1]
1. University of Potsdam, Institute of Geosciences, Germany
2. Instituto de Ciencias de la Tierra, Universidad Austral de Chile
3. Geothermal Development Company, Kenya

This chapter represents the accepted version of a manuscript that has been published as:
Riedl, S., Melnick, D., Mibei, G.K., Njue, L. and Strecker, M.R., 2020. Continental rifting at magmatic centres: structural implications from the Late Quaternary Menengai Caldera, central Kenya Rift. *Journal of the Geological Society*, 177, 153–169, https://doi.org/10.1144/jgs2019-021.
Supporting information is available in Appendix B and published as https://doi.org/10.6084/m9.figshare.c.4647818

Abstract

The structural evolution of calderas in rifts helps to characterize the spatiotemporal relationships between magmatism, long wavelength crustal deformation and the formation of tectonic deformation zones along the rift axis. We document the structural characteristics of the *c.* 36 ka old Menengai Caldera located within a young zone of extension in the central Kenya Rift. Field mapping and high-resolution digital surface models show that NNE-striking Holocene normal faults perpendicular to the regional ESE-WNW extension direction dominate the interior sectors of the rift. Inside the caldera, these structures are overprinted by post-collapse doming and faulting of the magmatic centre, resulting in obliquely slipping normal faults bounding a resurgence horst. Radiocarbon dating of faulted units as young as 5 ka cal BP and the palaeo-shorelines of a lake formed during the African Humid Period in the Nakuru Basin indicate that volcanism and fault activity inside and in the vicinity of Menengai must have been sustained during the Holocene. Our analysis confirms that the caldera is located at the centre of an extending rift segment and suggests that other magmatic centres and young zones of faulting along the volcano-tectonic axis of the Kenya Rift may constitute nucleation points of faulting that ultimately foster future continental break-up.

3.1 Introduction

Caldera volcanism is a widespread phenomenon in virtually all volcanic environments and constitutes an extreme form of the complex interaction between magmatic and tectonic processes. For this reason, the evolution of calderas is a common research topic with a main focus on understanding the spatiotemporal relationships between magmatic activity, the associated geothermal characteristics (Barcelona et al., 2019; e.g. Bibby et al., 1995), the evolution of the structural framework of rifts (e.g. Acocella, 2014; Keir et al., 2015), and the associated hazards and risks (e.g. Gudmundsson, 2012). Here, we present structural data from Menengai Caldera, Kenya in an attempt to assess how continental rifting processes in the Kenya Rift have been interacting with an active volcanic centre during the Late Quaternary.

Caldera volcanoes are very common in rift systems and well-known examples exist in Iceland (e.g. Gudmundsson, 1995), the Rio Grande Rift (Wilson et al., 2005), the Main Ethiopian Rift (e.g. Corti, 2009) and the Kenya Rift (e.g. King et al., 1972). However, establishing the link between volcanism and rift tectonism is challenging in young caldera settings of magmatically active rift zones because the tectonic structures may be masked by caldera-related effusive and explosive products. In addition, the magmatic products and faults associated with the active volcano-tectonic axis of the rift intercept the large eruptive centres, which will complicate the unambiguous assessment of the tectono-magmatic evolution of such regions.

In extensional tectonic regimes, caldera-related structures, the generation of linear magmatic pathways and the formation of regional tectonic structures beyond the caldera volcanoes may represent harbingers of early continental break-up (Ebinger et al., 2017; e.g. Karson and Curtis, 1989). In addition, the development of extensional fractures guided by pre-existing crustal anisotropies may facilitate the ascent of magma in these environments (e.g. Ebinger and Sleep, 1998) and potentially influence the locus of caldera volcanism (Lloyd et al., 2018). In the magmatic Kenya Rift, there is a very close relationship between calderas and linear, volcanically active young zones of extensional tectonism (e.g. Dunkley et al., 1993; Smith et al., 1995; Wadge et al., 2016). These calderas are aligned along the seismically and geothermally active volcano-tectonic axis in the present day rift centre. There is a total of 11 Mid to Late Pleistocene volcanoes with a horizontal spacing of *c.* 40 km between 2.5° N and 1° S latitude (Figure 3.1 shows the volcanoes up to 1.5° N latitude). One of the most prominent and youngest caldera volcanoes in the Kenya Rift is Menengai, a large-scale, Late Pleistocene volcanic edifice with a total diameter of *c.* 20 km and a collapse caldera with a diameter of 7–12 km (e.g. Leat, 1984), located in the central Kenya Rift close to the transition to the northern rift sector.

We first present a detailed account of the structures that are associated with Menengai Caldera and assess their spatiotemporal evolution. In a second step, we unravel how ongoing extensional processes result in a structural overprint of the spatially focussed manifestations of magmatic and deformation processes at the caldera. By contrast, the youngest zones of rift extension along the volcano-tectonic axis to the north and south of the caldera are not overprinted by these localized magmatic processes. We review the structural inventory of the caldera and adjacent regions in the light of the regional geodynamic setting to gain an insight into the role of regional-scale

structures and magmatic centres in a rift zone subjected to oblique extension. We discuss the formation of magmatic centres in the context of regional rift segmentation and review the potential role of large magmatic centres as centre points of extensional structures along the volcano-tectonic axis of the Kenya Rift.

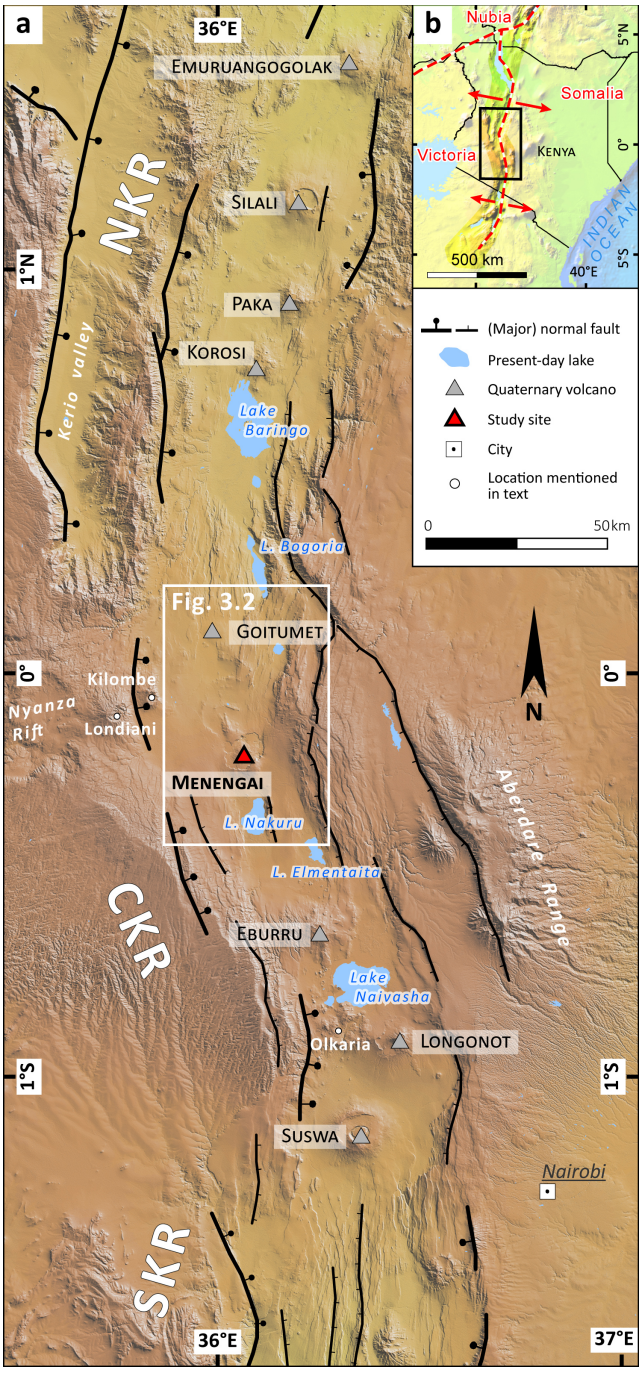

Figure 3.1. Overview map of Chapter 3
(a) *Topographic map of the central Kenya Rift, East Africa.The northern Kenya Rift and the southern Kenya Rift strike north to NNE; the oblique-spreading central Kenya Rift strikes NNW. Pleistocene volcanic centres (triangles) are regularly spaced along the rift axis. White rectangle denotes area of close-up map (Figure 3.2). Menengai Caldera is located in the central Kenya Rift at about 0° 10'S latitude.*
(b) *Overview map of the eastern branch of the East African Rift. Black rectangle shows location of Figure 3.1a. Tectonic plates are outlined and labelled red. The present-day full spreading rate at the rift is c. 2 – 3 mm a^{-1} (Saria et al., 2014), arrows denote spreading direction. CKR, central Kenya Rift; NKR, northern Kenya Rift; SKR, southern Kenya Rift. The topographic data is based on SRTM 1-arc digital elevation data, available from the U.S. Geological Survey Earth Resources Observation and Science (EROS) Center.*

3.2 Regional setting

The Menengai Caldera is one of the youngest large-scale volcanic manifestations of the eastern branch of the East African Rift System (EARS) (Blegen et al., 2016; Calais et al., 2006; McKenzie et al., 1970). It is located within the nascent plate boundary between the Victoria and Somalia plates (Fig. 3.1b), and is subject to a present day full-spreading rate of *c.* 2.3 mm a^{-1} (Saria et al., 2014; Stamps et al., 2008). Situated *c.* 2 km north of the city of Nakuru, Menengai Caldera (0.20° S, 36.07° E) is located at the northern terminus of the Mid-Pleistocene to Recent Lake Nakuru extension zone and the extension zone between Goitumet Volcano and Lake Baringo farther north (Figure 3.1a). The caldera covers an area of *c.* 84 km^2 and has walls up to 300 m tall. Menengai is located immediately above a rift-parallel central gravity high (Kanda et al., 2019; Searle, 1970), which is an integral part of the volcano-tectonic axis. The extension zones along the volcano-tectonic axis record protracted normal faulting, dyke intrusion, hydrothermal activity, and frequent, low-magnitude seismicity (Ibs-von Seht et al., 2001; Mulwa et al., 2014; Tongue et al., 1992).

Volcanotectonic history of the Kenya Rift

The present-day structural configuration of the Kenya Rift was established during the Miocene by protracted volcanism and coeval ENE–WSW- to east–west-oriented extension (Bosworth et al., 2003, 1986; Bosworth and Strecker, 1997). This resulted in a roughly north–south-oriented halfgraben system (Chapman et al., 1978; Crossley, 1979; Morley et al., 1992; Smith, 1994), which broadly follows the boundary between the Proterozoic Mozambique Belt and the Archean Tanzania Craton (Hetzel and Strecker, 1994; McConnell, 1972; Smith and Mosley, 1993). Associated NNW- to NW-striking shear zones in the underlying Mozambique Belt basement are thought to have been reactivated in this early rift phase (Robertson et al., 2015; Smith, 1994; e.g. Smith and Mosley, 1993). Since the early Pliocene, extension and volcanism have been focused on the inner trough, a *c.* 40 km wide inner full-graben (Baker et al., 1988; Dunkley et al., 1993).

A rotation of the extension direction, which may have been coaxial with the minimum horizontal stress (S_{hmin}), to a neotectonic ESE–WNW direction is documented by fault kinematic data, the orientations of dykes and aligned eruptive centres, borehole breakouts and earthquake focal mechanisms (Bosworth et al., 1992; Strecker et al., 1990; Strecker and Bosworth, 1991). The earliest manifestations of this kinematic change appear to be coeval with the emplacement of the ubiquitous mid-Pleistocene trachytes that cover virtually the entire inner graben of the Kenya Rift (Baker et al., 1971; e.g. McCall, 1967; Strecker, 1991). As a result of the kinematic change, dextrally oblique normal faulting has prevailed along the older rift-margin faults (Zielke and Strecker, 2009), whereas the Mid-Pleistocene to Recent fault arrays in the inner trough and the volcano-tectonic axis strike NNE, as observed in the northern and southern Kenya Rift. By contrast, in the NW–SE-oriented central Kenya Rift, the young zones of extension of the volcano-tectonic axis are not continuous, but define left-stepping zones of NNE-striking normal faults and small eruptive centres that are kinematically linked by transfer zones of closely spaced NNE-striking normal faults, such as between lakes Nakuru and Elmentaita, or constitute zones of coeval, WNW-striking dextral strike-slip faults and NNE-striking dip-slip normal faults, as

observed between Mt Longonot and the young zone of extension south of Mt Eburru (Strecker, 1991).

Similar structures exist in the transition between the graben system north of Menengai Caldera and the extension zone of the Molo Graben (Fig. 3.2). The Menengai area constitutes the northernmost such segment of the central Kenya Rift, forming the major transition zone towards the northern Kenya Rift. In addition, on this larger spatial scale, to the west of the area, the mostly Miocene to Early Pliocene structures of the inactive Nyanza Rift terminate (e.g. Jones and Lippard, 1979; Mboya, 1983) and, to the NE, the Kerio Valley of the northern Kenya Rift ends (Figure 3.1). These large-scale tectono-morphological changes intersect in the Menengai area, emphasizing its prominent location within the Kenya Rift.

Geology of the study area

In the central Kenya Rift, trachyte volcanism has been recorded to occur nearly continuously for the last 6 Ma (Baker et al., 1988; Leat, 1991; e.g. McCall, 1967). Early inner rift volcanoes in the greater Menengai-Nakuru area include the Londiani (*c.* 3.1 Ma) and Kilombe (*c.* 1.9 Ma) volcanoes on the western rift flanks (Figure 3.1) (Jones and Lippard, 1979). Areally extensive stratigraphic units in the greater Menengai-Nakuru area that pre-date caldera collapse include the 1-Ma-old Hannington Trachyphonolite Formation *c.* 30 km to the north of Menengai (Griffiths and Gibson, 1980; McCall, 1967) and the corresponding Mbaruk and West Lake Trachyte formations to the south (Leat, 1991). In addition, immediately north of Menengai, are found the Olrongai ignimbrite and the Athinai trachyte, which are probably older than 0.3 Ma (Leat, 1991). Silica-oversaturated peralkaline trachytes constitute most of the Menengai volcanics (Leat, 1984; Leat et al., 1984; Macdonald et al., 1994), associated with minor volumes of metaluminous trachytes and pantelleritic rhyolites (Macdonald et al., 2011). The petrology of the lava flows has been studied in detail by Leat (1991, 1984, 1983; Leat et al., 1984), Macdonald *et al.* (2011, 1994) and Geothermica Italiana (Cioni et al., 1987).

Activity at Menengai volcano is thought to have started at *c.* 0.2 Ma and early lavas of its NNW–SSE-oriented shield date to 0.18 ± 0.01 Ma (Leat, 1984). The Krakatau-style, piecemeal caldera collapse of Menengai (e.g. Leat, 1984; Macdonald et al., 1994) was coeval with the emplacement of the areally extensive Menengai tuff layer, which extends as far as lakes Victoria and Turkana and the Chalbi desert of Kenya (Blegen et al., 2016). This tuff has been radiometically dated to 35.62 ± 0.26 ka using the $^{40}Ar/^{39}Ar$ method (Blegen et al., 2016). A sequence of two major ignimbrites is described in the vicinity of the caldera (Cioni et al., 1987; Leat, 1991, 1984). Younger ash deposits retrieved from drill cores taken at the nearby lakes Nakuru and Elmenteita to the south (Richardson, 1972; Richardson and Dussinger, 1986) suggest a second, large eruptive phase not later than 14 ka (Leat, 1984). Age estimates of this phase range between younger than 15.619 – 20.229 cal ka BP (Cioni et al., 1987), older than 14.561 – 15.973 cal ka BP (Leat, 1984; Leat et al., 1984), or even as young as *c.* 8.900 cal ka BP (Macdonald et al., 1994) (Table 3.1). Nevertheless, none of the volcanic units of the second eruptive phase has been directly dated radiometrically and their age correlation and significance for the main caldera collapse has been a matter of dispute (Cioni et al., 1987; Jones and Leat, 1985).

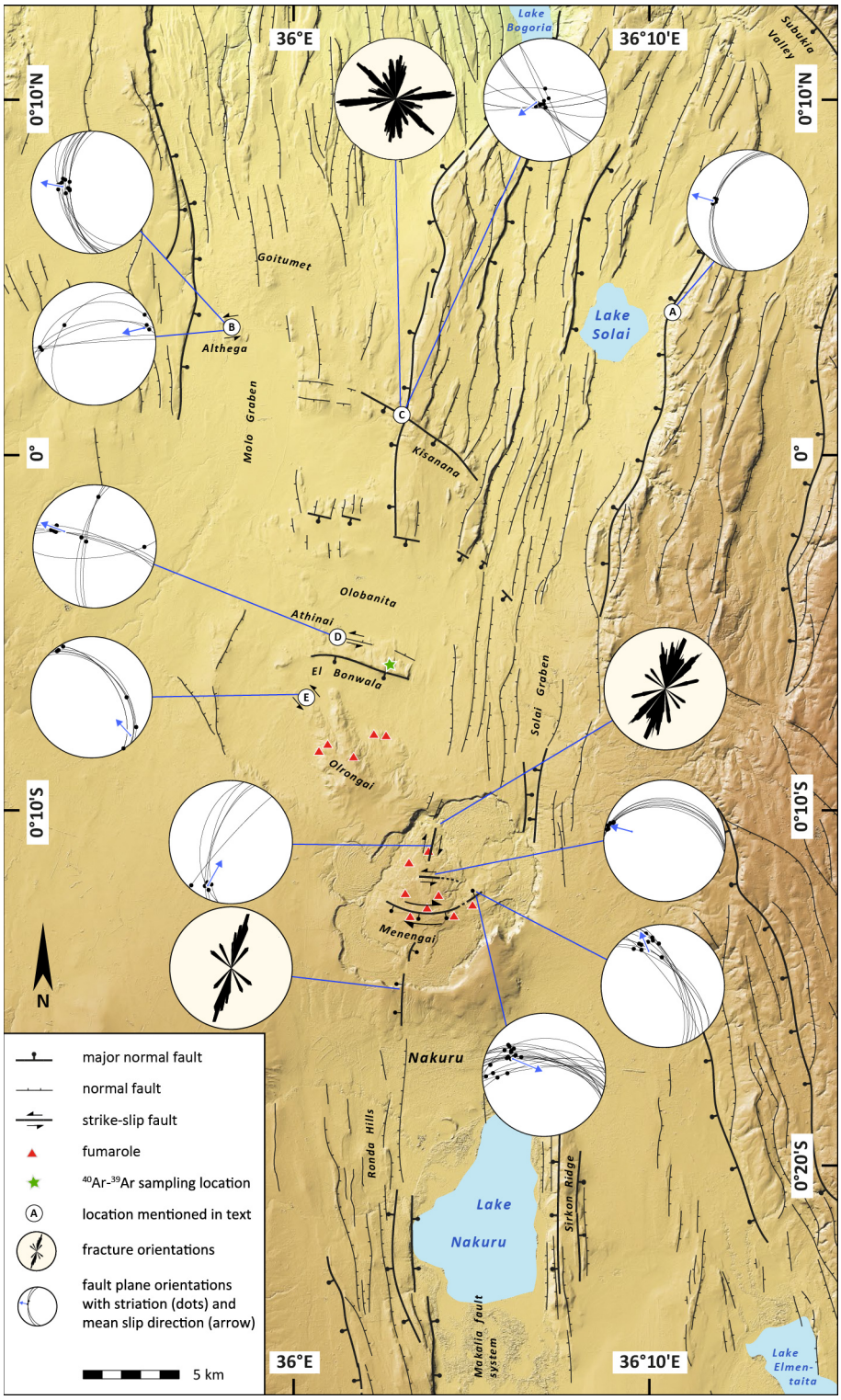

Figure 3.2. Structural overview of the Nakuru area and regions farther north.
Structures were field-mapped in this study, and complemented with previous field mapping of McCall (1967) , Leat (1991) and Strecker (1991). Fault orientations were measured on site and are represented as stereonet plots; blue arrows indicate representative movement direction in the fault plane. Rose diagrams show orientation of observed fractures. The predominantly north striking normal faults prevail in the area. Sinistral strike-slip faults in the north are interpreted as part of a transfer zone between individual rift segments (Figure 3.7). Inside the caldera, the regional extensional stress field is interfered by doming of the volcanic centre (Figure 3.3). The marked locations are discussed in the text. The elevations are based on the TanDEM-X Science DEM (© DLR 2017).

Post-caldera deposits cover the entire floor of Menengai. Particularly, a series of >60 lava flows records protracted volcanic activity after the latest events of caldera subsidence. These lava flows are 5–15 m thick and have mainly blocky, occasionally ropy, morphologies, with pressure ridges and flow levees (Leat, 1984; McCall, 1967). Individual flows are interbedded with air-fall tephra (Leat, 1984). Trachytic scoria cones related to this young episode are situated in the central and the southern part of the caldera and form distinct hills up to 50 m high (Leat, 1984). Limited areas of the outermost caldera floor are mantled by air-fall deposits and soils. In the lowermost northern and eastern parts of the caldera, where the caldera floor has a mean elevation of 1770 m and is as low as 1705 m, diatomites record the former existence of a post-caldera lake with a palaeo-highstand level at 1860 m (Leat, 1984). The Ruplax tuff, an intensely quarried, distinct, post-caldera tuff deposited at the eastern caldera wall, was associated with phreatomagmatic activity during this lake phase (Leat et al., 1984).

The vicinity of Menengai is mainly covered by post-caldera air-fall pumice and only one post-caldera lava flow is located outside the caldera. This flow overlies the 1940 m high palaeo-shoreline of an early Holocene highstand of Lake Nakuru (Leat, 1991, 1984). Active fumaroles are abundant in the caldera, but no historic eruption has been reported.

Dated unit	Location	Material used for dating	Radiometric date (^{14}C ka BP)	Calibrated 2σ age range (cal ka BP)	Reference
Menengai post-caldera palaeosol	SW caldera floor 0.24147° S 36.02588° E 2021°m a.s.l.	Palaeosol Total organic carbon	8.400 ± 0.175	8.979 – 9.889	Schwonke *et al.* 2008 (ID 4 middle Mussonic)
Base of Menengai airfall units	n/a	Plant fragments	8.000 *	(~ 8.900 *)	Macdonald *et al.* 1994
Palaeosol at a Menengai ignimbrite base	NE of Menengai 0.1316° S 36.1537° E	Palaeosol Total organic carbon	14.900 ± 0.900	15.619 – 20.229	Cioni *et al.* 1987
Ashes in Lake Nakuru sediments †	Lake Nakuru sediment core	Organic mud bands in ash layers	28.700 ± 3.100	26.766 – 39.471	Richardson 1972; Richardson & Dussinger 1986
Top of ashes in Lake Nakuru sediments ‡	Lake Nakuru sediment core	Organic mud above ash layers	12.850 ± 0.190	14.561 – 15.973	Richardson 1972; Richardson & Dussinger 1986
Palaeolake Nakuru highstand	0.5° S 36.25° E	Mixed shell	9.650 ± 0.250	10.257 – 11.773	Butzer *et al.* 1972

Table 3.1. Compilation of previously dated radiocarbon samples in the Menengai area
Radiocarbon dates of previous studies, which relate to syn- or post-caldera eruptive phases of Menengai. All ^{14}C dates were calibrated with the IntCal13 calibration data (Reimer et al., 2013) using the software CALIB (Stuiver and Reimer, 1993).

** No error values given in initial study; calibrated age was approximated by assuming a hypothetical radiometric age error of 1 kyr and using the median value of the calibrated age range*
† unit correlated to caldera forming event by Leat (1984) and Blegen et al. (2016)
‡ unit post-dates a second eruptive phase (Leat, 1984)

3.3 Methodology

To aid the investigation of the structural setting of Menengai Caldera and its post-collapse tectonic activity, two high-resolution digital surface models (DSMs) were generated using aerial imagery from two survey campaigns and structure-from-motion (SfM) analysis (Al-Halbouni et al., 2017; Bemis et al., 2014; Carrivick et al., 2016; James et al., 2017; Nex and Remondino, 2013; Sona et al., 2014; e.g. Westoby et al., 2012). A 57 km^2 area of the caldera area was surveyed at altitudes of 250–350 m above ground level using a senseFly eBee Classic unmanned aerial vehicle (UAV) equipped with a 16.1 megapixel camera (Canon Ixus ELPH, 5.0 mm focal length, 28 mm equivalent field of view, in-drone consumer-grade global positioning system geocoding). The image data were processed using Pix4D mapper. From a set of 28 survey points related to an independent infrastructure survey of the caldera by the Geothermal Development Company of Kenya, 12 points were integrated as ground control points in the processing workflow. The remaining 16 points were used for validation of the final three-dimensional point cloud, with an absolute elevation error <1.5 m. The final three-dimensional dense point cloud was converted to a DSM with a ground resolution of 25 cm using LAStools (Isenburg, 2016).

A second DSM was generated by using a series of aerial photographs taken in 2005 with a Wild RC10 camera and a Universal Aviogon Lens, covering a 20 km $\times$ 40 km area of Menengai and adjacent areas to the north (Schwonke et al., 2008). This dataset was processed with similar SfM techniques using Agisoft Photoscan (2016). The scanned aerial photographs were preliminarily geocoded based on the flight log of the airplane. In a second processing iteration, a total of 51, roughly evenly distributed, differential global positioning system ground-survey points from the same campaign (Schwonke et al., 2008) were integrated as ground-control points in the SfM processing chain. The final point cloud was converted to a DSM with 2.5 m ground resolution and associated orthorectified imagery was generated for the whole survey area. For the caldera area, this point cloud was merged with the UAV point cloud using a fine co-registering algorithm in CloudCompare (2016) and then converted with LAStools (Isenburg, 2016) to a 1 m DSM.

Point clouds and shaded-relief views of both digital elevation models were analyzed to distinguish lava flow fronts and fractured block lava surfaces from possible faults. Where accessible, the possible fault locations were then validated and surveyed in the field. The structural map of Menengai was complemented with structural data from areas outside the caldera shown on previously published regional maps (Cioni et al., 1987; McCall, 1967; Strecker, 1991).

The orientations of fault planes and kinematic indicators were measured in the field. Fiber growth, striations, crescent marks and step-like fault plane morphologies were recorded to determine the type of displacement and the sense of motion. Subsequent kinematic analysis was performed using the software tools StereoNet (Allmendinger et al., 2012; Cardozo and Allmendinger, 2013) and FaultKin (Allmendinger et al., 2012; Marrett and Allmendinger, 1990) to visualize fault slip directions on lower hemisphere equal-area stereonet plots. Rose diagrams of the measured fracture orientations were generated using a moving-average algorithm (Munro and Blenkinsop, 2012). In general, we considered that the fault movements derived from individual kinematic analysis were representative of the local principal strain orientations (Marrett

and Allmendinger, 1990; Marrett and Peacock, 1999). Furthermore, we assumed the overall strain to be coaxial with the regional stress field because the discussed faults are young and the finite strain is small; therefore, the inferred principal strain orientations can be expected to represent infinitesimal strain and hence can be assumed to be coaxial with modern principal stress orientations (e.g. Sanderson and Marchini, 1984). In addition, the high heat flow in the upper crust of the rift centre (Nyblade et al., 1990; Omenda, 1998; Sippel et al., 2017; Wheildon et al., 1994) and the volcanic rock types of the Quaternary units suggest quasi-isotropic materials when compared with the highly anisotropic basement rocks at the rift margins that were ruptured during the early stages of rifting (e.g. Smith and Mosley, 1993).

In an effort to use landforms and deposits associated with the Holocene Menengai palaeo-lake as age indicators of the youngest volcano-tectonic evolution of the caldera, organic material in a diatomite deposit was sampled for radiocarbon dating. In addition, two bulk soil samples for radiocarbon dating were taken at the base of a consolidated intra-caldera air-fall tuff (Table 3.2). The ^{14}C dates of the samples were determined at the Poznan Radiocarbon Laboratory, Poland using Accelerator mass spectrometry. For subsequent calibration of all the ^{14}C dates, the software CALIB (Stuiver and Reimer, 1993) was used with the IntCal13 data set (Reimer et al., 2013). The same calibration workflow was applied to previously published uncalibrated ^{14}C dates that are reported in the text as calibrated dates (Table 3.1).

Sample Identifier	Dated unit	Location	Material used for dating	Radiometric date (^{14}C ka BP)	Calibrated 2σ age range (cal ka BP)	Lab ID
MEN-DIA	Menengai Caldera diatomites	0° 10.896' S 36° 4.411' E 1742 m a.s.l. (Location U)	Plant remains	10.440 ± 0.210	11.600 – 12.728	Poz-59047
280805-2	Menengai Caldera diatomites	S 0° 09.784' E 36° 05.760' 1807 m a.s.l. (Location V)	Charcoal	4.555 ± 0.146	5.490 – 4.864	KIA28136*
MEN-RT1	Base of post-caldera Ruplax tuff	S 0° 10.452' E 36° 06.760' 1772 m (Location I)	palaeosol (total organic carbon)	7.900 ± 0.110	8.508 – 9.012	Poz-76366
MEN-RT2	Base of post-caldera Ruplax tuff	S 0° 10.452' E 36° 06.760' 1772 m (Location I)	palaeosol (total organic carbon)	5.720 ± 0.040	6.413 – 6.573 (84%) 6.579 – 6.632 (16%)	Poz-76367

Table 3.2. Overview of radiocarbon samples and dates from this study
Radiocarbon ages associated with units inside Menengai Caldera. The palaeolake Menengai was recorded in samples MEN-DIA and 280805-2, attesting lake phases at the beginning and the end of the African Humid Period. As the post-caldera Ruplax tuff shows evidence of magma-water interaction (Leat, 1984), it is thought to be coeval with such an intra-caldera lake. Faults are present in the Ruplax tuff and in units which post-date the earlier lake deposits; thus, both faulting and volcanism must have been active in the Holocene.

** Radiometric dating of this sample was done at Leibniz-Laboratory for Radiometric Dating and Stable Isotope Research, Kiel, Germany.*

A groundmass sample of a major tuff layer was dated using $^{40}Ar/^{39}Ar$ geochronology at the geochronology laboratory of the University of Potsdam (Table 3.3). The sample processing followed the methodology outlined in Uto et al. (1997). The sample was irradiated for four hours at the Oregon State University Reactor (OSTR); the neutron flux during irradiation was monitored using the Fish Canyon Tuff Sanidine (FC3S) reference sample prepared by Geological Survey of Japan with an apparent age of 27.5 ± 0.2 Ma (Uto et al., 1997). Co-irradiation of Alder Creek Sanidine (ACs-2) reference sample was carried out to check the accuracy of the system. A multi-grain incremental heating analysis of the sample was performed using a 50 W CO_2 laser (10.6 μm wavelength) and a Micromass 5400 single-detector noble gas mass spectrometer. All age calculations are based on the decay constant values reported in Steiger & Jäger (1977).

Sample ID	Dated unit	Location	Plateau age* (ka)	Inverse isochron age* (ka)	J value ($\times 10^{-3}$)	J value 1σ error ($\times 10^{-3}$)	Analysis ID
KMM01	consolidated Menengai tuff mantling Athinai trachytes	0° 6.0326′ S 36° 2.8787′ E	37.6 ± 5.7 ka	38.4 ± 5.8 ka	0.988	0.003952	C14042

Table 3.3. Summary of Menengai tuff incremental heating $^{40}Ar/^{39}Ar$ analysis
$^{40}Ar/^{39}Ar$-chronology of tuff sample collected at Emy quarry, El Bonwala Ridge, north of Menengai. Plateau age and inverse isochron age agree within 1σ error. The age correlates with the Menengai tuff dated by Blegen et al. (2016) to 35.62 ± 0.26 ka, which is associated with the main caldera collapse. This radiometric age thus constitutes the oldest age limit for all intra-caldera structures. The detailed results of the multi-grain stepwise-heating analysis are available in Appendix B.

** given error represents 1 σ uncertainty plus uncertainty of J value.*

3.4 Results

We describe the structures mapped in the study area, starting with the regional framework in the areas adjacent to Menengai Caldera (Figure 3.2), followed by the detailed areas within the caldera (Figure 3.3).

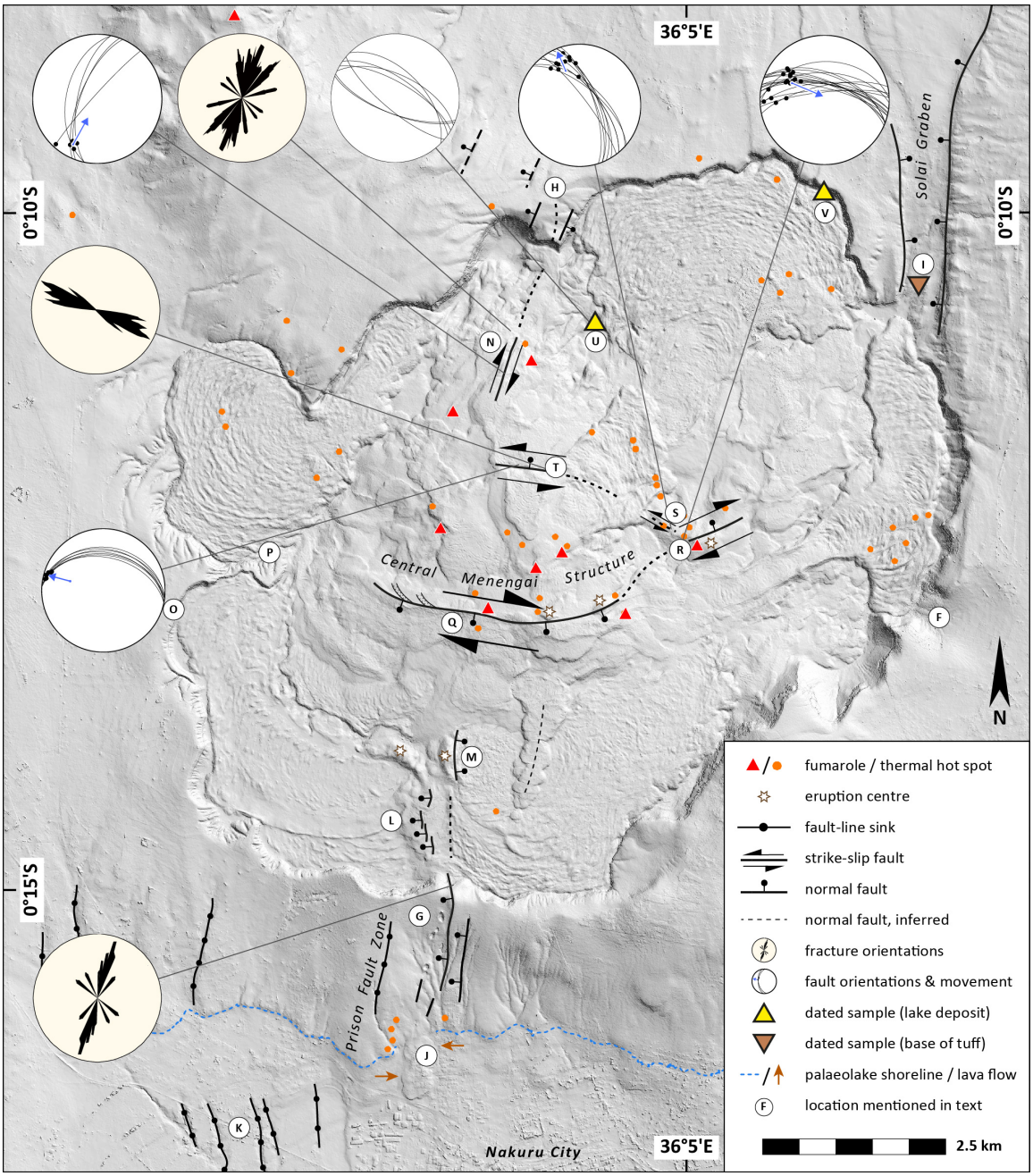

Figure 3.3. Structural map of Menengai Caldera.
Background shaded relief based on 1 m resolution digital surface model. Rose diagrams show orientations of fractures, stereonet plots show observed fault orientations with striation and representative movement direction. All structures were mapped and validated on-site. The north-striking faults that dominate the larger area traverse and offset the caldera rim, and must have been active after caldera collapse. Timing of faulting is bracketed by the caldera age, the dating of faulted units (triangles) and overprinted shorelines of palaeo-lake Nakuru (dashed blue line). Inside the caldera, the regional fault trend is disturbed; a central, dextrally oblique normal fault (Central Menengai Structure, CMS) traverses the caldera. This apex fault shows horsetail fractures and antithetic R' structures; adjacent feeder dykes (location S) indicate that it fed post-caldera lava flows. The structures in the caldera centre are interpreted to relate to post-caldera resurgence, which overprints the extensional stress field of the rift.

Regional structures in the Nakuru area

The regional structural character of the Nakuru–Menengai region is dominated by north- to NNE-striking horsts and graben, which are occasionally cut by east- to ENE-striking faults (Figure 3.2). The Lake Nakuru zone of extension (the Makalia fault system), located 10 km south of Menengai, comprises a north-striking horst to the east of Lake Nakuru (Sirkon ridge), and the Ronda hills to the west. Recent, NNE-striking fissures were mapped at the latter location (Leat, 1991; McCall, 1967). To the north of Menengai, at a distance of *c.* 30 km, a prominent horst-and-graben system characterizes the rift floor, including the Solai graben to the NE, which is bounded by a large NNE-striking, down-to-the-west normal fault with dip-slip kinematics (Figure 3.2, location A). In the NW, similar north-striking normal faults, which offset the Hannington trachyphonolites, dominate the area (Figure 3.2, north-striking normal faults at location B, rose diagram of fractures at location C) (Griffiths and Gibson, 1980; McCall, 1967).

These north-striking horsts are systematically traversed by roughly east-striking fractures and faults (Figure 3.2, locations B, C and D). This fault pattern is most apparent at Althega quarry, south of Goitumet, where east- to ENE-striking sinistral strike-slip faults cut the normal-faulted Hannington trachyphonolites (Figure 3.2, location B). In the Kisanana area (Figure 3.2, location C), the NNE-striking horst blocks are bounded by a SSW-dipping normal fault. At this location, the Hannington trachyphonolites are densely fractured and, although the fracture orientation is less distinct, east- and SE-striking orientations prevail.

The same structural pattern prevail closer to Menengai, but its morphologic expression in the landscape is less pronounced due to the ubiquitous pyroclastic cover in the low-elevation areas. About 10 km north of the caldera, the Athinai trachytes and phonolites (Leat, 1984) comprise the prominent ESE-striking, fault-bounded El Bonwala ridge (Figure 3.2, location D). The northern flank of this ridge is densely faulted by NNE-striking normal faults and dominant ESE-striking strike-slip faults within the Athinai trachytes. The striations on the latter fault surfaces again indicate sinistral strike-slip kinematics (Figure 3.2, stereonet at location D). The top of the ridge is partly mantled by a 0.5–4 m thick welded tuff (Figure 3.2, green star). The age of this tuff was dated by us to 37.6 ± 5.7 ka using the $^{40}Ar/^{39}Ar$ method (Table 3.3); the age and geochemistry of the tuff correlate with the Menengai tuff (Blegen et al., 2016) and it is therefore attributed to the caldera collapse. Because this tuff at El Bonwala is neither fractured nor faulted, the faulting of the Athinai trachytes must predate the deposition of the tuff.

Closer still to the caldera, the pre-caldera rocks of the Menengai volcanic edifice are exposed at the Olrongai hills (Figure 3.2, location E). The Olrongai trachytes terminate with a step-like morphology on the northern flanks of Olrongai; the trachytes are cut by NW-striking faults subparallel to the ridge. Subtle striations on the corresponding fault planes document sinistral strike-slip kinematics.

This arrangement of north- to NNE-striking normal faults with the systematic occurrence of roughly east-striking sinistral strike-slip faults north of Menengai is similar to the structural transition zone farther south between the Mt Longonot caldera volcano, the Olkaria and Ol Njorowa (Hell's Gate) area of recent faulting, and Mt Eburru (Figure 3.1) (Clarke et al., 1990; Strecker, 1991). Importantly, the coeval activity of dip-slip normal and strike–slip faulting in both areas

attests to the role of these young zones of faulting as kinematic transfer zones in a region of oblique rifting between spatially disparate zones of extension along the active volcano-tectonic axis.

Structures of the Menengai Caldera rim

The pre-caldera units are almost continuously exposed along the inner caldera walls. Only along a *c.* 1-km-long stretch of the eastern part is covered by fluvio-lacustrine deposits of the extensive Early Holocene Lake Nakuru highstand (Figure 3.3, location F) associated with the former northwards overflow of this lake; the lake is currently 180 m lower (Figure 3.4a). The excellent exposures of the caldera walls reveal a sequence of subhorizontal beds with evidence for post-caldera faulting found at the southern flank (Figure 3.3, location G) and two additional locations at the northern rim of Menengai (Figure 3.3, location H).

The most prominent structure at the northern wall of Menengai is the north-striking Solai graben (Leat, 1984; McCall, 1967), which comprises two principal normal faults that control a central depression connected with the intra-caldera basin (Figure 3.3, location I). The post-caldera Ruplax tuff, which is exposed throughout the floor of the Solai graben, is affected by north-striking normal faults and fractures (Figure 3.4b). Our radiocarbon dating of the base of this tuff, which stratigraphically superposes post-caldera lava flows, yields ages of *c.* 8.700 cal ka BP and *c.* 6.500 cal a BP (MEN-RT1 and MEN-RT2 in Table 3.2). Although these ages are considerably younger than previous age estimates of the tuff and the possibility of young contamination of the bulk soil samples cannot be excluded, the phreatomagmatic tuff is still coeval with a long-lived intra-caldera lake phase; even with older age estimates, the tuff must thus have been fractured during the Holocene. The faults are sealed by the younger post-caldera lava flows immediately south of the caldera border. Further west, the northern caldera rim has NNE-oriented, metre-scale topographic breaks (Figure 3.3, location H). These breaks are inferred to be extensional fault-line scarps, with down-to-the-west and down-to-the-east displacement, respectively, forming small horsts (Figure 3.4c). These topographic anomalies are only faintly expressed farther north of the caldera rim, where pyroclastic deposits form a smooth morphology (Figure 3.2).

On the southern flank of the caldera, NW of Nakuru, a 1 km wide NNE-oriented volcano-tectonic zone traverses the flank and rim of the caldera (Figure 3.3, location G; Figure 3.4d, e). This zone, termed Prison eruptive fissure in earlier studies (Cioni et al., 1987; Leat, 1983), is the northwards continuation of normal faults at Ronda hill (Figure 3.2). This zone hosts five NNE–SSW-elongated cones and craters, an array of normal faults and fractures with similar NNE-oriented strikes (8°) and metre-scale scarps, as well as an associated post-caldera lava flow. At the caldera rim, there are west-dipping normal faults with metre-scale offsets and a hanging-wall flexure, partially affected by antithetic faulting (Figure 3.4f). The direction and morphology of the flow indicate that the lava emanated from a fissure-shaped vent close to the caldera margin. It flowed both to the north inside the caldera, mantling its wall, as well as to the south, down the outer slope, probably fed by additional vents. The flow post-dates the Early Holocene shoreline of palaeo-lake Nakuru at 1940 m elevation (Figure 3.3, location J) (Leat, 1984, 1983). In the earlier publications on the Quaternary fluctuations in lake-level in East Africa, this shoreline was thought to be coeval with the Late Gamblian lake highstand (Washbourn-Kamau, 1971, i.e. 1970)

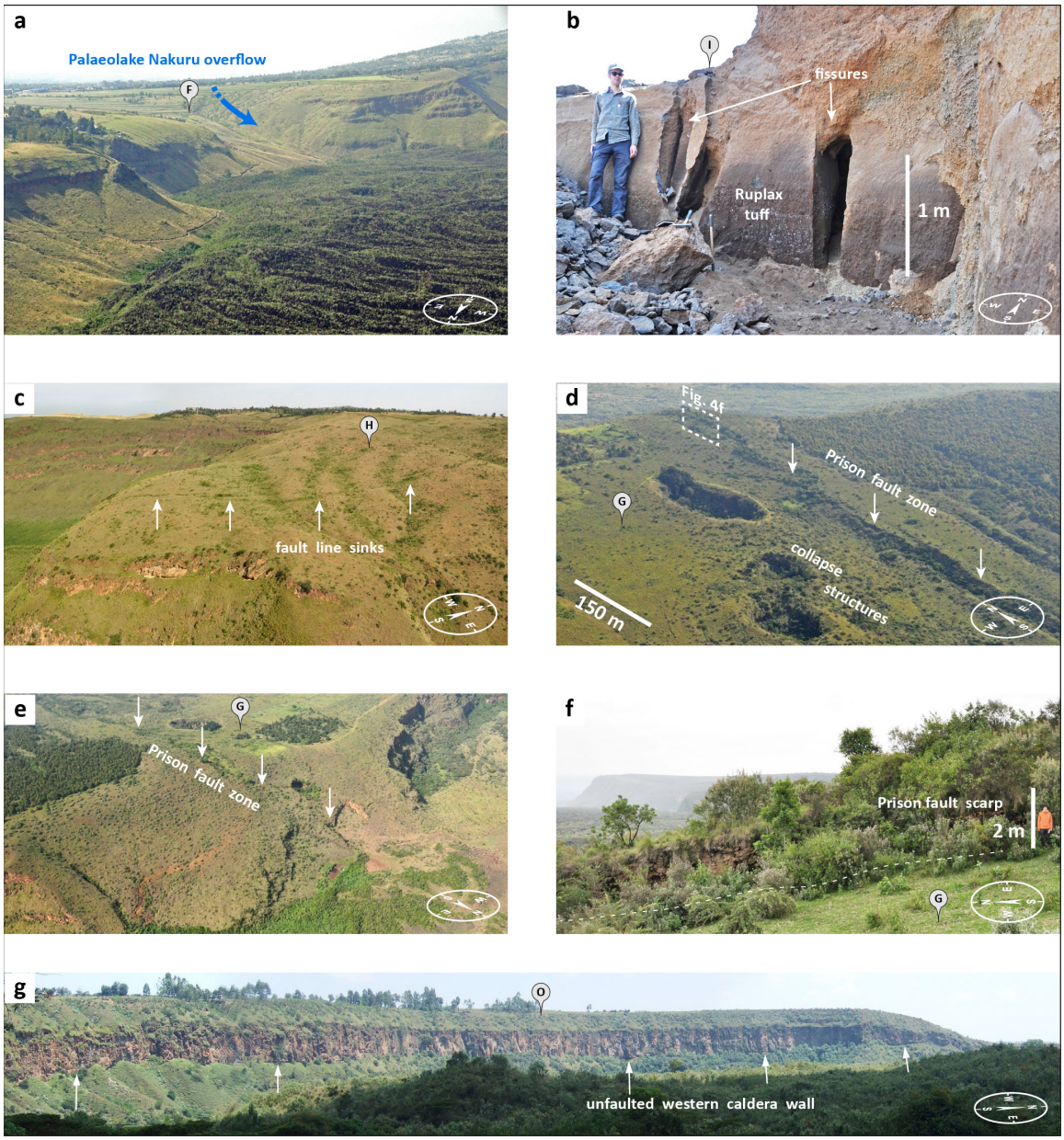

Figure 3.4. Photos of locations close to the Menengai Caldera rim.
(a) *Sediments of the early Holocene overflow of Lake Nakuru into the caldera (blue arrow) mantle a low-elevation zone in the SE rim (location F).* ***(b)*** *Fractures in the post-caldera Ruplax tuff inside Solai Graben indicate extension during the Holocene.* ***(c)*** *Fault line sinks in the northern rim indicate post-caldera fracturing (location H).* ***(d,e,f)*** *The Prison Fault Zone in on the southern caldera flanks traverses and cuts the rim. Normal faults have metre-scale offsets. Crater-like collapse structures are associated with a post-caldera lava flow which mantles the rim and the early Holocene shoreline of palaeolake Nakuru farther south.* ***(g)*** *Unfaulted units can be traced along the western caldera rim. As north-striking faults dominate due to the regional stress field, only the northern and southern caldera rim are cut by faults.*

in the Nakuru basin, which was ^{14}C-dated on freshwater molluscs, yielding an age of 10.257 – 11.773 cal ka BP (Butzer et al., 1972) (Table 3.1). This highstand is thus a manifestation of the Holocene African Humid Period, documented in adjacent sub-basins of the Kenya Rift (Garcin et al., 2017, 2012, 2009; e.g. Hillaire-Marcel et al., 1986; Roberts et al., 1993). Consequently, faulting and volcanic activity across the southern caldera flank must be considerably younger and records protracted extensional processes along the volcano-tectonic axis.

Data from an airborne thermal infrared survey (Schwonke et al., 2008) suggests that a series of thermal anomalies with a similar alignment is located along this young fault zone. Farther south, on the SW slopes of the caldera flank, aligned fault-line sinks in pyroclastic units indicate the continuation of this fault zone and the exploitation of the faulted deposits by southwards-flowing subterranean waters towards the city of Nakuru (Figure 3.3, location K). The cave- and collapse-doline-like volcanic features are partially cut by the faults, indicating that the faults were active after the post-caldera eruptive events.

Intra-caldera structures

The Nakuru (Prison) fault zone extends across the southern caldera wall into the Menengai Caldera affecting post-caldera units. It comprises a 300 m wide zone with densely spaced, NNE-striking extension fractures that affect an extensive lava flow, which originally flowed southwestwards (Figure 3.3, location L). The fractures have sigmoidal shapes and constitute a sequence of linked structures, each with a length between 40 and 250 m, and a steep west-facing scarp (Figure 3.5a). Although these features are very subtle in the field, they are prominently expressed on the DSM. We infer that these features are associated with down-to-the-west normal faulting, with a maximum displacement in the central part of the scarps. Farther north, approximately 1.3 km inside the caldera, these features terminate at a stepover to the east and transition into an inferred east-dipping normal fault (Figure 3.3, location M). This north-striking, 900-m-long crescent-shaped fault constitutes the eastern margin of a north–south-elongated scoriaceous eruption centre, which is located along the strike of the Nakuru-Prison fault zone farther south. The structure cannot be traced farther north, where its throw must be minimal. A younger lava flow also covers the area to the north, where additional structures may be buried. About 700 m to the west of the eruption centre, another scoria cone is elongated ENE–WSW and our DSM analysis suggests that this ridge may be affected by NNE-striking extensional fractures, similar to the ones described farther south. Approaching the Menengai Caldera floor from its northern rim, 1.5 km south of the northern wall, closely spaced, NNE-striking extensional fractures and normal faults are visible in artificial exposures in a lava flow (Figure 3.3, location N). Striations on the fault surfaces are scarce, but a limited data set suggests dextral strike-slip motion along the NNE-striking fault (Figure 3.5c). However, this observation may not be representative for the overall fault zone, given that pervasive, semi-parallel fractures and faults are also extensional. The exposure of the *c.* 20-m-wide fault zone is characterized by thick, white amorphous silica-sinter deposits and NNE-aligned active fumaroles. Further SSW, the fault zone continues towards the caldera centre, affecting *c.* 700 m of a north-directed blocky lava flow. The flow is intensely fractured along the fault, although a continuation of this fault farther inside the caldera is not evident.

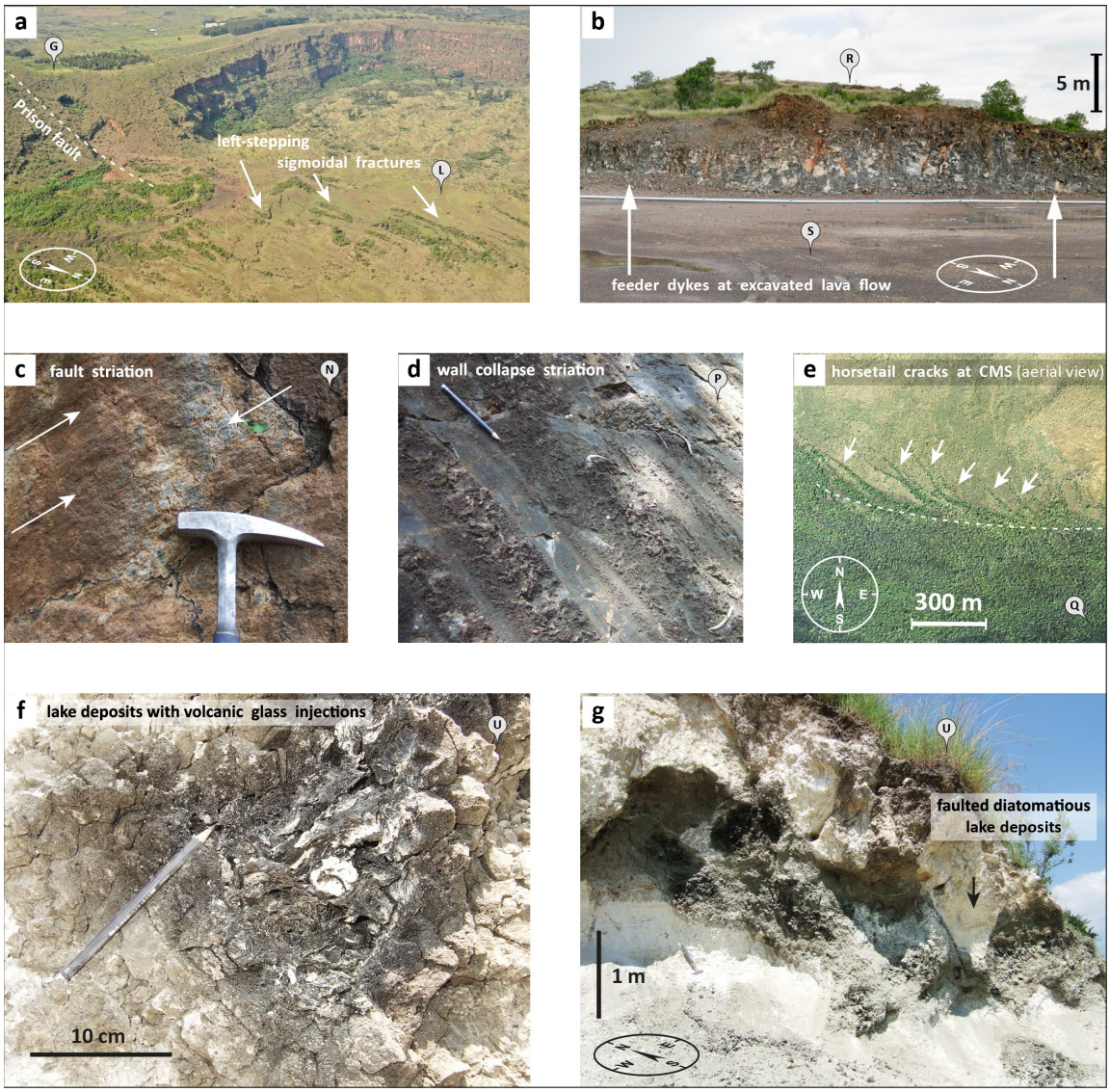

Figure 3.5. Photos of structures inside Menengai caldera.
(a) *The continuation of the Prison Fault Zone shows sigmoidal fractures in a left-stepping en-échelon pattern, indicating a disturbance of the regional stress field.* ***(b)*** *Feeder dykes in the caldera centre (location S) indicate that the central post-caldera faults facilitated magma ascent.* ***(c)*** *Striation at intra-caldera faults indicate that faults have an oblique-slip motion.* ***(d)*** *Metre-scale striation in the far west of the caldera is interpreted to relate to a caldera wall collapse.* ***(e)*** *Aerial view of horsetail fractures at the Central Menengai Structure, indicating a dextral strike-slip component of the apex fault.* ***(f)*** *Volcanic glass in diatomaceous post-caldera lake deposits indicate volcanic activity during the early Holocene intra-caldera lake.* ***(g)*** *Fractures in intra-caldera lake deposits show that normal faulting persisted during or after the lake phase.*

At the NE caldera wall, the normal faults of the Solai graben do not affect the youngest flows within the caldera. Similarly, at the SE caldera rim, the wall is partly covered and constitutes a low-elevation zone with a graben-like morphology (Figure 3.3, location F; Figure 3.4a). The presence of gullies and marked erosive scars and a freshwater spring suggest that the pre-caldera

sequence might be locally fractured. However, faults that extend inside the caldera floor could not be unambiguously recognized at this location. A distinct, quasi-horizontal, erosional syn-caldera surface (Leat, 1985) can be traced for several kilometres along the western caldera rim without interruption, highlighting the lack of tectonic overprint in this area (Figure 3.3, location O; Figure 3.4g). At the western promontory of the caldera (Figure 3.3, location P) the wall has locally experienced a break-off and partly collapsed, documented by a polished movement plane with well-developed metre-scale striations, indicating a local dip-slip, down-to-the-north motion, which is interpreted as a gravitational wall collapse (Figure 3.5d).

Structures bounding the central resurgent dome

The centre of the caldera is covered by a stack of lava flows, resulting in a topographic high of *c.* 2150 m a.s.l. with respect to the 1800–1900 m elevations of the caldera-floor sectors closer to the rim. A large, 3-km-long, east- to ESE-oriented linear ridge dominates the morphology, from which several large, south-directed lava flows were sourced (Figure 3.3, location Q). To the north, the flows clearly terminate, forming a prominent north-facing constructional flow front. The morphology of the flows suggests that they were sourced from an east-striking fissure, very close to the northern flow front, along a line where the blocky lava of the flow is intensely fractured. Based on these relationships, we suggest that a major fault associated with this flow, the 3-km-long Central Menengai Structure (CMS), had a down-to-the-south displacement, forcing the highly viscous lava to flow southwards. Fractures up to 100 m long with a maximum width of 3 m and a depth of up to 5 m occur further west. In our aerial imagery, these fractures are well expressed, curved features with localized densely vegetated zones that strike roughly NW, *c.* 15° with respect to the CMS (Figure 3.5e). Ultimately, these fractures converge with the CMS in a south-easterly direction, reminiscent of the horsetail structures associated with dextrally oblique-slipping normal faults (e.g. Kim and Sanderson, 2006). Parallel to these horsetail structures, fumaroles, which occur immediately north of the CMS, show a similar NW to WNW alignment.

Further east, the CMS is situated along-strike from two post-caldera eruption centres (Leat, 1984), where it is slightly bending, and its strike changes to an ENE direction. A major fault at this position was first proposed by Chorowicz (2005), although with a different and poorly-constrained geometry. Further NE along strike, the CMS continues into another east- to ENE-striking fault, which dips towards the north and cuts the post-caldera lava flows, accompanied by a cluster of similarly aligned fumaroles (Figure 3.3, location R). At this location, the dextral strike-slip kinematics of the CMS are very well expressed by striations along corresponding fault surfaces (stereonet at location R in Figure 3.3). In addition, a recently excavated lava flow reveals associated steeply dipping antithetic minor NW-striking faults with sinistrally oblique strike-slip kinematics (Figure 3.3, location S). These faults provided a pathway for two separate small dyke intrusions into the post-caldera flows that are exposed in the excavated flank of a geothermal well pad (Figure 3.5b). Although the spatial extent and thus the larger orientation of the small dykes could not be discerned, these features highlight the localization of Holocene intra-caldera volcanic effusions along existing fault systems.

About 2 km farther north of the CMS, a secondary east-striking fault exists; it causes a *c.* 45 m down-to-the-north drop in topography (Figure 3.3, location T). A sinistral offset between 60 and

110 m is estimated based on offset of lava flows. Slickensides indicate sinistral strike-slip motion, together with NNE-oriented fissures in a zone of pervasive fracturing, with a 110° strike. We interpret the entire zone as a sinistral strike-slip fault, although the throw associated with the main topographic break may also be partially caused by a step in the palaeo-topography beneath the lava flows caused by previous faulting.

Lacustrine deposits within the Menengai Caldera

In the NE sector of the caldera where the topography is lowest, the diatomaceous lacustrine deposits of Menengai Caldera are affected by faulting and magma injections, suggesting post-caldera intra-lake volcanic activity (Figure 3.5f-g). As the diatomite is not pervasively altered at the contact, we assume it was water-saturated during the eruption and that the magma injections are of phreatomagmatic origin. About 1 km south of the northern caldera rim, the elevation is lowest and forms a small basin between the lava flows, which does not contain a present-day lake, but is still significantly wetter than the surrounding area (Figure 3.3, location U). At 1742 m elevation, a layer of organic material inside the diatomites was radiocarbon-dated to 11.600 – 12.728 cal ka BP (Table 3.2). The age thus corresponds well to the onset of the African Humid Period (e.g. deMenocal et al., 2000; Garcin et al., 2012, 2009; Gasse, 2000) and the palaeo-lake age estimations of Leat (1984, 1983). The diatomites are cut by normal faults with an ESE-strike and metre-scale offsets forming small-scale graben structures that were generated during the last 12 ka.

Possibly correlative diatomite deposits are located at *c.* 1750 m elevation in the southeastern sector of the caldera. The deposits are not faulted in those exposures, but are affected by soft-sediment deformation and numerous, subsequently formed extensional fractures that have been infilled with sediment. An unambiguous determination of the orientation of these fractures was not possible due to limited outcrop conditions. In addition, close to the northern rim, a section of diatomaceous clay is exposed at *c.* 1807 m elevation (Figure 3.3, location V). Charcoal in these intra-caldera lake deposits was dated to 5.490 – 4.864 cal ka BP (Table 3.2), indicating the persistence of the palaeo-lake inside Menengai Caldera.

3.5 Discussion

The combination of our new field and remote sensing observations with previously published volcanic and stratigraphic data (Cioni et al., 1987; Leat, 1991, 1984), suggests that the greater Menengai and Nakuru regions have been affected by oblique extensional tectonism. Both regions are located in the kinematic transition zone between the NNW-striking central rift segment to the south and the NNE-striking northern-rift segment farther north (Figures 3.1 and 3.2). NNE-striking Quaternary normal faults to the north of Menengai are mainly characterized by dip-slip kinematics. This is compatible with joints in the Lake Hannington trachyphonolites, which also have the same orientation, thus suggesting that the Late Pleistocene direction of extension is WNW–ESE. This assessment agrees with earlier studies of the extension direction and tectonic stress field in the greater Kenya Rift (Bosworth et al., 1992; Haug and Strecker, 1995; Muirhead et al., 2015; e.g. Strecker et al., 1990). Importantly, a subset of structures inside Menengai is oriented along-strike with the NNE-striking Quaternary faults of the central Kenya Rift. This suggests that

caldera evolution in this environment is not only influenced by magmatism along the volcano-tectonic axis, but also by extensional structures that controlled the Menengai volcanic system during all stages of its evolution. In the following sections, we first discuss these relationships at caldera scale and then expand the focus to a regional scale to evaluate Menengai in light of the overall tectonic evolution of the eastern branch of the East African Rift System.

Timing of structural development at Menengai

Although the exact timing of the Menengai post-caldera units is not precisely known, the widespread Menengai tuff and its correlation with the Menengai ignimbrite indicate that a major caldera collapse must have occurred at 36 ka (Blegen et al., 2016); this is the earliest date when the intra-caldera structures could have been formed. However, portions of the caldera may be significantly younger, and a phase of high volcanic activity is indicated at *c.* 14 ka (Cioni et al., 1987; Leat, 1984), which has even been discussed in the context of a second caldera-forming collapse (Leat, 1984). Our new radiocarbon age of palaeo-lake Menengai confirms that the main caldera must have existed before 12 ka; younger caldera-age estimates, e.g. *c.* 8 ka as suggested by Macdonald et al. (1994), thus cannot represent a main caldera collapse, but still document phases of young post-collapse volcanic activity. In particular, the <9 ka radiocarbon dates of the base of the fractured Ruplax tuff, the caldera-cutting faults, and the post-caldera lava flow on the south flank of Menengai, which overlies the early Holocene shoreline of Lake Nakuru (Figure 3.3), further confirm protracted volcanic activity in the Holocene. Taken together, these age constraints imply that most of the post-caldera structures are probably younger than 14 ka and some even younger than 9 ka. This highlights that both the extensional faulting and volcanism are not restricted to a limited timespan following caldera collapse, but have been sustained until the present day.

Fault kinematics inside Menengai Caldera

Sustained Quaternary extensional tectonism in the central Kenya Rift until the present is clearly recorded by structures inside Menengai Caldera. To its south, the Makalia fault zone south of Lake Nakuru continues northwards, traverses the Ronda hills and ultimately cuts the caldera, forming the NNE-striking Nakuru–Prison eruptive fissure at the southern caldera rim. A less pronounced, but similarly striking zone of normal faulting can be inferred at the northern rim based on a step-like morphology. The normal faults of the Solai graben cut the caldera flank at the NE caldera rim and the post-caldera Ruplax tuff is normal-faulted and fractured. The chronology of these faulted units unambiguously confirms that both volcanism and extension must have been sustained throughout the Holocene. The rim of the caldera is exclusively affected by NNE-striking faults, which is compatible with the Mid-Pleistocene to Holocene regional extension direction. Young caldera-cutting faults similar to the structures at Menengai that also strike north to NNE, representing the present-day extension direction, have been observed at other Kenyan rift volcanoes, such as Silali (Smith et al., 1995), at volcanic eruptive centres in the Suguta Valley (Dunkley et al., 1993; Melnick et al., 2012), and further north in the Main Ethiopian Rift (Acocella, 2014; e.g. Corti, 2009).

Despite the similar characteristics of the Menengai faults to the regional, rift-related extensional structures, the majority of Menengai intra-caldera structures have orientations and kinematics

that differ from the regional rift structures. The structures in the central Kenya Rift are typically north- to NNE-striking dip-slip normal faults and east–west-oriented sinistral strike-slip faults that kinematically link left-stepping zones of extension. In the caldera, however, the NNE-striking structures often have strike-slip components and the major east-west-oriented CMS is a dextral strike-slip fault. This dextral kinematics is corroborated by horsetail-type fractures (location Q), slickensides (location R), and minor sinistral faults, which are interpreted as antithetic R' structures that strike at high angles with respect to the CMS (location S).

We propose that the dextral CMS and its northern, sinistral counterpart (location T) represent interference patterns between the regional tectonic stress field and a local disturbance of the stress field due to the post-caldera volcano-tectonic activity, including resurgence of a central dome. Although in previous studies the elevated centre of Menengai Caldera was regarded as a stack of lava flows (Cioni et al., 1987; Leat, 1984), gravity studies suggest a large intrusive body at *c.* 6 km depth (Kanda et al., 2019; Simiyu and Keller, 2001, 1997; Wamalwa, 2011; Wamalwa et al., 2013), which is further supported by the existence of a low-resistivity zone at 4–6 km depth in the centre of the caldera according to magnetotelluric data (Wamalwa, 2011; Wamalwa et al., 2013). These phenomena have been linked with the presence of a magma chamber, which is suggested to be most distinct in the NW part of the caldera and possibly extends farther NW beneath the Olrongai hills (e.g. Wamalwa et al., 2013). At even shallower depths of *c.* 2 km, high-density gravity anomalies in the caldera centre indicate smaller syenitic intrusions and the corresponding geothermal wells feature both fresh glass and temperatures close to 400°C at these depths (Kanda et al., 2019). The margin of these geophysical anomalies was hypothesized by Kanda *et al.* (2019) to be an arcuate, east–west-oriented subsurface structure. The location of these inferred subsurface structures are compatible with our identified surface faults – that is, the CMS including its dyke intrusions in the east (location R), and the east–west-striking fault north of the caldera centre. It is therefore likely that these central surface faults continue at depth and bound a central block of the caldera. Magmatic injection processes associated with the magma chamber are inferred to have caused the resurgence of this central block. This process is therefore interpreted to control the intra-caldera structures, forming an apical horst block that has been rising and moving laterally eastwards on a millennial timescale.

The development of such structures has been shown in experiments. For example, analogue and numerical models of caldera collapse indicate that a concentric set of outward-dipping reverse faults may form in the central part of a caldera during the collapse, which accommodates larger surface displacements of the subsiding central block (Holohan et al., 2013; e.g. Marti et al., 1994). In addition, during resurgence, such arcuate or ring faults can reactivate with the opposite kinematics (Acocella et al., 2000). Experiments specifically designed to simulate resurgence in extensional settings generated an elliptical resurgence dome, partly bounded by outward-dipping normal faults rather than the typically inward dipping circumferential faults (Acocella et al., 2004). These models explain subvertical to outward-dipping normal faults that bound central apical resurgence horsts, such as at Menengai.

An apical resurgence horst has also been proposed for Ischia caldera, Italy (Acocella and Funiciello, 1999), where a central block is bounded by pre-existing, reactivated and inward dipping

faults. The central block is uplifted and slightly tilting and has accommodated at least 800 m of uplift during the last 33 ka (Acocella and Funiciello, 1999). Although vertical displacements at the Menengai apical horst could not be quantified in our study, we propose that the structures in the centre of Menengai Caldera have a comparable general geometry. However, the apical block in Menengai is also laterally moving eastwards, as documented by the dextral kinematics of the CMS and the antiparallel sinistral horst-bounding fault further north. Recent models characterize similar oblique-slip fault kinematics during caldera subsidence and describe horizontal motion due to off-centred subsidence (Holohan et al., 2013). Such 'trapdoor-like' movement has also been observed during recent deformation at Tendürek volcano, Turkey (e.g. Bathke et al., 2015) and Sierra Negra volcano, Galápagos (Chadwick et al., 2006). Although the fault kinematics at Menengai are related to resurgence and are thus of opposite sense, the fault pattern is very similar to what Holohan *et al.* (2013) and Bathke *et al.* (2015) describe in their analogue and numerical models and could relate to an off-centred, asymmetric resurgence, which is more pronounced in the western part of the central block, causing uplift and also lateral sliding towards the east.

Local syn-caldera structures may have existed at Menengai due to multiple-block collapse (Leat, 1983) and may have been buried below the Menengai post-caldera volcanic sequence. Locally, steep gradients in subsurface resistivity data could be interpreted to reflect such structures (Wamalwa, 2011). In this scenario, updoming due to the inflation of a magma chamber may reactivate intra-caldera structures, both for resurgence processes and the formation of pathways for magma ascent.

On decadal timescales, an InSAR study of Kenyan volcanoes indicated subsidence of 2.8 cm at Menengai from 1997 to 2000 (Biggs et al., 2009b; Robertson et al., 2015) and recorded a series of deflating and (possibly) inflating events. However, the overall topography, the domal shape of the measured vertical displacements and the flow directions of lavas associated with fissure systems observed here clearly document that updoming must have been active over decadal to millennial timescales. We therefore conclude that Holocene resurgence is a main cause for the apical horst and the CMS (Figure 3.6).

Immediately at the periphery of the central Menengai horst block, faults are aligned parallel to the regional NNE-striking normal faults, but show strike-slip components. In the south, the intra-caldera segment of the Nakuru–Prison fault zone includes en-échelon, left-stepping faults that may represent dextrally oblique normal-fault arrays (location L). In the north, NNE-striking faults have dextral strike-slip kinematics (location N). Analogue modelling of resurgent domes have shown that radial faults are commonly surrounding a resurgence dome (Cole et al., 2005; e.g. Withjack and Scheiner, 1982) and that resurgent domes undergoing extension show incipient strike-slip faults at the periphery of upwarping areas (Withjack and Scheiner, 1982). As ongoing extension is regionally controlling the structures outside Menengai and at the caldera rim, it is likely that the intra-caldera continuation of these extensional structures interferes with the central resurgence block, resulting in a transtensional fault regime. In addition, the long-term resurgence in such a kinematic regime may not be completely restricted to the central apical

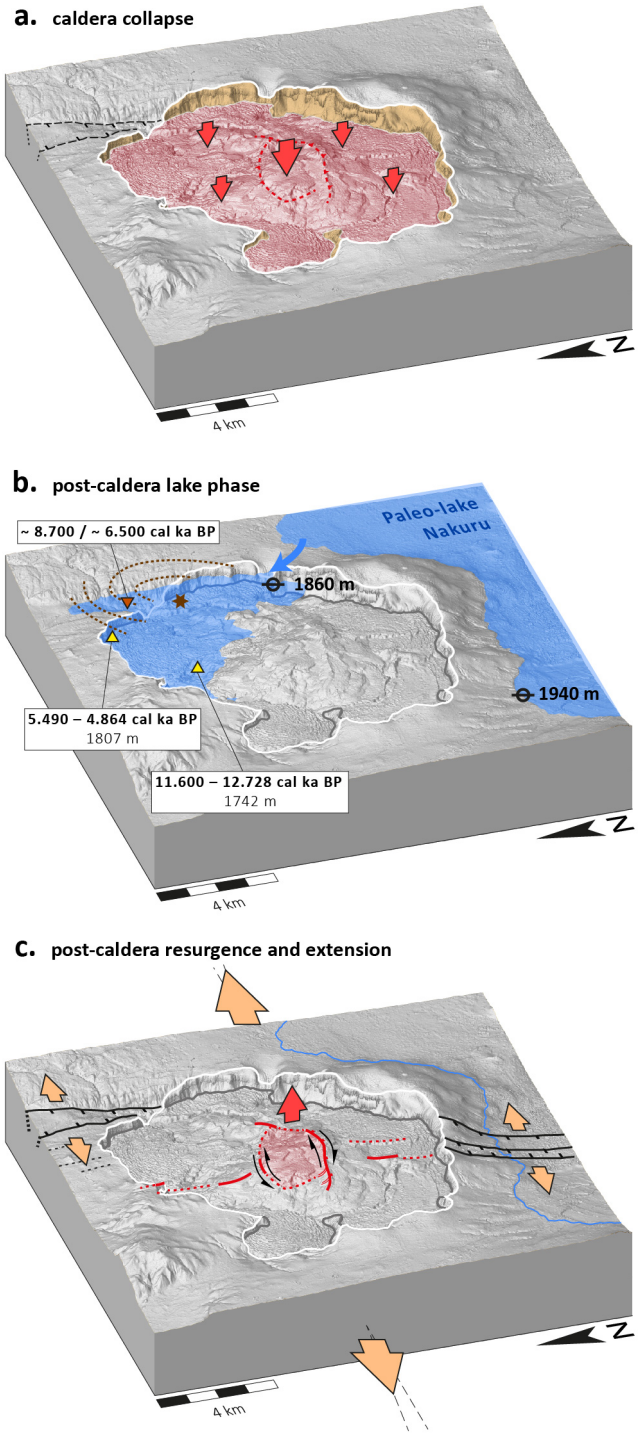

Figure 3.6. Conceptual model of the post-collapse history of Menengai.

From top to bottom (elevation not to scale). ***(a)*** *The caldera formed at ~36 ka (Blegen et al., 2016) at the earliest. During caldera subsidence, the caldera centre is faulted. Normal faults outside the caldera, e.g. the Solai graben in the NW, are assumed to have pre-existed in the area.* ***(b)*** *After the collapse, an intra-caldera lake existed during the African Humid Period (gauges indicate maximum lake levels). Yellow triangles indicate radiocarbon dates of diatomaceous lake deposits. The Ruplax tuff (brown stippled lines denote maximum pumice size isopleths (modified from Leat, 1983); star indicates possible eruption centre; brown triangle marks radiocarbon date of its palaeosol base) is coeval with the lake phase and indicates post-caldera volcanism during the Holocene.* ***(c)*** *The ongoing extension in the Central Kenya Rift entails persistent normal faulting in the whole study area. Caldera flanks, rim and margins are normal-faulted, including the Holocene Ruplax tuff. In the caldera centre, the stress field is perturbed by the doming of the underlying, shallow magma chamber, resulting in an apical horst block, bounded by outward-dipping normal faults, which is rising and laterally moving towards east due to resurgence. Outcrops of dyke intrusions indicate that this fault also facilitated magma ascent of post-caldera lava flows.*

horst, but probably also affects areas in the vicinity further north. Such a larger area of uplift could also explain the orientation of normal faults in the intra-caldera lake deposits (location U), which are oriented subparallel to a possible larger circumferential resurgence boundary. However, the extensional kinematics of these faults in the lake deposits could also be attributed to very local warping due to magmatic injection during the post-caldera lake phase.

With an estimated caldera volume of *c.* 50 km³ (Leat, 1983), the removal of mass due to the caldera-forming eruptions must have been significant. Such gravitational unloading may also facilitate circumferential and radial faults and influence the local stress field at the caldera (e.g. Corbi et al., 2015). It is therefore possible that an unloading effect at least partially contributed to the fault kinematics that we interpret in the context of resurgence, from which they are not easily differentiated.

Studies of caldera subsidence and post-caldera structures in other calderas suggest that caldera formation and resurgence often reactivate pre-existing faults and/or are controlled by regional structures. For example, the resurgent structures at the Long Valley, California (e.g. Bailey et al., 1976) and La Pacana, northern Chile (Lindsay et al., 2001) calderas are both aligned parallel to regional faults; the resurgence at the Caviahue caldera, Argentina is nested in a pull-apart structure along a regional strike-slip fault system (Melnick et al., 2006). Older fault zones were reactivated inside the Campi Flegrei and Ischia calderas (Acocella and Funiciello, 1999; Orsi et al., 1996) and at the Redondo Dome in the Valles Caldera, New Mexico, the apical graben of which is controlled by a pre-caldera fault zone (Nielson and Hulen, 1984; Self et al., 1986). Therefore the intra-caldera structures at Menengai need to be discussed in the context of the regional structural setting.

Orientation and evolution of structures in and around Menengai

In general, the orientation of volcanic centres and the ellipticity of calderas has been utilized to deduce the orientation of regional stress fields (e.g. Bosworth et al., 2003; Robertson et al., 2015; Wadge et al., 2016). Similar to giant borehole breakouts, originally spherical magma chambers in extensional regimes are envisaged to become ellipsoidal and elongated parallel to the extension direction due to stress-induced spalling at the magma chamber walls (Bosworth et al., 2003). As the shape of large calderas has been inferred to reflect the shape of the underlying magma chambers, elongated calderas may consequently represent the extension direction; in turn, the caldera short-axis is aligned with the maximum horizontal stress (S_{Hmax}) and thus the strike of normal faults (Bosworth et al., 2003). Menengai Caldera, however, shows an ENE-oriented long-axis and its short axis is oblique by 30° with respect to the intra-rift faults (Robertson et al., 2015).

Such a misalignment with respect to the present-day stress field could be explained by a rotation of the stress field since the formation of Menengai volcano. Previous studies have proposed such stress field rotations in the Kenya rift from the Miocene to the Quaternary (Bosworth et al., 2003, 1992; e.g. Strecker et al., 1990; Strecker and Bosworth, 1991). However, a WSW–ENE-oriented S_{hmin}, which would have been compatible with the orientation of Menengai Caldera, was inferred for the Pliocene at the latest (Strecker et al., 1990). Younger changes of the tectonic stress field are documented by oblique-slip on north-striking normal faults in volcanic rocks younger than 0.4 Ma in the Elmentaita area further south, by dextral strike-slip fault kinematics along border faults on the eastern rift margin (Bosworth and Strecker, 1997) and by very small dextral strike-slip components in some NNW-oriented normal faults of the <1 Ma Lake Hannington trachyphonolites (this study, Figure 3.2, location B) to the north. Bosworth *et al.* (2003) concluded that most Mid-Pleistocene calderas in the Kenya rift older than 0.1 Ma are oriented east–west, whereas the younger calderas are oriented WNW to NW. The ENE-oriented Menengai caldera is

not compatible with any of these predicted palaeo-stress orientations, neither at the time when the Menengai shield formed *c.* 0.2 Ma ago (and the generation of a large magma chamber can be assumed) nor at the time of caldera formation around 36 ka. Alternatively, the orientation of Menengai Caldera and the NW- to WNW-striking extensional faults in the area further north could also be attributed to a locally rotated stress field resulting from the bend in the transtensional rift in its transition between the central and the northern Kenya Rift. Menengai Caldera is therefore not a representative indicator of a rift-scale stress field oriented differently from the present day. However, assuming that the shape of Menengai Caldera is representative of the geometry of an underlying pre-caldera magma chamber situated at a depth of *c.* 4 to 6 km, this magma chamber would be situated in the pre-rift rocks below the <4 km thick Miocene to Recent Rift sedimentary and volcanic units (e.g. Henry et al., 1990). It is therefore conceivable that pre- and post- caldera structures do not only reflect different geological times, but also highlight processes in different layers of the upper crust.

Robertson et al. (2015) related the ENE orientation of Menengai Caldera to the orientation of deep-seated pre-rift basement structures, which are inferred to have bimodal NE and NW strike directions and which control the development of magmatic reservoirs in the lithosphere. Such older, pre-existing Proterozoic structures influencing rifting in the Kenya rift were also shown to affect fracture propagation, the rift geometry (Hetzel and Strecker, 1994; Smith and Mosley, 1993) and the thermochronological evolution (Torres Acosta et al., 2015a); it is likely that such anisotropies may control the orientation of deeper magmatic migration paths below Menengai. Deep crustal cross-rift structures have been shown to affect the position of calderas in other areas, such as the Okataina Volcanic Centre, New Zealand (Cole et al., 2010), or the Corbetti caldera in the Main Ethiopian Rift (Lloyd et al., 2018). It remains speculative whether an older and larger-scale, east–west-oriented pre-caldera structure is indeed situated below Menengai. Although the existence of basement anisotropies and also the proximity of the inactive, east–west-oriented Nyanza rift suggest possible structural inheritance and interference in the Menengai area, a rigorous conclusion about the reactivation of pre-existing structures is not possible at present. A systematic reactivation of older fault orientations similar to what has been observed in the southern Kenya Rift (Muirhead and Kattenhorn, 2018) was not documented by us and remains purely hypothetical.

The Menengai pre-caldera edifice is aligned with a NNW-oriented positive Bouguer gravity anomaly, situated below Menengai and extending further NNW below Olrongai (Kanda et al., 2019). This gravity high most probably reflects the igneous intrusions of the volcano-tectonic axis; the caldera is oriented perpendicular to the volcano-tectonic axis. In the central Kenya Rift, east–west oriented (sinistral) faults facilitate step-overs of the prevalent NNE-striking normal faults and it is conceivable that the apical horst inside Menengai similarly acts as a regional step-over zone along the volcano-tectonic axis. However, we did not observe a distinct cross-cutting of the intra-rift extensional faults along the structures in the centre of Menengai, neither on-site nor during analysis of the digital surface model. In addition to dextral strike-slip faulting, which is incompatible with the regional rift tectonics, the CMS becomes more subdued with increasing distance from the caldera centre and probably disappears or splays into minor faults towards the caldera rim. It is therefore not feasible to further consolidate the hypothesis of a tectonically rel-

evant strike-slip faulting regime in the caldera centre and thus in the centre of an extending segment within the Kenya Rift.

Implications for regional volcano-tectonic processes

The Pleistocene east-west to ESE–WNW-oriented direction of extension of the Kenya Rift causes the prevalent north to NNE-striking normal faults in the inner trough. However, the decomposition of plate-slip vectors with respect to the predominant orientation of rift margins also suggests a strong rift-parallel component of motion in the NW–SE-oriented central Kenya Rift (Melnick et al., 2012), which is obliquely aligned relative to the present-day regional extension direction. The horst-and-graben system of the inner rift is therefore obliquely traversed by east- to ENE-striking structures where the orientations between the zones of extension change or where lateral kinematic transfers are accommodated at fault terminations of equal strike (Bosworth et al., 1992). Most of these oblique structures record strike-slip motion and normal faulting. We consider these faults to be step-overs at the scale of the rift basin, which accommodate extension in spatially disparate zones of normal faulting (Figure 3.7) (Strecker, 1991). This setting is compatible with the kinematic evolution of obliquely extending plate boundaries (e.g. Withjack and Jamison, 1986), models of transtensional geometry which describe segments of extensional faults that are either connected by transfer faults or form en-échelon arrays (Tuckwell et al., 1996), and comparable en-échelon arrays of normal faults in the Main Ethiopian Rift (Corti, 2009, e.g. 2008). In this context, a seismic velocity model of the Main Ethiopian Rift (Keranen et al., 2004) highlights an en-échelon pattern of high-velocity zones below 7 km depth, indicating massive mafic axial intrusions below individual rift segments. Such an en-échelon segmentation of young zones of extension thus appears to be an integral structural and magmatic feature of obliquely extending rifts. In this context, we consider the sinistral strike-slip faults to the north of Menengai to represent such a step-over to the next separate zone of normal faulting further north along the volcano-tectonic axis that ultimately continues into the Lake Baringo basin. However, we show that Menengai itself, despite having strike-slip faults in its centre, does not facilitate a step-over, but is instead located closer to the centre of a zone of extension.

Menengai and all other Late Quaternary trachyte volcanoes of the central and northern Kenya Rift are aligned along positive gravity anomalies in such spatially separate zones of extension and not along regional-scale, left-stepping transfer zones (e.g. Simiyu and Keller, 2001). Similarly, Muirhead et al. (2015) described the central Kenya Rift as an evolved magmatic rift, where regional extension is accommodated by upper crustal dykes along the full length of evolved, segmented rift basins and where – as opposed to lesser evolved rifts – the transfer zones between rift basins do not constitute areas of increased magmatism. This suggests that axial magmatic processes are responsible for the generation of melts and large-scale eruption centres in the rift segments of the Kenya Rift, which are subsequently mechanically linked by the intervening transfer zones of extension (Figure 3.7) (e.g. Karson and Curtis, 1989). The evolved, yet spatially separated, areas of extension are similar to the areas of ‘oblique-discordant segmented spreading’ that have been proposed for oceanic spreading centres (Abelson and Agnon, 1997); there, the centres of segmented en-échelon zones of extension are the magmatically most active zones, but also the mechanically weakest sectors, from which incipient cracks propagate and link over time.

In Iceland, individual, discrete rift segments each have a magmatic centre acting as a nascent spreading centre (Siler and Karson, 2017). In the Kenya Rift, an axial pattern of lithospheric thinning was inferred from seismic refraction studies (Achauer et al., 1992; Henry et al., 1990; KRISP Working Group, 1991, e.g. 1987), which suggests that the Menengai area and the other Quaternary volcanoes of the rift are the sites of melt generation, upwelling and uplift, respectively (Biggs et al., 2016; Robertson et al., 2015). These areas may thus be envisaged as the precursors for more advanced extension associated with punctiform oceanic spreading centres (i.e. Bonatti, 1985), in a long-term transition from continental to future magma-assisted rifting in the marine realm.

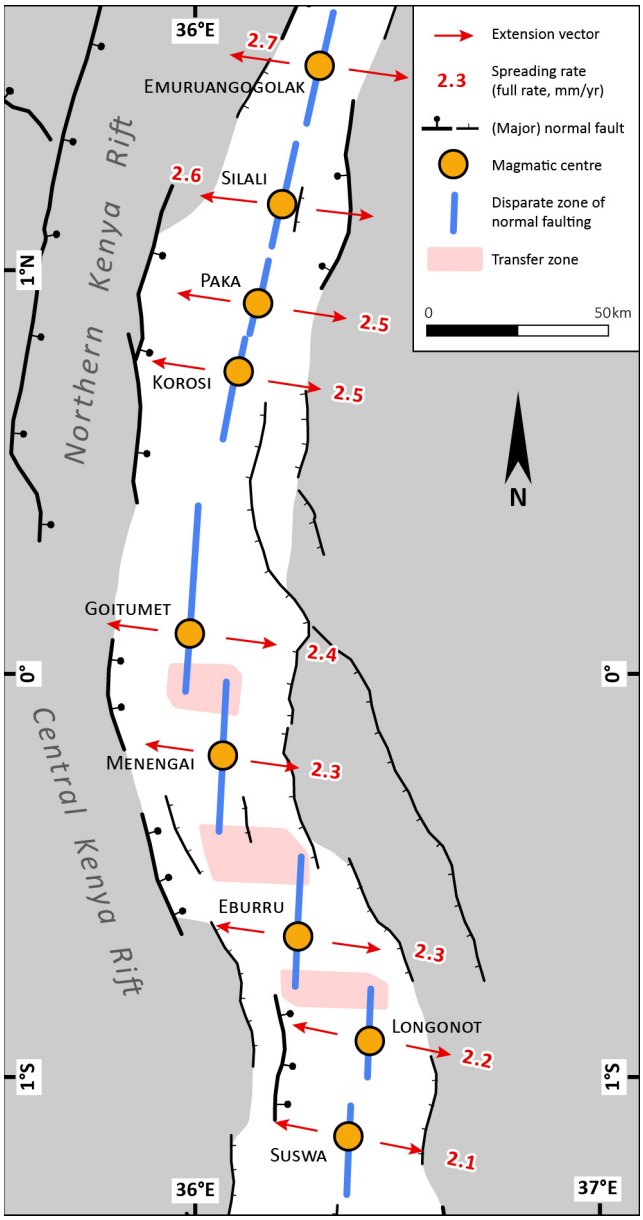

Figure 3.7. Conceptual model of extension in the Kenya Rift.
Magmatic activity along the rift is focussed at regularly-spaced magmatic centres (yellow). These magmatic centres constitute the centre points of individual rift segments, where normal faults form disparate zones of faulting (present-day full-spreading rate based on plate kinematic models by Saria et al. (2014)). In the Central Kenya Rift – where rift orientation is oblique with respect to the extension vector – the rift segments show a left-stepping en-échelon alignment and are kinematically linked by transfer zones, either by closely-spaced normal faults or by a set of NW-striking strike-slip faults and NNE-striking dip-slip normal faults.

3.6 Conclusion

Detailed structural mapping of the Menengai Caldera and its adjacent regions provides valuable insights into the interaction of rift-scale extension and local upwarping due to magmatic processes inside the caldera. Based on field mapping and SfM surveying, we identified faults inside the caldera, the most prominent being the CMS, an ENE to NE-oriented normal fault with a dextral strike-slip component. Feeder dykes suggest that this structure facilitated magma ascent in the post-caldera lava flows. Radiometric dating indicates that both volcanism and faulting continued after caldera collapse during the Late Pleistocene into the Holocene. The kinematics of the central caldera structures indicate that the regional ESE–WNW-oriented extension of the Kenya Rift interferes with the resurgence of the magma chamber, creating a set of faults that borders a central apical horst block in the centre of the caldera.

The structural inventory of the larger Nakuru-Menengai region exemplifies the rift-scale magmatic and protracted extensional processes that have impacted the central Kenya Rift. Structures at the caldera rim and in the area surrounding Menengai are mostly north- to NNE-striking faults; these are related to the 2–3 mm a^{-1} spreading rates of the rift and the east-striking faults with sinistral strike-slip kinematics, which are related to step-overs accommodating extension between individual, separate rift segments. Menengai is situated in the centre of such a rift segment, where magmatic activity is focused and where the lithosphere is weakest.

3.7 Acknowledgments

The Geothermal Development Company of Kenya team in Nakuru contributed to all the fieldwork of this study. The UAV survey of the Menengai Caldera was permitted by the Geothermal Development Company of Kenya. The 2005 aerial photography campaign and its corresponding ground-control survey were supervised by the German Federal Institute for Geosciences and Natural Resources (BGR) during the GEOTHERM project (Schwonke et al., 2008); the usage of this data was kindly authorized by the manangement of the Geothermal Development Company of Kenya. The radiocarbon date for sample KIA28136 was provided by M. H. Trauth, M. Dühnforth and U. Knieß. The TanDEM-X science DEM was granted by DLR (© DLR 2017). The global geography data is based on the GSHHG database (Wessel and Smith, 1996). Outlines of the Kenya Rift lakes were drawn using the Global Lakes and Wetlands Database (Lehner and Döll, 2004). We thank M. Smith and E. Holohan for their constructive and insightful reviews that helped to improve the quality of this manuscript.

Funding

The management of the Geothermal Development Company of Kenya and P. Omenda are thanked for their generous support of this project. Additional financial support was provided by funds of the graduate program Shaping Earth's Surface in a Variable Environment (GK 1364) of the German Science Foundation (DFG) granted to MS (grant number STR 373/19-1). DM was supported by DFG grant ME-3157/4-2. The GEOTHERM project of the German Federal Institute

for Geosciences and Natural Resources (BGR) was commissioned by the Federal Ministry for Economic Cooperation and Development, Germany (BMZ Project No. 2002.2061.1).

Chapter 4

Increased ecological resource variability during a critical transition in hominin evolution

Richard Potts[1,2*], René Dommain[1,3], Jessica W. Moerman[1], Anna K. Behrensmeyer[4], Alan L. Deino[5], Simon Riedl[3], Emily J. Beverly[6], Erik T. Brown[7], Daniel Deocampo[8], Rahab Kinyanjui[2], Rachel Lupien[9], R. Bernhart Owen[10], Nathan Rabideaux[11], James M. Russell[12], Mona Stockhecke[7,13], Peter deMenocal[9], J. Tyler Faith[14,15], Yannick Garcin[16], Anders Noren[17], Jennifer J. Scott[18], David Western[19], Jordon Bright[20], Jennifer B. Clark[1], Andrew S. Cohen[21], C. Brehnin Keller[22], John King[23], Naomi E. Levin[24], Kristina Brady Shannon[17], Veronica Muiruri[2], Robin W. Renaut[25], Stephen M. Rucina[2], Kevin Uno[9]

1. Human Origins Program, National Museum of Natural History Smithsonian Institution, Washington DC, USA
2. Dept. of Earth Sciences, National Museums of Kenya
3. Institute of Geosciences, University of Potsdam, Germany
4. Dept. of Paleobiology, Nat. Mus. of Natural Hist., Smithsonian Inst., USA
5. Berkeley Geochronology Center, USA
6. Earth and Atmospheric Sciences, University of Houston, USA
7. Large Lakes Obs. and Dept. of Earth and Env. Sciences, Univ. of Minnesota, USA
8. Dept. of Geosciences, Georgia State University, Atlanta, USA
9. Lamont-Doherty Earth Observatory, Columbia University, Palisades, USA
10. Dept. of Geography, Hong Kong Baptist University, Hong Kong
11. Dept. of Chemistry, Rutgers University Newark, USA
12. Dept. of Earth, Env., and Planet. Sciences, Brown University, Providence, USA
13. Dept. of Surface Waters-Research and Management, EAWAG, Switzerland
14. Natural History Museum of Utah, Univ. of Utah, Salt Lake City, USA
15. Dept. of Anthropology, Univ. of Utah, Salt Lake City, USA
16. Aix Marseille Univ, CEREGE, France
17. LacCore Facility, Univ. of Minnesota, Minneapolis, USA
18. Dept. of Earth and Env. Sciences, Mount Royal University, Calgary, Canada
19. African Conservation Centre, Nairobi, Kenya
20. School of Earth and Sustainability, Northern Arizona Univ., Flagstaff, USA
21. Dept. of Geosciences, University of Arizona, Tucson, USA
22. Dept. of Earth Sciences, Dartmouth College, Hanover, USA
23. Grad. School of Oceanography, Univ. of Rhode Island, Narragansett, USA
24. Dept. of Earth and Env. Sciences, Univ. of Michigan, Ann Arbor, USA
25. Dept. of Geological Sciences, Univ. of Saskatchewan, Saskatoon, Canada

Published as:
Potts, R., et. al, 2020. Increased ecological resource variability during a critical transition in hominin evolution. *Science Advances* 6, eabc8975. https://doi.org/10.1126/sciadv.abc8975.

Supporting information for this article is available in Appendix C.

Abstract

Although climate change is considered to have been a large-scale driver of African human evolution, landscape-scale shifts in ecological resources that may have shaped novel hominin adaptations are rarely investigated. We use well-dated, high-resolution, drill-core datasets to understand ecological dynamics associated with a major adaptive transition in the archeological record ~24 km from the coring site. Outcrops preserve evidence of the replacement of Acheulean by Middle Stone Age (MSA) technological, cognitive, and social innovations between 500 and 300 thousand years (ka) ago, contemporaneous with large-scale taxonomic and adaptive turnover in mammal herbivores. Beginning ~400 ka ago, tectonic, hydrological, and ecological changes combined to disrupt a relatively stable resource base, prompting fluctuations of increasing magnitude in freshwater availability, grassland communities, and woody plant cover. Interaction of these factors offers a resource-oriented hypothesis for the evolutionary success of MSA adaptations, which likely contributed to the ecological flexibility typical of *Homo sapiens* foragers.

4.1 Introduction

Hypotheses linking environmental change with human evolution have focused on temporal correlations between global or regional climate change and major evolutionary benchmarks. For African hominin evolution, one approach is to identify how increased aridity, humidity, or climate variability induced by orbital forcing broadly coincided with, and thus potentially initiated, the emergence of hominin adaptations and speciation events over time (deMenocal, 2011, 1995; Potts and Faith, 2015; Trauth et al., 2007; Vrba, 1995). It is not yet clear, however, whether any of these general paleoclimate hypotheses account for critical transitions in hominin evolution. A continuing challenge is to connect climate and environmental records with water availability, food, and other ecological resources critical to energy acquisition, yet susceptible to changes that may undermine an organism's existing adaptive strategies. Here, we integrate high-resolution drill core data with outcrop records from adjacent sub-basins in the southern Kenyan Rift Valley to examine how shifts in landscape-scale ecological resources could have influenced hominin adaptation during an interval of fundamental archeological and paleontological change in this region.

The sedimentary record recovered by the Olorgesailie Drilling Project (core ODP-OLO12-1A) from the Koora basin (1.8°S, 36.4°E) provides evidence for changes in water availability, vegetation, and overall resource landscapes associated with the demise of the Acheulean—the longest enduring Paleolithic technology—and its replacement by early Middle Stone Age (MSA) technology as documented in the adjacent Olorgesailie basin (1.5° to 1.6°S, 36.4° to 36.5°E; Figure 4.1). Olorgesailie preserves the oldest evidence currently known in East Africa of the permanent loss of the Acheulean (defined by handaxes and other large cutting tools (LCT)) and the emergence of MSA behavioral innovations (Brooks et al., 2018; Potts et al., 2018). This transition involved new technologies, long-distance obsidian transfer indicating resource exchange among interconnected social groups, and the use of coloring material potentially related to enhanced symbolic capability (Table 4.1).

The onset of these behavioral innovations in the southern Kenya rift occurred between 500 and 320 thousand years (ka) ago (Figure 4.1) (Deino et al., 2018), an interval that overlaps the estimated time of genomic divergence between *Homo sapiens* in Africa and the Neanderthal-Denisovan clade in Eurasia (Schlebusch et al., 2017). The oldest, widely acknowledged fossil evidence of *H. sapiens* (Jebel Irhoud, Morocco), dated roughly 320 to 300 ka old (Richter et al., 2017), coincided temporally with the oldest East African MSA evidence at Olorgesailie. Although other hominin species, such as *H. heidelbergensis* (or H. *rhodesiensis*, e.g., Kabwe, Zambia; Grün et al., 2020) and *Homo naledi* (Rising Star Cave, South Africa; Dirks et al., 2017) were also present in Africa at this time, neither of these taxa is securely associated with MSA artifacts, whereas the MSA is widely associated from 300 ka ago onward with early *H. sapiens* (Blinkhorn and Grove, 2018; Mcbrearty and Brooks, 2000). Hominin remains from southern Kenya dated 397 to 334 ka old consist of poorly preserved teeth and a femoral shaft from Lainyamok (Figure 4.1a), which are metrically consistent with early *H. sapiens* but otherwise cannot distinguish archaic and modern humans (Potts et al., 1988; Shipman et al., 1983). Other cranial remains of late middle Pleistocene age in eastern Africa typically combine *H. sapiens* and archaic traits, yet these finds

are either poorly constrained chronologically (e.g., Eliye Springs KNM-ES 11693, Kenya) or <200 ka old (e.g., Guomde Formation KNM-ER 3884, Kenya; Eyasi 1 and 2, Ngaloba LH 18, Tanzania; Kibish Formation Omo 1 and 2, Herto BOU-VP-16/1, Ethiopia) (reviewed in Stringer, 2016).

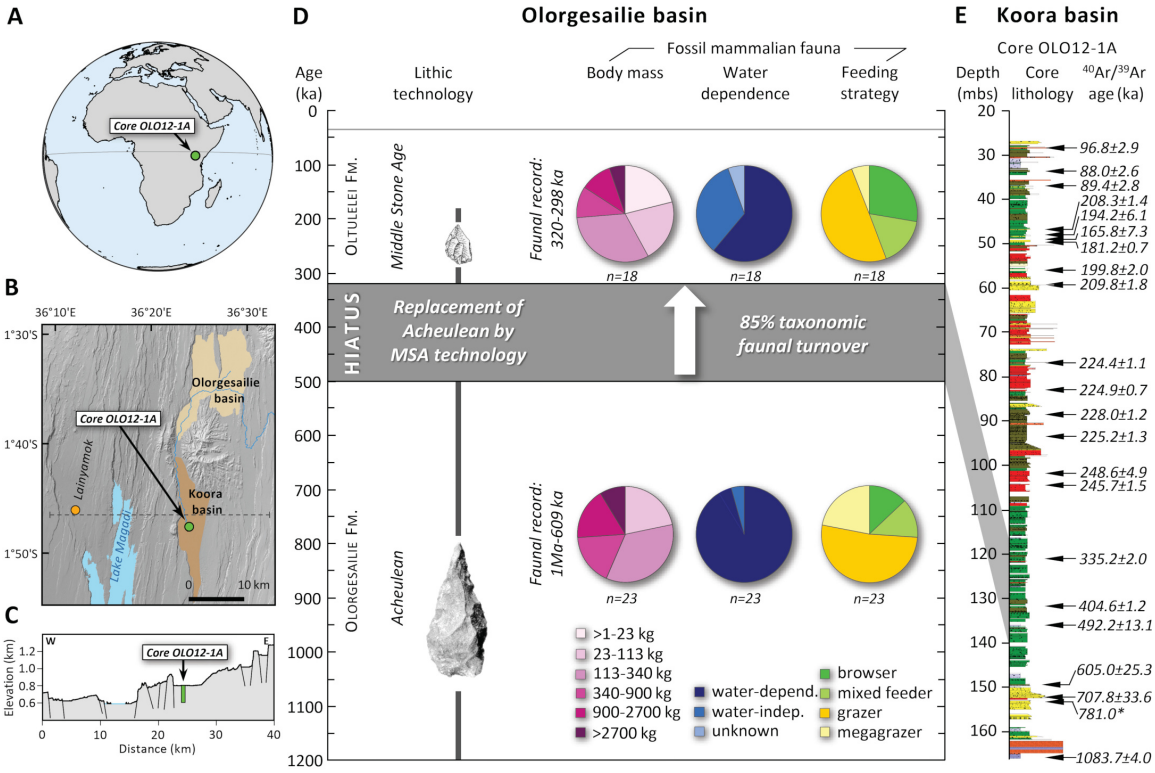

Figure 4.1. Archeological and faunal transitions in the Olorgesailie basin and location, lithology, and geochronology of the Olorgesailie Drilling Project core OLO12-1A.

*(**A** to **C**) Locations of Koora basin drill core, Olorgesailie, Lainyamok fossil site, and east-to-west faulted topography (cross section). (**D**) Olorgesailie basin Acheulean technology spanning ~1 Ma to 500 ka ago; replacement by Middle Stone Age technology ~320 ka ago; and turnover in the fossil mammalian fauna (Brooks et al., 2018; Deino et al., 2018; Potts et al., 2018), including community-level change in body mass, water dependence, and feeding strategies (table C.1). Fossil assemblages dated between ~397 and 300 ka ago recording the faunal turnover are from Olorgesailie and Lainyamok (Deino et al., 2018; Potts et al., 2018; Potts and Deino, 1995). The hominin behavioral and faunal transitions in the Olorgesailie basin occurred during an erosional hiatus dated ~500 to 320 ka old. (Map image: TanDEM-X DEM ©DLR; tool images: Smithsonian Institution.) (**E**) Koora basin drill core depth (meters below surface), lithological sequence, and age constraints spanning from ~1.084 Ma to ~83.5 ka ago, based on Bayesian age model ($^{40}Ar/^{39}Ar$ ages ± 1σ and Brunhes/Matuyama magnetostratigraphic boundary*) (Deino et al., 2019). Shaded zone indicates drill core lithological record during the hiatus in the Olorgesailie outcrop record. See Figure 4.2, Figure C.1 (lithological key), and Materials and Methods (Chapter 4.4).*

Comparisons (Olorgesailie basin)	Acheulean Olorgesailie Fm. (1.2 Ma to 499 ka ago)	MSA lower Oltulelei Fm. (~320 to 295 ka ago)
Artifact/tool size	Large tools, Large Cutting Tools dominant	Smaller, diversified tools
Focus of lithic source access	Local volcanic rocks, coarse, and fine-grain (98%)	Fine-grain rocks (e.g., obsidian, chert, and fine-grain local volcanics)
Stone transport distances	No more than 5 km	Obsidian transfer: 25 to 95 km, from multiple directions
Altered and used pigments	No	Yes
Depositional regime (horst-graben formation)	Stable, aggrading system (lake/fluvial/floodplain)	Highly dynamic landscape (sub-basin cutting-and-filling)
East Africa insolation (precipitation dynamics)	Alternating high-low climate variability	Sustained period of strong climate variability

Table 4.1. Comparison of Acheulean technology and MSA technology in the Olorgesailie basin
(Achulean typified by handaxes and other large cutting tools)
Behavioral and environmental comparison includes lithic source access and rock transport, pigment use, and environment evidence based on observations in the Olorgesailie basin (Behrensmeyer et al., 2018; Brooks et al., 2018; Deino et al., 2018; Potts et al., 2018), located 22 to 24 km from the OLO12-1A drilling site. Predicted insolation dynamics (high or low climate variability) based on Potts and Faith (2015).

Our study does not presume that either the MSA or *H. sapiens* originated in the southern Kenya rift. This region, however, has yielded what is currently the oldest record with precise dating (Deino et al., 2018) where MSA behavioral innovations permanently replaced the Acheulean.

In the southern Kenya rift, the Acheulean-to-MSA archeological transition was accompanied by a massive, ~85% turnover in mammalian species between ~394 and 320 ka ago (Potts et al., 2018). As part of the turnover, previously dominant megaherbivores disappear from the record ("megagrazers": body mass > 900 kg), while smaller, water-independent, mixed grazing/browsing herbivores increased in abundance (Figure 4.1d and Table C.1).

An important motivation of our study is that an erosional hiatus occurs in the Olorgesailie basin outcrop record between 500 and 320 ka ago—the interval in which the behavioral and faunal transitions described above took place (Figure 4.1 and 4.2). A structurally controlled southward slope and faulting episodes that created rift sub-basins have been recognized for some time in the southern Kenya rift (Baker et al., 1988). We thus reasoned that a drill core in the Koora basin adjacent to and directly downstream from the Olorgesailie basin could recover sediments preserving high-resolution environmental data for the critical time window missing in the north. The present-day Koora basin is an up to 6-km-wide, 40-km-long graben bounded by ~1-million-year-old (Ma) horst blocks of 50- to 150-m height above valley surface. The basin is filled with a sedimentary sequence that was drilled in its northernmost location, closest to Olorgesailie basin outcrops. We note that the Olorgesailie and Koora basins had demonstrable, although periodic, hydrological, and paleoenvironmental connections over time (Figure 4.2), which facilitates relating the core environmental records to the archeological and paleontological evidence from Olorgesailie.

An age model presented previously by our research team for the core (Deino et al., 2019) provides the most precisely dated environmental record covering the past 1 Ma in East Africa. The 139-m-long core spans the period from ~1084 ± 4 ka to 83 ± 3 ka old based on the age model constrained by ^{40}Ar-^{39}Ar ages on 22 intercalated tephra layers and the Brunhes-Matuyama magnetic reversal (Figure 4.1e, Figure. C.2, and Appendix text C.1) (Cohen et al., 2016; Deino et al., 2019). In this study, we examine how spatially localized data from the core can be connected to larger spatial scales of the regional environment and to the archeological and faunal evidence from the adjacent Olorgesailie basin.

We emphasize that the core data concerning vegetation, lithology, and hydrology provide evidence on a variety of spatial scales ranging from local to regional. The archeological data to which we link the core records also reflect wider spatial scales beyond the excavations themselves. Lithic sources used by the Olorgesailie hominins document an expansion of resource acquisition substantially larger than the Olorgesailie basin itself (Brooks et al., 2018). Obsidian used in MSA technology was transported from multiple volcanic outcrop sources located in different directions over distances of minimally 25 to 95 km from Olorgesailie, in contrast with ≤5 km distance of stone transport typical of the Acheulean tool assemblages (Table 4.1) (Brooks et al., 2018; Potts et al., 2018). Integrating these data and observations with evidence of regional tectonism and landscape partitioning provides a framework for connecting, at high geochronological resolution, the sequence of changing resource landscapes with the critical transitions in hominin behavior and fauna.

Data compilations on human foraging behavior, which include more than 150 hunter-gatherer societies from low-latitude environments, show that diet, foraging range, group mobility, and size, among other adaptive characteristics, are systematically related to environmental setting (Binford, 2001; Kelly, 2013; Marlowe, 2005). According to these ethnographic observations, hunter-gatherers tend to increase their investment in technology, expand their range of resource acquisition, and rely on distant social alliances and exchange networks in situations of heightened resource unpredictability and risk (Dyson-Hudson and Smith, 1978; Kelly, 2013). Given that these responses in modern human foragers have parallels in the archeological innovations of the Olorgesailie MSA (Brooks et al., 2018; Potts et al., 2018), we examined the core record to test the hypothesis that decreased resource predictability could have been a factor in the early appearance of MSA adaptations in the southern Kenya rift. The specific question we address is whether MSA behaviors replaced the Acheulean in this region during a period of increased resource fluctuation, an ecological factor that could have more broadly shaped the emergence of observed adaptive responses of *H. sapiens* foragers.

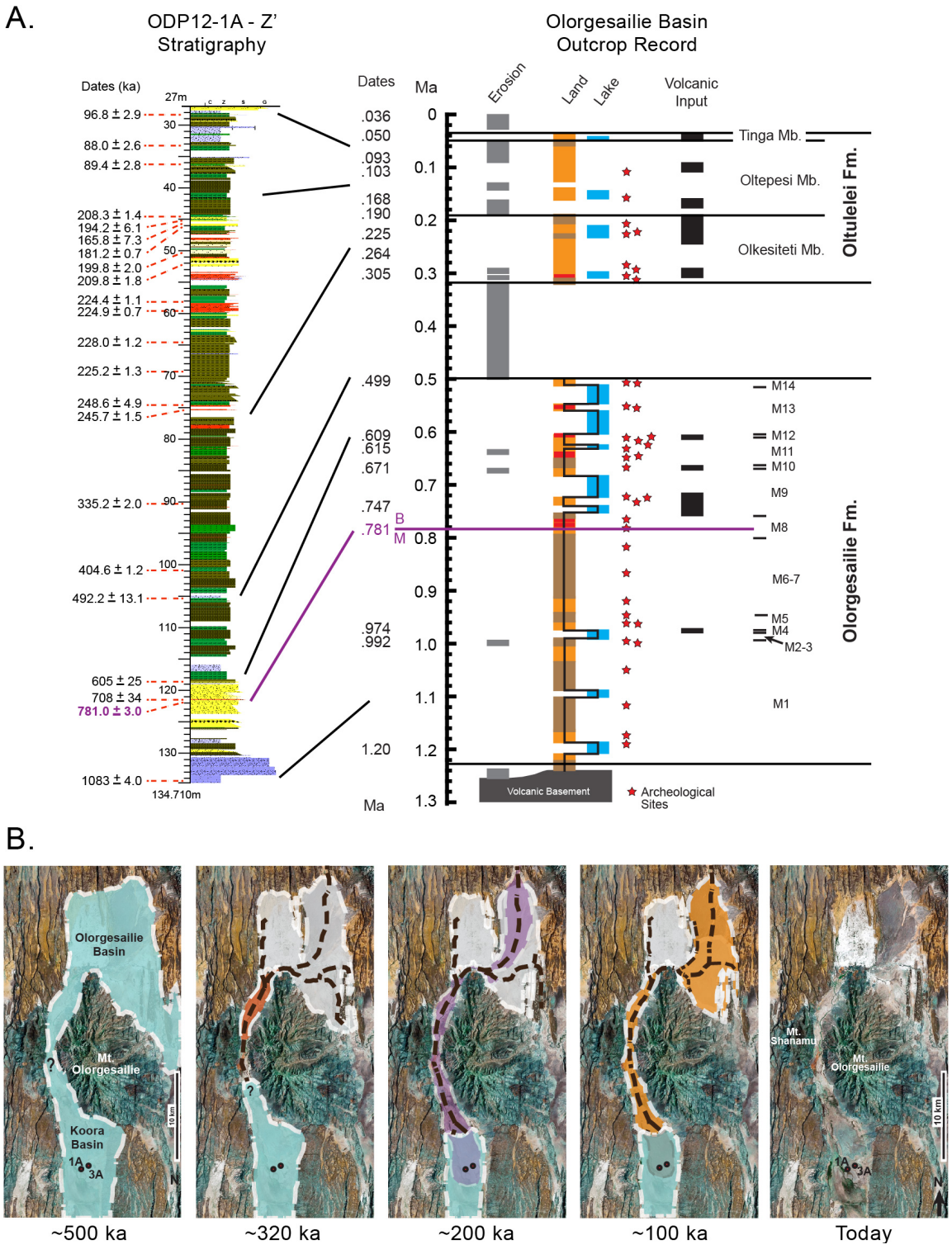

Figure 4.2. Stratigraphic and paleohydrologic relationships between the Koora and Olorgesailie basins.

(see caption on next page)

Figure 4.2 (previous page). Stratigraphic and paleohydrologic relationships between the Koora basin, where the ODP-OLO12-1A drill core was obtained, and the Olorgesailie basin, where the transitions in Acheulean-MSA behavior and mammalian fauna are recorded.
(A) *Correlation between OLO12-1A z-prime core stratigraphy and the Olorgesailie basin outcrop record (based on dates in Deino et al., 2019, 2018; Potts et al., 2018). The core's stratigraphic column is corrected for rapid and instantaneous deposits with thick volcanoclastic layers (red color) and event deposits removed. The overall z-prime core thickness is therefore lower than that of the recovered core (see Deino et al., 2019). Outcrop Land color code: orange, aggrading sediment; brown, stable land surface; red, burned zone.* ***(B)*** *Hypothesized reconstruction of basin history and drainage relationships of the Olorgesailie and Koora basins from 500 ka ago to present. The sequential maps show the connections between the two basins, based on sediment correlations and tephra dates, and illustrate increasing compartmentalization of this part of the southern Kenya rift over the past 500 ka (Behrensmeyer et al., 2018). This reconstruction conforms to the present-day topography; the spatial extent of the Koora basin paleolake is approximate. Question marks denote uncertainties in lake extent in the northern Koora basin. Color code: blue, lake; white, eroding outcrops of the Olorgesailie Fm.; red-orange, major paleosol (base of Olkesiteti Mb., Oltulelei Fm.); purple, major volcaniclastic influx (Olkesiteti Mb., Oltulelei Fm.); orange, volcaniclastics plus fluvial siliciclastic sediments (Oltepesi Mb., Oltulelei Fm.). Red dots in the Koora basin mark the locations of drill cores.*

4.2 Results

The sediment core was recovered in the Koora basin at a location ~24 km south of the Olorgesailie outcrops that preserve evidence of the large shifts in hominin behavior and faunal communities discussed above. The core's trachytic basement rock is overlain by a complex succession of diatomaceous, carbonate-rich, siliciclastic, and volcaniclastic fluvial and mostly lacustrine sediments, with multiple intervals of pedogenic alteration (Figure 4.2). Our analyses have yielded environmental data spanning most of the past 1 Ma, including, particularly, high-resolution data for the temporal window of interest between 500 and 300 ka ago. We focused on exploring changes in the availability of ecological resources by reconstructing vegetation dynamics, paleohydrology, and hydroclimatic signals.

Ecological indicators
The core datasets allow us to track the past availability of freshwater on the landscape, which is a limiting factor for most mammal species in eastern Africa and therefore strongly affects populations in the area (Western, 1975). To examine past changes in water supply, we used a set of paleohydrological proxies including sediment stratigraphy, diatom assemblage data (transfer functions), x-ray fluorescence (XRF) elemental profiles, and x-ray diffraction (XRD) minerology (Figure 4.3a). Diatom-based records of electrical conductivity (EC) and planktonic versus benthic taxa (diatom CA axis 1) were used to reconstruct changes in Koora basin salinity and relative lake depth (Fritz et al., 1991), respectively (Figure 4.3a and Fig. C.3), thus reflecting the availability of potable water contained in a lake source. We integrate these paleohydrological records with evidence of 30 paleosols, each broadly estimated to represent subaerial exposure of ~50 to ~5000

years duration on the basis of soil maturity and structure (see Chapter 4.4 Materials and Methods; Deino et al. (2019)), which together indicate repeated lake-land transitions. Sedimentary structures such as burrows that formed in subaerially exposed sediments document periods of lowered water table down to several meters below the emergent land surface (Table C.2 and Appendix text C.2). We measured the carbon isotopic composition of pedogenic carbonates ($\delta^{13}C_{pc}$) from the paleosols and obtained values of between −1.28 and 2.03 per mil (‰) (average 0.03‰), which consistently indicate local C_4 grasslands during subaerial intervals (Figure 4.3b). On the basis of the combined evidence, we conclude that each emergent land surface represents a period of marked lake regression and local to lake-basin-wide desiccation. Multiple lithological transitions between lacustrine sediments and paleosols throughout the core can thus be explained by marked variations in water supply to the Koora basin.

Figure 4.3 (next page). Paleoenvironmental data from core ODP-OLO12-1A.
Colored horizontal bars summarize intervals of similar paleoenvironmental conditions; darker to lighter colors represent lower to higher variability intervals. Vertical yellow bars denote paleosols, indicating lake desiccation.
*(**A**) Water availability data: XRD shows major mineral groups (zeolites: predominantly analcime and phillipsite). Correspondence analysis (CA) scores of diatom assemblage data indicate fluctuations in lake water depth. EC of paleolake waters are derived from a diatom transfer function (blue, fresh; green, brackish; red, saline; 2500 µS/cm assumed limit of potable water for humans). Ratio of silica and potassium counts from XRF analysis shows five-point moving average; high (low) values indicate high (low) diatom productivity (Appendix text C.3) (Brown, 2015).*
*(**B**) Vegetation dynamics data: Stable carbon isotope values of carbonate nodules ($\delta^{13}C_{pc}$) from paleosols (vegetation classes from Cerling et al., 2011). Tree cover density index (D/P) of phytolith assemblage data (Bremond et al., 2005a): higher values indicate dense woody cover; green dots denote absence of grass phytoliths. Stable isotope values of bulk sedimentary organic matter ($\delta^{13}C_{org}$; black) and proportion of C_3 versus C_4 plants from plant leaf wax isotopes ($\delta^{13}C_{wax}$; red). Phytolith index (Iph) from grass phytolith data indicate proportion of short (Chloridoideae) versus tall (Panicoideae) grasses (Bremond et al., 2005b).*
All datasets are plotted at their median age. Dots denote single data points; envelopes reflect 68% (dark) and 95% (light) confidence intervals (Deino et al., 2019). Continuity of data and uncertainty envelopes are interrupted at hiatuses, core gaps, and measurement gaps.

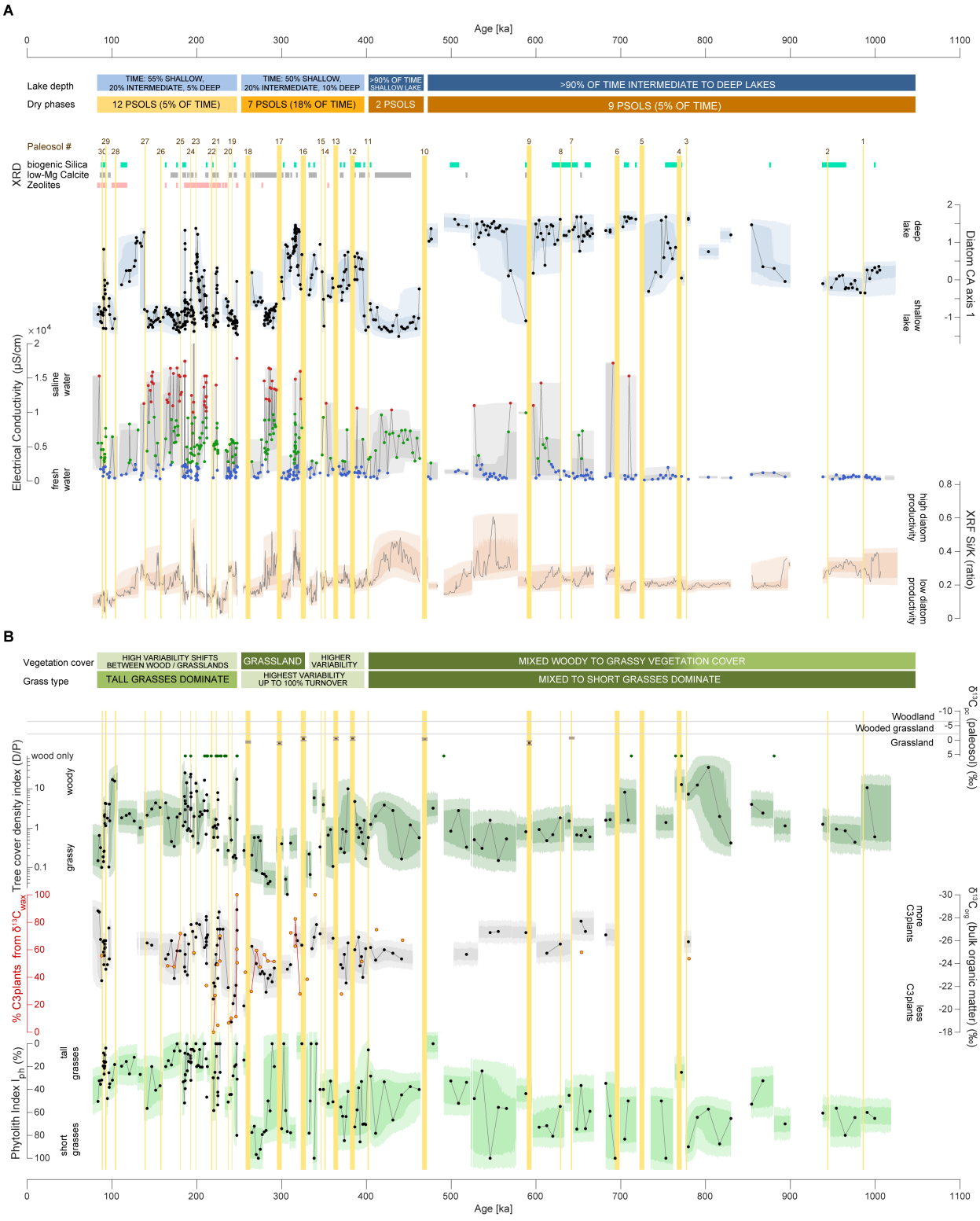

Figure 4.3. Paleoenvironmental data from core ODP-OLO12-1A.
(see caption on previous page)

Vegetation is also a critical resource for many mammal species, especially herbivores, and a primary determinant of habitat, dietary, and foraging opportunities. We reconstructed vegetation cover and composition on local to regional scales by using carbon isotopes of leaf waxes, bulk organic matter, and pedogenic carbonates ($\delta^{13}C_{wax}$, $\delta^{13}C_{org}$, and $\delta^{13}C_{pc}$) and also phytolith assemblage data (Figure 4.3b) (see Chapter 4.4 Materials and Methods). The carbon isotope data are interpreted in terms of the proportion C_3 to C_4 plants, with C_4 plants, mainly grasses, having higher water use efficiency adapted to arid conditions (Kellogg, 2013).

These carbon isotope–based proxies were necessarily obtained from different lithologies; they thus preserve vegetation signals representing different yet overlapping time periods and varied spatial scales. Whereas the $\delta^{13}C$ signature of pedogenic carbonates reflects only a localized signal preserved in dry and exposed land surfaces lacking sediment input (i.e., no aggradation), these conditions resulted in poor preservation of leaf waxes and organic matter. Thus, leaf wax and bulk organic $\delta^{13}C$ samples were extracted from lacustrine sediments. The bulk organic $\delta^{13}C$ measurements contain a mixed signal of basin-scale terrestrial vegetation and aquatic biomass (e.g., algae) originating from the lake itself. The source area of bulk organic $\delta^{13}C$ is smaller than that of the leaf wax $\delta^{13}C$ samples because the transport of waxes is partly fluvial and partly aeolian (wax aerosols), and the latter can result in long-distance dispersal. Leaf waxes are primarily produced by terrestrial vascular plants; therefore, the sediment leaf wax $\delta^{13}C$ signal reflects the past C_3/C_4 plant composition from the Koora basin and its catchment.

The phytolith data also record vegetation signals on local (during dry phases) to regional (fluvial transport during wet phases) scales. An advantage of including phytolith morphotypes in our analysis is that they can be resolved taxonomically (Barboni et al., 1999; Bremond et al., 2005b). From the phytolith assemblages, we determined the tree cover density index (D/P) and the phytolith index (Iph). The D/P ratio is the proportion of woody dicotyledons (D) over grasses (Poaceae, P), which we use to estimate woody plant cover on the paleolandscape (Alexandre et al., 1997; Bremond et al., 2005a). The Iph records the proportion of short (Chloridoideae) and tall grasses (Panicoideae) in savanna ecosystems, with values of >20 to 40% indicating short-grass dominance (Alexandre et al., 1997; Bremond et al., 2005b). In Africa today, areas of higher water availability generally favor woody vegetation and/or tall grasses (Panicoideae), whereas arid conditions favor short grasses (Chloridoideae) (Bremond et al., 2005b), which allows us to link past vegetation composition with paleohydrology.

A shift in ecological resources

The core record exhibits mostly subdued variability in both the lacustrine and terrestrial datasets during its first ~500 ka , followed by a 400-ka-long interval of marked variability and ecological disruptions (Figure 4.3). The division of the record into two major variability phases is also illustrated by a doubling of dry intervals of emergent land surface ($n = 9$ paleosols before 500 ka ago versus 20 paleosols after). Overall, the proxy data contain only weak orbital signals (11 to 17% of the variance), dominated by the 100-ka eccentricity period in the lake depth reconstruction (diatom CA axis 1), the XRF Si/K ratio, and D/P tree cover index (Figure 4.4 and Figure C.4).

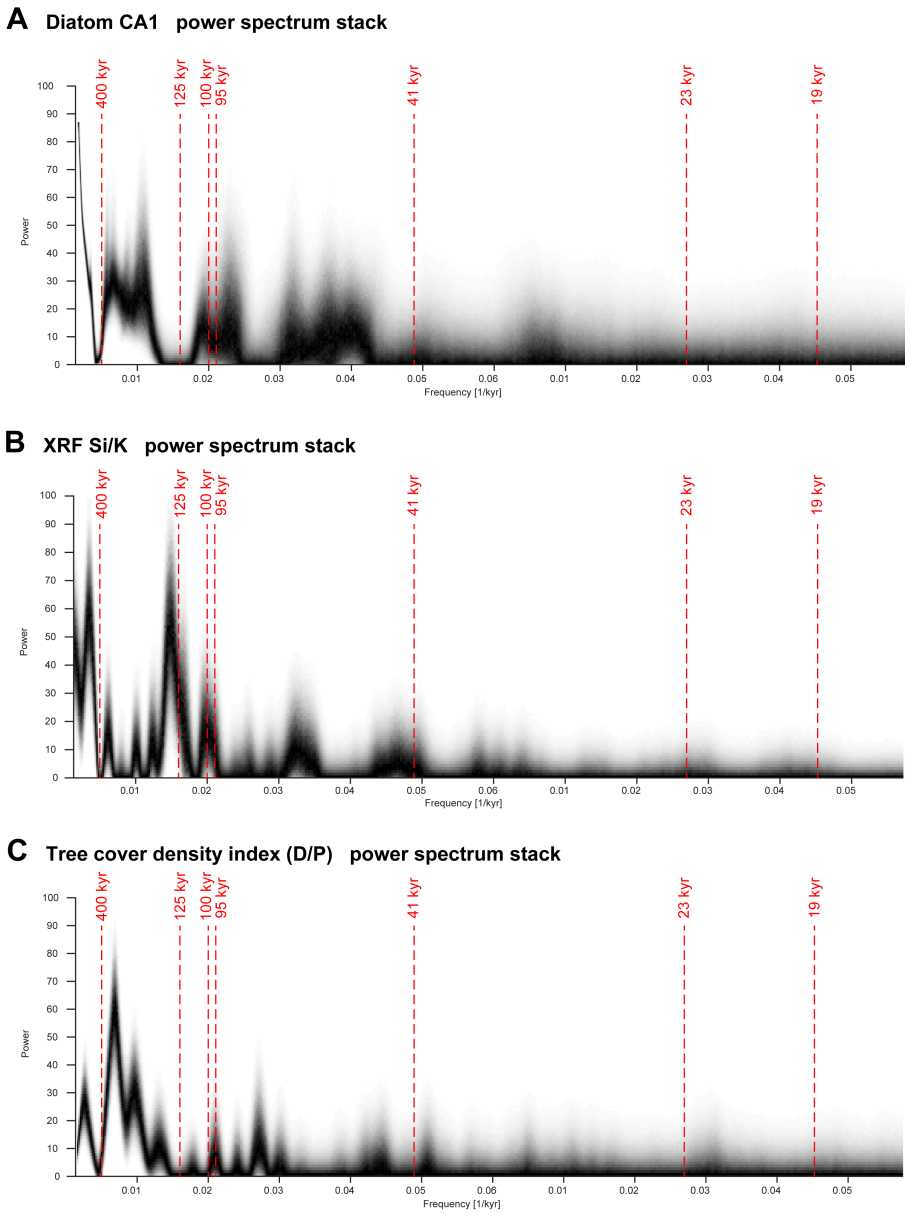

Figure 4.4. Time-series (power spectrum) analyses on ODP-OLO12-1A environmental indicator (proxy) records.

*Lomb-Scargle spectra for (**A**) the diatom CA1 axis, an indicator for lake depth, (**B**) the XRF Si/K ratio, an indicator of paleohydrology, and (**C**) the phytolith D/P index, an indicator of paleovegetation and tree cover. Orbital periods (400, 100, 41, and 23 to 19 ka) are shown with red dashed lines. Spectral analysis was used to explore orbital variability within the various time series, taking into account the uncertainty of the age model (see Materials and Methods). Darker colors represent spectral powers of the data that are more consistent across the full age model. Orbital variability is present but subdued in these records: The percentage of total variance occurring at orbital periods is only 11% in the diatom CA1 record (8% eccentricity, 2% obliquity, and 1% precessional periods), 17% in the XRF Si/K time series (8% eccentricity, 7% obliquity, and 1% precessional periods), and 16% in the phytolith D/P tree cover record (9% eccentricity, 3% obliquity, and 4% precessional periods). Records are shown in comparison with orbital cycles in Fig. C.4.*

4 Increased ecological resource variability during a critical transition in hominin evolution

Between ~1 Ma and 470 ± 15 ka ago, intermediate to deep freshwater lakes prevailed in the Koora basin as inferred from the diatom CA axis 1 and EC reconstruction (median EC <800 µS/cm; Figure 4.3a). These lake phases were interrupted by nine emergent land phases represented by paleosols that lasted for ~1000 to ~5000 years (Deino et al., 2019). Most of these dry phases occurred between 780 and 590 ka ago. However, the combined duration of all nine dry episodes represents only ~5% of this 530-ka-long period based on the age model (Deino et al., 2019). The evidence indicates that freshwater was generally available in the Koora basin (Figure 4.3a) during the period when Acheulean toolmakers were active at Olorgesailie.

A reliable freshwater supply would have sustained the predominantly water-dependent fauna of the region up to ~470 ka ago (Figure 4.1d). Before the major faunal and archeological transitions (i.e., before 500 ka ago), intermediate values of the D/P tree cover index with a median of 1 (range, 0.2 to 36; (Figure 4.3b and Figure C.5) indicate a mix of woody and grassy vegetation typical for African tall and short grass savannas (Bremond et al., 2005b). The stable isotope record for this interval shows depleted $\delta^{13}C_{org}$ values, ranging from −24.9 to −27.7‰ (average, −26.4‰), which are typical for C_3-dominated vegetation consistent with the D/P values of mixed vegetation. Coupled with evidence of intermediate-deep freshwater lakes, this vegetation composition points to relatively high moisture levels during the first 500 ka of the record. However, unexpectedly, we determine high Iph values with a median of ~60%, indicative of the concurrent predominance of short grasses (Chloridoideae; Figure 4.3b), which typically prevail in arid grasslands and conditions of low soil moisture (Bremond et al., 2005b). The concurrent predominance of short grasses suggests that vegetation was influenced by factors beyond water availability (precipitation).

The prolonged freshwater period was disrupted at 470 ± 15 ka ago, initially by a ~ 5-ka dry episode followed by >60-ka interval of shallow and saline lake conditions (median EC, >5500 µS/cm; Figure 4.3a), marking the transition to an interval of high environmental variability. During the critical time window between 500 to 300 ka ago, eight intervals of desiccation are recorded as paleosols, five of which are estimated to have lasted for ~5 ka each (Figure 4.3). The intervals between these dry phases are approximately 68, 16, 19.5, 15, 5.5, 18, and 29 ka long, which conform partly with precessional frequencies and partly with nonorbital rhythms (Figure C.4).

In concert with these more frequent wet-dry shifts, ecological resources began to fluctuate more widely by ~400 ka ago in both terrestrial and aquatic environments. Each of the lake phases during the critical window was distinct in terms of lake depth, salinity, diatom productivity, and composition (Si/K ratio; Figure 4.3a and Figure C.4), Together with the more frequent subaerial intervals, these variable lake conditions point to large fluctuations in lake level and highly variable moisture supply. Between ~400 ± 5 ka and 320 ± 7 ka ago, the D/P tree cover index (0.1 to 10; median, 0.7) reveals rapid shifts between woody vegetation and grassland in line with varying water availability (Figure 4.3b and Figure C.5), consistent with assemblage-based ecological variability (fig. S6). This varying woody plant cover is also evident in larger fluctuations of $\delta^{13}C_{org}$ (−27.4 to −22.3‰) and $\delta^{13}C_{wax}$ (−34.5 to −22.9 ‰), suggesting shifts between C_3-dominated (100%) and C_4-dominated (~70%) vegetation. The grassland composition as inferred by the Iph

implies pronounced variation in tall- and short-grass dominance and complete turnover between these two grassland types after 350 ± 8 ka ago (Figure 4.3b). From ~330 to ~250 ka ago, the Koora basin was apparently dominated by open grassland vegetation; few phytoliths of woody plants in this interval result in a low median D/P index of 0.15. These grasslands were either characterized by tall- or short-grass abundance but rarely of mixed composition.

The Olorgesailie Acheulean-to-MSA transition and the major faunal turnover thus coincided with the onset of an ecological landscape characterized by decreased reliability of potable water and increased variability of grassland vegetation-type beginning ~400 ka ago. The shift from megagrazers to a predominance of smaller-bodied herbivores, with a higher proportion of browsers and mixed feeders, suggests that change in the mammal community favored organisms that could adjust to diverse and/or fluctuating vegetation and dietary resources (Figure 4.1d). In addition, the more water-independent mammal taxa present in the fauna by at least 320 to 300 ka ago in the southern Kenya rift would have been more resilient to erratic freshwater availability.

Beginning ~250 ka ago, after these transitions occurred, the phytolith data indicate a shift toward tall grass dominance (median Iph, <20%) and the return of woody plants but with highly varying density. This vegetation change is also recorded by $\delta^{13}C_{wax}$, which exhibits its overall largest fluctuations (between −32.9 and −18.4‰), thus suggesting complete turnover between C_3 and C_4 plant dominance (Figure 4.3b and Figure C.5). Frequent ecological disruptions continued based on the recurrence of short dry intervals ($n = 12$, after 250 ka ago), strongly fluctuating lake depth, and more frequent saline lake conditions (Figure 4.3a).

4.3 Discussion

What factors could have led to the transitions in water and vegetation resources, the loss of megagrazers, and the replacement of Acheulean by MSA behaviors? Although orbitally paced climate variability is well documented in many East African paleoclimate records (deMenocal, 2011, 1995; Potts and Faith, 2015; Trauth et al., 2007; Vrba, 1995), evidence for orbital cyclicity in our core data is weak compared to the large, abrupt, and increasingly frequent landscape changes that we document. Our analyses show that rainfall variations during the past 1 Ma were influenced by orbital pacing, mainly the eccentricity cycle, but temporal changes in water availability and vegetation as recorded in the core cannot solely be explained by orbital forcing. Millennial-scale climate variations have been demonstrated in Northern Hemisphere mid-Pleistocene records (e.g., Hyodo et al., 2017; Tzedakis et al., 2015), but our indicator records at the current sampling resolution have not yet revealed this variability or temporal correlation with events documented at higher latitudes. The episodic prevalence of tall grasses (Figure 4.3b; Iph), furthermore, is inconsistent with progressive aridity, another prominent hypothesis often invoked to explain hominin evolutionary change. By focusing on ecological resources rather than climate alone, our study suggests that a combination of geological, climatic, and ecological factors directly influenced fundamental shifts in hominin and faunal adaptations in the southern Kenya rift.

4 Increased ecological resource variability during a critical transition in hominin evolution

Previous geological observations document extensive faulting throughout the region after ~500 ka ago, manifested in the deep erosion of Olorgesailie Fm. outcrops to the north between ~499 and ~320 ka ago, and by drag-faulted sedimentary units that onlap horst walls after 499 ka ago at Olorgesailie and after 397 ka ago at Lainyamok to the southwest (Baker et al., 1988; Behrensmeyer et al., 2018; Potts et al., 2018, 1988). Increased volcano-tectonic activity is further indicated by an abrupt, nearly twofold rise in sedimentation rate and increased volcanic tephra input in the Koora basin beginning ~400 ka ago (Fig. C.7) (Deino et al., 2019). One consequence of this tectonism was increased topographic relief and basin compartmentalization throughout the region (Figures 4.1c and 4.2) (Baker, 1986). Tectonic development of the Koora basin's graben morphology (Figure 4.1b and c) over time would have resulted in amplified lake level fluctuations due to higher sensitivity of graben-shaped lakes to changing moisture supply (Olaka et al., 2010).

As a result, spatial heterogeneity in runoff, soil moisture, water availability, and woody/grassy vegetation proportions was accentuated, with basins of varying size and morphology potentially developing different sensitivities and divergent resource landscapes in response to climate variations. These interactions may account for contrasting environmental histories apparent in the adjacent Magadi and Koora basins. The Magadi drill core provides the only other relatively high-resolution environmental sequence in the region relevant to the past 1 Ma. Its vegetation record is interpreted as evidence of progressive aridification (Owen et al., 2018), whereas the higher-resolution record presented here shows increased tall-grass dominance, mixed woody/grassy vegetation, and fluctuations in C_3 vegetation in the interval from 500 to 300 ka ago and after (Fig. C.8). This comparison indicates that, during the past 500,000 years, distinct ecological zones and resource landscapes developed over a distance of less than 20 km between the two rift basins (Figure 4.1b). According to the relevant archeological data, distances of MSA obsidian transport were minimally ~25 to 95 km as straight-line measures, which further suggest that hominin foraging ranges and potential interactions among groups encompassed diverse resource landscapes from the southern to the central Kenya rift (Brooks et al., 2018). This observation links the hominin and faunal transitions in southern Kenya with spatial heterogeneity in ecological resources in addition to the temporal variability shown here.

We note that the development of accentuated horst-graben topography also would have dissected and diminished the spatial continuity of grazing landscapes. Persistent high grazing pressure is known to transform broad areas of moist, wooded, and tall grass habitats into extensive short-grass grazing lawns (Coetsee et al., 2011; Hempson et al., 2015; McNaughton, 1985). From ~1.0 Ma ago until the faunal turnover after 500 ka ago, the megagrazers of the southern Kenya rift had craniodental specializations and estimated body masses up to ~20% (e.g., the zebra *Equus oldowayensis*) to 400% (e.g., the baboon *Theropithecus oswaldi*) larger than their modern counterparts (Potts, 1998; Werdelin and Sanders, 2010), which together suggests a unique grazing community that had the capacity to establish and sustain short-grass grazing lawns despite the prevailing moist conditions (Coetsee et al., 2011; Hempson et al., 2015).

We propose that the megagrazer decline and emergence of a different suite of mammal species was a response to a more spatially fragmented and fluctuating resource base, which began ~400

ka ago and thus within the critical window of faunal and archeological change (Figure 4.5). A combination of factors including accentuated topographic relief, climate variability, hydrological subdivision of the region, and fragmentation of vegetation types could have created an interactive cascade that diminished megagrazer populations in the region. This would have put specialized grazers dependent on predictable short-grass and freshwater availability at a disadvantage relative to mixed feeders and water-independent browsers, which increased between ~400 and 320 ka ago (Figure 4.1d) (Deino et al., 2018). Small obsidian points with retouched bases recovered from Olorgesailie archeological sites are suggestive of projectile armaments dated ~320 to 307 ka ago (Brooks et al., 2018) and thus potentially indicate hominin predation as a possible influence on herbivore turnover in this region. Since the definitive loss of megagrazer species in the region is recorded at 397 to 334 ka ago (Lainyamok fauna; Deino et al., 2018; Potts and Deino, 1995), the Olorgesailie MSA stone points could, however, reflect a technological innovation for hunting smaller prey following the loss of megagrazer species (see Figure 4.1d).

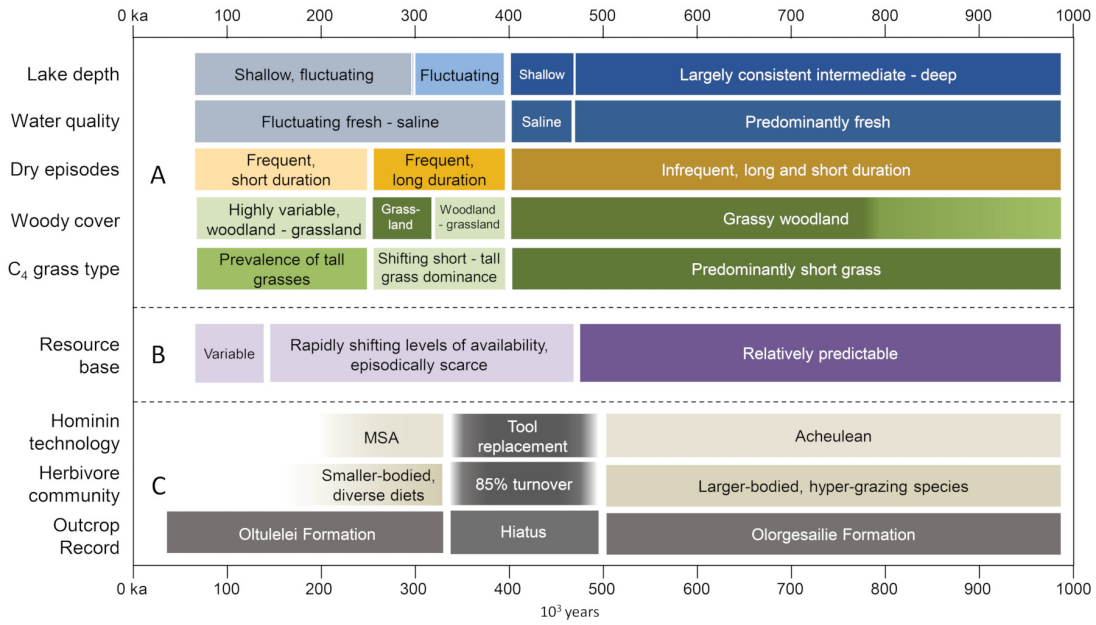

Figure 4.5. Transitions in resource dynamics, hominin behavior, and mammalian fauna over time based on the OLO12-1A drill core and Olorgesailie outcrop data.
(A) *Water availability and vegetation dynamics based on Figure 4.3 datasets (see text). Darker bars reflect relatively consistent resources, lighter colors more variable resources. Intermediate-to-deep lake conditions ~938 to 830 ka ago are based on lower-resolution data due to core gaps.* ***(B)*** *Change in resource base availability and predictability based on the synthesis in (A). The horizontal bars in (A) and (B) describe dominant inferred patterns for each time period of the core; the transitions are not typically abrupt.* ***(C)*** *Major transitions in hominin behavior and the herbivore community based on outcrop records of the southern Kenya rift. These transitions took place during the erosional hiatus between 500 and 320 ka ago. The marked shift from reliable to variable resource landscapes beginning ~400 ka ago in the adjacent Koora record (Fig. C.9) occurred within the interval of the Olorgesailie erosional hiatus and the major transitions.*

4 Increased ecological resource variability during a critical transition in hominin evolution

We further suggest that compartmentalizing of the southern Kenya rift into horst/graben-delimited basins with quasi-independent resource dynamics also favored the transition to MSA behavior. Even as mammalian populations experienced increased fragmentation of vegetation types due to topographic partitioning of the landscape, evidence of widespread obsidian exchange networks by ~320 to 295 ka ago (Brooks et al., 2018; Deino et al., 2018) implies that the MSA hominin groups actually became more connected across the larger region. This response was potentially critical to their evolutionary success in the changed resource regime. We hypothesize that MSA technological innovations and distant resource exchange, sustained by symbolic communication, reflect an ability to respond to increased instability in resource landscapes through risk mitigation, an adaptive strategy ultimately characteristic of human foragers today (Dyson-Hudson and Smith, 1978; Kelly, 2013).

On the basis of our study, concurrent reshaping of hominin behavior and the faunal community can be understood as distinctive responses to similar ecological stresses. We conclude that although MSA adaptations may have originated elsewhere, they took hold in the southern Kenya rift between 400 and 320 ka ago as a result of heterogeneity in selective conditions induced by the marked shift to a temporally and spatially varied and less predictable resource landscape, favoring hominin populations with resilient adaptations. Early evidence of this response suggests that fundamental aspects of human adaptability had emerged by the time of our species' African origin.

Our study prompts a wide range of questions for future investigation. We do not address here the continent-wide demise of the Acheulean and its replacement by the MSA but offer a resource landscape hypothesis that could be tested in other parts of Africa. Last records of the Acheulean occurred at various times in other African regions (e.g., Clark et al., 2003), later than in the southern Kenya rift. The onset of the MSA, furthermore, is recorded at varying times in different places, and MSA sites across the continent are associated with diverse environmental settings (Blinkhorn and Grove, 2018; Tryon and Faith, 2013). In our study, the oldest documented transition from Acheulean to MSA in eastern Africa occurred in the context of repeated environmental disruptions. The hypothesis that we present, which is limited to a conjunction of factors in the southern Kenya rift, should be examined elsewhere to see whether the MSA flourished at the expense of the Acheulean under similar circumstances of ecological disturbance. We recognize, however, that once MSA behaviors evolved, the adaptive flexibility they conferred would have been advantageous and sustained in other locations where the MSA spread, including in relatively stable habitats.

Integration of resource dynamics with regional tectonic and ecological history, as exemplified by our study, also suggests a new direction in the search for causal processes that shaped human evolution. Evolutionary adaptation entails not only the origin of behavioral variations (Potts et al., 2018) but also their increase within a population and spread across a wider geographic area. Studies of how environment may initiate evolution, therefore, need to further address the processes that underlie adaptive change rather than assume, for example, that correlations between evolution and either aridity, moisture, or variability provide a useful explanatory hypothesis for any given change (Potts and Faith, 2015). Robust ecological theory as applied to human hunter-

gatherers and mammal herbivores provided the framework for investigating the potential environmental influences on the hominin and faunal adaptations described here. We intend this approach to be useful in motivating future research on how environmental dynamics may have led to critical transitions in human evolution.

4.4 Materials and Methods

Bayesian age model (C.B.K.)
To constrain the absolute chronology of the ODP-OLO12-1A core, a high-resolution age-depth model (Fig. C.2) was constructed using a Bayesian stochastic sampling approach to combine quantitative age constraints from Ar-Ar geochronology, semiquantitative minimum estimates for the duration of observed exposure surfaces (depositional hiatuses), and the absolute constraint of stratigraphic superposition. As described in Deino et al. (2019), this Markov chain Monte Carlo model uses the Metropolis algorithm to estimate the posterior age distribution for each centimeter of core depth. At each step of the Markov chain, the previous age-depth model is perturbed by a symmetric Gaussian proposal distribution, checked for stratigraphic superposition, and evaluated against the combined quantitative constraints. Since adjacent proposals are highly correlated, this model was run with a burn-in of 20,000,000 steps, and a sieved stationary distribution collected over the subsequent 500,000,000 steps of the Markov chain.

Age and proxy uncertainty analysis (S.R. and Y.G.)
Paleoenvironmental proxy data were translated into the time domain considering both proxy and age model uncertainties by calculating uncertainty envelopes (shown in Fig. 4.3). Envelope width along the time direction (x axis) represents absolute age uncertainty based on the age model. Envelope height in the proxy direction (y axis) represents the analytical uncertainty of the proxy dataset. These uncertainty envelopes were generated by using the full age model output: For each proxy data point, its z-prime depth was assigned to the complete corresponding sieved age distribution ($n = 25{,}000$) of the full age model at sample depth. (Fig. C.2 shows the age model uncertainties on the z-prime depth scale.) The analytical uncertainties of the proxy data were assumed to have a normal distribution. These two individual uncertainties, in time domain (age model) and proxy domain (analytical uncertainty), were used to generate two-dimensional histograms for each data point. The obtained probabilities were then combined to composite probabilities per continuous section of the dataset. The environmental proxy records were treated as discontinuous sections wherever the record was interrupted either by a paleosol occurrence (hiatuses), by absence of core recovery (depth gaps), or by measurement gaps. A conservative discontinuity criterion was further applied if neighboring data points were too remotely spaced, either in time axis (threshold of 20 ka) or in the depth axis (threshold of 10 m). For each obtained continuous time interval, the obtained probability densities of individual data points were merged into a composite probability. The resulting 68 and 95% confidence envelopes were ultimately extracted from the obtained composite probability distributions. All the processing was undertaken using MATLAB (Mathworks, 2018).

Spectral analysis (S.R. and P.d.M.)

To analyze orbital variability within the time series, Lomb-Scargle power spectra were calculated because of their ability to work with unevenly spaced data as represented in this drill core. The absolute uncertainty of the age model was included by converting the proxy data into the time domain for each individual z-prime–time distribution of the full age model ($n = 25{,}000$). Lomb-Scargle power spectra were then calculated for each of the resulting time series of a specific proxy (Fig. 4.4). Individual spectra ($n = 25{,}000$) were stacked to create one representative spectral power density plot. This density plot shows the frequency spectrum of the proxy data, taking into account time uncertainty in the full age model. Higher densities in the stacked spectrum denote spectral powers, which are consistent across the full age model.

Diatoms (R.B.O.)

Diatom samples were collected every 30 cm and where facies changed, with sampling intervals reduced to 10 cm in relatively pure diatomites. Subsequent resampling of diatomaceous deposits was carried out to reduce intervals for these sediments to 10 to 12 cm. Samples were weighed and placed in a Calgon solution to assist dispersion. After washing with distilled water, 10% HCl was added to remove carbonates followed by further washing. Subsequently, 30% H_2O_2 was added, followed by washing. In the last stage, a known number of microspheres (8 μm in diameter) were added to enable quantitative counting. Smear slides were prepared using Naphrax. A minimum of 400 diatoms were counted, except where diatoms were rare in which case all frustules were tallied. Diatoms were included in counts when more than half of a frustule was present. Apices were counted for fragmentary long thin fragile taxa. Diatoms were identified at ×1000 magnification with the supplementary aid of a LEO 1530 field-emission scanning electron microscope. Identifications used standard taxonomic works and, especially, Gasse (1986, 1980). Correspondence analyses (CAs) were carried out using CANOCO 4.5 with taxa that formed ≥3% in at least two samples or ≥ 10% in at least one sample, included in analyses ($n = 476$). CA axis 1 tracks water depth, indicated by a high correlation with percentage of planktonic taxa, with negative values associated with abundant *Aulacoseira* spp. and rare *Stephanodiscus* ($r = -0.959$, $P < 0.001$) and positive values associated with benthic taxa (shallow). The percentage variance explained by CA axis 1 is 68%. Environmental reconstructions were performed using ERNIE software v. 1.2. EC for each sample ($n = 476$) was determined using the European Diatom Database (EDDI) "Combined Salinity Dataset", and "Locally weighted Weighted Averaging."

Phytoliths and pollen (R.K., R.D., and S.M.R.)

Two hundred seventy-two phytolith samples, 2 to 3 cm^3 in volume, were collected at 48-cm intervals with finer sampling at ±10-cm interval depending on core lithology. Samples were processed using a modified heavy liquid floatation (Katz et al., 2010) as outlined in Kinyanjui (2018): (i) dissolution of carbonates with HCL, (ii) oxidation of organic matter using HNO_3, (iii) heavy liquid floatation using Sodium Polytungstate at density of 2.4 g/cm^3, and (iv) gravitational removal of clay. The recovered fraction was mounted on microscope slides using Entellan New medium. Freshly mounted slides were viewed under an Olympus BX52 microscope at ×400 magnification for three-dimensional observation and counting. Because most samples had low phytolith abundances, phytoliths >5 μm in diameter in each sample were counted and classified with aim of

attaining a minimum of 200 grass short silica cells (GSSCs) to acquire a statistically robust dataset. Identification and classification of phytoliths largely followed the International Code of Phytoliths Nomenclature (Madella et al., 2005) with refined GSSCs classification (based on Rossouw, 2009; Twiss, 1992; Twiss et al., 1969) and with further consultation of other published studies (Albert et al., 2006; Ashley et al., 2010a, 2010b; Barboni et al., 2007, 1999; Barboni and Bremond, 2009; Fredlund and Tieszen, 1997, 1994; Kinyanjui, 2018, 2012; Mercader et al., 2010, 2009; Neumann et al., 2009; Novello et al., 2012; Piperno, 2006; Rapp Jr and Mulholland, 1992; Runge, 1999; Strömberg, 2003). Phytolith data interpretation was based on two approaches. First, abundance diagrams generated using Tilia program (Grimm, 1991) showed variation in phytolith assemblages throughout the core, which provided information about vegetation structure through time (Kinyanjui, 2018). Second, phytolith indices were computed to determine changes in vegetation composition and climatic conditions. Two phytolith indices were calculated: The D/P tree cover index is the ratio of woody dicotyledons to all grasses and indicates changes in tree cover density through time ($n = 218$) (Bremond et al., 2005a). The index was computed by dividing rough globular phytoliths with the sum of Poaceae phytoliths from the subfamilies Panicoideae, Chloridoideae, Arundinoideae, and Aristidoideae (dumbbell, cross, saddle, point-shaped, and fan-shaped types). The Phytolith index (Iph) presents the relative proportion of Chloridoideae (aridity affinity C_4 short grasses) versus Panicoideae (moist affinity C_{3+4} tall grasses) and was used to investigate temporal changes in this water availability indicator ($n = 183$). The Iph was computed as the ratio of Chloridoideae (saddle morphotype) to the sum of Chloridoideae and Panicoideae (saddle, cross, and dumbbell morphotypes) (Bremond et al., 2005b). Cores were also sampled for pollen: Samples were processed at Ghent University in Belgium following standard palynological procedure for concentrating pollen grains (Faegri and Iversen, 1975). Slides mounted for pollen counts were examined at the National Museums of Kenya, Department of Earth Sciences. Pollen was investigated using a Leitz microscope at ×400. Pollen preservation was very poor. Most slides had no pollen, but in rare cases, one or two grains were observed. Poor preservation might have been influenced by oxidation, high temperature, and low organic matter content, among other external factors.

Identification of hiatuses and paleosols (E.J.B.)

Thirty hiatuses marked by paleosols occur in core OLO12-1A and range from weakly to moderately develop. These paleosols are identified by diagnostic soil features such as bioturbation, soil peds, horizonation, and pedogenic carbonate. The top of each paleosol was identified by a lithologic change and loss of ped structure, and the bottom of each paleosol by the return of identifiable parent material lithology such as laminated lacustrine sediments. The presence or absence and degree of development of these features allows for classification of the paleosols using U.S. Department of Agriculture Soil Taxonomy as paleo-Entisols, paleo-Inceptisols, and paleo-Vertisols (Soil Survey Staff, 2014). The core ODP-OLO12-1A Entisols are very weakly developed soils with little or no evidence of soil horizons, and they often contain relict bedding. The Inceptisols are more strongly developed than Entisols with soil horizonation and ped formation but lack distinguishing features that would allow them to be classified as another soil order. The Vertisols are clay-rich soils with cracks, pedogenic slickensides, and other vertic features that form as a result of shrinking and swelling of clays during wetting and drying. These diagnostic

features also allow for classification of these paleosols into a paleosol maturity index modified from Cleveland et al. (2007). This paleosol maturity index can then be related to approximate the duration of pedogenesis as certain soil features form at different time scales. For additional discussion of the paleosol characterization and estimates of duration for the age modeling, see Deino et al. (2019).

$\delta^{13}C_{wax}$ and $\delta^{13}C_{org}$ (J.M.R., R.L., K.U., and P.d.M.)

We measured the carbon isotopic composition of terrestrial leaf waxes ($n = 37$) following the protocol outlined in Lupien et al. (2018). Lipids, which include leaf waxes, were extracted from freeze-dried and homogenized bulk sediment using a DIONEX Accelerated Solvent Extractor 350 with dichloromethane:methanol (9:1). The lipids were separated into neutral and acid fractions over an aminopropylsilyl gel column using dichloromethane:isopropanol (2:1) and ether:acetic acid (24:1). The acids were methylated using acidified methanol of known isotopic composition, and the resulting fatty acid methyl ethers (FAMEs) were purified via silica gel column chromatography. Relative abundances of the FAMEs were quantified using an Agilent 6890 gas chromatograph (GC) equipped with a HP1-MS column (30 m by 0.25 mm by 0.25 μm) and flame ionization detector. Carbon isotopes were measured on an Agilent 6890 GC equipped with HP1-MS column (30 m by 0.25 mm by 0.10 μm) coupled to a Thermo Delta V Plus isotope ratio mass spectrometer (IRMS) with a reactor held at 1100°C at Brown University. The IRMS was run with CO_2 of known isotopic composition as the external standard for normalization to the Vienna PeeDee Belemnite (VPDB), and a FAME internal standard containing four homologs was measured every sixth injection to monitor instrument performance and drift. Repeated measurement of the internal standard yielded a standard deviation (1σ) of 0.20‰. Carbon isotope ratios were measured in duplicate on each sample with a mean intersample difference of 0.20‰. All carbon isotope measurements were corrected for the isotopic composition of the added methyl group, where $\delta^{13}C_{MeOH} = -36.5‰$. We also analyzed the carbon isotopic composition of bulk sedimentary organic matter ($\delta^{13}C_{org}$). The samples ($n = 116$) were acidified in 2 N hydrochloric acid (HCl) for 1 hour at 80°C to remove carbonate minerals. The acid-treated samples were rinsed in deionized water and centrifuged four times to remove excess HCl and were then lyophilized and homogenized before isotopic analysis. The $\delta^{13}C_{org}$ values were measured using a Carlo Erba Elemental Analyzer coupled to a Thermo Delta Plus IRMS. The analytical precision determined through replicate measurements of internal sediment standards was 0.14‰. All $\delta^{13}C$ values are reported relative to the VPDB standard.

$\delta^{13}C_{wax}$ primarily records changes in the relative abundance of plants using the C_3 photosynthetic pathway (trees, shrubs, and cool season grasses) versus plants using the C_4 photosynthetic pathway (warm season grasses and sedges) (Bender, 1971; Collister et al., 1994). To quantify the relative abundance of C_3 and C_4 vegetation, we used a two end-member mixing model that uses a $\delta^{13}C$ of n-C_{30} acids of −32.9‰ for the C_3 end member and a $\delta^{13}C$ of n-C_{30} acid of −19.0‰ for the C_4 end member based on wax isotope measurements from the Turkana Basin in northern Kenya (Uno et al., 2016). Measurements of the $\delta^{13}C$ of n-C_{28} and n-C_{30} acids from the Turkana Basin and various terrestrial plants (Chikaraishi et al., 2004) indicate negligible offsets between these homologs, allowing us to apply the end member $\delta^{13}C$ compositions from the n-C_{30} acids. Our use

of −32.9‰ for the C_3 end member assumes that closed canopy forests, which can produce waxes with much more depleted $\delta^{13}C$ values (Russell et al., 2014; Vogts et al., 2009), were not substantial contributors to the waxes in the core. This assumption is justified by the multiproxy data from our sediment core that indicates generally dry conditions through the past 1 Ma. The bulk organic matter in lake sediment derives from both internal and terrestrial sources, and its $\delta^{13}C$ records both aquatic carbon cycling and the $\delta^{13}C$ of terrestrial organic inputs (Meyers and Teranes, 2001), largely driven by C_3/C_4 plant abundance. Although we cannot determine the relative abundances of aquatic versus terrestrial organic matter within the bulk sedimentary organic matter in the ODP-OLO12-1A drill core, recent work has shown that the $\delta^{13}C_{org}$ of tropical lakes responds strongly to changes in C_3/C_4 plant abundance (Russell et al., 2009; Webb et al., 2016). We interpret the $\delta^{13}C_{org}$ in the ODP core to reflect both aquatic ecosystem carbon cycling and C_3/C_4 plant abundance.

$\delta^{13}C_{pc}$ (J.W.M., N.E.L., and E.J.B.)

Pedogenic carbonates (pc) ($n = 8$) were collected and analyzed for carbon isotopic composition from the Bk horizons (zones of accumulation of carbonate) of eight paleosols focused on the interval from 642 to 261 ka ago. Pedogenic carbonate was collected at least 50 cm below the top of each paleosol (or a conservative estimate of the top) to ensure that $\delta^{13}C$ values of pedogenic carbonates ($\delta^{13}C_{pc}$) reflect the isotopic composition of vegetation and not that of atmospheric CO_2 (Cerling, 1991). These carbonates, which were at various stages of development, were sampled throughout the Bk horizons of moderately well-developed paleosols, with ped development and horizonation caused by the dissolution of carbonate and reprecipitation at depth. These Bk horizons showed increased Ca content at depth in scanning XRF unrelated to the parent material. These carbonates were also identified as pedogenic in origin by their size ($\lesssim$2 cm), micritic texture, and the incorporation of soil matrix into the carbonate material as they grew over time. Pedogenic carbonates less than 50 cm below the top of the paleosol, larger than 2 cm, or with sparry textures were excluded from analysis to avoid any potential for diagenetic alteration. Samples were powdered, homogenized, and dried at 40°C for 24 hours before analysis. Powders were digested in 100‰ phosphoric acid at 70°C in single reaction vessels using a NuCarb device. Carbon and oxygen isotope ratios of the resultant CO_2 were analyzed on a Nu Perspective gas source IRMS at the University of Michigan, Ann Arbor. Although not highlighted in this paper, $\delta^{18}O$ values of these samples are also reported here for completeness. A calcite working standard was measured every sixth sample and at the beginning and end of each analytical run, yielding a standard deviation of 0.03‰ (1σ) for $\delta^{13}C$ and 0.11‰ (1σ) for $\delta^{18}O$, where $\delta = [R_{sample}/R_{standard} - 1] \times 1000$. Carbon and oxygen isotope ratios of all samples were normalized via two-point linear calibration using international standards NBS-18 ($\delta^{13}C = -5.014$‰; $\delta^{18}O = -23.2$‰) and NBS-19 ($\delta^{13}C = 1.95$‰; $\delta^{18}O = -2.20$‰). For each paleosol with pedogenic carbonate, powders from two to nine unique carbonate samples were analyzed. Pedogenic carbonate samples include distinct nodules collected at discrete depths in the core and aggregates of less indurated carbonate material collected over 3- to 25-cm intervals within a single Bk horizon, as denoted in sample IDs. Each unique sample was analyzed in duplicate, yielding a mean intersample difference in $\delta^{13}C_{pc}$ of 0.14‰ and $\delta^{18}O_{pc}$ of 0.17‰. The mean $\delta^{13}C_{pc}$ values and 1σ SDs of the analyses from

these multiple nodules are plotted in Fig. 4.3. All $\delta^{13}C_{pc}$ and $\delta^{18}O_{pc}$ values are reported in ‰ relative to the VPDB standard. Age designations for mean pedogenic $\delta^{13}C_{pc}$ values are shown at the midpoint of paleosol age durations.

X-radiography and XRF core scanning (M.S. and E.T.B.)
The ITRAX XRF core scanner of the Large Lake Observatory, Duluth, MN, was used to measure bulk concentrations of major elements (e.g., Si, K, and Ca) on split core surfaces (n = 12,218) and to create x-radiographic images. X-radiographs were collected with 0.2-mm resolution (step size), with 60 kV, 50 mA, and exposure time ranging from 200 to 1500 ms. XRF data were collected at 1-cm resolution (step size) using the Mo x-ray tube with 30 kV, 20 mA, 60-s exposure time. Three National Institute of Standards and Technology Certified Reference Materials or Standard Reference Materials (SRM) with properties similar to the sediment cores were used to calibrate the elemental raw counts. The Si/K ratio reflects diatom productivity and preservation. High (low) Si/K may be interpreted to reflect an oligotropic, relatively fresh (eutrophic and alkaline) lake at the time of deposition. The good correlation of Si/K to diatom counts (by R.B.O. and V.M.) indicates an insignificant influence of biogenic silica from phytoliths or of quartz. The times series of %Ca (dominated by calcium carbonate content) can reflect autochthonous carbonate precipitation within a lake and/or carbonate nodules formed during postdepositional early diagenesis or pedogenesis. In sections that were not significantly affected by pedogenesis, we propose two scenarios to interpret %Ca variability: In periods when both Si/K and Ca% are high, carbonate precipitation was likely triggered by photosynthesis in a eutrophic, relatively fresh lake. By contrast, in intervals of low Si/K and high %Ca, carbonate precipitation was likely triggered by oversaturation in a relatively saline, alkaline lake.

X-ray diffraction (N.R. and D.D.)
Samples for XRD analysis were collected at 48-cm intervals and at higher resolution within sections of laminated lacustrine muds. A total of 402 samples were oven dried at 40°C for 48 hours and then ground to fine powder using ball and pestle impact grinders or mortar and pestle. At Georgia State University, the bulk mineralogy of core material was analyzed by powder XRD using a Panalytical X'pert Pro MPD using CuKα radiation, in the range 5°–70° 2θ, operating at 45 kV and 40 mA with a total scan time of 30 min. Powder diffraction patterns were analyzed using PANalytical High Score software suite with reference to PDF-2 database (Brindley and Brown, 1980; Moore and Reynolds Jr, 1997).

4.5 Acknowledgments

The Olorgesailie Drilling Project gratefully acknowledges the National Museums of Kenya, the Oldonyo Nyokie Group Ranch, and the Olorgesailie field team led by J.M. Nume and J.N. Mativo. Research and drilling permits were provided by the Kenyan National Council for Science and Technology, the Kenya Ministry of Petroleum and Mining, and the National Environmental Management Authority of Kenya and facilitated by the National Museums of Kenya. We thank

DOSECC Exploration Services for drilling supervision, Drilling and Prospecting International (DPI) for drilling services, and the LacCore and CSDCO facilities (University of Minnesota) for core handling, processing, and storage. Elevation data in Figure 4.1 was granted to S.R. by the German Space Agency (DLR) and is based on the TanDEM-X Science DEM (© DLR 2017). We are grateful for discussions with colleagues of the Hominin Sites and Paleolakes Drilling Project (HSPDP) and for comments by C. Stringer and anonymous reviewers.

Data and materials availability

The datasets generated and analyzed during the current study are available from the corresponding author (R.P.) on reasonable request. Source data for Fig. 4.3 are provided as Excel files in the digital data repository at https://dx.doi.org/10.1126/sciadv.abc8975. Appendix C contains supporting information.

Funding

Peter Buck Fund for Human Origins Research (Smithsonian), William H. Donner Foundation (R.P.), the Ruth and Vernon Taylor Foundation (R.P.), Whitney and Betty MacMillan (R.P.), National Science Foundation grants EAR 1322017 (A.L.D.) and EAR 1349599 (D.D.), Swiss National Science Foundation grant P300P2 158501 (M.S.), Hong Kong Research Grants Council (R.B.O. and V.M.), and the Smithsonian Human Origins Program (R.P.). Funding support for A.N. and K.B.S. provided by NSF awards EAR-1338322 and EAR-1462297.

Chapter 5

An early Holocene river system along the Kenya Rift valley and its influence on faunal exchange and longitudinal diversity gradients in East Africa

René Dommain[1,2], Simon Riedl[1], Lydia Olaka[3], Peter deMenocal[4,5], Alan Deino[6], R. Bernhart Owen[7], Veronica Muiruri[8], Johannes Müller[9], Richard Potts[2,8], Manfred R. Strecker[1]

1. Institute of Geosciences, University of Potsdam, Germany
2. Human Origins Program, National Museum of Natural History Smithsonian Institution, Washington DC, USA
3. Dept. of Geology, University of Nairobi, Kenya
4. Woods Hole Oceanographic Institution, Woods Hole, Massachusetts, USA
5. Lamont-Doherty Earth Observatory, Columbia University, Palisades, USA
6. Berkeley Geochronology Center, USA
7. Dept. of Geography, Hong Kong Baptist University, Hong Kong
8. Dept. of Earth Sciences, National Museums of Kenya
9. Museum für Naturkunde, Berlin, Germany

This chapter is a draft for a submission to the *Proceedings of the National Academy of Sciences*. An updated version of this chapter is in revision at PNAS as of February 01, 2022.
Supporting information is available in Appendix D.

Abstract

East Africa is a global biodiversity hotspot but exhibits distinct longitudinal diversity gradients from west to east for freshwater fishes and forest mammals. The assembly of this exceptional biodiversity and the drivers behind diversity gradients remain poorly understood as diversification is often studied at local scales, while biotic exchange between Afrotropical regions received less attention. Here, we reconstruct a river system that run along the presently dry Kenya Rift valley during the humid early Holocene and show how this river system influenced postglacial dispersal of fishes and mammals due to its dual role as a dispersal corridor and barrier. Using geomorphological, geochronological, isotopic, and fossil analyses and by integrating >160 radiocarbon dates we find that overflow of Kenyan rift lakes between 12 and 8 ka [kilo-years before present] formed a bidirectional river system consisting of a Northern River – connected to the Nile basin and a Southern River – an endorheic basin. The water divide between these rivers represented the only terrestrial dispersal corridor across the "fluvial" rift. The degree and duration of past hydrological connectivity between adjacent river basins determined spatial diversity gradients for East African fishes. Our reconstruction explains isolated distributions of Nilotic fish species in Kenya Rift lakes, of Guineo-Congolian mammal species in forests east of the Kenya Rift and recent incipient vertebrate speciation and local endemism in this region. Climate driven rearrangements of drainage networks in the absence of tectonic activity significantly contributed to the assembly of species diversity and modern faunas in the East African biodiversity hotspot.

5.1 Introduction

Equatorial East Africa is one of the most biodiverse regions on Earth and harbors the greatest vertebrate diversity in Africa (Jenkins et al., 2013; Plumptre et al., 2007). The East African highlands are a significant reservoir of highly diverse and threatened terrestrial fauna with many rare mammals and have consequently been designated as the Eastern Afromontane Biodiversity Hotspot (Mittermeier et al., 2004). The African Great Lakes such as Lake Victoria are outstanding centers of endemism and rapid speciation containing some of the most diverse lacustrine fish faunas in the world (Mittermeier et al., 2004; Salzburger et al., 2014; Verheyen et al., 2003). How was this exceptional biodiversity assembled? While *in situ* speciation in geographically isolated settings such as mountains or lakes (e.g., Anthony et al., 2007; Wagner et al., 2014) and adaptive radiation following colonization of newly available habitats have been shown to drive local species diversity (Seehausen, 2006), the influence of past faunal exchange between different Afrotropical regions in assembling faunas is less understood. Biotic interchange is an important driver in the assembly of regional biotas and of tropical biodiversity in general (Antonelli et al., 2018) and may be of particular relevance for East Africa where species richness shows marked spatial gradients (Fig. 5.1) and where peculiar disjunct distributional patterns suggest past dispersal across biomes and connectivity between distant regions. However, the drivers of diversity gradients as well as past dispersal routes for the immigration of presently isolated vertebrate populations remain poorly studied.

Spatial diversity patterns in East African fishes are complex (Fig. 5.1b). The richness of cichlid fish species (Cichlidae) ranges from over 500 known species in Lake Victoria (Verheyen et al., 2003) to just one species in most Kenyan rift lakes (Seegers et al., 2003) (Appendix Table D.1), while the overall richness in fish species is higher in the lakes of the Albertine Rift to the west than in those of the Kenya Rift to the east (Fig. 5.1b), despite the fact that most of the rift lakes fell dry during the Last Glacial Maximum and early deglaciation (ca. 24-16 ka) (Beuning et al., 1997; Salzburger et al., 2014) (Appendix Fig. D.1). In addition, along the Kenya Rift fish diversity declines from north to south and, importantly, some of the endorheic lakes in the northern Kenya Rift such as Lake Turkana harbor isolated populations of Nilotic species like Nile tilapia (*Oreochromis niloticus*) (Seegers et al., 2003) (Fig. 5.1g, Appendix Table D.1). These disjunctions have been interpreted to reflect past hydrological connectivity with the Nile (Beadle, 1974; Roberts, 1975). The last known time when Lake Turkana was connected with the Nile was from 11.5 to ca. 8.5 ka (Garcin et al., 2012) during the African Humid Period (AHP) – a significantly wetter climatic phase in East Africa (deMenocal et al., 2000). Yet the full extent of past hydrological connectivity between East African lakes and rivers needs to be established to better explain the assembly of the East African fish fauna (Carvajal-Quintero et al., 2019). In this regard the African Humid Period is a key time for consideration because dispersal was facilitated by longer contemporaneous rivers systems (Drake et al., 2011). Past river systems of East Africa are only fragmentarily known, however (Harvey and Grove, 1982).

Longitudinal diversity gradients across equatorial East Africa also exist for mammals (Fig. 5.1c). Species richness of forest-dependent mammals decreases linearly eastward from the Congo Basin

and Albertine Rift highlands in the west to the forests of eastern Kenya (Rodgers et al., 1982). The Victoria Nile in Uganda marks the easternmost range limit for more than 20 forest-adapted mammal species (Grubb et al., 1999) attesting to its role as a riverine barrier. Farther east, the Kenya Rift also affects mammalian species distributions, as the semi-arid rift valley represents an impassable barrier for rainforest taxa due to the lack of a forest cover (Grubb et al., 1999; Kingdon et al., 2013). Remarkably though, isolated Kenyan forests on the eastern side of the rift, including montane forests of the Aberdare Range and Mount Kenya (Fig. 5.1e), harbor various mammal species of Guineo-Congolian distribution such as bongo (*Tragelaphus euryceros*) and blackfronted duiker (*Cephalophus nigrifrons*) that are separated from their main ranges by up to 800 km distance (Kingdon, 1981; Kingdon et al., 2013) (Appendix Fig. D.2). Kingdon (1981, 1971) postulated two past dispersal pathways for these disjunct Guineo-Congolian forest species - a northern route passing to the north of Lake Victoria via Mt. Elgon and extending across the Kenya Rift towards east, and a southern route passing to the south of Lake Victoria via the Eastern Arc Mountains (Tanzania) and Kilimanjaro to eastern Kenya (Fig. 5.1c). Forest expansion during Quaternary humid periods is assumed to have opened up these proposed routes as forested corridors between the Congo Basin and Kenya (Hamilton, 1982; Kingdon, 1971). However, during past humid periods, such as the AHP, larger rivers may have severed forested corridors, so we tested the viability of these dispersal routes with a reconstruction of the paleodrainage network – explicitly acknowledging that rivers may represent important barriers to mammalian dispersal (Anthony et al., 2007; Wallace, 1854).

Here we hypothesize that the peculiar biogeography of isolated fish and mammal occurrences along the Kenya Rift and the longitudinal gradients in species diversity across East Africa were influenced by past river activity during the early Holocene. To test this hypothesis, we have reconstructed the past hydrological connectivity of lake basins in the Kenya Rift and investigated the dual role of (paleo)rivers as corridors and barriers to early Holocene vertebrate dispersal. Specific objectives of our investigations were (1) to reconstruct past rivers and connectivity between currently isolated lakes in the Kenya Rift for the African Humid Period, (2) to determine the degree of faunal connectivity and exchange for fish fauna within and between East African paleo-river basins, (3) to assess Kingdon's hypothesis of a northern and southern dispersal route for forest fauna against our reconstructions of early Holocene landscape configuration and river systems, and (4) to evaluate the relevance of riverine corridors and barriers on Quaternary faunal exchange and longitudinal diversity gradients in East Africa.

To address these issues we present new geomorphological, geochronological, sedimentological and paleontological evidence on the hydrological connectivity of lakes in the Kenya Rift during the AHP. We determined the timing of lake connectivity by integrating 162 radiocarbon dates from eight lake basins (including 22 new ^{14}C dates, two new $^{40}Ar/^{39}Ar$ dates and new ^{14}C-reservoir-corrected chronologies) and the permanence of river flow with a detailed oxygen isotope record from the southern Kenya Rift. New fossil fish discoveries, published fossil and taxonomic data and our reconstructions of dispersal pathways and dated area-cladograms were used to infer East African faunal exchange, geographic isolation and the Holocene assembly of regional faunas and diversity.

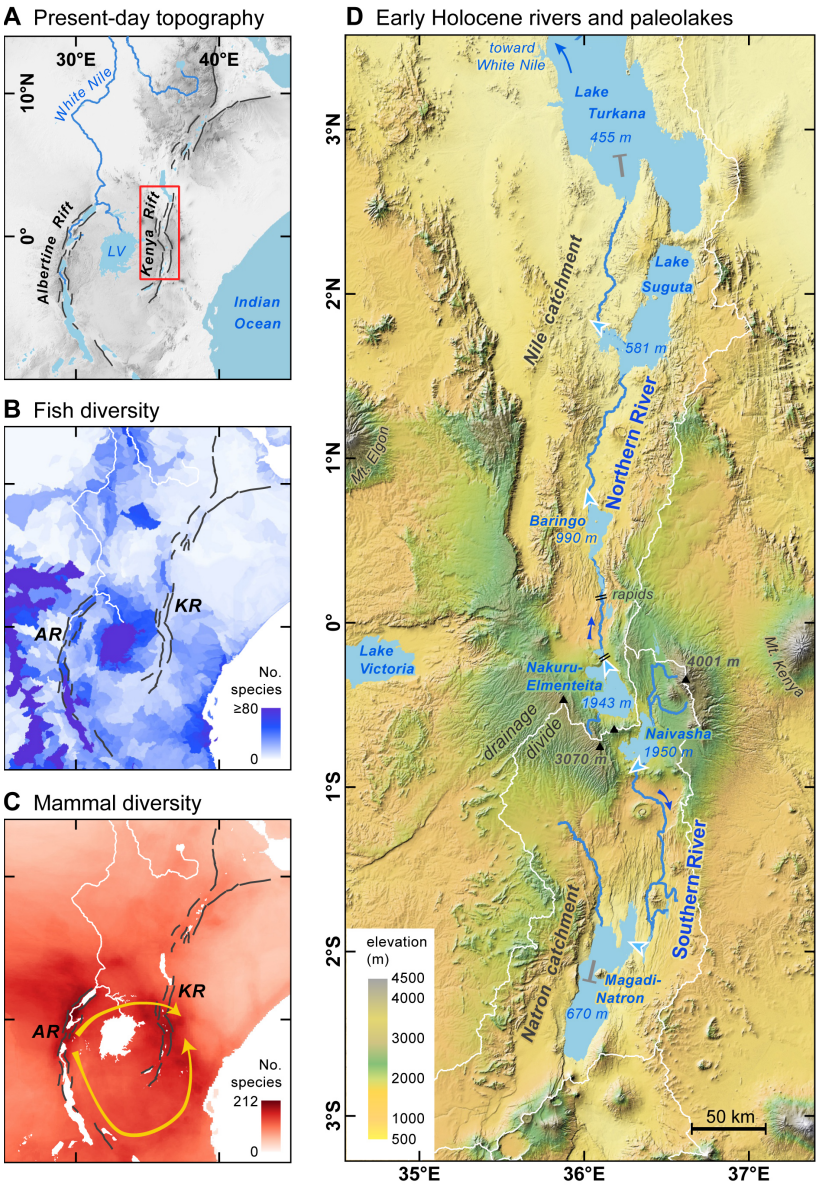

Figure 5.1. Study region and reconstruction of the early Holocene river system in the Kenya Rift valley.

Left page: (A) *Study region with modern topography of the East African Rift System.* ***(B)*** *Present-day species richness of fishes (class Actinopterygii) in East Africa (IUCN 2020).* ***(C)*** *Present-day species richness of mammals in East Africa (IUCN 2020), yellow arrows indicate proposed dispersal pathways of Kingdon (1971, 1981).* ***(D)*** *Reconstruction of the early Holocene river system between overflowing lakes along the Kenya Rift valley; elevations denote overflow levels, dark-blue arrows river flow directions.* ***Right page: (E)*** *Study sites, fossil localities and reconstruction of the early Holocene river system in the Central and South Kenya Rift.* ***(F)*** *Cross-sections of overflow gorges used by the Northern (1) and Southern (2-4) River (locations marked in F).* ***(G)*** *Longitudinal river profiles of the Northern and Southern River along the Kenya rift valley with data on present-day fish diversity and biogeography of Kenya rift lakes (Appendix Table D.1). Dark blue areas denote early Holocene lake levels and rivers, light blue denotes present-day lake levels. Dark grey area shows the topography of the rift valley floor used by the rivers and light grey the topography of the adjacent rift shoulders. Note the dome-shaped topography of the East African Plateau.*

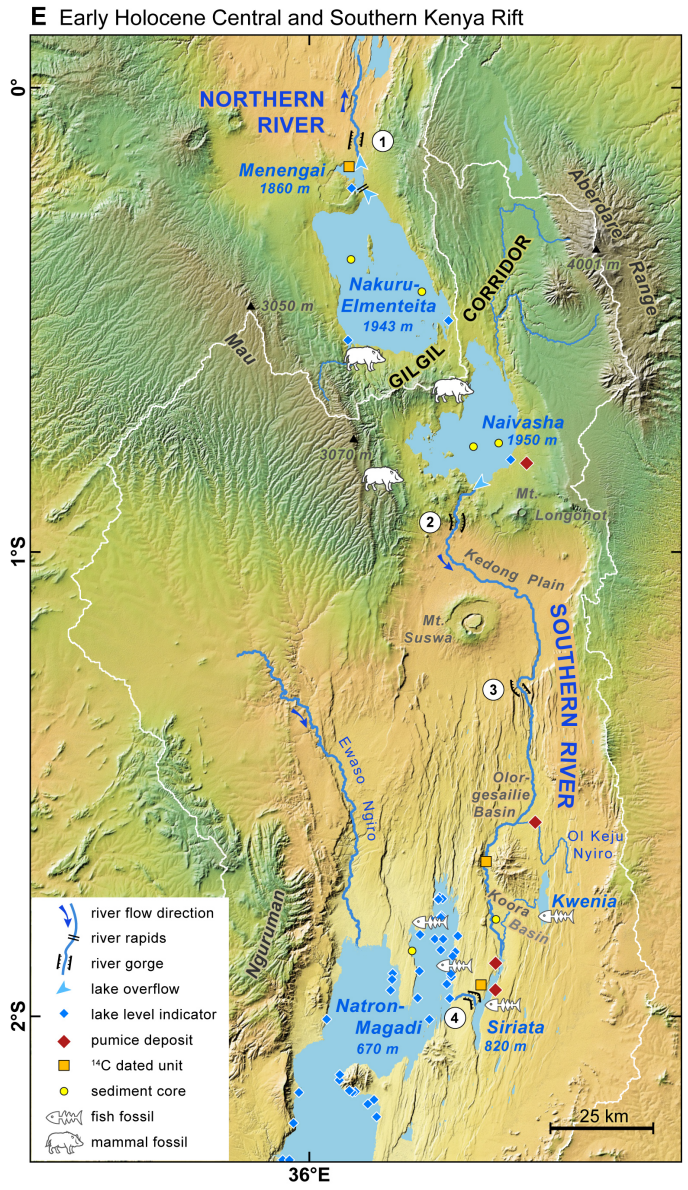

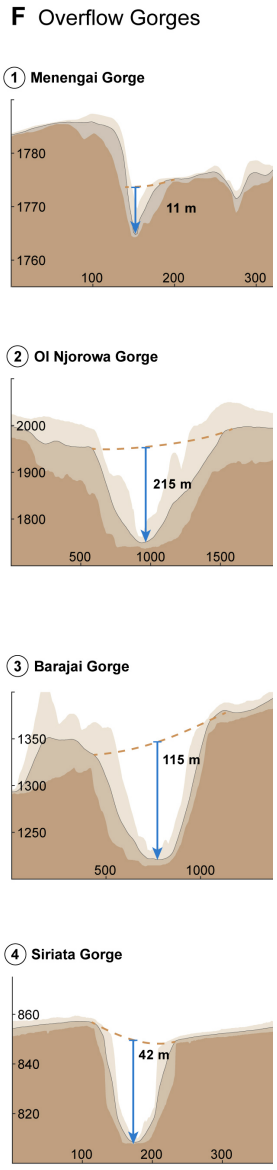

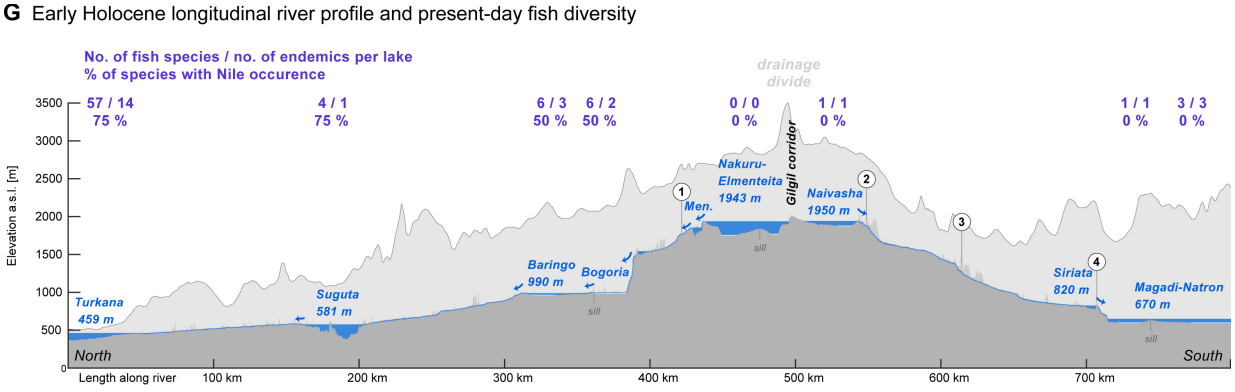

Figure 5.1 (continued).

5.2 Results

The early Holocene river system

We have reconstructed a 670-km-long, bidirectional river system along the entire Kenya Rift valley for the early Holocene (12-8 ka) consisting of two major rivers that run in opposite directions (Fig. 5.1a). Both rivers commenced in the highest area of the Central Kenya Rift at ~0.3° S and flowed down the over-1-km elevational decline of the East African Plateau, one towards the north and the other towards the south (Fig. 5.1g, Appendix Figs. D.1, D.3). The Northern River was fed by the overspill from Lake Nakuru-Elmenteita and the Southern River by the overspill of Lake Naivasha. A compilation of radiocarbon dates of overflow lake levels from all lake basins of the Kenya Rift reveals an almost synchronous onset of long-lasting connectivity at the beginning of the Holocene, indicating permanent flow in the two rivers over more than 3-4 millennia (Fig. 5.2). These two rivers connected all major, but presently isolated, lake basins of the Kenya Rift and thus represented aquatic dispersal routes between the connected lake chains. The Northern River connected a lake chain consisting of Lakes Nakuru-Elmenteita, Menengai, Baringo-Bogoria, Suguta and Turkana. Since Lake Turkana was also connected to the White Nile via the Pibor-Sobat River (Butzer et al., 1972; Harvey and Grove, 1982), the Nile catchment effectively extended all the way up into the central Kenyan highlands during this time. In contrast, the Southern River provided major inflow to the endorheic Lake Magadi-Natron in the southern Kenya Rift and connected Lake Naivasha with Lake Siriata and the joint Lake Magadi-Natron (Fig. 5.1e). The only permanent land bridge and hence only terrestrial corridor across the Kenya Rift during the interval of river activity was the 5 to 22-km-wide drainage divide at Gilgil (hereafter Gilgil corridor) between Lake Nakuru-Elmenteita and Lake Naivasha at an elevation of approximately 2050 m (Fig. 5.1e).

The Northern River

The Northern River ran over 450 km before flowing into Lake Turkana (Fig. 5.1). Along its course it dropped 1486 m in elevation, with a gradient that ranged between 1.5 and 8.4 m/km (mean: 3.8 m/km). This river integrated seven lake catchments of the central and north Kenya Rift valley into a large ~175,000 km^2 sub-catchment to the Nile River. The river's source was Lake Nakuru-Elmenteita, which maintained an overflow highstand at 1943 m between 12.0 and 8.6 ka (Appendix Table D.2). To the north this lake bordered directly on the Menengai Volcano and spilled via 80 m steep rapids into the volcano's caldera where a contemporaneous crater lake formed with a water level at 1860 m (Leat, 1984; Riedl et al., 2020) (Fig. 5.2, Appendix Figs. D.4-D.5). This Lake Menengai drained northward with its outflow carving a now abandoned gorge through the 36-ka-old Menengai pyroclastic deposits (Blegen et al., 2016) (Appendix Fig. D.5). This 4.5-km-long gorge is up to 11 m deep and hosted a 20 to 30 m wide river and represents the uppermost paleochannel bed of the Northern River (Figs. 5.1e–f). Thirty kilometers downstream of this gorge the river descended by 500 m over a course of only 10 km, which comprised a vertical drop over a 260 m steep escarpment, before entering Lake Baringo-Bogoria (Fig. 5.1g). These rapids must have acted as a major barrier for upstream dispersal of lotic organisms.

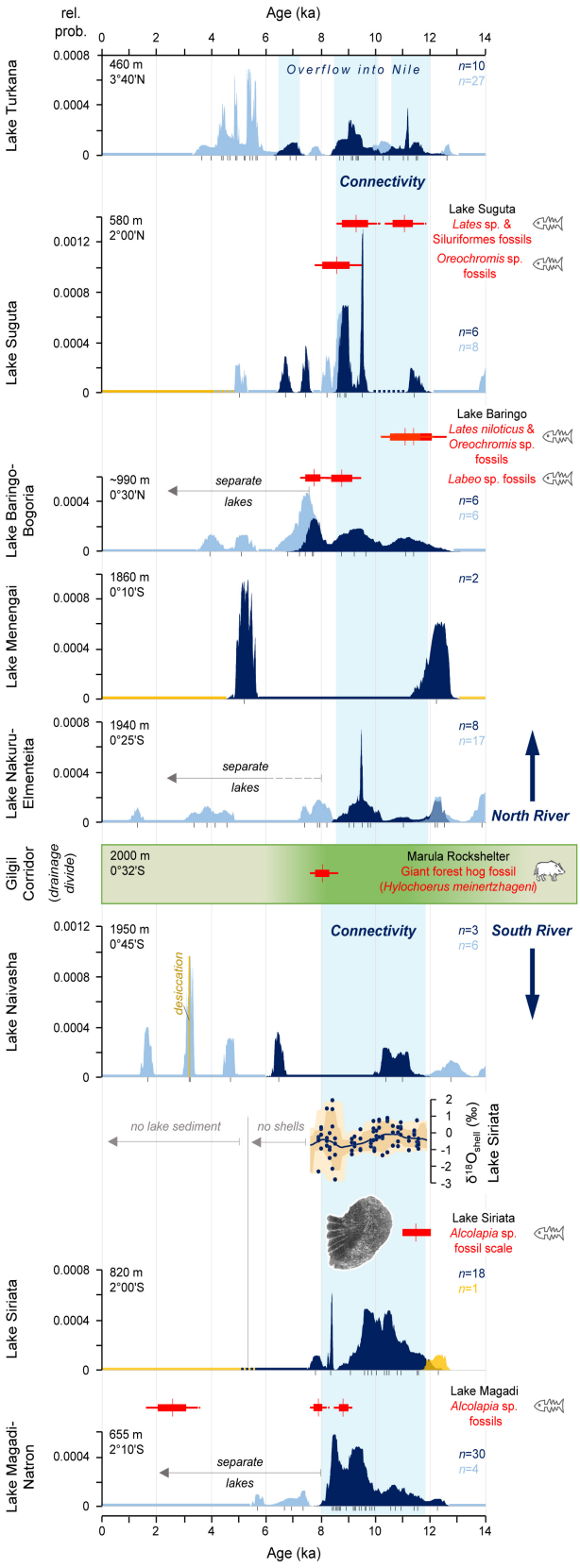

Figure 5.2. Chronology of river activity and lake overflow in the Kenya Rift valley over the past 14 ka.
Shown is the sequence of connected lakes and overflow dates for the Northern River (top) and Southern River (bottom) with the chronology based on cumulative probability distributions (CPDs) of radiocarbon dates (Appendix Table D.4) for each connected lake basin (dark blue: overflow periods, light blue: closed lake basin conditions, yellow: dry basins; vertical axis is probability in annual bins; black tick marks underneath CPDs show median ages of individual calibrated ^{14}C dates; n denotes number of radiocarbon dates/basin). Period of overflow along the entire Kenya Rift is indicated by the vertical light-blue band. Radiocarbon-dated fossil evidence for forest mammals and fishes is shown in red (calibrated ^{14}C dates of fossils: red bars: 1σ range, horizontal red line: 2σ range, vertical red line: median age; ^{14}C dates listed in Appendix Table D.2), oxygen isotope record for Siriata (dots denote single data points, line is median probability, envelopes are 68% (dark) and 95% (light) confidence intervals), and photo of Alcolapia *fossil fish scale from Siriata (Appendix Fig. D.8).*

Our TanDEM-X DEM-based river routing and ^{14}C reservoir-corrected overflow chronologies confirm earlier work that suggested a river connection between Lakes Baringo-Bogoria, Suguta and Turkana (Garcin et al., 2009; Owen and Renaut, 1980), which was, in fact, a section of the Northern River. Lake Baringo-Bogoria maintained an overflow level at 990 m between 12 and ca. 7.8 ka (Fig. 5.2, Appendix Table D.2) and was connected via the Northern River with Lake Suguta. Lake Suguta spilled over between 11.7 to 8.6 ka and again between ~7.6 and 6.5 ka and was connected with Lake Turkana immediately downstream (Garcin et al., 2009). Lastly, Lake Turkana maintained an overflow level at an elevation of 459 m (Garcin et al., 2012), from which it drained into the White Nile (Butzer et al., 1972; Harvey and Grove, 1982) during three intervals: from 12.0 to 10.6 ka, from 10.1 to 8.5 ka and from 7.2 to 6.5 ka – which documents ca. 3700 years of connectivity with the Nile. Fossils of various fish taxa, including Nilotic species such as Nile perch (*Lates niloticus*) have been found in early Holocene deposits of Lake Suguta and Lake Baringo (Tiercelin et al., 1987; Truckle, 1976) (Fig. 5.2, Appendix Fig. D.6) demonstrating active upstream dispersal along the Northern River and a contemporaneous biogeographic connection with the Nile basin.

The Southern River

The Southern River – an aquatic dispersal pathway between Lakes Naivasha and Magadi-Natron dropped over its 175-km-long course by 1221 m with a river gradient of 4.8 to 10 m/km (mean 7.0 m/km). This river integrated four, presently isolated, catchments into a single 31,950 km^2 large endorheic drainage basin: the Southern River basin (Appendix Figs. D.6 and D.3). The river started with an outlet immediately south of Lake Naivasha in the Ol Njorowa Gorge, which is up to 215 m deep and 150 to 300 m wide (Fig. 5.1f, Appendix, Fig. D.4); this gorge has previously been proposed as an outlet of Lake Naivasha (Butzer et al., 1972; Richardson and Richardson, 1972). According to diatom records from Lake Naivasha, which indicate the existence of an open freshwater lake (Richardson and Dussinger, 1986; Richardson and Richardson, 1972), the last time this gorge served as an outlet was between 11.4 and 6.2 ka (Fig. 5.2). Downstream from the outlet, the river flowed east of the Suswa Volcano and followed the (maximally) 115-m-deep and 50 to 200 m wide Barajai Gorge, part of the Kedong Valley and then flowed through the Olorgesailie Basin (Fig. 5.1e–g). The Southern River aggraded an almost level and at least 13 m thick alluvial plain within this basin, which we dated to 7.0 ka at 5.8 m below surface and to 4.1 ka at 1.8 m below surface (Appendix Table D.3, Fig. D.4). The river then entered the Koora Basin and provided the main inflow to Lake Siriata. Several radiocarbon-dated, mollusk-bearing lacustrine deposits (one of which overlies a paleosol dating with 12.3 ka to the Younger Dryas) and the presence of a single isolated shoreline at 819.5 m document the existence of a 30 km^2 and 55 m deep lake (Lake Siriata) between 12.0 and at least 7.6 ka, and probably until 5.5 ka (Fig. 5.2, Appendix Figs. D.4, D.6). This highstand shoreline, dated by $^{40}Ar/^{39}Ar$ to 10.7 ± 1.1 ka, has the same elevation as the outlet of this lake that drained with an up to 60-80 m wide river through a now dry 4-km-long and up to 42 m deep incised bedrock gorge into Lake Magadi-Natron (Fig. 5.1f, Appendix Figs. D.4, D.5). Dated stromatolites around modern Lakes Magadi and Natron confirm that these two basins formed a single, 55-m-deep lake (Hillaire-Marcel et al., 1986) (Fig. 5.1e) during the interval from ~12.4 to 8.2 ka, according to our ^{14}C reservoir correction. By about 8.0 ka the lake level had shrunk until it formed two discrete waterbodies, yet Lake Magadi continued to receive inflow from Lake Siriata via the last section of the Southern River and maintained a

higher water level until at least 7.7 ka, as indicated by dated *Alcolapia* fossils from several meters above the present lake level (Butzer et al., 1972) (Fig. 5.2).

The persistence of flow of the Southern River is inferred from our 4000-year-long $\delta^{18}O$ record on mollusk shells (n=90) from sediments deposited in Lake Siriata (Fig. 5.2). This record exhibits very subdued variability averaging -0.37‰ (S.D. ± 0.78‰). If inflow into Lake Siriata had been episodic, then the water would have been isotopically enriched during dry periods due to higher evaporation as observed in modern rift lakes with intermittent inflow (Olaka et al., 2016) and the $\delta^{18}O$ data should show fluctuations of several per mil (Beuning et al., 2002; Garcin et al., 2012). The presence of a single isolated shoreline at the outlet elevation also indicates a stable lake level with constant in- and outflow. The Southern River can thus be viewed as a perennial river that served as both a dispersal corridor for aquatic animals and a potential barrier for terrestrial organisms. The $\delta^{18}O$ data show greater variability and more enriched values (by up to 1.9‰) only between 8.35 and 8.15 ka, a period that also coincided with the cessation of overflow conditions along the Northern River (Fig. 5.2) and may suggest a regional hydrological response to the "8.2 ka event", which, in East Africa, was a dry interval (Thompson et al., 2002). Lake Siriata, however, is likely to have maintained a permanently open throughflow system between Lake Naivasha and Lake Magadi-Natron.

The inference of a 151-km-long direct hydrological connection between Lakes Naivasha and Siriata is further supported by the presence of well-rounded pumice that can be used as tracers for water flow due to their ability to float. We found rounded pumice clasts on a highstand shoreline of Lake Naivasha at 2005 m, pumice clasts on the Southern River's floodplain at Olorgesailie (972 m elevation), and pumice in beach and diatomite deposits of Lake Siriata (at 819.1 and 807 m elevation, dated to 10.7 ± 1.1 and 14.5 ± 2.2 ka) (Fig. 5.1e, Appendix Fig. D.4). These pumice clasts are likely to have originated from Central Kenya Rift volcanic centers within the Southern River's catchment area (Deino et al., 2019), such as Mt. Longonot or Mt. Suswa (Fig. 5.1e). A direct connection between Lakes Siriata and Magadi-Natron is confirmed by fish fossils found in the Siriata sediments. One fish scale retrieved from sediments dated ~11.4 ka was identified as a member of *Oreochromis* subgenus *Alcolapia* (Fig. 5.2 and Appendix Fig. D.8), which is today restricted to Lakes Natron and Magadi (Tichy and Seegers, 1999). We also discovered unidentifiable fish remains dated to approximately 16.9 ka in the adjacent Kwenia Basin to the east of Lake Siriata. These fossils provide clear evidence for aquatic faunal exchange between lakes in the southern Kenya Rift during the early Holocene.

5.3 Discussion

Influence on fish dispersal, distribution, and diversity

The opposing directions of the two rivers provide a unique framework for understanding the peculiar biogeography and relatively low species richness in freshwater fishes of lakes in the Kenya Rift. After prevailing aridity during the Last Glacial Maximum and consequent lake desiccation (24 to 16 ka), the East African lakes existed only as isolated basins for several thousand years. During their early postglacial existence, the young lakes could have received colonizing

species only from refugia that existed within their catchments, which would have contributed to low species richness. Only Lakes Turkana and Edward maintained waterbodies throughout the dry glacial period (Salzburger et al., 2014) – probably a significant factor contributing to their presently high levels of species richness and endemicity (Fig. 5.1g). Establishment of a larger river network in East Africa that connected many of the lakes during the early Holocene (Fig. 5.3a) would have enhanced faunal exchange, immigration, and local species richness in most rift lakes. The size of the paleorivers, which were more than 20-40 m wide (Fig. 5.1f) would have supported effective dispersal as the movement distance of fish is positively correlated with stream width (Radinger and Wolter, 2014). The large and deep early Holocene lakes provided more space, and hence probably more diverse habitats, while the general freshness of the lake waters (e.g., Richardson and Dussinger, 1986) would have imposed only few physiological constraints on immigrating species. These ecological conditions should theoretically have supported greater species richness of aquatic fauna in each lake (Wagner et al., 2014) than before and after the AHP.

The entire northern lake cascade, starting at Lake Nakuru-Elmenteita, was connected to the White Nile until ca. 8.6 ka (Fig. 5.3a) and consequently the entire Northern River basin became part of the Nilo-Sudan ichthyofaunal province (*sensu* Roberts, 1975) for at least 3400 years. This connection potentially allowed for faunal exchange between the Northern River and the Nile and further with Lakes Albert, Edward, Kyoga and Victoria, which were all connected to the White Nile by 14 or 13 ka (Beuning et al., 2002, 1997) (Fig. 5.3a). However, fish species dispersal was limited by physical barriers. The rapids of the Northern River upstream of Lake Baringo-Bogoria and into the Menengai Caldera (Figs. 5.1d, 5.1g) would have restricted postglacial colonization of Lake Nakuru-Elmenteita. This topographic isolation partly explains the complete absence of native fish species from the modern Lakes Nakuru and Elmenteita (Fig. 5.1g, Appendix Table D.1). Similarly, the Semliki River Rapids in the Albertine Rift restricted upstream dispersal towards Lake Edward and the 42-m-high Murchinson Falls of the Victoria Nile precluded the colonization of Lakes Victoria and Kyoga from the White Nile and connected the Northern River (Fryer and Iles, 1972; Roberts, 1975) (Fig. 5.3a). In contrast, Lakes Victoria, Kyoga, Edward and Albert were potential source areas for biota immigrating into the lakes of the Northern River between about 12 and 8.6-8.2 ka (Fig. 5.3a). The high proportion of Nilotic species (50-75%) in modern Lakes Turkana, Baringo, Bogoria and in the Suguta River (Fig. 5.1g) is clear evidence for the colonization of these lakes from source areas in the Nile Basin. The long recognized faunal similarities between Lake Turkana and Lake Albert (Beadle, 1974), which share 28 fish species (~47% of their fauna; Appendix Table D.1), provides further corroboration of biotic interchange along the 2500-km-long watercourse between Lakes Turkana and Albert (Fig. 5.3a). With a cumulative time of hydrological connectivity between these two lakes of about 3700 years, a species would have required a minimum dispersal rate of 0.7 km yr^{-1} to move successfully from one lake to the other. This rate is in accordance with predicted dispersal rates for the mobile component of fish populations (Radinger and Wolter, 2014).

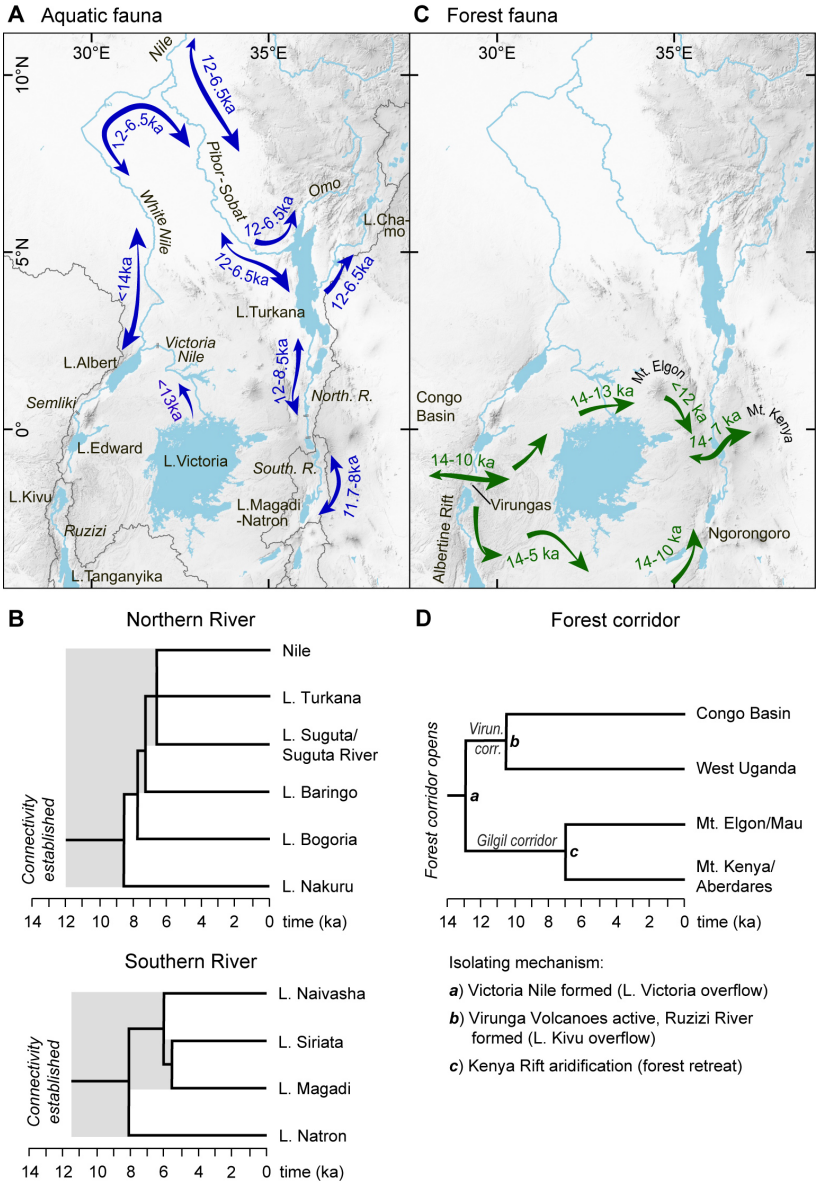

Figure 5.3. Reconstructed pathways for dispersal and faunal exchange during the early Holocene for aquatic and terrestrial-forest fauna and geological area cladograms for river systems and forests. *The cladograms provide a basis for deducing divergence dates of lacustrine fish and forest mammal populations.* ***(A)*** *shows reconstructed early Holocene river systems in East Africa with arrows denoting the directions and time of existing dispersal pathways for aquatic fauna (e.g. fishes).* ***(B)*** *Dated geological area cladograms showing the time of lake basin connectivity (grey background) and the sequence of lake separation (i.e. geographic isolation) for the Northern River lake cascade (top) and Southern River lake cascade (bottom).* ***(C)*** *shows early Holocene forest corridors as viable dispersal pathways for forest fauna with a northern route (akin to Kingdon's 1971 northern route) and a southern route following the southern catchment boundary of Lake Victoria (green arrows denote direction and time of possible dispersal).* ***(D)*** *Dated geological area cladogram indicating the time of forest connection from the eastern Congo Basin to the east of the Kenya Rift valley (i.e. Aberdares/Mt. Kenya forests) and of their separation (causes of separation indicated at each node). Roots of trees in B) and D) indicate onset of connections, while their nodes indicate divergence times for remaining local populations. Timescales for A-D based on calibrated radiocarbon dates.*

Lake Turkana was also connected via an overflow channel to Lakes Abaya, Chamo and Chew Bahir in the Ethiopian Rift during the early Holocene, until about 6.5 ka (Grove et al., 1975) (Fig. 5.3a). Nilotic species were able to colonize these Ethiopian lakes via the contemporaneous Nile-Turkana connection such as the elongate tigerfish (*Hydrocynus forskahlii*), for which closely related haplotypes demonstrate connectivity between Nilotic and Lake Chamo populations (Goodier et al., 2011). These past dispersal events combined produced the presently close faunal similarities between the lakes of the Northern River basin, the lakes in the southern Ethiopian Rift, and Lakes Albert, Edward and the White Nile.

Following the separation of the lakes of the Northern River system from 8.6 ka onward (Fig. 5.3b), lowered lake levels led to increasing salinities and adverse habitat conditions. The surviving Nilotic faunal elements in the now isolated lakes began to diverge from their Nile basin ancestors. This divergence is morphologically and genetically well exemplified in the Kenyan populations of the Nile tilapia (*Oreochromis niloticus*) with distinct subspecies present in Lakes Turkana, Baringo, Bogoria and the Suguta River (Ndiwa et al., 2014; Seegers et al., 2003) (Appendix Table D.1). For these populations Fig. 5.3b suggests divergence dates of between 8.2 ka (Bogoria) and 6.5 ka (Suguta and Turkana), suggesting that endemism and divergence developed as a result of vicariance in northern Kenya rift lakes very recently and within just a few thousand years.

The Northern River was separated from the Southern River by the Gilgil drainage divide, which acted as a major ichthyofaunal divide. This topographic barrier was responsible for the present divergent aquatic faunas between the northern and southern lakes of the Kenya Rift valley (Fig. 5.1g), which do not have a single fish species in common (Appendix Table D.1). The Southern River and the lakes it connected remained an isolated hydrological, and hence biogeographic unit because of the lack of any Holocene hydrological connectivity with adjacent drainage basins. As a result, the present-day lakes Natron, Magadi and Naivasha do not contain any Nilotic elements, but harbor exclusively local endemic species (Fig. 5.1g). Together Lakes Natron and Magadi contain four species of soda tilapia (*Alcolapia* spp.) (Appendix Table D.1), which are adapted to the extreme temperatures (20-42°C) and very high alkalinity (pH>10) that prevail in these shallow soda lakes (Tichy and Seegers, 1999). The four soda tilapias derive from a common freshwater ancestor (Ford et al., 2015), so the monophyly of the *Alcolapia* species flock (Ford et al., 2015) is consistent with a merged Magadi-Natron freshwater lake between 12.4-8.2 ka. Species divergence and adaptation to sodic conditions must have evolved rapidly in response to mid-Holocene lake isolation, declining lake-water levels, and increasing alkalinity. Whereas these adverse habitat conditions can explain the low species richness in modern Lakes Magadi and Natron, the hydrological isolation of the Southern River drainage basin during the early Holocene had a major control on their present aquatic biodiversity, because it prevented any colonization from distant source areas and refugia.

Apart from local adaptive radiations, the diversity gradients observed in fish species across East Africa at present can be attributed to the degree of historical hydrological connectivity between adjacent river systems, which reflect the regional topography and hydrological sensitivity to past climatic change. We have shown that (1) an isolated river system that had no interconnectivity

with other river systems possesses the lowest species richness (e.g. the Southern River basin), (2) a river system with episodic connection to adjacent catchments in the past possesses medium species richness (e.g. the Northern River basin), and (3) continuous connectivity (e.g., the lakes of the Nile drainage system in the Albertine Rift) resulted in the highest species richness. Faunal exchange between adjacent drainage basins was a key process in assembling the modern fish faunas and diversity in East Africa while geographic isolation promoted local endemicity.

Influence on forest mammal dispersal, distribution, and diversity

Lowland forests spread across East Africa during the humid early Holocene (e.g., Hamilton, 1982) in concert with the expansion of the river network. Extensive forest cover during this time would have facilitated the eastward dispersal of forest-dependent mammals from their Congo Basin source area. Kingdon (1981, 1971) postulated that presently isolated forest mammal populations in Kenya derive from past dispersal events via a northern and southern route (Fig. 5.1c). An integration of pollen records with our chronology of river flow establishes the timeframe and routing of viable dispersal pathways as a test of Kingdon's model for the Late Quaternary (Fig. 5.3c).

Lowland forests expanded rapidly in the region north of Lake Victoria from 14 ka until a return to drier conditions during the Younger Dryas (~13-12 ka) (Beuning et al., 1997; Kendall, 1969). By 13 ka, Lake Victoria had reached its overflow level and the Victoria Nile started to flow (Beuning et al., 2002), creating a major dispersal barrier for terrestrial fauna (Grubb et al., 1999) and disrupting Kingdon's northern route (Fig. 5.3c). Thus, an approximately 1000-year-long window of opportunity existed for the uninterrupted eastward dispersal of Guineo-Congolian mammals across a rain forest belt that extended from the eastern Congo Basin via the Albertine Rift north of Lake Kivu (Tocheri et al., 2016) to the northeastern Lake Victoria region (Fig. 5.3c). A minimum dispersal rate of 0.5 km yr^{-1} would have enabled the movement of species across this region before the Victoria Nile severed this corridor. Further eastward dispersal was possible via Mt. Elgon (Hamilton, 1982), whose forests could have acted as a "stepping stone" for the forest-dependent mammals (Fig. 5.3c). Pollen data from Lake Naivasha (Maitima, 1991) and nearby isotope records (Ambrose and DeNiro, 1989) indicate that the over 2000-m-high Gilgil corridor was covered with closed forest during the early Holocene when elsewhere in the Kenya Rift the Northern and Southern River would have blocked further eastward dispersion of various forest mammals. Although this most elevated part of the rift at Gilgil was an effective barrier for fish dispersal between the Northern and Southern River, it acted as a narrow gateway for the eastward dispersal of forest mammals across the Kenya rift valley until 7 ka when forests retreated again (Fig. 5.3c). This corridor can explain the presently isolated populations of several Guineo-Congolian forest mammals such as bongo or black-fronted duiker east of the rift valley. Its function as a dispersal pathway is confirmed by fossil finds of the forest-dependent Giant Forest Hog (*Hylocherus meinterzhageni*) in the 8-ka-old Marula Rock shelter (2000 m) and in Gambles Cave (1934 m) both located on the Gilgil corridor (Gifford-Gonzalez, 1985; Hopwood, 1931) (Figs. 5.1e, 5.2). Although Giant Forest Hog is a good swimmer (Reyna-Hurtado et al., 2017), early Holocene *Hylocherus* fossils have also been found on the western bank of the Northern River close to Lake Bogoria but not on its eastern side (Farrand et al., 1976), further suggesting that the Northern

River functioned as a barrier. Butynski and de Jong (2007) proposed that a 150-km-long section of the Central Kenya Rift Valley provided a forest corridor for the rainforest primate Potto (*Perodicticus ibeanus*), but this hypothesis is not consistent with the active river system. Yet, Butynski and de Jong (2007) independently proposed the Gilgil area as the most viable corridor due to its high elevation. As the only viable corridor, the Gilgil bridge's narrowness may have limited the number of mammal species that could cross the rift, and it thus rather represented a dispersal filter than a perfect corridor. We propose that this spatial constraint together with the actively flowing rivers contributed to the present longitudinal gradients in mammal species richness (Fig. 5.1c). Presently isolated populations of several Guineo-Congolian forest mammals only present west of the Kenya Rift (e.g. red-tailed monkey (*Cercopithecus ascanius*), yellow-backed duiker (*Cephalophus silvicultor*), tree pangolin (*Phataginus tricuspis*) (Kingdon, 2015)) support this idea as they likely failed to cross the rift.

While the continuity of the northern dispersal route was of relatively short duration, here we suggest an alternative southern route as a direct link between both rift arms, which existed without separation by rivers (Fig. 5.3c). This route directly follows the southern catchment boundary of Lake Victoria (Figs. 5.3a, 5.3c), extending from the Virunga highlands southward along the eastern shoulder of the Albertine Rift, then eastwards south of Lake Victoria towards the Ngorongoro Highlands and then northwards along the western rift shoulder of the Kenya Rift until Gilgil. Pollen data indicate that this route was forested between at least 14-10 ka (Ryner et al., 2006). Several presently disjunct populations of forest mammal species overlap along parts of this potential dispersal route (Appendix Fig. D.2).

Accordingly, we propose that boundaries of (paleo)catchments represented viable terrestrial dispersal routes because of their higher position within a geographic area and the lack of waterways on these boundaries. Consistent with this argument, the Gilgil and Virunga corridors are the highest portions of the Kenya and Albertine Rifts, respectively, simultaneously representing drainage divides and past terrestrial dispersal pathways (Tocheri et al., 2016). Identifying paleocatchment boundaries may therefore help in locating Quaternary dispersal routes for terrestrial fauna also in other parts of the world.

The eastward longitudinal decline in species richness of forest mammals in East Africa (Fig. 5.1c) can be attributed to increasing distance from the Congolese source area (MacArthur and Wilson, 1967; Rodgers et al., 1982), competitive exclusion of immigrants by resident fauna (Kingdon, 1981), and, as shown here, to the disruption of migration pathways by developing rivers during the humid early Holocene. The mid-Holocene aridification of East Africa caused further fragmentation of forests (Fig. 5.3d), which must have exacerbated the isolation of forest mammal populations and possibly induced local extinctions of small populations *sensu* MacArthur and Wilson (1967). While forest fragmentation potentially reduced local diversity it also likely enhanced genetic divergence of surviving populations as perhaps manifested in the Kenyan subspecies of Potto (*Perodicticus ibeanus stockleyi*), Bongo (*Tragelaphus eurycerus isaaci*) and Black-fronted duiker (*Cephalophus nigrifrons hooki*) (Butynski and de Jong, 2007; Kingdon, 2015). Given the dramatic Holocene landscape history of East Africa, incipient speciation in these

mammals may be as recent an evolutionary phenomenon as that of cichlids in the Kenyan rift lakes.

Quaternary East African perspectives

The East African Plateau was uplifted between 17 and 13.5 Ma (Wichura et al., 2015) while full-graben faulting of this domed plateau since at least the early Pliocene (Baker et al., 1988) formed the rift valley with its substantial N-S aligned elevational gradients (>1000 m/200 km; Fig. 5.1g). Given that orbital forcing (e.g., precessional cyclicity) and interglacial warming induced numerous wet episodes in East Africa during the Pleistocene (e.g., Kutzbach et al., 2020; Owen et al., 2018), the topographic and climatic conditions that in combination contributed to bi-directional river flow along the rift valley existed many times throughout the Quaternary. Indeed, a drill core record of the past 1 million years from the Koora Basin (Fig. 5.1e) in the South Kenya Rift shows evidence for Pleistocene hydrological connectivity and multiple episodes of rapid lake infilling following dry intervals (Deino et al., 2019; Potts et al., 2020) similar to the Younger Dryas-Holocene transition at Siriata (Appendix Fig. D.9). Hydrological connectivity with upstream sources is suggested by dated layers of rounded pumices for 790 ka, from 270-210 ka, 200-170 ka and 120-100 ka (Deino et al., 2019) – partly corresponding to periods of high orbital eccentricity and interglacials. Our Holocene reconstruction provides a general model for inferring the impact of river activity during such earlier humid periods and may help in understanding Pleistocene dispersal events and the faunal assemblages recorded in fossil sites of the rift.

The precondition for aquatic faunal exchange between biogeographic provinces were sufficiently wet climatic conditions that produced overflow across major water divides – e.g., the boundary between the Nile and Turkana basins. The Quaternary biogeographic history of East African fish and forest fauna can be understood as a cyclic history of immigration during humid periods, followed by population isolation, genetic divergence and possible extinction during dry phases, with subsequent recolonization. Connectivity with refugia was critical for successful recolonization of East African lakes as documented by molecular phylogenetic studies for the last postglacial period (Elmer et al., 2009; Seehausen, 2002). Rivers likely played a significant role in shaping the diversity and distribution of the Quaternary East African fauna.

5.4 Conclusions

Here we show how the interplay of topography, climate and hydrology governed the formation of an early Holocene river system in the presently dry Kenya Rift valley, which in turn strongly influenced the contemporaneous expansion of aquatic and terrestrial organisms. Our spatially and temporally specific reconstruction of East African paleo-drainage basins and associated dispersal and divergence events provide a testable *a priori* model for phylogeographic studies (Knowles and Maddison, 2002).

Whereas range disjunctions of freshwater fishes in coastal regions have been attributed to drainage basin connectivity during the last glacial sea-level lowstand (Carvajal-Quintero et al., 2019; de Bruyn et al., 2013), we present a mechanism for drainage basin connectivity of inland regions that rests on overflow across drainage divides during wet (high-eccentricity, interglacial)

periods. We show that orbitally-driven increases in rainfall on multi-millennial (Holocene) timescales led to overflow of lake basins, merging of catchments, and episodic connection of presently isolated river basins. Tectonism over million-year timescales had previously been invoked as a physical mechanism permitting fish dispersal between African river basins (Schwarzer et al., 2012). Tectonism during the last 1 Ma shaped the compartmentalized topography of the Kenya Rift, which is prone to episodic hydrologic connection and isolation. The rather short-lived connections presented here, allowed for postglacial recolonization of Kenyan Rift lakes, followed by genetic and phenotypic divergence and incipient speciation of the local fauna in a drier climate over the past few millennia. Climate-driven rearrangements of drainage basins thus provide an additional explanation for Plio-Pleistocene dispersal events and faunal exchange of African aquatic biota. African disjunctions of forest mammals also resulted from early Holocene dispersal followed by mid-Holocene vicariance. But as barriers – rivers had an opposing effect to the dispersal success of mammals, which instead had to move along drainage divides.

The longitudinal gradients in vertebrate species richness across East Africa can be attributed to the differing extent and durations of past river flow and lake connectivity. Drainage-basin connectivity due to overflowing lakes was a key mechanism for Holocene faunal exchange between Albertine and Kenyan rift lakes and for the assembly of the biological diversity of the Kenya Rift. The present species of Kenyan rift lakes and forest fragments with their high degree of endemicity and adaptations are a window into a recent past of substantial environmental fluctuations, yet their localized occurrence makes them highly vulnerable to extinctions and should stimulate their conservation.

5.5 Material and Methods

Spatial Analysis

We used the TanDEM-X digital elevation model (DEM, spatial resolution 12 m) for visualization purposes and to model the stream network, determine (paleo-)catchments and derive swath profiles for the entire Kenya Rift with Topo Toolbox 2 in MATLAB (Mathworks, 2018; Schwanghart and Scherler, 2014). With the ALOS World DEM (spatial resolution 5 m) we identify locations of river gorges, quantify their dimensions (gorge widths reported represent bottom widths of gorges), visualize them for the South Kenya Rift, and also quantify the lake volume of Lake Siriata. In the Koora Basin and in the Menengai region, we use Structure-from-Motion (SfM) based digital elevation and -surface models (DSM) to detect erosive shoreline features and map outlet channels. For Menengai, we analyzed a 25-cm-resolution DSM of Riedl et al. (2020; Chapter 3). In the Koora Basin we generated a 20-cm-resolution DEM using aerial images of an UAV survey (sensefly eBee classic, flown at 250 to 300 m above ground). The SfM processing was done with Agisoft Photoscan (now Metashape) (Agisoft, 2016), with a final filtering and vegetation removal step using LAStools (Isenburg, 2016). The ground elevation of the final point cloud was aligned to match our dGPS survey points (see below) and has an average point density of 28 pts/m^2. All elevation data is reported with EGM96 / WGS84 datums.

In the Koora, Olorgesailie, and Naivasha Basins we determined absolute elevations of outcrop sections and land surfaces at high-precision (decimeter-scale absolute vertical accuracy) by differential GPS measurements in February and July 2016. Point measurements at field sites were collected using a Leica Viva GS10 receiver with AS10 antenna (logging of GPS L1, L2 and L5 with carrier phase) or using a related Geomax reciever setup. At the same time, at fixed base locations, multi-day GNSS data was logged respectively (equipment see above, maximum baseline distance 25 km). In post-processing, our base station data was first corrected using positional data from the IGS (International GNSS Service) station "RCMN" in Nairobi (baseline distance ~100 km). These processed base station data was then used for positional correction of the individual measurements from the moving receiver. All post-processing was done with Leica Geo Office and included application of global navigation broadcast files, satellite ephemerals and NOAA final GPS orbits. The final point data was referenced to the EGM96 / WGS84 datums. To precisely determine paleo-lake elevations, we used the dGPS elevations to align the ground altitudes of our SfM datasets to the same absolute reference frame.

Overflow Chronology

We collated 137 published ^{14}C dates from Kenyan rift lakes from the literature and integrated them with our new ^{14}C chronology for Lake Siriata (n=19). To constrain the timing of lake overflow we only considered ^{14}C dates from material that could be clearly related to overflow elevations (e.g. shorelines) or, alternatively, from elevations that indicated closed-basin conditions (no overflow; see Appendix D for further details on sample selection). Dated material obtained from sediment cores or exposed sediment profiles was only utilized when it unequivocally indicated open or closed lake conditions (e.g. diatom records; e.g. Richardson & Dussinger, 1986). The Magadi-Natron and the Baringo-Bogoria basins receive radiocarbon depleted CO_2 from the subsurface via hydrothermal springs (Lee et al., 2016; Tiercelin et al., 1987), which necessitated a reservoir correction for their chronologies. We applied a 2050±63 ^{14}C yr subtraction to the Magadi-Natron ^{14}C dates based on a U/Th date from Taieb et al. (1991) and a 3980 ^{14}C year subtraction to Baringo-Bogoria ^{14}C dates following De Cort et al. (2013) (see Appendix D for further details on reservoir correction). For each lake basin we calibrated all (reservoir-corrected) ^{14}C dates to calendar years before present (present = AD 1950; reported as kilo-years (ka)) with Calib 7.0.4 (Stuiver and Reimer, 1993) using the IntCal13 calibration curve (Reimer et al., 2013). For each lake basin we calculated the cumulative probability distribution (CPD) from all used ^{14}C dates to determine and visualize the most probable time of overflow, for which we used the two-sigma ranges of the CPDs (Appendix Table D.4; in Fig 5.2 color-coded CPDs: overflow level - dark blue, closed-basin level - light blue, and dry conditions – yellow).

Sedimentology, Paleontology, and Geochronology

In July 2015, February 2016 and July 2016 we mapped and sampled lacustrine and fluvial deposits in the Central and South Kenya Rift, including sites in the Olorgesailie, Siriata, Kwenia and Naivasha basins and in the wider area of the Menengai volcanic complex. In the Siriata area we collected bulk sediment samples from three key outcrops (designated "1A", "3E", "6B"; Appendix Fig. D.4) at intervals of 10-25 cm. Samples were shipped to the Smithsonian Institution's National Museum of Natural History (Washington, DC, USA), where sediment was sieved

and examined for charcoal, mollusk shells and fish fossils. Fish fossils were further examined and photographed under a Leica MZ8 light microscope and with a JEOL JSM-6510 scanning electron microscope after coating with a gold-palladium alloy and identified using Tichy and Seegers (1999). Shell samples of the mollusk *Corbicula* cf. *fluminalis* (n=63) and the gastropod *Melanoides tuberculata* (n=27) were cleaned with deionized water in an ultra-sonic bath and their $\delta^{18}O$ isotopic composition determined at the Lamont-Doherty Earth Observatory stable isotope laboratory. $\delta^{18}O$ was measured on either four (n=21) or three (n=2) shell samples per sampling interval (SD 0.08-1.83‰; Appendix Table D.5).

We obtained AMS radiocarbon dates from mollusk shells, charcoal, fish bone, and sediment bulk samples (n= 22) collected at Siriata, Kwenia, and Olorgesailie. Samples were submitted to the Poznan Radiocarbon Laboratory for accelerator mass spectrometry, where shells were pretreated by selective acid leaching. Three sample pairs of shells and charcoal from Siriata showed significant, but consistent offsets in the ^{14}C ages by 3930 ± 120, 3980 ± 260 and 4380 ± 120 yrs indicating an average reservoir effect of 4095 ± 180 ^{14}C years, which was subtracted from all individual shell ^{14}C dates (Appendix Table D.3). We constructed Bayesian age models for two Lake Siriata outcrops with the rbacon package 2.3.8 (Blaauw and Christen, 2011) (Appendix Fig. D.7). Using the age model output we calculated medians and uncertainty envelopes with 68% and 95% confidence intervals for the Siriata $\delta^{18}O$ record in MATLAB. Pumice clasts were collected in Siriata in 2016 for $^{40}Ar/^{39}Ar$ dating at Berkeley Geochronology Center.

Biogeographic Analysis

We generated geological area-cladograms based on our overflow chronology (for lakes) and published radiocarbon-dated pollen records (for forests; Appendix Table D.6) to infer the sequence of Holocene connectivity and isolation of lakes and forests in East Africa. We developed maps that illustrate pathways of aquatic and terrestrial faunal exchange for the early Holocene based on the contemporaneous East African river network, forest extent (inferred from pollen records: Appendix Table D.6) and fossil records. Holocene fossil vertebrate occurrence data were obtained from various published sources (Appendix Table D.6, Fig. D.6) and own finds. We also considered available evidence for past range connectivity from published taxonomic studies and modern range maps for freshwater fishes (class: Actinopterygii) and terrestrial mammals from the IUCN (2020) (Appendix Table D.1, Fig. D.2).

5.6 Acknowledgements

We are grateful to the Siriata Maasai community who allowed us to access and study their land. For their help during field work we greatly acknowledge Moses Saitoti, Oloishiro Kuresha, Nicholas Liarrash and George Gachie. We thank Angela Dial for lab support at Lamont, Tomasz Goslar (Poznan Radiocarbon Laboratory) for radiocarbon dating, and Herbert Tichy, Lukas Rüber and Bettina Reichenbacher for their information on fish fossils.

R.D. was funded by a Smithsonian Postdoctoral Fellowship and by Geo.X - the Research Network for Geosciences in Berlin and Potsdam. This work is a contribution of the Olorgesailie Drilling Project, for which support from the National Museums of Kenya, the Oldonyo Nyokie Group

Ranch, the Peter Buck Fund for Human Origins Research (Smithsonian Institution), the William H. Donner Foundation, the Ruth and Vernon Taylor Foundation, Whitney and Betty MacMillan, and the Smithsonian's Human Origins Program is gratefully acknowledged. LacCore is acknowledged for support in drilling and core storage. The use of the TanDEM-X science DEM (© DLR 2017) was granted by the German Aerospace Center (DLR).

Chapter 6

Discussion and Conclusions

In this thesis I focused on the identification, characterization, and quantification of the youngest manifestations of normal faulting in the inner graben of the Northern Kenya Rift and its relationship with volcanic processes. In addition, the structural analysis of the NKR was integrated with observations from the Central and Southern Kenya rifts to evaluate the role of faulting and volcanism on the possible fluvial connectivity between the different sub-basins of the Kenya Rift during the Holocene African Humid Period, a time of greater moisture availability, runoff, and increased lake levels that impacted the dispersal of species along the rift and the overall character of biodiversity in the region around the equator. The implications of these different research results are discussed in detail in the individual research chapters (Chapters 2 to 5). For this reason, in this final section I will address some of the overarching aspects of my study and discuss them in the context of the four principal research questions in chapter 1 that guided my work.

6.1 Morphometric analysis and identification of active fault zones in the inner graben of the NKR: regional implications

I used a 12-m-TanDEM X DEM to develop a cartographic basis for the unambiguous localization and mapping of active faults that was carried out to understand the spatial character of structures that have accommodated Quaternary extension and to decipher the maximum and the minimum timing of faulting in the inner graben of the Kenya Rift. In addition, the DEM and the remotely-generated fault map of the study area guided my field inspection and validation efforts during consecutive field visits. Although the detectability of small faults is limited and the potential effects of erosion and sedimentation along the fault scarps may have introduced a bias in the analysis, it was possible to identify the minimum length and throw of 328 fault scarp zones in the study area. Combined with a vertical precision of 2 m this study allowed a representative synopsis of Mid-Pleistocene to Holocene fault scarps with a minimum length of 300 m. The presented data is the first detailed structural and geomorphic account of young zones of faulting in the Northern Kenya Rift. This database enabled me to determine the cumulative vertical offset and extension history of faults in the inner graben.

My analysis furthermore showed that the inner graben is highly differentiated into subordinate fault-bounded basins that under current conditions constitute isolated zones of faulting and sedimentation. Horst-and-graben morphologies and associated lava flows and volcanic edifices in the areas between these basins are ultimately responsible for this isolation. During wetter periods in the recent geological past, these barriers helped to maintain the individual character of these basins as depositional environments, but under protracted humid conditions and increased runoff, the lakes that formed within them eventually overflowed and thus provided fluvial connectivity between different volcano-tectonic depressions. Importantly, the DEM and high-resolution UAV-surveys at suspected spill points of these basins afforded a characterization of the fluvial network and the identification of lacustrine terraces and overflow areas along the basin flanks that constitute valuable markers of climatic change as well as chronologically well-defined reference horizons to assess tectonic deformation (chapters 2.5, 5.3). In combination with published radiometric ages of lacustrine deposits and terraces, this part of the analysis allowed for the first time to develop a model of structurally and climatically controlled fluvial connectivity in the Kenya Rift during the AHP of the early Holocene (Fig. 5.1).

6.2 Structural mapping and analysis

The faults in the inner graben are characterized by pure dip-slip normal faulting in a field of WNW-ESE-oriented extension. This contrasts with reports from the virtually inactive principal rift-bounding structures and reactivated older normal faults outside of the inner graben that document oblique slip (e.g., Strecker et al., 1990). The inner graben is therefore a new entity in the protracted tectono-geomorphic evolution of the Kenya Rift, where the current volcano-tectonic axis reflects an advanced stage in the process of continental separation. It is interesting to note that the Quaternary zones of extension in the Northern Kenya Rift are symmetrically oriented along the volcano-tectonic-axis, and that the kinematic transfer between individual zones of extension is accomplished by closely-spaced normal faults with similar strikes with respect to these areas and the faults that bound the inner graben (e.g., Bosworth et al., 1992; Muirhead et al., 2015; Strecker et al., 1990). Conversely, in the transition from the NKR to the Central Kenya Rift, and within the CKR proper, the young zones of extension have a left-stepping en-échelon configuration; the kinematic transfer between these zones takes place in sectors with obliquely-slipping normal faults and transfer faults that are perpendicular to the normal faults (e.g., Omenda, 1998; Strecker et al., 1990). Both types of the Quaternary extension zones in the inner graben are characterized by gravity anomalies (e.g., Kanda et al., 2019; Lichoro et al., 2019; Petit and Ebinger, 2000; Roecker et al., 2017; Simiyu and Keller, 1997; Sippel et al., 2017; Swain, 1992; Tessema and Antoine, 2004), a systematic distribution of seismicity (e.g., Atmaoui and Hollnack, 2003; Hollnack and Stangl, 1998; Ibs-von Seht et al., 2001; Tongue et al., 1994; Weinstein et al., 2017), bimodal volcanic activity (e.g., Baker, 1986; Clément et al., 2003; Macdonald, 2002; Macdonald et al., 2014, 2011; Macdonald and Bagiński, 2009; Mibei et al., 2021a; Rooney, 2020), and areas of pronounced hydrothermal alteration (e.g., Clarke et al., 1990; Darling et al., 1995; Dunkley et al., 1993; Karingithi et al., 2010; Renaut et al., 2017, 2002; Sturchio et al., 1993; Tarits et al., 2006). In this scenario, the inner graben is an area of focused extension and volcanism, which is closely associated with fissure eruptions and isolated, large eruptive centers, such as Menengai

and the volcanoes of the NKR that were studied in this thesis. In areas along the inner graben where volcanic activity is pronounced, volcanic unrest such as resurgence may superimpose the regional stress field (e.g. inside Menengai caldera; chapter 3).

In this context, it is intriguing that the spacing of large volcanic edifices and the intervening zones of extension in the inner graben is rather regular. Overall, the distance between the edifices is on the order of 40 km and spatially coincides with the area where the boundary between the lithosphere and the asthenosphere is shallow. Although different with respect to the degree of continental separation, this setting reminiscent of the punctiform spreading centers in the Red Sea (i.e., Bonatti, 1985) that were suggested to represent precursors of impending continental separation (Fig 3.7).

6.3 Geochronology and rates of deformation

In combination with previously published data (Dunkley et al., 1993; Friese, 2015; Smith et al., 1995; Sturchio et al., 1993), my new radioisotopic ages of volcanic units in the Northern Kenya Rift form the basis for the calculation of extension and subsidence rates within the inner graben of the Kenya Rift since about 0.4 Ma. The calculated extension rate in the NKR locally reaches 2.0 mm yr^{-1}. The analysis has also shown that locally the extensional processes in the NKR can be quantified with a maximum temporal resolution of approximately 10,000 years. In contrast to observations from the Main Ethiopian Rift, my analysis does not allow to further test the hypothesis of pulses in the tectono-magmatic activity and faulting, as shown by Siegburg et al. (2020). Yet, the comparison of extension rates in the area between the Paka and Silali volcanoes with rates that were derived in the adjacent Suguta Valley to the north (i.e., Melnick et al., 2012) has shown that such episodes may have potentially existed.

Overall, the extension rate of up to 2 mm yr^{-1} must represent a minimum value, because it constitutes a snapshot of activity in the inner graben, manifested in form of the brittle deformation that generated the normal faults. However, given the magmatic activity of this part of the EARS and the associated intrusive volumes of magmas in the crust (Guth, 2015; Karson and Curtis, 1989), it can be assumed that the process of diking must also influence the rate and total amount of extension. Repeated earthquakes along the volcano-tectonic axis in the NKR (Tongue et al., 1994) and in the SKR (Ibs-von Seht et al., 2001; Weinstein et al., 2017) have been interpreted in the context of dike emplacement parallel to the developing zones of normal faulting in both areas. The scarcity of both young tectonic and magmatic phenomena beyond the inner graben support the notion of focused crustal extension in this area that is accomplished by combined diking accompanied by frequent, low-magnitude earthquakes as well as faulting and fissuring. In consideration of the magmatic activity in deeper crustal sectors of the inner graben, a combined extension rate of approximately 2.3 mm yr^{-1} appears to be a reasonable value. This value is compatible with the geodetically determined rate of 2.5 to 2.6 mm yr^{-1} (Saria et al., 2014), and thus supports the interpretation of focused extension in the inner graben and its pivotal role in the process of continental separation. These results are also supported by studies in other sectors of the Kenya Rift (Weinstein et al., 2017).

Unfortunately, the geological extension rates determined in this thesis and the geodetic rates (Saria et al., 2014) cannot be compared with the long-term plate-kinematic extension rates for East Africa that cover a multi-million-year timescale (DeMets and Merkouriev, 2016), because those long-term rates only describe the overall extension rates between the Nubia and Somalia plates, but do not consider the Victoria plate in between both plates and thus do not subdivide between the extension in the Western and the Eastern branch of the EARS. For this reason, it is not possible to review my data further in the context of potential decelerations or accelerations that may have governed episodes of the rifting process on much longer timescales.

6.4 High lake levels in the Kenya Rift during the Holocene AHP: a template for repeated earlier phases of fluvial connectivity and lake-level highstands

The ongoing continental separation in the EARS has had a fundamental impact on the evolution of Pleistocene normal faults and volcanic edifices of the inner graben of the Kenya Rift valley. This narrow zone of volcanism and normal faulting along the rift axis has segmented the rift valley into a series of individual basins with intervening volcanic and structurally controlled high-relief areas. Presently, most of these sub-basins are sedimentologically and hydrologically isolated. However, during the African Humid Period (AHP) of the early Holocene, when climate was ~20% wetter than in the present, the rift basins hosted freshwater lakes (e.g., Bergner et al., 2003; Butzer et al., 1972; Dühnforth et al., 2006; Garcin et al., 2012, 2009; Hillaire-Marcel et al., 1986; Richardson and Dussinger, 1986), and lake-highstand shorelines and adjacent overflow sills indicate a paleo-drainage system between the different sub-basins (chapter 5). Such a hydrological connection existed during the AHP in the NKR between the Baringo basin, the Suguta basin, and the Turkana basin, from where waters flowed into the White Nile (e.g., Garcin et al., 2012; Junginger and Trauth, 2013; Owen and Renaut, 1980). Our study for the first time shows the synchronicity of this entire cascade of lake-filled basins and overflows; the study also documents that this hydrological connection of the NKR extended even farther south and included the lakes Nakuru and Elmenteita (Fig. 5.1). With the TanDEM-X DEM and structure-from-motion-derived DEM a paleo-river channel could be identified, which connected these lakes with each other. This analysis also shows that there existed a second lake-river-cascade directed southward, which connected Lake Naivasha with Lake Magadi and Lake Natron via a series of gorges and a newly-identified paleolake basin (paleolake Siriata), indicating that this fluvial connection was sustained for several thousands of years during the early Holocene (Fig. 5.2). Such a long-lasting hydrological connection between the sub-basins of the rift functioned as a dispersal corridor for fish species in the early Holocene, and explains the present-day occurrence of Nilotic fish species in the Kenya Rift lakes. In contrast, the highest-elevated area of the rift valley floor between the Lakes Elmenteita and Naivasha was not crossed by a river and acted as a permanent continental drainage divide between the two paleo-drainage systems. This drainage divide, the Gilgil corridor, in turn acted as a dispersal path for forest fauna between the highland areas to the west and to the east of the Kenya Rift, and reconciles the present-day endemic occurrence of Guineo-Congolian mammal species east of the Kenya Rift.

Taken together, the sustained normal faulting in the Kenya Rift continues to create a topographic partitioning inside the larger rift depressions, with sub-basins bounded by normal faults and by volcanic edifices, and this basin compartmentalization is responsible for a threshold response to changes of water availability. In turn, this results in both, episodes of isolated, dry basins and episodes of interconnected freshwater lakes. While we investigated this scenario for the early Holocene, the sedimentary record of the Kenya Rift shows that repeated earlier phases of both wet and dry episodes must have existed (e.g., Bergner et al., 2003; Owen et al., 2014; Richardson and Dussinger, 1986). For example, in the SKR, the sediment drill core of the Koora basin (Muiruri et al., 2021; Potts et al., 2020; Chapter 4) shows that since 1 Ma sustained phases of freshwater-lake conditions alternated with dry phases, as indicated, for instance, by phytolith assemblages, diatom species and numerous paleosol horizons (Fig 4.3). While the influence of orbital forcing is a common explanation for the wet and dry conditions in the EARS, the time-series analysis of the environmental proxies of these drill-core sediments shows that orbital variability plays a subdued role, and can only account for less than 20% of the total variance in the sedimentary record (Fig 4.4). The major shifts in the paleo-environmental conditions recorded in the drill core, however, coincide with phases where volcano-tectonic activity affected the basin. For example, the abrupt, twofold rise in the sedimentation rate and the higher variability of the environmental conditions since ~400 ka coincides with faulting in the adjacent Olorgesailie basin immediately to the North (e.g., Behrensmeyer et al., 2018), and also correlates with phases of pronounced volcanic activity in the SKR (Deino et al., 2019). It is therefore likely that such volcano-tectonic activity significantly influenced the environmental conditions of the lake basins in the Kenya Rift, changing the basin geometry and the topography of the catchment area (e.g., Behrensmeyer et al., 2018; Deino et al., 2019). In turn, the tectonic activity of the KR influences the paleo-environmental conditions and thus the resource landscape of the rift basins in addition to the climatic variability which is forced by orbital cycles.

In the light of these long-term observations, which are manifested in the drill-core data of the SKR, the paleo-hydrological reconstruction of the rift valley for the early Holocene (chapter 5) can be seen as a template scenario of sub-basin-connectivity, which is likely to have occurred multiple times in the geological past of the Kenya Rift. Some features of the AHP's paleo-drainage network must have existed prior to the Holocene, such as the Ol Njorowa and the Barajaj gorges of the SKR (e.g., Behrensmeyer et al., 2018). In addition, in the SKR, remnants of lake shorelines also exist on a now-faulted horst block, which also indicates that earlier lake basins have existed, but their geometry has been affected by normal faulting; adjacent, widespread fluvial deposits have been hypothesized to relate to an overflow of such a paleo-basin prior to the Holocene (e.g., Baker, 1958; Marsden, 1979; Muiruri et al., 2021). In the NKR, wind gaps in the Baringo area (e.g., Carney, 1972) are additional vestiges of earlier phases of basin interconnectivity. Hence, the tectonic morphology and the sustained tectonic activity of the Kenya Rift can be seen as a long-term driving factor that contributed to the resource availability, and the assembly of species diversity as well as modern faunas in the East African biodiversity hotspot.

Chapter 7

References

Abbey, A.L., Niemi, N.A., 2020. Perspectives on continental rifting processes from spatiotemporal patterns of faulting and magmatism in the Rio Grande Rift, USA. Tectonics 39, e2019TC005635. https://doi.org/10.1029/2019tc005635

Abelson, M., Agnon, A., 1997. Mechanics of oblique spreading and ridge segmentation. Earth Planet. Sci. Lett. 148, 405–421. https://doi.org/10.1016/s0012-821x(97)00054-x

Achauer, U., Maguire, P.K.H., Mechie, J., Green, W.V., The KRISP Working Group, 1992. Some remarks on the structure and geodynamics of the Kenya Rift. Tectonophysics, Geodynamics of Rifting, Volume II Case History Studies on Rifts: North and South America and Africa 213, 257–268. https://doi.org/10.1016/0040-1951(92)90262-5

Achauer, U., Masson, F., 2002. Seismic tomography of continental rifts revisited: from relative to absolute heterogeneities. Tectonophysics, Structure of the continental lithosphere and upper mantle 358, 17–37. https://doi.org/10.1016/S0040-1951(02)00415-8

Acocella, V., 2014. Structural control on magmatism along divergent and convergent plate boundaries: Overview, model, problems. Earth-Sci. Rev. 136, 226–288. https://doi.org/10.1016/j.earscirev.2014.05.006

Acocella, V., Cifelli, F., Funiciello, R., 2000. Analogue models of collapse calderas and resurgent domes. J. Volcanol. Geotherm. Res. 104, 81–96. https://doi.org/10.1016/S0377-0273(00)00201-8

Acocella, V., Funiciello, R., 1999. The interaction between regional and local tectonics during resurgent doming: the case of the island of Ischia, Italy. J. Volcanol. Geotherm. Res. 88, 109–123. https://doi.org/10.1016/S0377-0273(98)00109-7

Acocella, V., Funiciello, R., Marotta, E., Orsi, G., de Vita, S., 2004. The role of extensional structures on experimental calderas and resurgence. J. Volcanol. Geotherm. Res., The role of laboratory experiments in volcanology 129, 199–217. https://doi.org/10.1016/S0377-0273(03)00240-3

Agisoft, 2016. Agisoft PhotoScan Professional version 1.2.6 build 2834. Retrieved from http://www.agisoft.com/downloads/installer/.

Albert, R.M., Bamford, M.K., Cabanes, D., 2006. Taphonomy of phytoliths and macroplants in different soils from Olduvai Gorge (Tanzania) and the application to Plio-Pleistocene palaeoanthropological samples. Quat. Int., Linking African palaeoenvironments and modern environments: PAGES Workshop 148, 78–94. https://doi.org/10.1016/j.quaint.2005.11.026

Alexandre, A., Meunier, J.-D., Lézine, A.-M., Vincens, A., Schwartz, D., 1997. Phytoliths: indicators of grassland dynamics during the late Holocene in intertropical Africa. Palaeogeogr. Palaeoclimatol. Palaeoecol. 136, 213–229. https://doi.org/10.1016/S0031-0182(97)00089-8

Al-Halbouni, D., Holohan, E.P., Saberi, L., Alrshdan, H., Sawarieh, A., Closson, D., Walter, T.R., Dahm, T., 2017. Sinkholes, subsidence and subrosion on the eastern shore of the Dead Sea as revealed by a close-range photogrammetric survey. Geomorphology 285, 305–324. https://doi.org/10.1016/j.geomorph.2017.02.006

7 References

Allmendinger, R.W., Cardozo, N., Fisher, D.M., 2012. Structural geology algorithms: vectors and tensors. Cambridge University Press, Cambridge ; New York.

Ambrose, S.H., 1985. Excavations at Masai Gorge Rockshelter, Naivasha. Azania Archaeol. Res. Afr. 20, 29–67. https://doi.org/10.1080/00672708509511358

Ambrose, S.H., DeNiro, M.J., 1989. Climate and habitat reconstruction using stable carbon and nitrogen isotope ratios of collagen in prehistoric herbivore teeth from Kenya. Quat. Res. 31, 407–422. https://doi.org/10.1016/0033-5894(89)90048-3

Anthony, N.M., Johnson-Bawe, M., Jeffery, K., Clifford, S.L., Abernethy, K.A., Tutin, C.E., Lahm, S.A., White, L.J.T., Utley, J.F., Wickings, E.J., Bruford, M.W., 2007. The role of Pleistocene refugia and rivers in shaping gorilla genetic diversity in central Africa. Proc. Natl. Acad. Sci. 104, 20432–20436. https://doi.org/10.1073/pnas.0704816105

Antonelli, A., Zizka, A., Carvalho, F.A., Scharn, R., Bacon, C.D., Silvestro, D., Condamine, F.L., 2018. Amazonia is the primary source of Neotropical biodiversity. Proc. Natl. Acad. Sci. 115, 6034–6039. https://doi.org/10.1073/pnas.1713819115

Ashley, G.M., Barboni, D., Dominguez-Rodrigo, M., Bunn, H.T., Mabulla, A.Z.P., Diez-Martin, F., Barba, R., Baquedano, E., 2010a. A spring and wooded habitat at FLK Zinj and their relevance to origins of human behavior. Quat. Res., Paleoecology and Hominin Behavior during Bed I at Olduvai Gorge (Tanzania) 74, 304–314. https://doi.org/10.1016/j.yqres.2010.07.015

Ashley, G.M., Barboni, D., Dominguez-Rodrigo, M., Bunn, H.T., Mabulla, A.Z.P., Diez-Martin, F., Barba, R., Baquedano, E., 2010b. Paleoenvironmental and paleoecological reconstruction of a freshwater oasis in savannah grassland at FLK North, Olduvai Gorge, Tanzania. Quat. Res., Paleoecology and Hominin Behavior during Bed I at Olduvai Gorge (Tanzania) 74, 333–343. https://doi.org/10.1016/j.yqres.2010.08.006

Atmaoui, N., Hollnack, D., 2003. Neotectonics and extension direction of the Southern Kenya Rift, Lake Magadi area. Tectonophysics 364, 71–83. https://doi.org/10.1016/S0040-1951(03)00051-9

Ayele, A., Jacques, E., Kassim, M., Kidane, T., Omar, A., Tait, S., Nercessian, A., de Chabalier, J.-B., King, G., 2007. The volcano–seismic crisis in Afar, Ethiopia, starting September 2005. Earth Planet. Sci. Lett. 255, 177–187. https://doi.org/10.1016/j.epsl.2006.12.014

Bailey, R.A., Dalrymple, G.B., Lanphere, M.A., 1976. Volcanism, structure, and geochronology of Long Valley Caldera, Mono County, California. J. Geophys. Res. 81, 725–744. https://doi.org/10.1029/JB081i005p00725

Baker, B.H., 1986. Tectonics and volcanism of the southern Kenya Rift Valley and its influence on rift sedimentation. Geol. Soc. Lond. Spec. Publ. 25, 45–57. https://doi.org/10.1144/GSL.SP.1986.025.01.05

Baker, B.H., 1958. Geology of the Magadi area, degree sheet 51, SW Quarter (No. 42), Geological Survey of Kenya Report. Geological Survey of Kenya.

Baker, B.H., Mitchell, J.G., Williams, L. a. J., 1988. Stratigraphy, geochronology and volcano-tectonic evolution of the Kedong–Naivasha–Kinangop region, Gregory Rift Valley, Kenya. J. Geol. Soc. 145, 107–116. https://doi.org/10.1144/gsjgs.145.1.0107

Baker, B.H., Williams, L.A.J., Miller, J.A., Fitch, F.J., 1971. Sequence and geochronology of the Kenya rift volcanics. Tectonophysics 11, 191–215. https://doi.org/10.1016/0040-1951(71)90030-8

Baker, B.H., Wohlenberg, J., 1971. Structure and Evolution of the Kenya Rift Valley. Nature 229, 538–542. https://doi.org/10.1038/229538a0

Barboni, D., Bonnefille, R., Alexandre, A., Meunier, J.D., 1999. Phytoliths as paleoenvironmental indicators, West Side Middle Awash Valley, Ethiopia. Palaeogeogr. Palaeoclimatol. Palaeoecol. 152, 87–100. https://doi.org/10.1016/S0031-0182(99)00045-0

Barboni, D., Bremond, L., 2009. Phytoliths of East African grasses: An assessment of their environmental and taxonomic significance based on floristic data. Rev. Palaeobot. Palynol. 158, 29–41. https://doi.org/10.1016/j.revpalbo.2009.07.002

Barboni, D., Bremond, L., Bonnefille, R., 2007. Comparative study of modern phytolith assemblages from inter-tropical Africa. Palaeogeogr. Palaeoclimatol. Palaeoecol. 246, 454–470. https://doi.org/10.1016/j.palaeo.2006.10.012

Barcelona, H., Yagupsky, D., Vigide, N., Senger, M., 2019. Structural model and slip-dilation tendency analysis at the Copahue geothermal system: Inferences on the reservoir geometry. J. Volcanol. Geotherm. Res. 375, 18–31. https://doi.org/10.1016/j.jvolgeores.2019.03.007

Bathke, H., Nikkhoo, M., Holohan, E.P., Walter, T.R., 2015. Insights into the 3D architecture of an active caldera ring-fault at Tendürek volcano through modeling of geodetic data. Earth Planet. Sci. Lett. 422, 157–168. https://doi.org/10.1016/j.epsl.2015.03.041

Beadle, L.C., 1974. The Inland Waters of Tropical Africa: An Introduction to Tropical Limnology. Longman.

Beck, C.C., Allen, M.M., Feibel, C.S., Beverly, E.J., Stone, J.R., Wegter, B., Wilson, C.L., 2019a. Living in a swampy paradise: Paleoenvironmental reconstruction of an African Humid Period lacustrine margin, West Turkana, Kenya. J. Afr. Earth Sci. 154, 20–34. https://doi.org/10.1016/j.jafrearsci.2019.03.007

Beck, C.C., Feibel, C.S., Wright, J.D., Mortlock, R.A., 2019b. Onset of the African Humid Period by 13.9 kyr BP at Kabua Gorge, Turkana Basin, Kenya. The Holocene 29, 1011–1019. https://doi.org/10.1177/0959683619831415

Behrensmeyer, A.K., Potts, R., Deino, A., 2018. The Oltulelei Formation of the southern Kenyan Rift Valley: A chronicle of rapid landscape transformation over the last 500 k.y. GSA Bull. 130, 1474–1492. https://doi.org/10.1130/B31853.1

Behrensmeyer, A.K., Potts, R., Deino, A., Ditchfield, P., 2002. Olorgesailie, Kenya: A million years in the life of a rift basin, in: Renaut, R.W., Ashley, G.M. (Eds.), Sedimentation in Continental Rifts, SEPM Special Publication 73. pp. 97–106. https://doi.org/10.2110/pec.02.73.0097

Bell, R.E., McNeill, L.C., Henstock, T.J., Bull, J.M., 2011. Comparing extension on multiple time and depth scales in the Corinth Rift, Central Greece. Geophys. J. Int. 186, 463–470. https://doi.org/10.1111/j.1365-246X.2011.05077.x

Bemis, S.P., Micklethwaite, S., Turner, D., James, M.R., Akciz, S., Thiele, S.T., Bangash, H.A., 2014. Ground-based and UAV-Based photogrammetry: A multi-scale, high-resolution mapping tool for structural geology and paleoseismology. J. Struct. Geol. 69, Part A, 163–178. https://doi.org/10.1016/j.jsg.2014.10.007

Bender, M.M., 1971. Variations in the 13C/12C ratios of plants in relation to the pathway of photosynthetic carbon dioxide fixation. Phytochemistry 10, 1239–1244. https://doi.org/10.1016/S0031-9422(00)84324-1

Berger, R., Protsch, R., 1989. UCLA Radiocarbon Dates XI. Radiocarbon 31, 55–67. https://doi.org/10.1017/S0033822200044611

Bergner, A.G.N., Strecker, M.R., Trauth, M.H., Deino, A., Gasse, F., Blisniuk, P., Dühnforth, M., 2009. Tectonic and climatic control on evolution of rift lakes in the Central Kenya Rift, East Africa. Quat. Sci. Rev. 28, 2804–2816. https://doi.org/10.1016/j.quascirev.2009.07.008

Bergner, A.G.N., Trauth, M.H., Bookhagen, B., 2003. Paleoprecipitation estimates for the Lake Naivasha basin (Kenya) during the last 175 k.y. using a lake-balance model. Glob. Planet. Change 36, 117–136. https://doi.org/10.1016/S0921-8181(02)00178-9

Beuning, K.R.M., Kelts, K., Russell, J., Wolfe, B.B., 2002. Reassessment of Lake Victoria–Upper Nile River paleohydrology from oxygen isotope records of lake-sediment cellulose. Geology 30, 559–562. https://doi.org/10.1130/0091-7613(2002)030<0559:ROLVUN>2.0.CO;2

7 References

Beuning, K.R.M., Talbot, M.R., Kelts, K., 1997. A revised 30,000-year paleoclimatic and paleohydrologic history of Lake Albert, East Africa. Palaeogeogr. Palaeoclimatol. Palaeoecol. 136, 259–279. https://doi.org/10.1016/S0031-0182(97)00034-5

Bibby, H.M., Caldwell, T.G., Davey, F.J., Webb, T.H., 1995. Geophysical evidence on the structure of the Taupo Volcanic Zone and its hydrothermal circulation. J. Volcanol. Geotherm. Res., Taupo Volcanic Zone, New Zealand 68, 29–58. https://doi.org/10.1016/0377-0273(95)00007-H

Biggs, J., Amelung, F., Gourmelen, N., Dixon, T.H., Kim, S.-W., 2009a. InSAR observations of 2007 Tanzania rifting episode reveal mixed fault and dyke extension in an immature continental rift. Geophys. J. Int. 179, 549–558. https://doi.org/10.1111/j.1365-246X.2009.04262.x

Biggs, J., Anthony, E.Y., Ebinger, C.J., 2009b. Multiple inflation and deflation events at Kenyan volcanoes, East African Rift. Geology 37, 979–982. https://doi.org/10.1130/G30133A.1

Biggs, J., Robertson, E., Cashman, K., 2016. The lateral extent of volcanic interactions during unrest and eruption. Nat. Geosci. 9, 308–311. https://doi.org/10.1038/ngeo2658

Binford, L.R., 2001. Constructing frames of reference: an analytical method for archaeological theory building using ethnographic and environmental data sets, First Edition. ed. University of California Press, Berkeley.

Bishop, W.W., 1975. Geological reconnaissance of the Lower Suguta Valley and its eastern flank, north Kenya rift Valley, in: Proceedings of the IGU Meeting on Desertification, Cambridge, 22-26 September 1975. Cambridge, pp. 62–63.

Bishop, W.W., Pickford, M., Hill, A., 1975. New evidence regarding the Quaternary geology, archaeology and hominids of Chesowanja, Kenya. Nature 258, 204–208. https://doi.org/10.1038/258204a0

Blaauw, M., Christen, J.A., 2011. Flexible paleoclimate age-depth models using an autoregressive gamma process. Bayesian Anal. 6, 457–474. https://doi.org/10.1214/11-BA618

Blegen, N., Brown, F.H., Jicha, B.R., Binetti, K.M., Faith, J.T., Ferraro, J.V., Gathogo, P.N., Richardson, J.L., Tryon, C.A., 2016. The Menengai Tuff: A 36 ka widespread tephra and its chronological relevance to Late Pleistocene human evolution in East Africa. Quat. Sci. Rev. 152, 152–168. https://doi.org/10.1016/j.quascirev.2016.09.020

Blinkhorn, J., Grove, M., 2018. The structure of the Middle Stone Age of eastern Africa. Quat. Sci. Rev. 195, 1–20. https://doi.org/10.1016/j.quascirev.2018.07.011

Bloszies, C., Forman, S.L., Wright, D.K., 2015. Water level history for Lake Turkana, Kenya in the past 15,000years and a variable transition from the African Humid Period to Holocene aridity. Glob. Planet. Change 132, 64–76. https://doi.org/10.1016/j.gloplacha.2015.06.006

Bonatti, E., 1985. Punctiform initiation of seafloor spreading in the Red Sea during transition from a continental to an oceanic rift. Nature 316, 33–37. https://doi.org/10.1038/316033a0

Boone, S.C., Seiler, C., Kohn, B.P., Gleadow, A.J.W., Foster, D.A., Chung, L., 2018. Influence of rift superposition on lithospheric response to East African Rift System extension: Lapur Range, Turkana, Kenya. Tectonics 37, 182–207. https://doi.org/10.1002/2017TC004575

Bosworth, W., Burke, K., Strecker, M.R., 2003. Effect of stress fields on magma chamber stability and the formation of collapse calderas. Tectonics 22, 1042. https://doi.org/10.1029/2002TC001369

Bosworth, W., Lambiase, J., Keisler, R., 1986. A new look at Gregory's Rift: The structural style of continental rifting. Eos Trans. Am. Geophys. Union 67, 577–583. https://doi.org/10.1029/EO067i029p00577

Bosworth, W., Maurin, A., 1993. Structure, geochronology and tectonic significance of the northern Suguta Valley (Gregory Rift), Kenya. J. Geol. Soc. 150, 751–762. https://doi.org/10.1144/gsjgs.150.4.0751

Bosworth, W., Strecker, M.R., 1997. Stress field changes in the Afro-Arabian rift system during the Miocene to Recent period. Tectonophysics, Structure and Dynamic Processes in the Lithosphere of the Afro-Arabian Rift System 278, 47–62. https://doi.org/10.1016/S0040-1951(97)00094-2

Bosworth, W., Strecker, M.R., Blisniuk, P.M., 1992. Integration of east African Paleostress and present-day stress data: Implications for continental stress field dynamics. J. Geophys. Res. Solid Earth 97, 11851–11865. https://doi.org/10.1029/90JB02568

Bower, J.R.F., Nelson, C.M., 1978. Early Pottery and Pastoral Cultures of the Central Rift Valley, Kenya. Man 13, 554–566. https://doi.org/10.2307/2801248

Bower, J.R.F., Nelson, C.M., Waibel, A.F., Wandibba, S., 1977. The University of Massachusetts' Later Stone Age/Pastoral 'Neolithic' Comparative Study in Central Kenya: an Overview. Azania Archaeol. Res. Afr. 12, 119–146. https://doi.org/10.1080/00672707709511251

Bremond, L., Alexandre, A., Hély, C., Guiot, J., 2005a. A phytolith index as a proxy of tree cover density in tropical areas: calibration with Leaf Area Index along a forest–savanna transect in southeastern Cameroon. Glob. Planet. Change 45, 277–293. https://doi.org/10.1016/j.gloplacha.2004.09.002

Bremond, L., Alexandre, A., Peyron, O., Guiot, J., 2005b. Grass Water Stress Estimated from Phytoliths in West Africa. J. Biogeogr. 32, 311–327.

Brindley, G.W., Brown, G., 1980. Crystal Structures of Clay Minerals and their X-Ray Identification. https://doi.org/10.1180/mono-5

Brooks, A.S., Yellen, J.E., Potts, R., Behrensmeyer, A.K., Deino, A.L., Leslie, D.E., Ambrose, S.H., Ferguson, J.R., d'Errico, F., Zipkin, A.M., Whittaker, S., Post, J., Veatch, E.G., Foecke, K., Clark, J.B., 2018. Long-distance stone transport and pigment use in the earliest Middle Stone Age. Science 360, 90–94. https://doi.org/10.1126/science.aao2646

Brown, E.T., 2015. Estimation of Biogenic Silica Concentrations Using Scanning XRF: Insights from Studies of Lake Malawi Sediments, in: Croudace, I.W., Rothwell, R.G. (Eds.), Micro-XRF Studies of Sediment Cores: Applications of a Non-Destructive Tool for the Environmental Sciences, Developments in Paleoenvironmental Research. Springer Netherlands, Dordrecht, pp. 267–277. https://doi.org/10.1007/978-94-017-9849-5_9

Brune, S., Williams, S.E., Butterworth, N.P., Müller, R.D., 2016. Abrupt plate accelerations shape rifted continental margins. Nature 536, 201–204. https://doi.org/10.1038/nature18319

Buck, W.R., 2006. The role of magma in the development of the Afro-Arabian Rift System. Geol. Soc. Lond. Spec. Publ. 259, 43–54. https://doi.org/10.1144/GSL.SP.2006.259.01.05

Buck, W.R., 2004. Consequences of asthenospheric variability on continental rifting., in: Karner, G.D., Taylor, B., Driscoll, N.W., Kohlstedt, D.L., Morris, J.D., Driscoll, N.W., Silver, A.E. (Eds.), Rheology and Deformation of the Lithosphere at Continental Margins, MARGINS Theoretical and Experimental Earth Science Series. Columbia University Press, New York, pp. 1–30.

Burke, K., 1996. The African Plate. South Afr. J. Geol. 99, 341–409.

Burke, K., Dewey, J.F., 1973. Plume-Generated Triple Junctions: Key Indicators in Applying Plate Tectonics to Old Rocks. J. Geol. 81, 406–433. https://doi.org/10.1086/627882

Butynski, T.M., de Jong, Y.A., 2007. Distribution of the Potto Perodicticus potto (Primates: Lorisidae) in Eastern Africa, with a Description of a New Subspecies from Mount Kenya. J. East Afr. Nat. Hist. 96, 113–147. https://doi.org/10.2982/0012-8317(2007)96[113:DOTPPP]2.0.CO;2

Butzer, K.W., Isaac, G.L., Richardson, J.L., Washbourn-Kamau, C., 1972. Radiocarbon Dating of East African Lake Levels. Science 175, 1069–1076. https://doi.org/10.1126/science.175.4026.1069

Butzer, K.W., Thurber, D.L., 1969. Some Late Cenozoic Sedimentary Formations of the Lower Omo Basin. Nature 222, 1138–1143. https://doi.org/10.1038/2221138a0

Calais, E., d'Oreye, N., Albaric, J., Deschamps, A., Delvaux, D., Déverchère, J., Ebinger, C.J., Ferdinand, R.W., Kervyn, F., Macheyeki, A.S., Oyen, A., Perrot, J., Saria, E., Smets, B., Stamps, D.S., Wauthier, C., 2008. Strain accommodation by slow slip and dyking in a youthful continental rift, East Africa. Nature 456, 783–787. https://doi.org/10.1038/nature07478

7 References

Calais, E., Ebinger, C.J., Hartnady, C., Nocquet, J.M., 2006. Kinematics of the East African Rift from GPS and earthquake slip vector data. Geol. Soc. Lond. Spec. Publ. 259, 9–22. https://doi.org/10.1144/GSL.SP.2006.259.01.03

Cardozo, N., Allmendinger, R.W., 2013. Spherical projections with OSXStereonet. Comput. Geosci. 51, 193–205. https://doi.org/10.1016/j.cageo.2012.07.021

Carney, J.N., 1972. The geology of the Eastern part of the Rift Valley in Baringo District, Kenya (Ph.D.). Royal Holloway, University of London.

Carrivick, J.L., Smith, M.W., Quincey, D.J., 2016. Structure from Motion in the Geosciences. John Wiley & Sons, Ltd, Chichester, UK. https://doi.org/10.1002/9781118895818

Cartwright, J.A., Trudgill, B.D., Mansfield, C.S., 1995. Fault growth by segment linkage: an explanation for scatter in maximum displacement and trace length data from the Canyonlands Grabens of SE Utah. J. Struct. Geol. 17, 1319–1326. https://doi.org/10.1016/0191-8141(95)00033-A

Carvajal-Quintero, J., Villalobos, F., Oberdorff, T., Grenouillet, G., Brosse, S., Hugueny, B., Jézéquel, C., Tedesco, P.A., 2019. Drainage network position and historical connectivity explain global patterns in freshwater fishes' range size. Proc. Natl. Acad. Sci. 116, 13434–13439. https://doi.org/10.1073/pnas.1902484116

Casanova, J., Hillaire-Marcel, C., Page, N., Taieb, M., Vincens, A., 1988. Stratigraphie et paléohydrologie des épisodes lacustres du Quaternaire récent du rift Suguta (Kenya). Comptes Rendus Acad. Sci. Paris, Série II 307, 1251–1258.

Cerling, T.E., 1991. Carbon dioxide in the atmosphere: Evidence from cenozoic and mesozoic paleosols. Am. J. Sci. U. S. 291:4. https://doi.org/10.2475/ajs.291.4.377

Cerling, T.E., Wynn, J.G., Andanje, S.A., Bird, M.I., Korir, D.K., Levin, N.E., Mace, W., Macharia, A.N., Quade, J., Remien, C.H., 2011. Woody cover and hominin environments in the past 6 million years. Nature 476, 51–56. https://doi.org/10.1038/nature10306

Chadwick, W.W., Geist, D.J., Jónsson, S., Poland, M., Johnson, D.J., Meertens, C.M., 2006. A volcano bursting at the seams: Inflation, faulting, and eruption at Sierra Negra volcano, Galápagos. Geology 34, 1025–1028. https://doi.org/10.1130/G22826A.1

Chapman, G.R., Brook, M., 1978. Chronostratigraphy of the Baringo Basin, Kenya. Geol. Soc. Lond. Spec. Publ. 6, 207–223. https://doi.org/10.1144/GSL.SP.1978.006.01.16

Chapman, G.R., Lippard, S.J., Martyn, J.E., 1978. The stratigraphy and structure of the Kamasia Range, Kenya Rift Valley. J. Geol. Soc. 135, 265–281. https://doi.org/10.1144/gsjgs.135.3.0265

Chikaraishi, Y., Naraoka, H., Poulson, S.R., 2004. Hydrogen and carbon isotopic fractionations of lipid biosynthesis among terrestrial (C3, C4 and CAM) and aquatic plants. Phytochemistry 65, 1369–1381. https://doi.org/10.1016/j.phytochem.2004.03.036

Child, G., Parris, R., Riché, E.L., 1971. Use of Mineralised Water by Kalahari Wildlife and Its Effects on Habitats. Afr. J. Ecol. 9, 125–142. https://doi.org/10.1111/j.1365-2028.1971.tb00224.x

Chorowicz, J., 2005. The East African rift system. J. Afr. Earth Sci., Phanerozoic Evolution of Africa 43, 379–410. https://doi.org/10.1016/j.jafrearsci.2005.07.019

Cioni, R., Navarro, J.M., Ambrosio, M., Fagioli, M.T., Fanelli, G., Barberi, F., Duprat, A., Marini, L., Ferrara, G., Caldini, F., Sommaruga, C., Mnaura, L., Ameya, P., Jacca, P.L., Mungania, J., Gachigua, M., Wambugu, J.T., Kanynjua, A.W., 1987. Geothermal Reconnaissance Survey in the Menengai-Bogoria Area of the Kenya Rift Valley. TCD CON 7/85 KEN82/002. Final Report. 2 - Geovolcanology. United Nations (D.T.C.D.), Republic of Kenya (M.O.E.R.D.), Geothermica Italiana, Pisa, Italy.

Clark, J.D., Beyene, Y., WoldeGabriel, G., Hart, W.K., Renne, P.R., Gilbert, H., Defleur, A., Suwa, G., Katoh, S., Ludwig, K.R., Boisserie, J.-R., Asfaw, B., White, T.D., 2003. Stratigraphic, chronological and behavioural contexts of Pleistocene Homo sapiens from Middle Awash, Ethiopia. Nature 423, 747–752. https://doi.org/10.1038/nature01670

Clarke, M.C.G., Woodhall, D.G., Allen, D., Darling, G., 1990. Geological, volcanological and hydrogeological controls on the occurrence of geothermal activity in the area surrounding Lake Naivasha, Kenya. Republic of Kenya, Ministry of Energy, Nairobi.

Clément, J.-P., Caroff, M., Hémond, C., Tiercelin, J.-J., Bollinger, C., Guillou, H., Cotton, J., 2003. Pleistocene magmatism in a lithospheric transition area: petrogenesis of alkaline and peralkaline lavas from the Baringo-Bogoria Basin, central Kenya Rift. Can. J. Earth Sci. 40, 1239–1257. https://doi.org/10.1139/e03-046

Cleveland, D.M., Atchley, S.C., Nordt, L.C., 2007. Continental Sequence Stratigraphy of the Upper Triassic (Norian–Rhaetian) Chinle Strata, Northern New Mexico, U.S.A.: Allocyclic and Autocyclic Origins of Paleosol-Bearing Alluvial Successions. J. Sediment. Res. 77, 909–924. https://doi.org/10.2110/jsr.2007.082

CloudCompare, 2016. CloudCompare version 2.7. GPL software. Retrieved from http://www.cloudcompare.org/.

Coetsee, C., Stock, W.D., Craine, J.M., 2011. Do grazers alter nitrogen dynamics on grazing lawns in a South African savannah? Afr. J. Ecol. 49, 62–69. https://doi.org/10.1111/j.1365-2028.2010.01236.x

Cohen, A., Campisano, C., Arrowsmith, R., Asrat, A., Behrensmeyer, A.K., Deino, A., Feibel, C., Hill, A., Johnson, R., Kingston, J., Lamb, H., Lowenstein, T., Noren, A., Olago, D., Owen, R.B., Potts, R., Reed, K., Renaut, R., Schäbitz, F., Tiercelin, J.-J., Trauth, M.H., Wynn, J., Ivory, S., Brady, K., O'Grady, R., Rodysill, J., Githiri, J., Russell, J., Foerster, V., Dommain, R., Rucina, S., Deocampo, D., Russell, J., Billingsley, A., Beck, C., Dorenbeck, G., Dullo, L., Feary, D., Garello, D., Gromig, R., Johnson, T., Junginger, A., Karanja, M., Kimburi, E., Mbuthia, A., McCartney, T., McNulty, E., Muiruri, V., Nambiro, E., Negash, E.W., Njagi, D., Wilson, J.N., Rabideaux, N., Raub, T., Sier, M.J., Smith, P., Urban, J., Warren, M., Yadeta, M., Yost, C., Zinaye, B., 2016. The Hominin Sites and Paleolakes Drilling Project: inferring the environmental context of human evolution from eastern African rift lake deposits. Sci. Drill. 21, 1–16. https://doi.org/10.5194/sd-21-1-2016

Cohen, A.S., Soreghan, M.J., Scholz, C.A., 1993. Estimating the age of formation of lakes: An example from Lake Tanganyika, East African Rift system. Geology 21, 511–514. https://doi.org/10.1130/0091-7613(1993)021<0511:ETAOFO>2.3.CO;2

Cole, J.W., Milner, D.M., Spinks, K.D., 2005. Calderas and caldera structures: a review. Earth-Sci. Rev. 69, 1–26. https://doi.org/10.1016/j.earscirev.2004.06.004

Cole, J.W., Spinks, K.D., Deering, C.D., Nairn, I.A., Leonard, G.S., 2010. Volcanic and structural evolution of the Okataina Volcanic Centre; dominantly silicic volcanism associated with the Taupo Rift, New Zealand. J. Volcanol. Geotherm. Res., Making and Breaking the Arc: a volume in honour of Professor John Gamble 190, 123–135. https://doi.org/10.1016/j.jvolgeores.2009.08.011

Collister, J.W., Rieley, G., Stern, B., Eglinton, G., Fry, B., 1994. Compound-specific δ 13C analyses of leaf lipids from plants with differing carbon dioxide metabolisms. Org. Geochem., Compound-Specific Isotope Analysis in Biogeochemistry and Petroleum Research 21, 619–627. https://doi.org/10.1016/0146-6380(94)90008-6

Corbi, F., Rivalta, E., Pinel, V., Maccaferri, F., Bagnardi, M., Acocella, V., 2015. How caldera collapse shapes the shallow emplacement and transfer of magma in active volcanoes. Earth Planet. Sci. Lett. 431, 287–293. https://doi.org/10.1016/j.epsl.2015.09.028

Corti, G., 2009. Continental rift evolution: From rift initiation to incipient break-up in the Main Ethiopian Rift, East Africa. Earth-Sci. Rev. 96, 1–53. https://doi.org/10.1016/j.earscirev.2009.06.005

Corti, G., 2008. Control of rift obliquity on the evolution and segmentation of the main Ethiopian rift. Nat. Geosci. 1, 258–262. https://doi.org/10.1038/ngeo160

Crossley, R., 1979. The Cenozoic stratigraphy and structure of the western part of the Rift Valley in southern Kenya. J. Geol. Soc. 136, 393–405. https://doi.org/10.1144/gsjgs.136.4.0393

7 References

Crossley, R., Knight, R.M., 1981. Volcanism in the western part of the rift valley in Southern Kenya. Bull. Volcanol. 44, 117–128. https://doi.org/10.1007/BF02597699

Daget, J., Gosse, J.P., Thys van den Audenaerde, D.F.E. (Eds.), 1984. Check-list of the Freshwater Fishes of Africa (CLOFFA), Volume 1. ORSTOM - MRAC, Paris.

Darling, W.G., Griesshaber, E., Andrews, J.N., Armannsson, H., O'Nions, R.K., 1995. The origin of hydrothermal and other gases in the Kenya Rift Valley. Geochim. Cosmochim. Acta 59, 2501–2512. https://doi.org/10.1016/0016-7037(95)00145-X

de Bruyn, M., Rüber, L., Nylinder, S., Stelbrink, B., Lovejoy, N.R., Lavoué, S., Tan, H.H., Nugroho, E., Wowor, D., Ng, P.K.L., Siti Azizah, M.N., Von Rintelen, T., Hall, R., Carvalho, G.R., 2013. Paleo-drainage basin connectivity predicts evolutionary relationships across three Southeast Asian biodiversity hotspots. Syst. Biol. 62, 398–410. https://doi.org/10.1093/sysbio/syt007

De Cort, G., Bessems, I., Keppens, E., Mees, F., Cumming, B., Verschuren, D., 2013. Late-Holocene and recent hydroclimatic variability in the central Kenya Rift Valley: The sediment record of hypersaline lakes Bogoria, Nakuru and Elementeita. Palaeogeogr. Palaeoclimatol. Palaeoecol. 388, 69–80. https://doi.org/10.1016/j.palaeo.2013.07.029

Decru, E., Vranken, N., Bragança, P.H.N., Snoeks, J., Steenberge, M.V., 2020. Where ichthyofaunal provinces meet: the fish fauna of the Lake Edward system, East Africa. J. Fish Biol. 96, 1186–1201. https://doi.org/10.1111/jfb.13992

Deino, A.L., Behrensmeyer, A.K., Brooks, A.S., Yellen, J.E., Sharp, W.D., Potts, R., 2018. Chronology of the Acheulean to Middle Stone Age transition in eastern Africa. Science 360, 95–98. https://doi.org/10.1126/science.aao2216

Deino, A.L., Dommain, R., Keller, C.B., Potts, R., Behrensmeyer, A.K., Beverly, E.J., King, J., Heil, C.W., Stockhecke, M., Brown, E.T., Moerman, J., deMenocal, P., Olorgesailie Drilling Project Scientific Team, 2019. Chronostratigraphic model of a high-resolution drill core record of the past million years from the Koora Basin, south Kenya Rift: Overcoming the difficulties of variable sedimentation rate and hiatuses. Quat. Sci. Rev. 215, 213–231. https://doi.org/10.1016/j.quascirev.2019.05.009

Deino, A.L., McBrearty, S., 2002. 40Ar/39Ar dating of the Kapthurin Formation, Baringo, Kenya. J. Hum. Evol. 42, 185–210. https://doi.org/10.1006/jhev.2001.0517

deMenocal, P.B., 2011. Climate and Human Evolution. Science 331, 540–542. https://doi.org/10.1126/science.1190683

deMenocal, P.B., 1995. Plio-Pleistocene African Climate. Science 270, 53–59. https://doi.org/10.1126/science.270.5233.53

deMenocal, P.B., Ortiz, J., Guilderson, T., Adkins, J., Sarnthein, M., Baker, L., Yarusinsky, M., 2000. Abrupt onset and termination of the African Humid Period: rapid climate responses to gradual insolation forcing. Quat. Sci. Rev. 19, 347–361. https://doi.org/10.1016/S0277-3791(99)00081-5

DeMets, C., Merkouriev, S., 2019. High-resolution reconstructions of South America plate motion relative to Africa, Antarctica and North America: 34 Ma to present. Geophys. J. Int. 217, 1821–1853. https://doi.org/10.1093/gji/ggz087

DeMets, C., Merkouriev, S., 2016. High-resolution estimates of Nubia–Somalia plate motion since 20 Ma from reconstructions of the Southwest Indian Ridge, Red Sea and Gulf of Aden. Geophys. J. Int. 207, 317–332. https://doi.org/10.1093/gji/ggw276

Dirks, P.H., Roberts, E.M., Hilbert-Wolf, H., Kramers, J.D., Hawks, J., Dosseto, A., Duval, M., Elliott, M., Evans, M., Grün, R., Hellstrom, J., Herries, A.I., Joannes-Boyau, R., Makhubela, T.V., Placzek, C.J., Robbins, J., Spandler, C., Wiersma, J., Woodhead, J., Berger, L.R., 2017. The age of Homo naledi and associated sediments in the Rising Star Cave, South Africa. eLife 6, e24231. https://doi.org/10.7554/eLife.24231

Doser, D.I., Yarwood, D.R., 1991. Strike-slip faulting in continental rifts: examples from Subukia, East Africa (1928), and other regions. Tectonophysics 197, 213–224. https://doi.org/10.1016/0040-1951(91)90042-Q

Drake, N.A., Blench, R.M., Armitage, S.J., Bristow, C.S., White, K.H., 2011. Ancient watercourses and biogeography of the Sahara explain the peopling of the desert. Proc. Natl. Acad. Sci. 108, 458–462. https://doi.org/10.1073/pnas.1012231108

Dühnforth, M., Bergner, A.G.N., Trauth, M.H., 2006. Early Holocene water budget of the Nakuru-Elmenteita basin, Central Kenya Rift. J. Paleolimnol. 36, 281–294. https://doi.org/10.1007/s10933-006-9003-z

Dunkelman, T.J., Karson, J.A., Rosendahl, B.R., 1988. Structural style of the Turkana Rift, Kenya. Geology 16, 258–261. https://doi.org/10.1130/0091-7613(1988)016<0258:SSOTTR>2.3.CO;2

Dunkelman, T.J., Rosendahl, B.R., Karson, J.A., 1989. Structure and stratigraphy of the Turkana rift from seismic reflection data. J. Afr. Earth Sci. Middle East 8, 489–510. https://doi.org/10.1016/S0899-5362(89)80041-7

Dunkley, P.N., Smith, M., Allen, D.J., Darling, W.G., 1993. The geothermal activity and geology of the northern sector of the Kenya Rift Valley (British Geological Survey Research Report No. SC/93/1). British Geological Survey, Keyworth, Nottingham. http://pubs.bgs.ac.uk/publications.html?pubID=B04104

Duringer, P., Schuster, M., Genise, J.F., Mackaye, H.T., Vignaud, P., Brunet, M., 2007. New termite trace fossils: Galleries, nests and fungus combs from the Chad basin of Africa (Upper Miocene–Lower Pliocene). Palaeogeogr. Palaeoclimatol. Palaeoecol. 251, 323–353. https://doi.org/10.1016/j.palaeo.2007.03.029

Dyson-Hudson, R., Smith, E.A., 1978. Human Territoriality: An Ecological Reassessment. Am. Anthropol. 80, 21–41. https://doi.org/10.1525/aa.1978.80.1.02a00020

Ebinger, C.J., 1989. Tectonic development of the western branch of the East African rift system. GSA Bull. 101, 885–903. https://doi.org/10/bd5pw2

Ebinger, C.J., Ayele, A., Keir, D., Rowland, J., Yirgu, G., Wright, T., Belachew, M., Hamling, I., 2010. Length and timescales of rift faulting and magma intrusion: the Afar rifting cycle from 2005 to Present. Annu. Rev. Earth Planet. Sci. 38, 439–466. https://doi.org/10.1146/annurev-earth-040809-152333

Ebinger, C.J., Keir, D., Bastow, I.D., Whaler, K., Hammond, J.O.S., Ayele, A., Miller, M.S., Tiberi, C., Hautot, S., 2017. Crustal structure of active deformation zones in Africa: implications for global crustal processes. Tectonics 36, 3298–3332. https://doi.org/10.1002/2017TC004526

Ebinger, C.J., Scholz, C.A., 2011. Continental Rift Basins: The East African Perspective, in: Busby, C., Azor, A. (Eds.), Tectonics of Sedimentary Basins. John Wiley & Sons, Ltd, pp. 183–208. https://doi.org/10.1002/9781444347166.ch9

Ebinger, C.J., Sleep, N.H., 1998. Cenozoic magmatism throughout east Africa resulting from impact of a single plume. Nature 395, 788–791. https://doi.org/10.1038/27417

Ebinger, C.J., Yemane, T., Harding, D.J., Tesfaye, S., Kelley, S., Rex, D.C., 2000. Rift deflection, migration, and propagation: Linkage of the Ethiopian and Eastern rifts, Africa. Geol. Soc. Am. Bull. 112, 163–176. https://doi.org/10.1130/0016-7606(2000)112<163:RDMAPL>2.0.CO;2

Elmer, K.R., Reggio, C., Wirth, T., Verheyen, E., Salzburger, W., Meyer, A., 2009. Pleistocene desiccation in East Africa bottlenecked but did not extirpate the adaptive radiation of Lake Victoria haplochromine cichlid fishes. Proc. Natl. Acad. Sci. 106, 13404–13409. https://doi.org/10.1073/pnas.0902299106

Faegri, K., Iversen, Jons., 1975. Textbook of Pollen Analysis, 3. Edition. ed. Blackwell Science Ltd, Oxford.

Farrand, W.R., Redding, R.W., Wolpoff, M.H., Wright III, H.T., 1976. An Archaeological Investigation on the Loboi Plain, Baringo District, Kenya, Technical Reports. Museum of Anthropology, University of Michigan, Ann Arbor, MI. https://doi.org/10.3998/mpub.11395769

Fleck, R.J., Sutter, J.F., Elliot, D.H., 1977. Interpretation of discordant 40Ar/39Ar age-spectra of mesozoic tholeiites from antarctica. Geochim. Cosmochim. Acta 41, 15–32. https://doi.org/10.1016/0016-7037(77)90184-3

Ford, A.G.P., Bullen, T.R., Pang, L., Genner, M.J., Bills, R., Flouri, T., Ngatunga, B.P., Rüber, L., Schliewen, U.K., Seehausen, O., Shechonge, A., Stiassny, M.L.J., Turner, G.F., Day, J.J., 2019. Molecular phylogeny of Oreochromis (Cichlidae: Oreochromini) reveals mito-nuclear discordance and multiple colonisation of

adverse aquatic environments. Mol. Phylogenet. Evol. 136, 215–226. https://doi.org/10.1016/j.ympev.2019.04.008

Ford, A.G.P., Dasmahapatra, K.K., Rüber, L., Gharbi, K., Cezard, T., Day, J.J., 2015. High levels of interspecific gene flow in an endemic cichlid fish adaptive radiation from an extreme lake environment. Mol. Ecol. 24, 3421–3440. https://doi.org/10.1111/mec.13247

Forman, S.L., Wright, D.K., Bloszies, C., 2014. Variations in water level for Lake Turkana in the past 8500 years near Mt. Porr, Kenya and the transition from the African Humid Period to Holocene aridity. Quat. Sci. Rev. 97, 84–101. https://doi.org/10.1016/j.quascirev.2014.05.005

Fredlund, G.G., Tieszen, L.L., 1997. Calibrating grass phytolith assemblages in climatic terms: Application to late Pleistocene assemblages from Kansas and Nebraska. Palaeogeogr. Palaeoclimatol. Palaeoecol. 136, 199–211. https://doi.org/10.1016/S0031-0182(97)00040-0

Fredlund, G.G., Tieszen, L.T., 1994. Modern Phytolith Assemblages from the North American Great Plains. J. Biogeogr. 21, 321–335. https://doi.org/10.2307/2845533

Friese, A., 2015. InSAR, structural analyses and dating of Paka volcanic products, Northern Kenya Rift. (Final Report). Federal Institute for Geosciences and Natural Resources (BGR), Hannover.

Fritz, S.C., Cumming, B.F., Gasse, F., Laird, K.R., 2010. Diatoms as indicators of hydrologic and climaticchange in saline lakes, in: Smol, J.P., Stoermer, E.F. (Eds.), The Diatoms: Applications for the Environmental and Earth Sciences. Cambridge University Press, Cambridge ; New York, pp. 186–208.

Fritz, S.C., Juggins, S., Battarbee, R.W., Engstrom, D.R., 1991. Reconstruction of past changes in salinity and climate using a diatom-based transfer function. Nature 352, 706–708. https://doi.org/10.1038/352706a0

Froese, R., Pauly, D., 2021. FishBase. Version (02/2021) [WWW Document]. URL www.fishbase.se (accessed 5.5.21).

Frostick, L.E., Reid, I., 1990. Structural control of sedimentation patterns and implication for the economic potential of the East African Rift basins. J. Afr. Earth Sci. Middle East 10, 307–318. https://doi.org/10.1016/0899-5362(90)90062-J

Fryer, G., Iles, T.D., 1972. The Cichlid Fishes of the Great Lakes of Africa: Their Biology and Evolution. Oliver and Boyd.

Garcin, Y., Junginger, A., Melnick, D., Olago, D.O., Strecker, M.R., Trauth, M.H., 2009. Late Pleistocene–Holocene rise and collapse of Lake Suguta, northern Kenya Rift. Quat. Sci. Rev. 28, 911–925. https://doi.org/10.1016/j.quascirev.2008.12.006

Garcin, Y., Melnick, D., Strecker, M.R., Olago, D., Tiercelin, J.-J., 2012. East African mid-Holocene wet–dry transition recorded in palaeo-shorelines of Lake Turkana, northern Kenya Rift. Earth Planet. Sci. Lett. 331–332, 322–334. https://doi.org/10.1016/j.epsl.2012.03.016

Garcin, Y., Schildgen, T.F., Torres Acosta, V., Melnick, D., Guillemoteau, J., Willenbring, J., Strecker, M.R., 2017. Short-lived increase in erosion during the African Humid Period: Evidence from the northern Kenya Rift. Earth Planet. Sci. Lett. 459, 58–69. https://doi.org/10.1016/j.epsl.2016.11.017

Gasse, F., 2000. Hydrological changes in the African tropics since the Last Glacial Maximum. Quat. Sci. Rev. 19, 189–211. https://doi.org/10.1016/S0277-3791(99)00061-X

Gasse, F., 1986. East African diatoms: taxonomy, ecological distribution, Bibliotheca Diatomologica. J. Cramer, Berlin.

Gasse, F., 1980. Les diatomées lacustres plio-pléistocenes du Gadeb (Éthiopie): systématique, paléoécologie, biostratigraphie. Revue algologique, Paris.

GBIF, 2021. The Global Biodiversity Information Facility [WWW Document]. URL https://www.gbif.org (accessed 5.5.21).

Genise, J.F., 2017. Ichnoentomology: Insect Traces in Soils and Paleosols, Topics in Geobiology. Springer International Publishing. https://doi.org/10.1007/978-3-319-28210-7

Gifford-Gonzalez, D., 1998. Early Pastoralists in East Africa: Ecological and Social Dimensions. J. Anthropol. Archaeol. 17, 166–200. https://doi.org/10.1006/jaar.1998.0322

Gifford-Gonzalez, D.P., 1985. Faunal Assemblages from Masai Gorge Rockshelter and Marula Rockshelter. Azania Archaeol. Res. Afr. 20, 69–88. https://doi.org/10.1080/00672708509511359

Goodier, S.A.M., Cotterill, F.P.D., O'Ryan, C., Skelton, P.H., Wit, M.J. de, 2011. Cryptic Diversity of African Tigerfish (Genus Hydrocynus) Reveals Palaeogeographic Signatures of Linked Neogene Geotectonic Events. PLOS ONE 6, e28775. https://doi.org/10.1371/journal.pone.0028775

Greenwood, P.H., 1980. Towards a phyletic classification of the "genus" Haplochromis (Pisces, Cichlidae) and related taxa. Part 2; the species from Lakes Victoria, Nabugabo, Edward, George and Kivu. Bull. Br. Mus. Nat. Hist. Zool. 39, 1–101. https://doi.org/10.5962/bhl.part.13268

Greenwood, P.H., 1973. A revision of the haplochromis and related species (pisces: cichlidae) from lake George Uganda. Bull. Br. Mus. Nat. Hist. Zool. 25, 141–242.

Greenwood, P.H., 1962. A revision of certain Barbus species (Pisces, Cyprinidae) from East, Central and South Africa. Bull. Br. Mus. Nat. Hist. Zool. 8, 151–208. https://doi.org/10.5962/p.118628

Griffiths, P.S., Gibson, I.L., 1980. The geology and petrology of the Hannington Trachyphonolite formation, Kenya Rift Valley. Lithos 13, 43–53. https://doi.org/10.1016/0024-4937(80)90060-2

Grimm, E.C., 1991. Tilia and Tilia-graph. Illinois State Museum, Springfield.

Grove, A.T., Street, F.A., Goudie, A.S., 1975. Former Lake Levels and Climatic Change in the Rift Valley of Southern Ethiopia. Geogr. J. 141, 177–194. https://doi.org/10.2307/1797205

Grubb, P., Sandrock, O., Kullmer, O., Kaiser, T.M., Schrenk, F., 1999. Relationships between Eastern and Southern African Mammal Faunas, in: Bromage, T.G., Schrenk, F. (Eds.), African Biogeography, Climate Change, and Human Evolution, Human Evolution Series. Oxford University Press, Oxford, New York, pp. 253–267.

Grün, R., Pike, A., McDermott, F., Eggins, S., Mortimer, G., Aubert, M., Kinsley, L., Joannes-Boyau, R., Rumsey, M., Denys, C., Brink, J., Clark, T., Stringer, C., 2020. Dating the skull from Broken Hill, Zambia, and its position in human evolution. Nature 580, 372–375. https://doi.org/10.1038/s41586-020-2165-4

Gudmundsson, A., 2012. Strengths and strain energies of volcanic edifices: implications for eruptions, collapse calderas, and landslides. Nat Hazards Earth Syst Sci 12, 2241–2258. https://doi.org/10.5194/nhess-12-2241-2012

Gudmundsson, A., 1995. Infrastructure and mechanics of volcanic systems in Iceland. J. Volcanol. Geotherm. Res. 64, 1–22. https://doi.org/10.1016/0377-0273(95)92782-Q

Guth, A., 2014. Maps of the Southern Kenya Rift. Geological Society of America. https://doi.org/10.1130/2014.DMCH016

Guth, A.L., 2015. Volcanic volumes associated with the Kenya Rift: recognition and correction of preservation biases. Geol. Soc. Lond. Spec. Publ. 420, SP420.3. https://doi.org/10.1144/SP420.3

Hackman, B.D., 1988. Geology of the Baringo-Laikipia area. (No. 104), Geological Survey of Kenya Report. Ministry of Environment and Natural Resources, Mines and Geological Department, Nairobi, Kenya.

Hamilton, A., 1982. Environmental History of East Africa: Study of the Quaternary. Academic Press Inc, London ; New York.

Hansen, S.E., Nyblade, A.A., Benoit, M.H., 2012. Mantle structure beneath Africa and Arabia from adaptively parameterized P-wave tomography: Implications for the origin of Cenozoic Afro-Arabian tectonism. Earth Planet. Sci. Lett. 319–320, 23–34. https://doi.org/10.1016/j.epsl.2011.12.023

7 References

Hardman, M., 2008. A new species of Chrysichthys (Siluriformes: Claroteidae) from Lake Turkana, Kenya. Proc. Acad. Nat. Sci. Phila. 157, 25–36. https://doi.org/10/d9gw7q

Harvey, C.P.D., Grove, A.T., 1982. A Prehistoric Source of the Nile. Geogr. J. 148, 327–336. https://doi.org/10.2307/633150

Haug, G.H., Strecker, M.R., 1995. Volcano-tectonic evolution of the Chyulu Hills and implications for the regional stress field in Kenya. Geology 23, 165–168. https://doi.org/10.1130/0091-7613(1995)023<0165:VTEOTC>2.3.CO;2

Hautot, S., Tarits, P., Whaler, K., Le Gall, B., Tiercelin, J.-J., Le Turdu, C., 2000. Deep structure of the Baringo Rift Basin (central Kenya) from three-dimensional magnetotelluric imaging: Implications for rift evolution. J. Geophys. Res. Solid Earth 105, 23493–23518. https://doi.org/10.1029/2000JB900213

Hempson, G.P., Archibald, S., Bond, W.J., Ellis, R.P., Grant, C.C., Kruger, F.J., Kruger, L.M., Moxley, C., Owen-Smith, N., Peel, M.J.S., Smit, I.P.J., Vickers, K.J., 2015. Ecology of grazing lawns in Africa. Biol. Rev. 90, 979–994. https://doi.org/10.1111/brv.12145

Henry, W.J., Mechie, J., Maguire, P.K.H., Khan, M.A., Prodehl, C., Keller, G.R., Patel, J., 1990. A Seismic Investigation of the Kenya Rift Valley. Geophys. J. Int. 100, 107–130. https://doi.org/10.1111/j.1365-246X.1990.tb04572.x

Hetzel, R., Strecker, M.R., 1994. Late Mozambique Belt structures in western Kenya and their influence on the evolution of the Cenozoic Kenya Rift. J. Struct. Geol. 16, 189–201. https://doi.org/10.1016/0191-8141(94)90104-X

Hillaire-Marcel, C., Carro, O., Casanova, J., 1986. 14C and ThU dating of Pleistocene and Holocene stromatolites from East African paleolakes. Quat. Res. 25, 312–329. https://doi.org/10.1016/0033-5894(86)90004-9

Hollnack, D., Stangl, R., 1998. The seismicity related to the southern part of the Kenya Rift. J. Afr. Earth Sci., Tectonics, Sedimentation and Volcanism in the East African Rift System 26, 477–495. https://doi.org/10.1016/S0899-5362(98)00027-X

Holohan, E.P., Walter, T.R., Schöpfer, M.P.J., Walsh, J.J., van Wyk de Vries, B., Troll, V.R., 2013. Origins of oblique-slip faulting during caldera subsidence. J. Geophys. Res. Solid Earth 118, 1778–1794. https://doi.org/10.1002/jgrb.50057

Hopwood, A.T., 1931. Appendix C. Preliminary report on the fossils mammals, in: The Stone Age Cultures of Kenya Colony. Cambridge University Press, pp. 271–275.

Hyodo, M., Bradák, B., Okada, M., Katoh, S., Kitaba, I., Dettman, D.L., Hayashi, H., Kumazawa, K., Hirose, K., Kazaoka, O., Shikoku, K., Kitamura, A., 2017. Millennial-scale northern Hemisphere Atlantic-Pacific climate teleconnections in the earliest Middle Pleistocene. Sci. Rep. 7, 10036. https://doi.org/10.1038/s41598-017-10552-2

Ibs-von Seht, M., Blumenstein, S., Wagner, R., Hollnack, D., Wohlenberg, J., 2001. Seismicity, seismotectonics and crustal structure of the southern Kenya Rift—new data from the Lake Magadi area. Geophys. J. Int. 146, 439–453. https://doi.org/10.1046/j.0956-540x.2001.01464.x

Isaac, G.L., 1978. The Olorgesailie Formation: Stratigraphy, tectonics and the palaeogeographic context of the Middle Pleistocene archaeological sites. Geol. Soc. Lond. Spec. Publ. 6, 173–206. https://doi.org/10.1144/GSL.SP.1978.006.01.15

Isaac, G.L., Merrick, H.V., Nelson, C.M., 1972. Stratigraphic and archaeological studies in the Lake Nakuru Basin. Palaeoecol. Afr. 6, 225–232.

Isenburg, M., 2016. LAStools - efficient LiDAR processing software. Version 160910 (academic). rapidlasso GmbH. http://rapidlasso.com/LAStools.

Ishizuka, O., 1998. Vertical and horizontal variations of the fast neutron flux in a single irradiation capsule and their significance in the laser-heating 40Ar/39Ar analysis: Case study for the hydraulic rabbit facility of the JMTR reactor, Japan. Geochem. J. 32, 243–252. https://doi.org/10.2343/geochemj.32.243

IUCN, 2020. The International Union for Conservation of Nature's Red List of Threatened Species. Version 2020-3 [WWW Document]. URL https://www.iucnredlist.org (accessed 3.11.20).

James, M.R., Robson, S., d'Oleire-Oltmanns, S., Niethammer, U., 2017. Optimising UAV topographic surveys processed with structure-from-motion: Ground control quality, quantity and bundle adjustment. Geomorphology 280, 51–66. https://doi.org/10.1016/j.geomorph.2016.11.021

Jenkins, C.N., Pimm, S.L., Joppa, L.N., 2013. Global patterns of terrestrial vertebrate diversity and conservation. Proc. Natl. Acad. Sci. 110, E2602–E2610. https://doi.org/10.1073/pnas.1302251110

Jones, W.B., Leat, P.T., 1985. Discussion on the geological evolution of the trachytic caldera volcano Menengai, Kenya Rift Valley. J. Geol. Soc. 142, 711–712. https://doi.org/10.1144/gsjgs.142.4.0711

Jones, W.B., Lippard, S.J., 1979. New age determinations and the geology of the Kenya Rift-Kavirondo Rift junction, W Kenya. J. Geol. Soc. 136, 693–704. https://doi.org/10.1144/gsjgs.136.6.0693

Junginger, A., Roller, S., Olaka, L.A., Trauth, M.H., 2014. The effects of solar irradiation changes on the migration of the Congo Air Boundary and water levels of paleo-Lake Suguta, Northern Kenya Rift, during the African Humid Period (15–5 ka BP). Palaeogeogr. Palaeoclimatol. Palaeoecol. 396, 1–16. https://doi.org/10.1016/j.palaeo.2013.12.007

Junginger, A., Trauth, M.H., 2013. Hydrological constraints of paleo-Lake Suguta in the Northern Kenya Rift during the African Humid Period (15–5 ka BP). Glob. Planet. Change 111, 174–188. https://doi.org/10.1016/j.gloplacha.2013.09.005

Kanda, I., Fujimitsu, Y., Nishijima, J., 2019. Geological structures controlling the placement and geometry of heat sources within the Menengai geothermal field, Kenya as evidenced by gravity study. Geothermics 79, 67–81. https://doi.org/10.1016/j.geothermics.2018.12.012

Karingithi, C.W., Arnórsson, S., Grönvold, K., 2010. Processes controlling aquifer fluid compositions in the Olkaria geothermal system, Kenya. J. Volcanol. Geotherm. Res. 196, 57–76. https://doi.org/10.1016/j.jvolgeores.2010.07.008

Karson, J.A., Curtis, P.C., 1989. Tectonic and magmatic processes in the Eastern Branch of the East African Rift and implications for magmatically active continental rifts. J. Afr. Earth Sci. Middle East 8, 431–453. https://doi.org/10.1016/S0899-5362(89)80037-5

Katz, O., Cabanes, D., Weiner, S., Maeir, A.M., Boaretto, E., Shahack-Gross, R., 2010. Rapid phytolith extraction for analysis of phytolith concentrations and assemblages during an excavation: an application at Tell es-Safi/Gath, Israel. J. Archaeol. Sci. 37, 1557–1563. https://doi.org/10.1016/j.jas.2010.01.016

Keir, D., Bastow, I.D., Corti, G., Mazzarini, F., Rooney, T.O., 2015. The origin of along-rift variations in faulting and magmatism in the Ethiopian Rift. Tectonics 34, 2014TC003698. https://doi.org/10.1002/2014TC003698

Keir, D., Hamling, I.J., Ayele, A., Calais, E., Ebinger, C.J., Wright, T.J., Jacques, E., Mohamed, K., Hammond, J.O.S., Belachew, M., Baker, E., Rowland, J.V., Lewi, E., Bennati, L., 2009. Evidence for focused magmatic accretion at segment centers from lateral dike injections captured beneath the Red Sea rift in Afar. Geology 37, 59–62. https://doi.org/10.1130/G25147A.1

Kellogg, E.A., 2013. C4 photosynthesis. Curr. Biol. 23, R594–R599. https://doi.org/10.1016/j.cub.2013.04.066

Kelly, R.L., 2013. The Lifeways of Hunter-Gatherers: The Foraging Spectrum, 2. Edition. ed. Cambridge University Press, Cambridge.

Kendall, R.L., 1969. An Ecological History of the Lake Victoria Basin. Ecol. Monogr. 39, 121–176. https://doi.org/10.2307/1950740

Keranen, K., Klemperer, S.L., Gloaguen, R., Group, E.W., 2004. Three-dimensional seismic imaging of a protoridge axis in the Main Ethiopian rift. Geology 32, 949–952. https://doi.org/10.1130/G20737.1

Kim, Y.-S., Sanderson, D.J., 2006. Structural similarity and variety at the tips in a wide range of strike–slip faults: a review. Terra Nova 18, 330–344. https://doi.org/10.1111/j.1365-3121.2006.00697.x

7 References

King, B.C., Chapman, G.R., Robson, D.A., McConnell, R.B., 1972. Volcanism of the Kenya Rift Valley [and Discussion]. Philos. Trans. R. Soc. Lond. Math. Phys. Eng. Sci. 271, 185–208. https://doi.org/10.1098/rsta.1972.0006

Kingdon, J., 2015. The Kingdon Field Guide to African Mammals, Second Edition. ed. Bloomsbury Publishing.

Kingdon, J., 1982. East African Mammals. Volume III, Part C: Bovids. Academic Press.

Kingdon, J., 1981. Where have the colonists come from? A zoogeographical examination of some mammalian isolates in eastern Africa. Afr. J. Ecol. 19, 115–124. https://doi.org/10.1111/j.1365-2028.1981.tb00656.x

Kingdon, J., 1979. East African Mammals. Volume III, Part B: Large Mammals. Academic Press.

Kingdon, J., 1977. East African Mammals. Volume III, Part A: Carnivores. Academic Press.

Kingdon, J., 1971. East African Mammals, Volume I. Academic Press, London.

Kingdon, J., Happold, D., Hoffmann, M., Butynski, T., Happold, M., Kalina, J. (Eds.), 2013. Mammals of Africa: Volume I: Introductory Chapters and Afrotheria. Bloomsbury Natural History, London. https://doi.org/10.5040/9781472926913

Kinyanjui, R., 2018. Phytolith analysed to Compare Changes in Vegetation Structure of Koobi Fora and Olorgesailie Basins through the Mid-Pleistocene-Holocene Periods (PhD thesis). University of Witwatersrand, Johannesburg, South Africa. https://t.co/JxhDDR5olF

Kinyanjui, R., 2012. Phytolith Analysis as a Palaeoecological Tool for Reconstructing Mid-to Late-Pleistocene Environments in the Olorgesailie Basin, Kenya (MSc thesis). University of Cape Town, Cape Town, South Africa.

Kirschvink, J.L., 1980. The least-squares line and plane and the analysis of palaeomagnetic data. Geophys. J. Int. 62, 699–718. https://doi.org/10.1111/j.1365-246X.1980.tb02601.x

Knowles, L.L., Maddison, W.P., 2002. Statistical phylogeography. Mol. Ecol. 11, 2623–2635. https://doi.org/10.1046/j.1365-294x.2002.01637.x

Kombe, E.Y., Muguthu, J., 2019. Geothermal Energy Development in East Africa: Barriers and Strategies. J. Energy Res. Rev. 1–6. https://doi.org/10.9734/jenrr/2019/v2i129722

KRISP Working Group, 1991. Large-scale variation in lithospheric structure along and across the Kenya rift. Nature 354, 223. https://doi.org/10.1038/354223a0

KRISP Working Group, 1987. Structure of the Kenya rift from seismic refraction. Nature 325, 239. https://doi.org/10.1038/325239a0

Kübler, S., Friedrich, A.M., Gold, R.D., Strecker, M.R., 2018. Historical coseismic surface deformation of fluvial gravel deposits, Schafberg fault, Lower Rhine Graben, Germany. Int. J. Earth Sci. 107, 571–585. https://doi.org/10.1007/s00531-017-1510-9

Kuntz, M.A., Covington, H.R., Schorr, L.J., 1992. An overview of basaltic volcanism of the eastern Snake River Plain, Idaho, in: Link, P.K., Kuntz, M.A., Platt, L.B. (Eds.), Regional Geology of Eastern Idaho and Western Wyoming, Geological Society of America Memoir. Geological Society of America, Boulder, Colorado, pp. 227–267.

Kutzbach, J.E., 1981. Monsoon Climate of the Early Holocene: Climate Experiment with the Earth's Orbital Parameters for 9000 Years Ago. Science 214, 59–61. https://doi.org/10.1126/science.214.4516.59

Kutzbach, J.E., Guan, J., He, F., Cohen, A.S., Orland, I.J., Chen, G., 2020. African climate response to orbital and glacial forcing in 140,000-y simulation with implications for early modern human environments. Proc. Natl. Acad. Sci. 117, 2255–2264. https://doi.org/10.1073/pnas.1917673117

Kutzbach, J.E., Street-Perrott, F.A., 1985. Milankovitch forcing of fluctuations in the level of tropical lakes from 18 to 0 kyr BP. Nature 317, 130–134. https://doi.org/10.1038/317130a0

Lamarche, G., Barnes, P.M., Bull, J.M., 2006. Faulting and extension rate over the last 20,000 years in the offshore Whakatane Graben, New Zealand continental shelf. Tectonics 25. https://doi.org/10.1029/2005TC001886

Laskar, J., Robutel, P., Joutel, F., Gastineau, M., Correia, A.C.M., Levrard, B., 2004. A long-term numerical solution for the insolation quantities of the Earth. Astron. Astrophys. 428, 261–285. https://doi.org/10.1051/0004-6361:20041335

Leat, P.T., 1991. Volcanological development of the Nakuru area of the Kenya rift valley. J. Afr. Earth Sci. Middle East 13, 483–498. https://doi.org/10.1016/0899-5362(91)90111-B

Leat, P.T., 1985. Interaction of a rheomorphic peralkaline ash-flow tuff and underlying deposits, Menengai volcano, Kenya. J. Volcanol. Geotherm. Res. 26, 131–145. https://doi.org/10.1016/0377-0273(85)90049-6

Leat, P.T., 1984. Geological evolution of the trachytic caldera volcano Menengai, Kenya Rift Valley. J. Geol. Soc. 141, 1057–1069. https://doi.org/10.1144/gsjgs.141.6.1057

Leat, P.T., 1983. The structural and geochemical evolution of Menengai Caldera volcano, Kenya rift valley. (PhD Thesis). University of Lancaster.

Leat, P.T., MacDonald, R., Smith, R.L., 1984. Geochemical evolution of the Menengai Caldera Volcano, Kenya. J. Geophys. Res. Solid Earth 89, 8571–8592. https://doi.org/10.1029/JB089iB10p08571

Lee, H., Muirhead, J.D., Fischer, T.P., Ebinger, C.J., Kattenhorn, S.A., Sharp, Z.D., Kianji, G., 2016. Massive and prolonged deep carbon emissions associated with continental rifting. Nat. Geosci. 9, 145–149. https://doi.org/10.1038/ngeo2622

Lehner, B., Döll, P., 2004. Development and validation of a global database of lakes, reservoirs and wetlands. J. Hydrol. 296, 1–22. https://doi.org/10.1016/j.jhydrol.2004.03.028

Lévêque, C., Paugy, D., Teugels, G.G., 1991. Annotated check-list of the freshwater fishes of the Nilo-sudan river basins, in Africa. Rev. Hydrobiol. Trop. 24, 131–154.

Levin, N.E., Zipser, E.J., Cerling, T.E., 2009. Isotopic composition of waters from Ethiopia and Kenya: Insights into moisture sources for eastern Africa. J. Geophys. Res. Atmospheres 114, D23306. https://doi.org/10.1029/2009JD012166

Lichoro, C.M., Árnason, K., Cumming, W., 2019. Joint interpretation of gravity and resistivity data from the Northern Kenya volcanic rift zone: Structural and geothermal significance. Geothermics 77, 139–150. https://doi.org/10.1016/j.geothermics.2018.09.006

Lindsay, J.M., de Silva, S., Trumbull, R., Emmermann, R., Wemmer, K., 2001. La Pacana caldera, N. Chile: a re-evaluation of the stratigraphy and volcanology of one of the world's largest resurgent calderas. J. Volcanol. Geotherm. Res. 106, 145–173. https://doi.org/10.1016/S0377-0273(00)00270-5

Lippard, S.J., 1972. Stratigraphy and structure of the Elgeyo escarpment southern Kamasia Hills and adjoining regions, Rift Valley Province, Kenya (Ph.D.). Royal Holloway, University of London.

Lippitsch, E., 2003. Redescription of Haplochromis' nubilus (Teleostei: Cichlidae), with description of two new species. Ichthyol. Explor. Freshw. 14, 85–95.

Lloyd, R., Biggs, J., Wilks, M., Nowacki, A., Kendall, J.-M., Ayele, A., Lewi, E., Eysteinsson, H., 2018. Evidence for cross rift structural controls on deformation and seismicity at a continental rift caldera. Earth Planet. Sci. Lett. 487, 190–200. https://doi.org/10.1016/j.epsl.2018.01.037

Lupien, R.L., Russell, J.M., Feibel, C., Beck, C., Castañeda, I., Deino, A., Cohen, A.S., 2018. A leaf wax biomarker record of early Pleistocene hydroclimate from West Turkana, Kenya. Quat. Sci. Rev. 186, 225–235. https://doi.org/10.1016/j.quascirev.2018.03.012

MacArthur, R.H., Wilson, E.O., 1967. The Theory of Island Biogeography. Princeton University Press.

Macdonald, R., 2002. Magmatism of the Kenya Rift Valley: a review. Earth Environ. Sci. Trans. R. Soc. Edinb. 93, 239–253. https://doi.org/10.1017/S0263593300000420

7 References

Macdonald, R., Bagiński, B., 2009. The central Kenya peralkaline province: a unique assemblage of magmatic systems. Mineral. Mag. 73, 1–16. https://doi.org/10.1180/minmag.2009.073.1.1

Macdonald, R., Bagiński, B., Leat, P.T., White, J.C., Dzierżanowski, P., 2011. Mineral stability in peralkaline silicic rocks: Information from trachytes of the Menengai volcano, Kenya. Lithos 125, 553–568. https://doi.org/10.1016/j.lithos.2011.03.011

Macdonald, R., Bagiński, B., Upton, B.G.J., 2014. The volcano–pluton interface; The Longonot (Kenya) and Kûngnât (Greenland) peralkaline complexes. Lithos 196–197, 232–241. https://doi.org/10.1016/j.lithos.2014.03.009

Macdonald, R., Davies, G.R., Bliss, C.M., Leat, P.T., Bailey, D.K., Smith, R.L., 1987. Geochemistry of High-silica Peralkaline Rhyolites, Naivasha, Kenya Rift Valley. J. Petrol. 28, 979–1008. https://doi.org/10.1093/petrology/28.6.979

Macdonald, R., Davies, G.R., Upton, B.G.J., Dunkley, P.N., Smith, M., Leat, P.T., 1995. Petrogenesis of Silali volcano, Gregory Rift, Kenya. J. Geol. Soc. 152, 703–720. https://doi.org/10.1144/gsjgs.152.4.0703

Macdonald, R., Navarro, J.M., Upton, B.G.J., Davies, G.R., 1994. Strong compositional zonation in peralkaline magma: Menengai, Kenya Rift Valley. J. Volcanol. Geotherm. Res. 60, 301–325. https://doi.org/10.1016/0377-0273(94)90057-4

Madella, M., Alexandre, A., Ball, T., ICPN Working Group, 2005. International Code for Phytolith Nomenclature 1.0. Ann. Bot. 96, 253–260. https://doi.org/10.1093/aob/mci172

Maetens, H., Steenberge, M.V., Snoeks, J., Decru, E., 2020. Revalidation of Enteromius alberti and presence of Enteromius cf. mimus (Cypriniformes: Cyprinidae) in the Lake Edward system, East Africa. Eur. J. Taxon. https://doi.org/10.5852/ejt.2020.700

Maitima, J.M., 1991. Vegetation response to climatic change in central Rift Valley, Kenya. Quat. Res. 35, 234–245. https://doi.org/10.1016/0033-5894(91)90070-L

Marean, C.W., 1992. Hunter to herder: large mammal remains from the hunter-gatherer occupation at Enkapune Ya Muto rock-shelter, Central Rift, Kenya. Afr Archaeol Rev 10, 65–127. https://doi.org/10.1007/BF01117697

Mariita, N.O., Keller, G.R., 2007. An integrated geophysical study of the northern Kenya rift. J. Afr. Earth Sci., The East African Rift System: Dynamics, Evolution and Environment 48, 80–94. https://doi.org/10.1016/j.jafrearsci.2006.05.008

Marlowe, F.W., 2005. Hunter-gatherers and human evolution. Evol. Anthropol. Issues News Rev. 14, 54–67. https://doi.org/10.1002/evan.20046

Marrett, R., Allmendinger, R.W., 1990. Kinematic analysis of fault-slip data. J. Struct. Geol. 12, 973–986. https://doi.org/10.1016/0191-8141(90)90093-E

Marrett, R., Peacock, D.C.P., 1999. Strain and stress. J. Struct. Geol. 21, 1057–1063. https://doi.org/10.1016/S0191-8141(99)00020-6

Marsden, M., 1979. Origin and Evolution of the Pleistocene Olorgesailie Lake Series: Kenya Rift Valley (PhD thesis). McGill University, Montreal, Canada.

Marti, J., Ablay, G.J., Redshaw, L.T., Sparks, R.S.J., 1994. Experimental studies of collapse calderas. J. Geol. Soc. 151, 919–929. https://doi.org/10.1144/gsjgs.151.6.0919

Mathworks, 2020. MATLAB Release 2020a. The MathWorks, Inc., Natick, Massachusetts, United States.

Mathworks, 2018. MATLAB Release 2018a. The MathWorks, Inc., Natick, Massachusetts, United States.

Mboya, B., 1983. The genesis and tectonics of the N.E. Nyanza rift valley, Kenya. J. Afr. Earth Sci. 1983, Geology for Development: Mineral Resources and Exploration Potential of Africa—GSA'82 1, 315–320. https://doi.org/10.1016/S0731-7247(83)80016-0

Mcbrearty, S., Brooks, A.S., 2000. The revolution that wasn't: a new interpretation of the origin of modern human behavior. J. Hum. Evol. 39, 453–563. https://doi.org/10.1006/jhev.2000.0435

McCall, G.J.H., 1999. Silali Volcano, Baringo, Kenya: sedimentary structures at the western fringe, in: Andrews, P., Banham, P. (Eds.), Late Cenozoic Environments and Hominid Evolution: A Tribute to Bill Bishop. Geological Society, London.

McCall, G.J.H., 1967. Geology of the Nakuru-Thompson's Falls - Lake Hannington area. Degree sheet No. 35 SW quarter and 43 NW quarter (No. 78), Geological Survey of Kenya Report. Geological Survey of Kenya.

McCalpin, J.P., 2005. Late Quaternary activity of the Pajarito fault, Rio Grande rift of northern New Mexico, USA. Tectonophysics, Paleoseismology 408, 213–236. https://doi.org/10.1016/j.tecto.2005.05.038

McConnell, R.B., 1972. Geological Development of the Rift System of Eastern Africa. Geol. Soc. Am. Bull. 83, 2549–2572. https://doi.org/10.1130/0016-7606(1972)83[2549:GDOTRS]2.0.CO;2

McKenzie, D.P., Davies, D., Molnar, P., 1970. Plate Tectonics of the Red Sea and East Africa. Nature 226, 243–248. https://doi.org/10.1038/226243a0

McNaughton, S.J., 1985. Ecology of a Grazing Ecosystem: The Serengeti. Ecol. Monogr. 55, 259–294. https://doi.org/10.2307/1942578

Medynski, S., Pik, R., Burnard, P., Dumont, S., Grandin, R., Williams, A., Blard, P.-H., Schimmelpfennig, I., Vye-Brown, C., France, L., Ayalew, D., Benedetti, L., Yirgu, G., 2016. Magmatic cycles pace tectonic and morphological expression of rifting (Afar depression, Ethiopia). Earth Planet. Sci. Lett. 446, 77–88. https://doi.org/10.1016/j.epsl.2016.04.014

Medynski, S., Pik, R., Burnard, P., Williams, A., Vye-Brown, C., Ferguson, D., Blard, P.-H., France, L., Yirgu, G., Seid, J.I., Ayalew, D., Calvert, A., 2013. Controls on magmatic cycles and development of rift topography of the Manda Hararo segment (Afar, Ethiopia): Insights from cosmogenic 3He investigation of landscape evolution. Earth Planet. Sci. Lett. 367, 133–145. https://doi.org/10.1016/j.epsl.2013.02.006

Melnick, D., Folguera, A., Ramos, V.A., 2006. Structural control on arc volcanism: The Caviahue–Copahue complex, Central to Patagonian Andes transition (38°S). J. South Am. Earth Sci. 22, 66–88. https://doi.org/10.1016/j.jsames.2006.08.008

Melnick, D., Garcin, Y., Quinteros, J., Strecker, M.R., Olago, D., Tiercelin, J.-J., 2012. Steady rifting in northern Kenya inferred from deformed Holocene lake shorelines of the Suguta and Turkana basins. Earth Planet. Sci. Lett. 331–332, 335–346. https://doi.org/10.1016/j.epsl.2012.03.007

Mercader, J., Astudillo, F., Barkworth, M., Bennett, T., Esselmont, C., Kinyanjui, R., Grossman, D.L., Simpson, S., Walde, D., 2010. Poaceae phytoliths from the Niassa Rift, Mozambique. J. Archaeol. Sci. 37, 1953–1967. https://doi.org/10.1016/j.jas.2010.03.001

Mercader, J., Bennett, T., Esselmont, C., Simpson, S., Walde, D., 2009. Phytoliths in woody plants from the Miombo woodlands of Mozambique. Ann. Bot. 104, 91–113. https://doi.org/10.1093/aob/mcp097

Meyers, P.A., Teranes, J.L., 2001. Sediment Organic Matter, in: Last, W.M., Smol, J.P. (Eds.), Tracking Environmental Change Using Lake Sediments: Physical and Geochemical Methods, Developments in Paleoenvironmental Research. Kluwer Academic Publishers, Dordrecht, pp. 239–269. https://doi.org/10.1007/0-306-47670-3_9

Mibei, G., Bali, E., Geirsson, H., Guðfinnsson, G.H., Harðarson, B.S., Franzson, H., 2021a. Partial melt generation and evolution of magma reservoir conditions at the Paka volcanic complex in Kenya: Constraints from geochemistry, petrology and geophysics. Lithos 106385. https://doi.org/10.1016/j.lithos.2021.106385

Mibei, G., Harðarson, B.S., Franzson, H., Bali, E., Geirsson, H., Guðfinnsson, G.H., 2021b. Eruptive history and volcano-tectonic evolution of Paka volcanic complex in the northern Kenya rift: Insights into the geothermal heat source. J. Afr. Earth Sci. 173, 103951. https://doi.org/10.1016/j.jafrearsci.2020.103951

Ministry of Energy of Kenya, 1987. Geological map of Kenya, with structural contours.

Mittermeier, R.A., Gil, P.R., Hoffman, M., Pilgrim, J.D., Brooks, T.M., Mittermeier, C.G., Lamoreux, J., Da Fonesca, G.A.B., 2004. Hotspots Revisited: Earth's Biologically Richest and Most Endangered Terrestrial Ecoregions. CEMEX.

Moore, D.M., Reynolds Jr, R.C., 1997. X-Ray Diffraction and the Identification and Analysis of Clay Minerals, 2nd Edition. ed. Oxford University Press, Oxford ; New York.

Morley, C.K., Wescott, W.A., Stone, D.M., Harper, R.M., Wigger, S.T., Karanja, F.M., 1992. Tectonic evolution of the northern Kenyan Rift. J. Geol. Soc. 149, 333–348. https://doi.org/10.1144/gsjgs.149.3.0333

Morrissey, A., Scholz, C.A., 2014. Paleohydrology of Lake Turkana and its influence on the Nile River system. Palaeogeogr. Palaeoclimatol. Palaeoecol. 403, 88–100. https://doi.org/10.1016/j.palaeo.2014.03.029

Mortimer, E., Paton, D.A., Scholz, C.A., Strecker, M.R., Blisniuk, P., 2007. Orthogonal to oblique rifting: effect of rift basin orientation in the evolution of the North basin, Malawi Rift, East Africa. Basin Res. 19, 393–407. https://doi.org/10.1111/j.1365-2117.2007.00332.x

Moucha, R., Forte, A.M., 2011. Changes in African topography driven by mantle convection. Nat. Geosci. 4, 707–712. https://doi.org/10.1038/ngeo1235

Mouslopoulou, V., Nicol, A., Walsh, J.J., Begg, J.G., Townsend, D.B., Hristopulos, D.T., 2012. Fault-slip accumulation in an active rift over thousands to millions of years and the importance of paleoearthquake sampling. J. Struct. Geol. 36, 71–80. https://doi.org/10.1016/j.jsg.2011.11.010

Mugisha, F., Ebinger, C.J., Strecker, M., Pope, D., 1997. Two-stage rifting in the Kenya rift: implications for half-graben models. Tectonophysics 278, 63–81. https://doi.org/10.1016/S0040-1951(97)00095-4

Muirhead, J.D., Kattenhorn, S.A., 2018. Activation of preexisting transverse structures in an evolving magmatic rift in East Africa. J. Struct. Geol. 106, 1–18. https://doi.org/10.1016/j.jsg.2017.11.004

Muirhead, J.D., Kattenhorn, S.A., Le Corvec, N., 2015. Varying styles of magmatic strain accommodation across the East African Rift. Geochem. Geophys. Geosystems 16, 2775–2795. https://doi.org/10.1002/2015GC005918

Muirhead, J.D., Kattenhorn, S.A., Lee, H., Mana, S., Turrin, B.D., Fischer, T.P., Kianji, G., Dindi, E., Stamps, D.S., 2016. Evolution of upper crustal faulting assisted by magmatic volatile release during early-stage continental rift development in the East African Rift. Geosphere 12, 1670–1700. https://doi.org/10.1130/GES01375.1

Muiruri, V., Owen, R.B., Potts, R., Deino, A.L., Behrensmeyer, A.K., Riedl, S., Rabideaux, N., Beverly, E.J., Renaut, R.W., Moerman, J.W., Deocampo, D., Faith, J.T., Noren, A., Cohen, A.S., Shannon, K.B., Dommain, R., 2021. Quaternary diatoms and palaeoenvironments of the Koora Plain, southern Kenya rift. Quat. Sci. Rev. 267, 107106. https://doi.org/10.1016/j.quascirev.2021.107106

Mukasa, S.B., Wilson, A.H., Carlson, R.W., 1998. A multielement geochronologic study of the Great Dyke, Zimbabwe: significance of the robust and reset ages. Earth Planet. Sci. Lett. 164, 353–369. https://doi.org/10.1016/S0012-821X(98)00228-3

Mulwa, J.K., Kimata, F., Suzuki, S., Kuria, Z.N., 2014. The seismicity in Kenya (East Africa) for the period 1906–2010: A review. J. Afr. Earth Sci. 89, 72–78. https://doi.org/10.1016/j.jafrearsci.2013.10.008

Munro, M.A., Blenkinsop, T.G., 2012. MARD—A moving average rose diagram application for the geosciences. Comput. Geosci. 49, 112–120. https://doi.org/10.1016/j.cageo.2012.07.012

Nagy, B., Watters, B., 2018. Distribution and habitat conditions of Nothobranchius fishes in Uganda. J. Am. Killifish Assoc. 51, 176–192.

Nagy, B., Watters, B.R., van der Merwe, P.D.W., Cotterill, F.P.D., Bellstedt, D.U., 2020. Review of the Nothobranchius ugandensis species group from the inland plateau of eastern Africa with descriptions of six new species (Teleostei: Nothobranchiidae). Ichthyol. Explor. Freshw. 30, 21–73. https://doi.org/10.23788/IEF-1129

Ndiwa, T.C., Nyingi, D.W., Agnese, J.-F., 2014. An Important Natural Genetic Resource of Oreochromis niloticus (Linnaeus, 1758) Threatened by Aquaculture Activities in Loboi Drainage, Kenya. PLOS ONE 9, e106972. https://doi.org/10.1371/journal.pone.0106972

Neumann, K., Fahmy, A., Lespez, L., Ballouche, A., Huysecom, E., 2009. The Early Holocene palaeoenvironment of Ounjougou (Mali): Phytoliths in a multiproxy context. Palaeogeogr. Palaeoclimatol. Palaeoecol. 276, 87–106. https://doi.org/10.1016/j.palaeo.2009.03.001

Nex, F., Remondino, F., 2013. UAV for 3D mapping applications: a review. Appl. Geomat. 6, 1–15. https://doi.org/10.1007/s12518-013-0120-x

Nicholson, S.E., 2017. Climate and climatic variability of rainfall over eastern Africa. Rev. Geophys. https://doi.org/10.1002/2016RG000544

Nielson, D.L., Hulen, J.B., 1984. Internal geology and evolution of the Redondo Dome, Valles Caldera, New Mexico. J. Geophys. Res. Solid Earth 89, 8695–8711. https://doi.org/10.1029/JB089iB10p08695

Nomade, S., Renne, P.R., Vogel, N., Deino, A.L., Sharp, W.D., Becker, T.A., Jaouni, A.R., Mundil, R., 2005. Alder Creek sanidine (ACs-2): A Quaternary $^{40}Ar/^{39}Ar$ dating standard tied to the Cobb Mountain geomagnetic event. Chem. Geol. 218, 315–338. https://doi.org/10.1016/j.chemgeo.2005.01.005

Novello, A., Barboni, D., Berti-Equille, L., Mazur, J.-C., Poilecot, P., Vignaud, P., 2012. Phytolith signal of aquatic plants and soils in Chad, Central Africa. Rev. Palaeobot. Palynol. 178, 43–58. https://doi.org/10.1016/j.revpalbo.2012.03.010

Nyblade, A.A., Pollack, H.N., Jones, D.L., Podmore, F., Mushayandebvu, M., 1990. Terrestrial heat flow in east and southern Africa. J. Geophys. Res. Solid Earth 95, 17371–17384. https://doi.org/10.1029/JB095iB11p17371

Odada, E.O., Olago, D.O., Bugenyi, F., Kulindwa, K., Karimumuryango, J., West, K., Ntiba, M., Wandiga, S., Aloo-Obudho, P., Achola, P., 2003. Environmental assessment of the East African Rift Valley lakes. Aquat. Sci. 65, 254–271. https://doi.org/10.1007/s00027-003-0638-9

Ogg, J.G., 2012. Geomagnetic Polarity Time Scale, in: Gradstein, F.M., Ogg, James G., Schmitz, M.D., Ogg, G.M. (Eds.), The Geologic Time Scale. Elsevier, Boston, pp. 85–113. https://doi.org/10.1016/B978-0-444-59425-9.00005-6

Olaka, L.A., Odada, E.O., Trauth, M.H., Olago, D.O., 2010. The sensitivity of East African rift lakes to climate fluctuations. J. Paleolimnol. 44, 629–644. https://doi.org/10.1007/s10933-010-9442-4

Olaka, L.A., Wilke, F.D.H., Olago, D.O., Odada, E.O., Mulch, A., Musolff, A., 2016. Groundwater fluoride enrichment in an active rift setting: Central Kenya Rift case study. Sci. Total Environ. 545–546, 641–653. https://doi.org/10.1016/j.scitotenv.2015.11.161

Oliva, S.J., Ebinger, C.J., Wauthier, C., Muirhead, J.D., Roecker, S.W., Rivalta, E., Heimann, S., 2019. Insights into fault-magma interactions in an early-stage continental rift from source mechanisms and correlated volcano-tectonic earthquakes. Geophys. Res. Lett. 46, 2065–2074. https://doi.org/10.1029/2018GL080866

Omenda, P., Simiyu, S., 2015. Country Update Report for Kenya 2010-2014, in: Proceedings World Geothermal Congress 2015. Presented at the World Geothermal Congress 19-25 April 2015, Melbourne, Australia.

Omenda, P.A., 1998. The geology and structural controls of the Olkaria geothermal system, Kenya. Geothermics 27, 55–74. https://doi.org/10.1016/S0375-6505(97)00028-X

Orsi, G., De Vita, S., di Vito, M., 1996. The restless, resurgent Campi Flegrei nested caldera (Italy): constraints on its evolution and configuration. J. Volcanol. Geotherm. Res. 74, 179–214. https://doi.org/10.1016/S0377-0273(96)00063-7

Otto-Bliesner, B.L., Russell, J.M., Clark, P.U., Liu, Z., Overpeck, J.T., Konecky, B., deMenocal, P., Nicholson, S.E., He, F., Lu, Z., 2014. Coherent changes of southeastern equatorial and northern African rainfall during the last deglaciation. Science 346, 1223–1227. https://doi.org/10.1126/science.1259531

7 References

Owen, R.B., Barthelme, J.W., Renaut, R.W., Vincens, A., 1982. Palaeolimnology and archaeology of Holocene deposits north-east of Lake Turkana, Kenya. Nature 298, 523–529. https://doi.org/10.1038/298523a0

Owen, R.B., Muiruri, V.M., Lowenstein, T.K., Renaut, R.W., Rabideaux, N., Luo, S., Deino, A.L., Sier, M.J., Dupont-Nivet, G., McNulty, E.P., Leet, K., Cohen, A., Campisano, C., Deocampo, D., Shen, C.-C., Billingsley, A., Mbuthia, A., 2018. Progressive aridification in East Africa over the last half million years and implications for human evolution. Proc. Natl. Acad. Sci. 201801357. https://doi.org/10.1073/pnas.1801357115

Owen, R.B., Renaut, R.W., 1980. The early Holocene palaeogeography of the northern Kenya Rift Valley. Rech. Géologiques En Afr. 5, 143–146.

Owen, R.B., Renaut, R.W., Behrensmeyer, A.K., Potts, R., 2014. Quaternary geochemical stratigraphy of the Kedong–Olorgesailie section of the southern Kenya Rift valley. Palaeogeogr. Palaeoclimatol. Palaeoecol. 396, 194–212. https://doi.org/10.1016/j.palaeo.2014.01.011

Parsons, T., Thompson, G.A., 1991. The Role of Magma Overpressure in Suppressing Earthquakes and Topography: Worldwide Examples. Science 253, 1399–1402. https://doi.org/10.1126/science.253.5026.1399

Petit, C., Ebinger, C.J., 2000. Flexure and mechanical behavior of cratonic lithosphere: Gravity models of the East African and Baikal rifts. J. Geophys. Res. Solid Earth 105, 19151–19162. https://doi.org/10.1029/2000JB900101

Pickford, M., 1982. The tectonics, volcanics and sediments of the Nyanza Rift Valley, Kenya (with 17 figures and 2 tables), in: Graben Geology and Geomorphogenesis, Zeitschrift Für Geomorphologie, Supplementary Issues, Volume 42. Schweizerbart, pp. 1–33.

Piperno, D.R., 2006. Phytoliths: A Comprehensive Guide for Archaeologists and Paleoecologists. Altamira Press, Lanham, MD.

Plasman, M., Tiberi, C., Ebinger, C.J., Gautier, S., Albaric, J., Peyrat, S., Déverchère, J., Le Gall, B., Tarits, P., Roecker, S., Wambura, F., Muzuka, A., Mulibo, G., Mtelela, K., Msabi, M., Kianji, G., Hautot, S., Perrot, J., Gama, R., 2017. Lithospheric low-velocity zones associated with a magmatic segment of the Tanzanian Rift, East Africa. Geophys. J. Int. 210, 465–481. https://doi.org/10.1093/gji/ggx177

Plumptre, A.J., Davenport, T.R.B., Behangana, M., Kityo, R., Eilu, G., Ssegawa, P., Ewango, C., Meirte, D., Kahindo, C., Herremans, M., Peterhans, J.K., Pilgrim, J.D., Wilson, M., Languy, M., Moyer, D., 2007. The biodiversity of the Albertine Rift. Biol. Conserv., Conservation in areas of high population density in Sub-Saharan Africa 134, 178–194. https://doi.org/10.1016/j.biocon.2006.08.021

Potts, R., 2013. Hominin evolution in settings of strong environmental variability. Quat. Sci. Rev. 73, 1–13. https://doi.org/10.1016/j.quascirev.2013.04.003

Potts, R., 1998. Variability selection in hominid evolution. Evol. Anthropol. Issues News Rev. 7, 81–96. https://doi.org/10.1002/(SICI)1520-6505(1998)7:3<81::AID-EVAN3>3.0.CO;2-A

Potts, R., Behrensmeyer, A.K., Faith, J.T., Tryon, C.A., Brooks, A.S., Yellen, J.E., Deino, A.L., Kinyanjui, R., Clark, J.B., Haradon, C.M., Levin, N.E., Meijer, H.J.M., Veatch, E.G., Owen, R.B., Renaut, R.W., 2018. Environmental dynamics during the onset of the Middle Stone Age in eastern Africa. Science 360, 86–90. https://doi.org/10.1126/science.aao2200

Potts, R., Deino, A., 1995. Mid-Pleistocene Change in Large Mammal Faunas of East Africa. Quat. Res. 43, 106–113. https://doi.org/10.1006/qres.1995.1010

Potts, R., Dommain, R., Moerman, J.W., Behrensmeyer, A.K., Deino, A.L., Riedl, S., Beverly, E.J., Brown, E.T., Deocampo, D., Kinyanjui, R., Lupien, R., Owen, R.B., Rabideaux, N., Russell, J.M., Stockhecke, M., deMenocal, P., Faith, J.T., Garcin, Y., Noren, A., Scott, J.J., Western, D., Bright, J., Clark, J.B., Cohen, A.S., Keller, C.B., King, J., Levin, N.E., Shannon, K.B., Muiruri, V., Renaut, R.W., Rucina, S.M., Uno, K., 2020. Increased ecological resource variability during a critical transition in hominin evolution. Sci. Adv. 6, eabc8975. https://doi.org/10.1126/sciadv.abc8975

Potts, R., Faith, J.T., 2015. Alternating high and low climate variability: The context of natural selection and speciation in Plio-Pleistocene hominin evolution. J. Hum. Evol., Environmental Variability and Hominin Dispersal 87, 5–20. https://doi.org/10.1016/j.jhevol.2015.06.014

Potts, R., Shipman, P., Ingall, E., 1988. Taphonomy, paleoecology, and hominids of Lainyamok, Kenya. J. Hum. Evol. 17, 597–614. https://doi.org/10.1016/0047-2484(88)90087-5

Prodehl, C., Ritter, J.R.R., Mechie, J., Keller, G.R., Khan, M.A., Jacob, B., Fuchs, K., Nyambok, I.O., Obel, J.D., Riaroh, D., 1997. The KRISP 94 lithospheric investigation of southern Kenya — the experiments and their main results. Tectonophysics, Structure and Dynamic Processes in the Lithosphere of the Afro-Arabian Rift System 278, 121–147. https://doi.org/10.1016/S0040-1951(97)00098-X

Protsch, R., 1978. The chronological position of Gamble's Cave II and Bromhead's Site (Elmenteita) of the Rift Valley, Kenya. J. Hum. Evol. 7, 101–109. https://doi.org/10.1016/S0047-2484(78)80001-3

Protsch, R., 1976. The Naivasha Hominid and its confirmed Late Upper Pleistocene age. Anthropol. Anz. 35, 97–102.

Purinton, B., Bookhagen, B., 2017. Validation of digital elevation models (DEMs) and comparison of geomorphic metrics on the southern Central Andean Plateau. Earth Surf. Dyn. 5, 211–237. https://doi.org/10.5194/esurf-5-211-2017

Radinger, J., Wolter, C., 2014. Patterns and predictors of fish dispersal in rivers. Fish Fish. 15, 456–473. https://doi.org/10.1111/faf.12028

Rapp Jr, G., Mulholland, S.C. (Eds.), 1992. Phytolith Systematics: Emerging Issues, Advances in Archaeological and Museum Science. Springer US. https://doi.org/10.1007/978-1-4899-1155-1

Reimer, P.J., Bard, E., Bayliss, A., Beck, J.W., Blackwell, P.G., Bronk Ramsey, C., Buck, C.E., Cheng, H., Edwards, R.L., Friedrich, M., Grootes, P.M., Guilderson, T.P., Haflidason, H., Hajdas, I., Hatté, C., Heaton, T.J., Hoffmann, D.L., Hogg, A.G., Hughen, K.A., Kaiser, K.F., Kromer, B., Manning, S.W., Niu, M., Reimer, R.W., Richards, D.A., Scott, E.M., Southon, J.R., Staff, R.A., Turney, C.S.M., Plicht, J. van der, 2013. IntCal13 and Marine13 Radiocarbon Age Calibration Curves 0–50,000 Years cal BP. Radiocarbon 55, 1869–1887. https://doi.org/10.2458/azu_js_rc.55.16947

Renaut, R.W., 1982. Late quaternary geology of the Lake Bogoria fault-trough, Kenya Rift Valley (PhD thesis). Queen Mary, University of London, London.

Renaut, R.W., Jones, B., Le Turdu, C., 1999. Calcite lilypads and ledges at Lorusio Hot Springs, Kenya Rift Valley: travertine precipitation at the air-water interface. Can. J. Earth Sci. 36, 649–666. https://doi.org/10.1139/e99-061

Renaut, R.W., Jones, B., Tiercelin, J.-J., Tarits, C., 2002. Sublacustrine precipitation of hydrothermal silica in rift lakes: evidence from Lake Baringo, central Kenya Rift Valley. Sediment. Geol., Lacustrine depositional systems 148, 235–257. https://doi.org/10.1016/S0037-0738(01)00220-2

Renaut, R.W., Owen, R.B., Ego, J.K., 2017. Geothermal activity and hydrothermal mineral deposits at southern Lake Bogoria, Kenya Rift Valley: Impact of lake level changes. J. Afr. Earth Sci. 129, 623–646. https://doi.org/10.1016/j.jafrearsci.2017.01.012

Reyna-Hurtado, R., d'Huart, J.P., Turkalo, A.K., 2017. Forest hog Hylochoerus meinertzhageni (Thomas 1904), in: Melletti, M., Meijaard, E. (Eds.), Ecology, Conservation and Management of Wild Pigs and Peccaries. Cambridge University Press, pp. 114–121. https://doi.org/10.1017/9781316941232.013

Riaroh, D., Okoth, W., 1994. The geothermal fields of the Kenya rift. Tectonophysics 236, 117–130. https://doi.org/10.1016/0040-1951(94)90172-4

Richardson, J.L., 1972. Palaeolimnological records from Rift lakes in central Kenya, in: van Zinderen Bakker, E.M. (Ed.), Palaeolimnology of Africa, the Surrounding Islands and Antarctica. Balkema, Cape Town, pp. 131–136.

Richardson, J.L., 1966. Changes in Level of Lake Naivasha, Kenya, during Postglacial Times. Nature 209, 290–291. https://doi.org/10.1038/209290a0

Richardson, J.L., Dussinger, R.A., 1986. Paleolimnology of mid-elevation lakes in the Kenya Rift Valley. Hydrobiologia 143, 167–174. https://doi.org/10.1007/BF00026659

Richardson, J.L., Richardson, A.E., 1972. History of an African Rift Lake and Its Climatic Implications. Ecol. Monogr. 42, 499–534. https://doi.org/10.2307/1942169

Richter, D., Grün, R., Joannes-Boyau, R., Steele, T.E., Amani, F., Rué, M., Fernandes, P., Raynal, J.-P., Geraads, D., Ben-Ncer, A., Hublin, J.-J., McPherron, S.P., 2017. The age of the hominin fossils from Jebel Irhoud, Morocco, and the origins of the Middle Stone Age. Nature 546, 293–296. https://doi.org/10.1038/nature22335

Richter, M.J.E.A., Brune, S., Riedl, S., Glerum, A., Neuharth, D., Strecker, M.R., 2021. Controls on asymmetric rift dynamics: numerical modeling of strain localization and fault evolution in the Kenya Rift. Tectonics 40, e2020TC006553. https://doi.org/10.1029/2020tc006553

Ricketts, J.W., Karlstrom, K.E., Priewisch, A., Crossey, L.J., Polyak, V.J., Asmerom, Y., 2014. Quaternary extension in the Rio Grande rift at elevated strain rates recorded in travertine deposits, central New Mexico. Lithosphere 6, 3–16. https://doi.org/10.1130/L278.1

Riedl, S., Melnick, D., Mibei, G.K., Njue, L., Strecker, M.R., 2020. Continental rifting at magmatic centres: structural implications from the Late Quaternary Menengai Caldera, central Kenya Rift. J. Geol. Soc. 177, 153–169. https://doi.org/10.1144/jgs2019-021

Riedl, S., Melnick, D., Njue, L., Sudo, M., Strecker, M.R., 2021a. Scarp height extraction tool for normal fault scarps visible in the TanDEM-X Science DEM. MATLAB Script. Figshare. https://doi.org/10.6084/m9.figshare.15156954

Riedl, S., Melnick, D., Njue, L., Sudo, M., Strecker, M.R., 2021b. Vertical offsets of normal fault scarps at the Paka and Silali volcanoes, Northern Kenya Rift, derived from the TanDEM-X science DEM. GIS dataset. https://doi.org/10.6084/m9.figshare.15156834

Riedl, S., Melnick, D., Njue, L., Sudo, M., Strecker, M.R., 2021c. Radiometric ages from faulted volcanic units of Silali volcano, Kenya Rift, in: Earthchem Library. Interdisciplinary Earth Data Alliance (IEDA). https://doi.org/10.26022/IEDA/111911

Ring, U., Schwartz, H.L., Bromage, T.G., Sanaane, C., 2005. Kinematic and sedimentological evolution of the Manyara Rift in northern Tanzania, East Africa. Geol. Mag. 142, 355–368. https://doi.org/10.1017/S0016756805000841

Robbins, L.H., 1972. Archeology in the Turkana District, Kenya. Science 176, 359–366. https://doi.org/10.1126/science.176.4033.359

Roberts, E.M., Stevens, N.J., O'Connor, P.M., Dirks, P.H.G.M., Gottfried, M.D., Clyde, W.C., Armstrong, R.A., Kemp, A.I.S., Hemming, S., 2012. Initiation of the western branch of the East African Rift coeval with the eastern branch. Nat. Geosci. 5, 289–294. https://doi.org/10.1038/ngeo1432

Roberts, E.M., Todd, C.N., Aanen, D.K., Nobre, T., Hilbert-Wolf, H.L., O'Connor, P.M., Tapanila, L., Mtelela, C., Stevens, N.J., 2016. Oligocene Termite Nests with In Situ Fungus Gardens from the Rukwa Rift Basin, Tanzania, Support a Paleogene African Origin for Insect Agriculture. PLOS ONE 11, e0156847. https://doi.org/10.1371/journal.pone.0156847

Roberts, N., Taieb, M., Barker, P., Damnati, B., Icole, M., Williamson, D., 1993. Timing of the Younger Dryas event in East Africa from lake-level changes. Nature 366, 146–148. https://doi.org/10.1038/366146a0

Roberts, T.R., 1975. Geographical distribution of African freshwater fishes. Zool. J. Linn. Soc. 57, 249–319. https://doi.org/10.1111/j.1096-3642.1975.tb01893.x

Robertson, E.A.M., Biggs, J., Cashman, K.V., Floyd, M.A., Vye-Brown, C., 2015. Influence of regional tectonics and pre-existing structures on the formation of elliptical calderas in the Kenyan Rift. Geol. Soc. Lond. Spec. Publ. 420, SP420.12. https://doi.org/10.1144/SP420.12

Rodgers, W.A., Owen, C.F., Homewood, K.M., 1982. Biogeography of East African Forest Mammals. J. Biogeogr. 9, 41–54. https://doi.org/10.2307/2844729

Roecker, S., Ebinger, C.J., Tiberi, C., Mulibo, G., Ferdinand-Wambura, R., Mtelela, K., Kianji, G., Muzuka, A., Gautier, S., Albaric, J., Peyrat, S., 2017. Subsurface images of the Eastern Rift, Africa, from the joint inversion of body waves, surface waves and gravity: investigating the role of fluids in early-stage continental rifting. Geophys. J. Int. 210, 931–950. https://doi.org/10.1093/gji/ggx220

Rooney, T.O., 2020. The Cenozoic magmatism of East Africa: Part V – Magma sources and processes in the East African Rift. Lithos 360–361, 105296. https://doi.org/10.1016/j.lithos.2019.105296

Rooney, T.O., 2017. The Cenozoic magmatism of East-Africa: Part I — Flood basalts and pulsed magmatism. Lithos 286–287, 264–301. https://doi.org/10.1016/j.lithos.2017.05.014

Rossouw, L., 2009. The application of fossil grass-phytolith analysis in the reconstruction of cainozoic environments in the South African interior (Thesis). University of the Free State.

Runge, F., 1999. The opal phytolith inventory of soils in central Africa —quantities, shapes, classification, and spectra. Rev. Palaeobot. Palynol. 107, 23–53. https://doi.org/10.1016/S0034-6667(99)00018-4

Russell, J.M., McCoy, S.J., Verschuren, D., Bessems, I., Huang, Y., 2009. Human impacts, climate change, and aquatic ecosystem response during the past 2000 yr at Lake Wandakara, Uganda. Quat. Res. 72, 315–324. https://doi.org/10.1016/j.yqres.2009.06.008

Russell, J.M., Vogel, H., Konecky, B.L., Bijaksana, S., Huang, Y., Melles, M., Wattrus, N., Costa, K., King, J.W., 2014. Glacial forcing of central Indonesian hydroclimate since 60,000 y B.P. Proc. Natl. Acad. Sci. 111, 5100–5105. https://doi.org/10.1073/pnas.1402373111

Ryner, M.A., Bonnefille, R., Holmgren, K., Muzuka, A., 2006. Vegetation changes in Empakaai Crater, northern Tanzania, at 14,800–9300 cal yr BP. Rev. Palaeobot. Palynol. 140, 163–174. https://doi.org/10.1016/j.revpalbo.2006.03.006

Sagnotti, L., 2013. Demagnetization Analysis in Excel (DAIE). An open source workbook in Excel for viewing and analyzing demagnetization data from paleomagnetic discrete samples and u-channels. https://doi.org/10.4401/ag-6282

Salzburger, W., Van Bocxlaer, B., Cohen, A.S., 2014. Ecology and Evolution of the African Great Lakes and Their Faunas. Annu. Rev. Ecol. Evol. Syst. 45, 519–545. https://doi.org/10.1146/annurev-ecolsys-120213-091804

Sanderson, D.J., Marchini, W.R.D., 1984. Transpression. J. Struct. Geol. 6, 449–458. https://doi.org/10.1016/0191-8141(84)90058-0

Sands, W.A., 1987. Ichnocoenoses of probably termite origin from Laetoli, in: Laetoli: A Pliocene Site in Northern Tanzania. Oxford University Press, Oxford, pp. 409–433.

Saneyoshi, M., Nakayama, K., Sakai, T., Sawada, Y., Ishida, H., 2006. Half graben filling processes in the early phase of continental rifting: The Miocene Namurungule Formation of the Kenya Rift. Sediment. Geol. 186, 111–131. https://doi.org/10.1016/j.sedgeo.2005.11.012

Saria, E., Calais, E., Stamps, D.S., Delvaux, D., Hartnady, C.J.H., 2014. Present-day kinematics of the East African Rift. J. Geophys. Res. Solid Earth 119, 3584–3600. https://doi.org/10.1002/2013JB010901

Schlebusch, C.M., Malmström, H., Günther, T., Sjödin, P., Coutinho, A., Edlund, H., Munters, A.R., Vicente, M., Steyn, M., Soodyall, H., Lombard, M., Jakobsson, M., 2017. Southern African ancient genomes estimate modern human divergence to 350,000 to 260,000 years ago. Science 358, 652–655. https://doi.org/10.1126/science.aao6266

Scholz, C.A., Finney, B.P., 1994. Late Quaternary sequence stratigraphy of Lake Malawi (Nyasa), Africa. Sedimentology 41, 163–179. https://doi.org/10.1111/j.1365-3091.1994.tb01397.x

Scholz, C.A., Johnson, T.C., Cohen, A.S., King, J.W., Peck, J.A., Overpeck, J.T., Talbot, M.R., Brown, E.T., Kalindekafe, L., Amoako, P.Y.O., Lyons, R.P., Shanahan, T.M., Castañeda, I.S., Heil, C.W., Forman, S.L., McHargue, L.R., Beuning, K.R., Gomez, J., Pierson, J., 2007. East African megadroughts between 135 and 75 thousand years ago and bearing on early-modern human origins. Proc. Natl. Acad. Sci. 104, 16416–16421. https://doi.org/10.1073/pnas.0703874104

Schultz, R.A., Soliva, R., Okubo, C.H., Mège, D., 2009. Fault populations, in: Schultz, R.A., Watters, T.R. (Eds.), Planetary Tectonics, Cambridge Planetary Science. Cambridge University Press, Cambridge, pp. 457–510. https://doi.org/10.1017/CBO9780511691645.011

Schwanghart, W., Scherler, D., 2014. Short Communication: TopoToolbox 2 – MATLAB-based software for topographic analysis and modeling in Earth surface sciences. Earth Surf. Dyn. 2, 1–7. https://doi.org/10.5194/esurf-2-1-2014

Schwarzer, J., Swartz, E.R., Vreven, E., Snoeks, J., Cotterill, F.P.D., Misof, B., Schliewen, U.K., 2012. Repeated trans-watershed hybridization among haplochromine cichlids (Cichlidae) was triggered by Neogene landscape evolution. Proc. R. Soc. B Biol. Sci. 279, 4389–4398. https://doi.org/10.1098/rspb.2012.1667

Schwonke, F., Kraml, M., Ochmann, N., 2008. Geothermal Exploration at Menengai-Olbanita Prospect, Kenya. Final Report. Federal Institute for Geosciences and Natural Resources (BGR), Hannover.

Scott, J.J., Renaut, R.W., Buatois, L.A., Owen, R.B., 2009. Biogenic structures in exhumed surfaces around saline lakes: An example from Lake Bogoria, Kenya Rift Valley. Palaeogeogr. Palaeoclimatol. Palaeoecol., Lacustrine bioturbation and ichnofacies 272, 176–198. https://doi.org/10.1016/j.palaeo.2008.12.002

Searle, R.C., 1970. Evidence from Gravity Anomalies for Thinning of the Lithosphere beneath the Rift Valley in Kenya. Geophys. J. Int. 21, 13–31. https://doi.org/10.1111/j.1365-246X.1970.tb01764.x

Seegers, L., Tichy, H., 1999. The Oreochromis alcalicus flock (Teleostei: Cichlidae) from lakes Natron and Magadi, Tanzania and Kenya, with descriptions of two new species. Ichthyol. Explor. Freshw. 10, 97–146.

Seegers, L., Vos, L.D., Okeyo, D.O., 2003. Annotated Checklist of the Freshwater Fishes of Kenya (excluding the lacustrine haplochromines from Lake Victoria). J. East Afr. Nat. Hist. 92, 11–47. https://doi.org/10/b4mtjv

Seehausen, O., 2006. African cichlid fish: a model system in adaptive radiation research. Proc. R. Soc. B Biol. Sci. 273, 1987–1998. https://doi.org/10.1098/rspb.2006.3539

Seehausen, O., 2002. Patterns in fish radiation are compatible with Pleistocene desiccation of Lake Victoria and 14 600 year history for its cichlid species flock. Proc. R. Soc. Lond. B Biol. Sci. 269, 491–497. https://doi.org/10.1098/rspb.2001.1906

Self, S., Goff, F., Gardner, J.N., Wright, J.V., Kite, W.M., 1986. Explosive rhyolitic volcanism in the Jemez Mountains: Vent locations, caldera development and relation to regional structure. J. Geophys. Res. Solid Earth 91, 1779–1798. https://doi.org/10.1029/JB091iB02p01779

Sepulchre, P., Ramstein, G., Fluteau, F., Schuster, M., Tiercelin, J.-J., Brunet, M., 2006. Tectonic Uplift and Eastern Africa Aridification. Science 313, 1419–1423. https://doi.org/10.1126/science.1129158

Shackleton, R.M., 1955. Pleistocene movements in the Gregory Rift Valley. Geol. Rundsch. 43, 257–263. https://doi.org/10.1007/BF01764109

Shipman, P., Potts, R., Pickford, M., 1983. Lainyamok, a new middle Pleistocene hominid site. Nature 306, 365–368. https://doi.org/10.1038/306365a0

Shmela, A.K., Paton, D.A., Collier, R.E., Bell, R.E., 2021. Normal fault growth in continental rifting: Insights from changes in displacement and length fault populations due to increasing extension in the Central Kenya Rift. Tectonophysics 814, 228964. https://doi.org/10.1016/j.tecto.2021.228964

Siegburg, M., Bull, J.M., Nixon, C.W., Keir, D., Gernon, T.M., Corti, G., Abebe, B., Sanderson, D.J., Ayele, A., 2020. Quantitative Constraints on Faulting and Fault Slip Rates in the Northern Main Ethiopian Rift. Tectonics 39, e2019TC006046. https://doi.org/10.1029/2019TC006046

Siler, D.L., Karson, J.A., 2017. Along-Axis Structure and Crustal Construction Processes of Spreading Segments in Iceland: Implications for Magmatic Rifts. Tectonics 36, 2068–2084. https://doi.org/10.1002/2017TC004629

Simiyu, S.M., Keller, G.R., 2001. An integrated geophysical analysis of the upper crust of the southern Kenya rift. Geophys. J. Int. 147, 543–561. https://doi.org/10.1046/j.0956-540x.2001.01542.x

Simiyu, S.M., Keller, G.R., 1997. An integrated analysis of lithospheric structure across the East African plateau based on gravity anomalies and recent seismic studies. Tectonophysics, Structure and Dynamic Processes in the Lithosphere of the Afro-Arabian Rift System 278, 291–313. https://doi.org/10.1016/S0040-1951(97)00109-1

Sippel, J., Meeßen, C., Cacace, M., Mechie, J., Fishwick, S., Heine, C., Scheck-Wenderoth, M., Strecker, M.R., 2017. The Kenya rift revisited: insights into lithospheric strength through data-driven 3-D gravity and thermal modelling. Solid Earth 8, 45–81. https://doi.org/10.5194/se-8-45-2017

Smith, M., 1994. Stratigraphic and structural constraints on mechanisms of active rifting in the Gregory Rift, Kenya. Tectonophysics, Crustal and upper mantle structure of the Kenya Rift 236, 3–22. https://doi.org/10.1016/0040-1951(94)90166-X

Smith, M., Dunkley, P.N., Deino, A., Williams, L.A.J., McCall, G.J.H., 1995. Geochronology, stratigraphy and structural evolution of Silali volcano, Gregory Rift, Kenya. J. Geol. Soc. 152, 297–310. https://doi.org/10.1144/gsjgs.152.2.0297

Smith, M., Mosley, P., 1993. Crustal heterogeneity and basement influence on the development of the Kenya Rift, East Africa. Tectonics 12, 591–606. https://doi.org/10.1029/92TC01710

Soil Survey Staff, 2014. Illustrated Guide to Soil Taxonomy, version 1. ed. U.S. Department of Agriculture, Natural Resources Conservation Service, National Soil Survey Center, Lincoln, Nebraska.

Sona, G., Pinto, L., Pagliari, D., Passoni, D., Gini, R., 2014. Experimental analysis of different software packages for orientation and digital surface modelling from UAV images. Earth Sci. Inform. 7, 97–107. https://doi.org/10.1007/s12145-013-0142-2

Stamps, D.S., Calais, E., Saria, E., Hartnady, C., Nocquet, J.-M., Ebinger, C.J., Fernandes, R.M., 2008. A kinematic model for the East African Rift. Geophys. Res. Lett. 35, L05304. https://doi.org/10.1029/2007GL032781

Steiger, R.H., Jäger, E., 1977. Subcommission on geochronology: Convention on the use of decay constants in geo- and cosmochronology. Earth Planet. Sci. Lett. 36, 359–362. https://doi.org/10.1016/0012-821X(77)90060-7

Strecker, M.R., 1991. Das Zentrale und Südliche Kenia Rift unter besonderer Berücksichtigung der neotektonischen Entwicklung. (Habilitation thesis). University of Karlsruhe, Germany, Karlsruhe, Germany.

Strecker, M.R., Blisniuk, P.M., Eisbacher, G.H., 1990. Rotation of extension direction in the central Kenya Rift. Geology 18, 299–302. https://doi.org/10.1130/0091-7613(1990)018<0299:ROEDIT>2.3.CO;2

Strecker, M.R., Bosworth, W., 1991. Quaternary stress-field change in the Gregory rift, Kenya. Eos Trans. Am. Geophys. Union 72, 17–22. https://doi.org/10.1029/90EO00017

Street-Perrott, F.A., Perrott, R.A., 1990. Abrupt climate fluctuations in the tropics: the influence of Atlantic Ocean circulation. Nature 343, 607–612. https://doi.org/10.1038/343607a0

Stringer, C., 2016. The origin and evolution of Homo sapiens. Philos. Trans. R. Soc. B Biol. Sci. 371, 20150237. https://doi.org/10.1098/rstb.2015.0237

7 References

Strömberg, C.A.E., 2003. The origin and spread of grass-dominated habitats in North America during the Tertiary and how it relates to the evolution of hypsodonty in equids. (PhD thesis). Univerity of California, Berkeley.

Stuiver, M., 1969. Yale Natural Radiocarbon Measurements IX. Radiocarbon 11, 545–658. https://doi.org/10.1017/S0033822200011413

Stuiver, M., Reimer, P.J., 1993. Extended C-14 data base and revised CALIB 3.0 C-14 age calibration program. Radiocarbon 35, 215–230. https://doi.org/10.1017/S0033822200013904

Sturchio, N.C., Dunkley, P.N., Smith, M., 1993. Climate-driven variations in geothermal activity in the northern Kenya rift valley. Nature 362, 233–234. https://doi.org/10.1038/362233a0

Swain, C.J., 1992. The Kenya rift axial gravity high: a re-interpretation. Tectonophysics 204, 59–70. https://doi.org/10.1016/0040-1951(92)90269-C

Taieb, M., Barker, P., Bonnefille, R., Damnati, B., Gasse, F., Goetz, C., Hillaire-Marcel, C., Icole, M., Massault, M., Roberts, N., Vincens, A., Williamson, D., 1991. Historie paléohydrologique du lac Magadi (Kenya) au Pléistocène Supérieur. Comptes Rendus Acad. Sci. Paris, Série II 313, 339–346.

Tarits, C., Renaut, R.W., Tiercelin, J.-J., Le Hérissé, A., Cotten, J., Cabon, J.-Y., 2006. Geochemical evidence of hydrothermal recharge in Lake Baringo, central Kenya Rift Valley. Hydrol. Process. 20, 2027–2055. https://doi.org/10.1002/hyp.6046

Tarras-Wahlberg, H., Everard, M., Harper, D.M., 2002. Geochemical and physical characteristics of river and lake sediments at Naivasha, Kenya. Hydrobiologia 488, 27–41. https://doi.org/10.1023/A:1023301808624

Tauxe, L., Badgley, C., 1988. Stratigraphy and remanence acquisition of a palaeomagnetic reversal in alluvial Siwalik rocks of Pakistan. Sedimentology 35, 697–715. https://doi.org/10.1111/j.1365-3091.1988.tb01245.x

Tessema, A., Antoine, L.A.G., 2004. Processing and interpretation of the gravity field of the East African Rift: implication for crustal extension. Tectonophysics 394, 87–110. https://doi.org/10.1016/j.tecto.2004.07.057

Thompson, A.O., Dodson, R.G., 1963. Geology of the Naivasha Area (No. 67), Geological Survey of Kenya Report. Geological Survey of Kenya.

Thompson, L.G., Mosley-Thompson, E., Davis, M.E., Henderson, K.A., Brecher, H.H., Zagorodnov, V.S., Mashiotta, T.A., Lin, P.-N., Mikhalenko, V.N., Hardy, D.R., Beer, J., 2002. Kilimanjaro Ice Core Records: Evidence of Holocene Climate Change in Tropical Africa. Science 298, 589–593. https://doi.org/10.1126/science.1073198

Thomson, K.S., 1966. Quaternary fish fossils from west of Lake Rudolf, Kenya. Breviora 243, 1–10.

Tichy, H., Seegers, L., 1999. The Oreochromis alcalicus flock (Teleostei: Cichlidae) from lakes Natron and Magadi, Tanzania and Kenya: a model for the evolution of “new” species flocks in historical times? Ichthyol. Explor. Freshw. 10, 147–174.

Tiercelin, J.-J., Lezzar, K.-E., 2002. A 300 Million years history of rift lakes in Central and East Africa: an updated broad review, in: Odada, E.O., Olago, D.O. (Eds.), The East African Great Lakes: Limnology, Palaeolimnology and Biodiversity, Advances in Global Change Research. Springer Netherlands, pp. 3–60. https://doi.org/10.1007/0-306-48201-0_1

Tiercelin, J.J., Renaut, R.W., Delibrias, G., Le Fournier, J., Bieda, S., 1981. Late Pleistocene and Holocene lake level fluctuations in the Lake Bogoria basin, northern Kenya Rift Valley. Palaeoecol. Afr. 13, 105–120.

Tiercelin, J.-J., Thuo, P., Potdevin, J.-L., Nalpas, T., 2012. Hydrocarbon Prospectivity in Mesozoic and Early–Middle Cenozoic Rift Basins of Central and Northern Kenya, Eastern Africa, in: Gao, D. (Ed.), AAPG Memoir 100: Tectonics and Sedimentation: Implications for Petroleum Systems. pp. 179–207. https://doi.org/DOI:10.1306/13351553M1001742

Tiercelin, J.-J., Vincens, A., Barton, C.E., Carbonel, P., Casanova, J., Delibrias, G., Gasse, F., Grosdidier, E., Herbin, J.-P., Huc, A.Y., Jardiné, S., Le Fournier, J., Mélières, F., Owen, R.B., Pagé, P., Palacios, C., Paquet, H., Péniguel, G., Peypouquet, J.-P., Raynaud, J.-F., Renaut, R.W., Renéville, P., Richert, J.-P., Riff, R., Robert, P., Seyve, C., Vandenbroucke, M., Vidal, G., 1987. Le demi-graben de Baringo-Bogoria, Rift Gregory, Kenya. 30000 ans d'histoire hydrologique et sédimentaire. (The Baringo-Bogoria half-graben, Gregory Rift, Kenya. 30 000 years of hydrological and sedimentary history). Bull. Cent. Rech. Explor.-Prod. Elf-Aquitaine, Bulletin des centres de recherches exploration-production Elf-Aquitaine 11, 249–540. https://bit.ly/3orya0j

Tierney, J.E., Lewis, S.C., Cook, B.I., LeGrande, A.N., Schmidt, G.A., 2011. Model, proxy and isotopic perspectives on the East African Humid Period. Earth Planet. Sci. Lett. 307, 103–112. https://doi.org/10.1016/j.epsl.2011.04.038

Tocheri, M.W., Dommain, R., McFarlin, S.C., Burnett, S.E., Troy Case, D., Orr, C.M., Roach, N.T., Villmoare, B., Eriksen, A.B., Kalthoff, D.C., Senck, S., Assefa, Z., Groves, C.P., Jungers, W.L., 2016. The evolutionary origin and population history of the grauer gorilla. Am. J. Phys. Anthropol. 159, S4–S18. https://doi.org/10.1002/ajpa.22900

Tongue, J., Maguire, P., Burton, P., 1994. An earthquake study in the Lake Baringo basin of the central Kenya Rift. Tectonophysics, Crustal and upper mantle structure of the Kenya Rift 236, 151–164. https://doi.org/10.1016/0040-1951(94)90174-0

Tongue, J.A., Maguire, P.K.H., Young, P.A.V., 1992. Seismicity distribution from temporary earthquake recording networks in Kenya. Tectonophysics 204, 71–79. https://doi.org/10.1016/0040-1951(92)90270-G

Torres Acosta, V., Bande, A., Sobel, E.R., Parra, M., Schildgen, T.F., Stuart, F., Strecker, M.R., 2015a. Cenozoic extension in the Kenya Rift from low-temperature thermochronology: Links to diachronous spatiotemporal evolution of rifting in East Africa. Tectonics 2015TC003949. https://doi.org/10.1002/2015TC003949

Torres Acosta, V., Schildgen, T.F., Clarke, B.A., Scherler, D., Bookhagen, B., Wittmann, H., Blanckenburg, F. von, Strecker, M.R., 2015b. Effect of vegetation cover on millennial-scale landscape denudation rates in East Africa. Lithosphere 7, 408–420. https://doi.org/10.1130/L402.1

Trauth, M.H., Maslin, M.A., Deino, A.L., Strecker, M.R., Bergner, A.G.N., Dühnforth, M., 2007. High- and low-latitude forcing of Plio-Pleistocene East African climate and human evolution. J. Hum. Evol., African Paleoclimate and Human Evolution 53, 475–486. https://doi.org/10.1016/j.jhevol.2006.12.009

TRMM, 2011. Tropical Rainfall Measuring Mission (TRMM) Combined Precipitation Radar and Microwave Imager Rainfall Profile L2 1.5 hours V7. Goddard Earth Sciences Data and Information Services Center (GES DISC), Greenbelt, MD.

Truckle, P.H., 1976. Geology and late Cainozoic lake sediments of the Suguta Trough, Kenya. Nature 263, 380–383. https://doi.org/10.1038/263380a0

Tryon, C.A., Faith, J.T., 2013. Variability in the Middle Stone Age of Eastern Africa. Curr. Anthropol. 54, S234–S254. https://doi.org/10.1086/673752

Tschinkel, W.R., 2010. The foraging tunnel system of the Namibian Desert termite, Baucaliotermes hainesi. J. Insect Sci. 10. https://doi.org/10.1673/031.010.6501

Tuckwell, G.W., Bull, J.M., Sanderson, D.J., 1996. Models of fracture orientation at oblique spreading centres. J. Geol. Soc. 153, 185–189. https://doi.org/10.1144/gsjgs.153.2.0185

Twiss, P.C., 1992. Predicted World Distribution of C3 and C4 Grass Phytoliths, in: Rapp, G., Mulholland, S.C. (Eds.), Phytolith Systematics: Emerging Issues, Advances in Archaeological and Museum Science. Springer US, Boston, MA, pp. 113–128. https://doi.org/10.1007/978-1-4899-1155-1_6

Twiss, P.C., Suess, E., Smith, R.M., 1969. Morphological Classification of Grass Phytoliths. Soil Sci. Soc. Am. J. 33, 109–115. https://doi.org/10.2136/sssaj1969.03615995003300010030x

Tzedakis, P.C., Margari, V., Hodell, D.A., 2015. Coupled ocean–land millennial-scale changes 1.26 million years ago, recorded at Site U1385 off Portugal. Glob. Planet. Change 135, 83–88. https://doi.org/10.1016/j.gloplacha.2015.10.008

Uno, K.T., Polissar, P.J., Kahle, E., Feibel, C., Harmand, S., Roche, H., deMenocal, P.B., 2016. A Pleistocene palaeovegetation record from plant wax biomarkers from the Nachukui Formation, West Turkana, Kenya. Philos. Trans. R. Soc. B Biol. Sci. 371, 20150235. https://doi.org/10.1098/rstb.2015.0235

Uto, K., Ishizuka, O., Matsumoto, A., Kamioka, H., Togashi, S., 1997. Laser-heating $^{40}Ar/^{39}Ar$ dating system of the Geological Survey of Japan: System outlines and preliminary result. Bull. Geol. Surv. Jpn. 48, 23–46.

Vanneste, K., Verbeeck, K., Camelbeeck, T., Paulissen, E., Meghraoui, M., Renardy, F., Jongmans, D., Frechen, M., 2001. Surface-rupturing history of the Bree fault scarp, Roer Valley graben: Evidence for six events since the late Pleistocene. J. Seismol. 5, 329–359. https://doi.org/10.1023/A:1011419408419

Verheyen, E., Salzburger, W., Snoeks, J., Meyer, A., 2003. Origin of the Superflock of Cichlid Fishes from Lake Victoria, East Africa. Science 300, 325–329. https://doi.org/10.1126/science.1080699

Verschuren, D., Sinninghe Damsté, J.S., Moernaut, J., Kristen, I., Blaauw, M., Fagot, M., Haug, G.H., Geel, B. van, Batist, M.D., Barker, P., Vuille, M., Conley, D.J., Olago, D.O., Milne, I., Plessen, B., Eggermont, H., Wolff, C., Hurrell, E., Ossebaar, J., Lyaruu, A., Plicht, J. van der, Cumming, B.F., Brauer, A., Rucina, S.M., Russell, J.M., Keppens, E., Hus, J., Bradley, R.S., Leng, M., Mingram, J., Nowaczyk, N.R., 2009. Half-precessional dynamics of monsoon rainfall near the East African Equator. Nature 462, 637–641. https://doi.org/10.1038/nature08520

Vincens, A., Casanova, J., Tiercelin, J.J., 1986. Palaeolimnology of Lake Bogoria (Kenya) during the 4500 BP high lacustrine phase. Geol. Soc. Lond. Spec. Publ. 25, 323–330. https://doi.org/10.1144/GSL.SP.1986.025.01.26

Vogts, A., Moossen, H., Rommerskirchen, F., Rullkötter, J., 2009. Distribution patterns and stable carbon isotopic composition of alkanes and alkan-1-ols from plant waxes of African rain forest and savanna C3 species. Org. Geochem. 40, 1037–1054. https://doi.org/10.1016/j.orggeochem.2009.07.011

Vranken, N., Steenberge, M.V., Balagizi, A., Snoeks, J., 2020a. The synonymy of Haplochromis pharyngalis and Haplochromis petronius (Cichlidae). J. Fish Biol. 97, 1554–1559. https://doi.org/10.1111/jfb.14455

Vranken, N., Steenberge, M.V., Snoeks, J., 2020b. Similar ecology, different morphology: Three new species of oral-mollusc shellers from Lake Edward. J. Fish Biol. 96, 1202–1217. https://doi.org/10.1111/jfb.14107

Vranken, N., Van Steenberge, M., Kayenbergh, A., Snoeks, J., 2020c. The lobed-lipped species of Haplochromis (Teleostei, Cichlidae) from Lake Edward, two instead of one. J. Gt. Lakes Res. 46, 1079–1089. https://doi.org/10.1016/j.jglr.2019.05.005

Vranken, N., Van Steenberge, M., Snoeks, J., 2019. Grasping ecological opportunities: not one but five paedophagous species of Haplochromis (Teleostei: Cichlidae) in the Lake Edward system. Hydrobiologia 832, 105–134. https://doi.org/10.1007/s10750-018-3742-5

Vrba, E.S., 1995. On the Connections between Paleoclimate and Evolution, in: Paleoclimate and Evolution, with Emphasis on Human Origins. Yale University Press, pp. 24–45.

Wadge, G., Biggs, J., Lloyd, R., Kendall, J.-M., 2016. Historical Volcanism and the State of Stress in the East African Rift System. Front. Earth Sci. 4. https://doi.org/10.3389/feart.2016.00086

Wagner, C.E., Harmon, L.J., Seehausen, O., 2014. Cichlid species-area relationships are shaped by adaptive radiations that scale with area. Ecol. Lett. 17, 583–592. https://doi.org/10.1111/ele.12260

Wakjira, M., Getahun, A., 2017. Ichthyofaunal diversity of the Omo-Turkana basin, East Africa, with specific reference to fish diversity within the limits of Ethiopian waters. Check List - J. Biodivers. Data 13(2), 1–22. https://doi.org/10.15560/13.2.2059

Wallace, A.R., 1854. On the Monkeys of the Amazon. Ann. Mag. Nat. Hist. 14, 451–454. https://doi.org/10.1080/037454809494374

Wamalwa, A.M., 2011. Joint geophysical data analysis for geothermal energy exploration (PhD thesis). University of Texas at El Paso, El Paso, Texas.

Wamalwa, A.M., Mickus, K.L., Serpa, L.F., 2013. Geophysical characterization of the Menengai volcano, Central Kenya Rift from the analysis of magnetotelluric and gravity data. Geophysics 78, B187–B199. https://doi.org/10.1190/geo2011-0419.1

Wamalwa, A.M., Serpa, L.F., 2013. The investigation of the geothermal potential at the Silali volcano, Northern Kenya Rift, using electromagnetic data. Geothermics 47, 89–96. https://doi.org/10.1016/j.geothermics.2013.02.001

Wandera, S.B., Balirwa, J.S., 2010. Fish species diversity and relative abundance in Lake Albert—Uganda. Aquat. Ecosyst. Health Manag. 13, 284–293. https://doi.org/10.1080/14634988.2010.507120

Washbourn-Kamau, C.K., 1971. Late Quaternary Lakes in the Nakuru-Elmenteita Basin, Kenya. Geogr. J. 137, 522–535. https://doi.org/10.2307/1797148

Washbourn-Kamau, C.K., 1970. Late Quaternary Chronology of the Nakuru–Elmenteita Basin, Kenya. Nature 226, 253–254. https://doi.org/10.1038/226253c0

Webb, M., Barker, P.A., Wynn, P.M., Heiri, O., Hardenbroek, M. van, Pick, F., Russell, J.M., Stott, A.W., Leng, M.J., 2016. Interpretation and application of carbon isotope ratios in freshwater diatom silica. J. Quat. Sci. 31, 300–309. https://doi.org/10.1002/jqs.2837

Weinstein, A., Oliva, S.J., Ebinger, C.J., Roecker, S., Tiberi, C., Aman, M., Lambert, C., Witkin, E., Albaric, J., Gautier, S., Peyrat, S., Muirhead, J.D., Muzuka, A.N.N., Mulibo, G., Kianji, G., Ferdinand-Wambura, R., Msabi, M., Rodzianko, A., Hadfield, R., Illsley-Kemp, F., Fischer, T.P., 2017. Fault-magma interactions during early continental rifting: Seismicity of the Magadi-Natron-Manyara basins, Africa. Geochem. Geophys. Geosystems 18, 3662–3686. https://doi.org/10.1002/2017GC007027

Werdelin, L., Sanders, W.J. (Eds.), 2010. Cenozoic Mammals of Africa, 1st edition. ed. University of California Press, Berkeley.

Wessel, P., Smith, W.H.F., 1996. A global, self-consistent, hierarchical, high-resolution shoreline database. J. Geophys. Res. Solid Earth 101, 8741–8743. https://doi.org/10.1029/96JB00104

Western, D., 1975. Water availability and its influence on the structure and dynamics of a savannah large mammal community. Afr. J. Ecol. 13, 265–286. https://doi.org/10.1111/j.1365-2028.1975.tb00139.x

Westoby, M.J., Brasington, J., Glasser, N.F., Hambrey, M.J., Reynolds, J.M., 2012. 'Structure-from-Motion' photogrammetry: A low-cost, effective tool for geoscience applications. Geomorphology 179, 300–314. https://doi.org/10.1016/j.geomorph.2012.08.021

Wheildon, J., Morgan, P., Williamson, K.H., Evans, T.R., Swanberg, C.A., 1994. Heat flow in the Kenya rift zone. Tectonophysics, Crustal and upper mantle structure of the Kenya Rift 236, 131–149. https://doi.org/10.1016/0040-1951(94)90173-2

Wichura, H., Bousquet, R., Oberhänsli, R., Strecker, M.R., Trauth, M.H., 2010. Evidence for middle Miocene uplift of the East African Plateau. Geology 38, 543–546. https://doi.org/10.1130/G31022.1

Wichura, H., Jacobs, L.L., Lin, A., Polcyn, M.J., Manthi, F.K., Winkler, D.A., Strecker, M.R., Clemens, M., 2015. A 17-My-old whale constrains onset of uplift and climate change in east Africa. Proc. Natl. Acad. Sci. 112, 3910–3915. https://doi.org/10.1073/pnas.1421502112

Wilks, M., Kendall, J.-M., Nowacki, A., Biggs, J., Wookey, J., Birhanu, Y., Ayele, A., Bedada, T., 2017. Seismicity associated with magmatism, faulting and hydrothermal circulation at Aluto Volcano, Main Ethiopian Rift. J. Volcanol. Geotherm. Res. 340, 52–67. https://doi.org/10.1016/j.jvolgeores.2017.04.003

Williams, L. a. J., MacDonald, R., Chapman, G.R., 1984. Late Quaternary caldera volcanoes of the Kenya Rift Valley. J. Geophys. Res. Solid Earth 89, 8553–8570. https://doi.org/10.1029/JB089iB10p08553

Williams, L.A.J., 1978. The Volcanological Development of the Kenya Rift, in: Neumann, E.-R., Ramberg, I.B. (Eds.), Petrology and Geochemistry of Continental Rifts, NATO Advanced Study Institutes Series. Springer Netherlands, Dordrecht, pp. 101–121. https://doi.org/10.1007/978-94-009-9803-2_10

Williams, R.E.G., Johnson, A.S., 1976. Birmingham University Radiocarbon Dates X. Radiocarbon 18, 249–267. https://doi.org/10.1017/S0033822200003155

Wilson, A.H., 1996. The Great Dyke of Zimbabwe, in: Cawthorn, R.G. (Ed.), Developments in Petrology, Layered Intrusions. Elsevier, pp. 365–402. https://doi.org/10.1016/S0167-2894(96)80013-3

Wilson, D., Aster, R., West, M., Ni, J., Grand, S., Gao, W., Baldridge, W.S., Semken, S., Patel, P., 2005. Lithospheric structure of the Rio Grande rift. Nature 433, 851–855. https://doi.org/10.1038/nature03297

Wilson, J.T., 1968. Static or Mobile Earth: The Current Scientific Revolution. Proc. Am. Philos. Soc. 112, 309–320.

Wilson, K.E., Maslin, M.A., Leng, M.J., Kingston, J.D., Deino, A.L., Edgar, R.K., Mackay, A.W., 2014. East African lake evidence for Pliocene millennial-scale climate variability. Geology G35915.1. https://doi.org/10.1130/G35915.1

Withjack, M.O., Jamison, W.R., 1986. Deformation produced by oblique rifting. Tectonophysics 126, 99–124. https://doi.org/10.1016/0040-1951(86)90222-2

Withjack, M.O., Scheiner, C., 1982. Fault Patterns Associated with Domes - An Experimental and Analytical Study. AAPG Bull. 66, 302–316.

World Health Organisation, 2018. A global overview of national regulations and standards for drinking-water quality. World Health Organisation, Geneva.

Worst, B.G., 1960. The Great Dyke of Southern Rhodesia. Southern Rhodesia Geological Survey Bulletin No. 47, Southern Rhodesia Geological Survey Bulletin. Salisbury.

Wright, T.J., Ayele, A., Ferguson, D., Kidane, T., Vye-Brown, C., 2016. Magmatic rifting and active volcanism: introduction. Geol. Soc. Lond. Spec. Publ. 420, SP420.18. https://doi.org/10.1144/SP420.18

Wright, T.J., Ebinger, C.J., Biggs, J., Ayele, A., Yirgu, G., Keir, D., Stork, A., 2006. Magma-maintained rift segmentation at continental rupture in the 2005 Afar dyking episode. Nature 442, 291–294. https://doi.org/10.1038/nature04978

Yamasaki, F., Hamada, C., Hamada, T., 1972. Riken Natural Radiocarbon Measurements VII. Radiocarbon 14, 223–238. https://doi.org/10.1017/S0033822200001090

Yamasaki, F., Hamada, C., Hamada, T.J., 1974. Riken Natural Radiocarbon Measurements VIII. Radiocarbon 16, 331–357. https://doi.org/10.1017/S0033822200059646

Young, J. a. T., Renaut, R.W., 1979. A radiocarbon date from Lake Bogoria, Kenya Rift Valley. Nature 278, 243–245. https://doi.org/10.1038/278243a0

Zielke, O., Strecker, M.R., 2009. Recurrence of large earthquakes in magmatic continental rifts: insights from a paleoseismic study along the Laikipia–Marmanet Fault, Subukia Valley, Kenya Rift. Bull. Seismol. Soc. Am. 99, 61–70. https://doi.org/10.1785/0120080015

Zijderveld, J.D.A., 1967. A. C. Demagnetization of Rocks: Analysis of Results, in: Collinson, D.W., Creer, K.M., Runcorn, S.K. (Eds.), Methods in Palaeomagnetism, Developments in Solid Earth Geophysics. Elsevier, pp. 254–286. https://doi.org/10.1016/B978-1-4832-2894-5.50049-5

Appendix A

Supporting information for Chapter 2

Supporting information for Chapter 2, *"Mid-Pleistocene to recent crustal extension in the inner graben of the Northern Kenya Rift"* are a geological map of the study area (Figure A.1), which has been compiled using published sources (Dunkley et al., 1993; Friese, 2015; Mibei et al., 2021b) and which was also used to assign the mapped fault scarps to their geological units. A compilation of all used radiometric dates, their coordinates and original references is presented in Table A.1. This table includes previously published data and four new radiometric ages, which were collected for this study during a sampling campaign in 2014. These four new samples were dated using $^{40}Ar/^{39}Ar$ geochronology in the geochronology lab of the University of Potsdam. The complete analytical data of these new geochronological analyses is presented in Table A.2, and is also available as data file in the Geochron database (Riedl et al., 2021c).

Additional digital data are available at the following data repositories:

The MATLAB script to extract fault scarp heights from DEM is available at Figshare (Riedl et al., 2021a): https://dx.doi.org/10.6084/m9.figshare.15156954
Temporary link during the peer-review phase of chapter 2:
https://figshare.com/s/5b999ee5f88a9edea679

The fault scarp heights at the Paka and Silali volanoes are available as a GIS dataset at Figshare (Riedl et al., 2021b): https://dx.doi.org/10.6084/m9.figshare.15156834
Temporary link during the peer-review phase of chapter 2:
https://figshare.com/s/60ce21a6d81862ef5c59

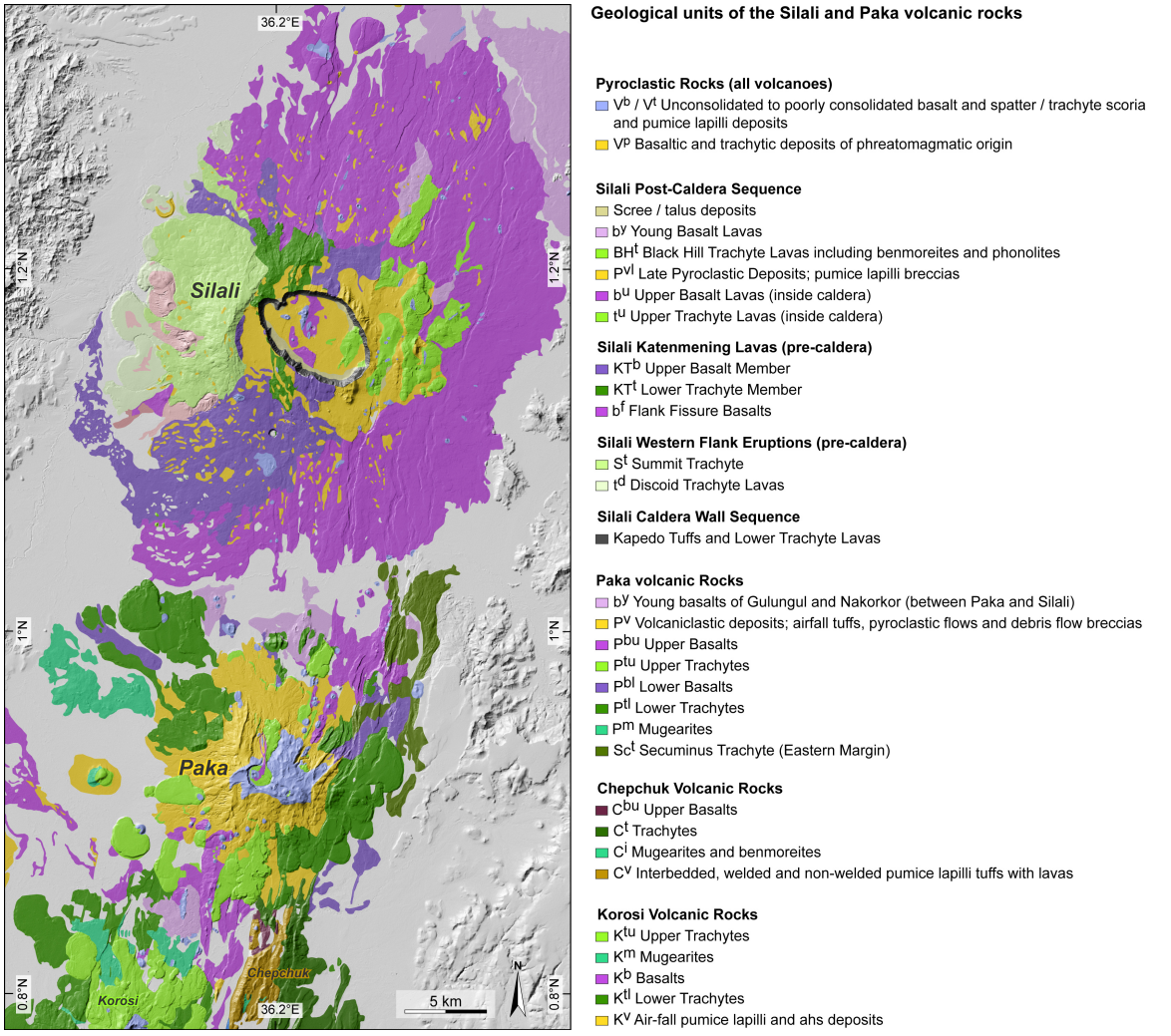

Figure A.1. Geological map of the Paka and Silali volcanoes.
The volcanic rocks of the two rift volcanoes Silali and Paka, located in inner graben of the Northern Kenya Rift, as used in chapter 2. Mapping and unit names from Dunkley et al. (1993), with minor stratigraphic revisions by Friese (2015) and Mibei et al. (2021b).

Approximate location	Original sample ID	Unit name	Dating method	Age ± 1σ (Ma)	Easting (m)	Northing (m)	Reference
Korosi, NW flanks	AL 1815 0885	Upper Trachytes (Korosi)	$^{40}Ar/^{39}Ar$	0.104 ± 0.002	181600	88200	Dunkley et al. (1993), p. 24
Chepchuk	*n/a*	Silica at Faults	U series	0.430 ± 0.120	187400*	92400*	Sturchio et al. (1993)
Chepchuk	*n/a*	Silica at Faults	U series	0.350 ± 0.060	187400*	92400*	Sturchio et al. (1993)
SW of Paka, Muruase	PK-29	Upper Trachytes	$^{40}Ar/^{39}Ar$	0.039 ± 0.006	179152	99350	Friese (2015)
Paka, S flanks	PK-27	Upper Trachytes	$^{40}Ar/^{39}Ar$	0.071 ± 0.013	187155	96084	Friese (2015)
Paka, SW flanks	PK-26	Upper Trachytes	$^{40}Ar/^{39}Ar$	0.150 ± 0.006	184649	98087	Friese (2015)
Paka, SE flanks	PK-8	Upper Trachytes	$^{40}Ar/^{39}Ar$	0.205 ± 0.006	191724	97097	Friese (2015)
Paka summit caldera	*n/a*	*Caldera collapse*	stratigraphic bracketing based on Ar/Ar dating	approx. 0.01 (0.011 ± 0.003 vs. 0.008 ± 0.004)	187500*	101800*	Dunkley et al. (1993)
Paka, NE flanks	PK-5	Upper Trachytes	$^{40}Ar/^{39}Ar$	0.234 ± 0.013	192546	104595	Friese (2015)
NW of Paka	PK-16	Lower Trachytes	$^{40}Ar/^{39}Ar$	0.386 ± 0.005	183224	103324	Friese (2015)
NE of Paka	PK-6	Lower Trachytes	$^{40}Ar/^{39}Ar$	0.389 ± 0.006	195262	104907	Friese (2015)
NE of Paka	PK-10	Lower Trachytes	$^{40}Ar/^{39}Ar$	0.405 ± 0.007	196304	110561	Friese (2015)
NW of Paka	PK-15	Upper Trachytes	$^{40}Ar/^{39}Ar$	0.139 ± 0.035	183623	106043	Friese (2015)
Far WNW of Paka	PK-22	Lower Mugearites	$^{40}Ar/^{39}Ar$	0.471 ± 0.013	176221	106350	Friese (2015)
Far NW of Paka	PK-19	Lower Trachytes	$^{40}Ar/^{39}Ar$	0.415 ± 0.028	179068	111411	Friese (2015)
N of Paka	PK-13	Upper Basalts	$^{40}Ar/^{39}Ar$	0.145 ± 0.023	186938	111141	Friese (2015)
Lava flows N of Paka	AM 1883 1093	Upper Trachytes	$^{40}Ar/^{39}Ar$	0.219 ± 0.004	188400	109000	Dunkley et al. (1993), p. 32
NE of Paka	AM 1962 1097	Lower Trachytes	$^{40}Ar/^{39}Ar$	0.390 ± 0.006	196300	109400	Dunkley et al. (1993), p. 31
Silali, S flanks	**S06-03**	**Lava flows on SE flanks**	**$^{40}Ar/^{39}Ar$**	**0.18 ± 0.07**	**194660**	**124644**	**this study, IGSN IERIS000B**
Silali, S flanks	**S07-01**	**Young basaltic cone**	**$^{40}Ar/^{39}Ar$**	**0.08 ± 0.06**	**193528**	**123098**	**this study, IGSN IERIS000C**
Silali, W flanks	AM 1817 1288	Arzett Tuffs	$^{40}Ar/^{39}Ar$	0.117 ± 0.005	181800	128500	Dunkley et al. (1993), p. 48
Silali, W flanks	SIL-5	Arzett Tuffs	$^{40}Ar/^{39}Ar$	0.123 ± 0.003	181800†	128500†	Smith et al. (1995)
Silali, W flanks	n/a	Summit Trachyte	$^{40}Ar/^{39}Ar$	> 0.100			Smith et al. (1995)
Silali caldera	KGP-255	Katenmening Lavas (Pre- to Syn-Caldera)	$^{40}Ar/^{39}Ar$	0.063 ± 0.011	187400†	130400†	Smith et al. (1995)
Silali caldera	AM 1873 1307	Katenmening Lavas (Youngest Pre-caldera lava)	$^{40}Ar/^{39}Ar$	0.064 ± 0.002	187400	130400	Dunkley et al. (1993), p. 52
Silali caldera	**S04-01**	**Intracaldera Trachyte**	**$^{40}Ar/^{39}Ar$**	**0.031 ± 0.005**	**193206**	**128700**	**this study, IGSN IERIS0006**
Silali caldera	KGP-256	Post-Caldera Basalt	$^{40}Ar/^{39}Ar$	0.009 ± 0.009			Smith et al. (1995)
Silali caldera	SIL-1	Post-Caldera Trachyte	$^{40}Ar/^{39}Ar$	0.008 ± 0.003	193900†	126900†	Smith et al. (1995)
Silali, N of caldera	**S01-01**	**Pre-Caldera Tephra**	**$^{40}Ar/^{39}Ar$**	**0.119 ± 0.010**	**189622**	**131449**	**this study, IGSN IERIS0001**
Silali, E flanks	KGP-253	Black Hill Trachytes	$^{40}Ar/^{39}Ar$	0.009 ± 0.002	197500†	124900†	Smith et al. (1995)
Silali, E flanks	KGP-254	Black Hill Trachytes	$^{40}Ar/^{39}Ar$	0.007 ± 0.002	195200†	128000†	Smith et al. (1995)
Silali, N flanks	n/a	Pre-Caldera Basalts		> 0.100			Dunkley et al. (1993)

*) inferred coordinate †) inferred coordinate based on similar sample reported in Dunkley et al. (1993)

Table A.1. List of all radiometric ages used or mentioned in chapter 2.
Samples are ordered from South to North, new samples from this study are marked bold. All coordinates are given in UTM system, zone 37N, on WGS-84 ellipsoid. The unit names refer to the geological maps of Dunkley et al. (1993) and their stratigraphic revision in Friese (2015) and Mibei et al. (2021b).

Appendix A: Supporting information for Chapter 2

Sample S06-03 IGSN: IERIS000B Lab ID: 1157 J value: (1.040 ± 0.003) ×10^{-3} stepwise-heating of groundmass

Step #	Lab ID	Laser Output %	Relative Isotopic Abundances (×10^{-2} nA) ^{40}Ar ±1σ	^{39}Ar ±1σ	^{38}Ar ±1σ	^{37}Ar ±1σ	^{36}Ar ±1σ	^{39}Ar % of total	Ca/K ±1σ	%^{40}Ar*	Age (Ma) ±1σ
1	1157-01	1.6	701.5752 ± 3.0000	11.9834 ± 0.0601	0.6064 ± 0.0140	8.4483 ± 0.1568	2.4842 ± 0.0110	7.2	1.20 ± 0.02	- 4.5	-5.000 ± 1.300
2	1157-02	2.0	424.4451 ± 1.2001	44.7400 ± 0.2302	0.8894 ± 0.0160	63.5810 ± 0.5176	1.4388 ± 0.0083	26.7	2.42 ± 0.02	1.0	0.176 ± 0.199
3	1157-03	2.3	146.0459 ± 0.5519	36.5408 ± 0.2002	0.5418 ± 0.0120	110.4418 ± 0.6634	0.5091 ± 0.0099	21.8	5.14 ± 0.04	3.0	0.223 ± 0.168
4	1157-04	2.6	75.5786 ± 0.4623	27.1814 ± 0.1501	0.4015 ± 0.0094	106.7183 ± 0.8086	0.2766 ± 0.0038	16.2	6.67 ± 0.06	3.1	0.159 ± 0.098
5	1157-05	2.9	50.5629 ± 0.3729	16.6183 ± 0.1301	0.2366 ± 0.0150	69.7832 ± 0.7848	0.1837 ± 0.0036	9.9	7.14 ± 0.10	3.6	0.205 ± 0.140
6	1157-06	3.2	48.2643 ± 0.3332	11.4148 ± 0.0701	0.1621 ± 0.0100	48.5299 ± 0.4470	0.1694 ± 0.0028	6.8	7.23 ± 0.08	4.3	0.339 ± 0.166
7	1157-07	3.6	67.2245 ± 0.1810	9.4704 ± 0.0391	0.1639 ± 0.0073	70.7462 ± 0.4728	0.2360 ± 0.0029	5.7	12.70 ± 0.10	4.7	0.626 ± 0.210
8	1157-08	4.0	59.7744 ± 0.1910	5.2436 ± 0.0241	0.1149 ± 0.0064	121.6161 ± 0.7398	0.2220 ± 0.0038	3.1	39.43 ± 0.31	6.6	1.438 ± 0.464
9	1157-09	4.4	53.7667 ± 0.1314	4.1269 ± 0.0201	0.0952 ± 0.0057	161.0317 ± 0.7402	0.2055 ± 0.0032	2.5	66.33 ± 0.46	11.2	2.798 ± 0.498

Nucleogenic production ratios:

(^{36}Ar/^{37}Ar)$_{Ca}$ (2.730 ± 0.032) × 10^{-4}

(^{39}Ar/^{37}Ar)$_{Ca}$ (6.638 ± 0.263) × 10^{-4}

(^{40}Ar/^{39}Ar)$_{K}$ (50.966 ± 24.353) × 10^{-4}

(^{38}Ar/^{39}Ar)$_{K}$ (1.1816 ± 0.00266) × 10^{-2}

Decay constants from Steiger & Jäger (1977)

Age calculation:

Total Gas Age	-0.05 ± 0.19 Ma		
Plateau Age (steps 2-5)	**0.18 ± 0.07 Ma**		
Normal isochron age (all steps)	0.43 ± 0.12 Ma	Initial ^{40}Ar/^{36}Ar:	286 ± 4 MSWD: 1.7
Inverse isochron age (all steps)	0.43 ± 0.11 Ma	Initial ^{40}Ar/^{36}Ar:	286 ± 4 MSWD: 1.7
Normal isochron age (steps 2-5)	0.18 ± 0.14 Ma	Initial ^{40}Ar/^{36}Ar:	296 ± 5 MSWD: 0.07
Inverse isochron age (steps 2-5)	0.18 ± 0.13 Ma	Initial ^{40}Ar/^{36}Ar:	296 ± 5 MSWD: 0.07

Sample S07-01 IGSN: IERIS000C Lab ID: 1199 J value: (1.047 ± 0.004) ×10^{-3} stepwise-heating of groundmass

Step #	Lab ID	Laser Output (%)	Relative Isotopic Abundances (×10^{-2} nA) ^{40}Ar ±1σ	^{39}Ar ±1σ	^{38}Ar ±1σ	^{37}Ar ±1σ	^{36}Ar ±1σ	^{39}Ar % of total	Ca/K ±1σ	%^{40}Ar*	Age (Ma) ±1σ
1	1199-01	1.6	85.3237 ± 0.4603	1.906 ± 0.017	0.0863 ± 0.0034	5.8034 ± 0.2657	0.2808 ± 0.0036	1.3	5.18 ± 0.24	3.28	2.774 ± 1.386
2	1199-02	1.8	47.1542 ± 0.2905	7.531 ± 0.046	0.1348 ± 0.0050	15.6705 ± 0.4616	0.1538 ± 0.0030	5.1	3.54 ± 0.11	6.21	0.735 ± 0.259
3	1199-03	2.0	80.0933 ± 0.4655	19.858 ± 0.130	0.3035 ± 0.0096	34.4192 ± 0.4179	0.2754 ± 0.0041	13.3	2.95 ± 0.04	1.74	0.132 ± 0.143
4	1199-04	2.3	200.8465 ± 0.6042	32.803 ± 0.150	0.5168 ± 0.0048	51.3619 ± 0.6309	0.6938 ± 0.0033	22.1	2.66 ± 0.04	-0.01	0.130 ± 0.126
5	1199-05	2.5	124.0050 ± 0.3705	17.919 ± 0.053	0.3031 ± 0.0073	29.5066 ± 0.3648	0.4277 ± 0.0046	12.0	2.80 ± 0.04	-0.01	0.190 ± 0.192
6	1199-06	2.8	64.2137 ± 0.1910	19.674 ± 0.052	0.2689 ± 0.0065	37.4842 ± 0.5914	0.2219 ± 0.0034	13.2	3.24 ± 0.05	2.45	0.151 ± 0.112
7	1199-07	3.1	86.0004 ± 0.4104	14.778 ± 0.075	0.2435 ± 0.0063	34.0014 ± 0.4239	0.2978 ± 0.0035	9.9	3.91 ± 0.05	0.79	0.087 ± 0.174
8	1199-08	3.5	114.2898 ± 0.5606	12.749 ± 0.055	0.2444 ± 0.0060	46.5417 ± 0.7188	0.3782 ± 0.0047	8.6	6.21 ± 0.10	5.46	0.926 ± 0.267
9	1199-09	3.9	248.1124 ± 0.7804	10.618 ± 0.031	0.3216 ± 0.0064	140.9316 ± 1.5200	0.8662 ± 0.0060	7.1	22.56 ± 0.26	1.40	0.621 ± 0.538
10	1199-10	4.4	289.3326 ± 0.9603	5.913 ± 0.028	0.2764 ± 0.0049	181.4635 ± 1.0989	0.9940 ± 0.0073	4.0	52.17 ± 0.41	3.53	3.326 ± 1.150
11	1199-11	5.0	368.9120 ± 1.0003	5.007 ± 0.022	0.2998 ± 0.0055	225.8947 ± 2.0280	1.2324 ± 0.0078	3.4	76.70 ± 0.78	6.22	8.903 ± 1.598

Nucleogenic production ratios:

(^{36}Ar/^{37}Ar)$_{Ca}$ (2.730 ± 0.032) × 10^{-4}

(^{39}Ar/^{37}Ar)$_{Ca}$ (6.638 ± 0.263) × 10^{-4}

(^{40}Ar/^{39}Ar)$_{K}$ (50.966 ± 24.353) × 10^{-4}

(^{38}Ar/^{39}Ar)$_{K}$ (1.1816 ± 0.00266) × 10^{-2}

Decay constants from Steiger & Jäger (1977)

Age calculation:

Total Gas Age	0.70 ± 0.20 Ma		
Plateau Age (steps 3-7)	**0.08 ± 0.06 Ma**		
Normal isochron age (all steps)	-0.11 ± 0.13 Ma	Initial ^{40}Ar/^{36}Ar:	303 ± 3 MSWD: 1.5
Inverse isochron age (all steps)	-0.11 ± 0.04 Ma	Initial ^{40}Ar/^{36}Ar:	303 ± 3 MSWD: 1.6
Normal isochron age (steps 3-7)	0.30 ± 0.20 Ma	Initial ^{40}Ar/^{36}Ar:	288 ± 7 MSWD: 0.054
Inverse isochron age (steps 3-7)	0.30 ± 0.20 Ma	Initial ^{40}Ar/^{36}Ar:	288 ± 7 MSWD: 0.055

Sample S04-01 IGSN: IERIS0006 Lab ID: C16018 J value: (0.965 ± 0.004) ×10^{-3} stepwise-heating of feldspar phenocrysts

Step #	Lab ID#	Laser Output (%)	Relative Isotopic Abundances (×10^{-6} V) ^{40}Ar ±1σ	^{39}Ar ±1σ	^{38}Ar ±1σ	^{37}Ar ±1σ	^{36}Ar ±1σ	^{39}Ar% of total	Ca/K ±1σ	%^{40}Ar*	Age (Ma) ±1σ
1	C1601701	1.6	6835.1430 ± 14.8367	25.0743 ± 0.1844	4.1924 ± 0.0583	0.4997 ± 1.8080	22.2071 ± 0.1240	0.1	0.020 ± 0.072	4.0	18.855 ± 2.734
2	C1601702	2.2	13323.2030 ± 22.6385	766.3364 ± 1.6464	17.9648 ± 0.1519	46.1227 ± 3.3906	45.3906 ± 0.2120	2.6	0.060 ± 0.004	-0.6	-0.196 ± -0.151
3	C1601703	2.9	1311.1330 ± 3.6276	2075.1323 ± 5.5236	24.9124 ± 0.2184	132.4375 ± 4.5043	3.8368 ± 0.0873	7.0	0.064 ± 0.002	14.3	0.157 ± 0.022
4	C1601704	3.7	4792.5460 ± 10.2656	4924.5731 ± 12.3973	89.4447 ± 0.4727	319.0716 ± 6.7239	14.8348 ± 0.1365	16.6	0.065 ± 0.001	9.0	0.153 ± 0.015
5	C1601705	4.8	18188.2560 ± 8.7832	15470.7110 ± 9.9708	195.2354 ± 0.5316	1046.8528 ± 9.3238	60.8431 ± 0.2505	52.0	0.068 ± 0.001	1.6	0.032 ± 0.009
6	C1601706	5.2	1307.0060 ± 1.8053	6492.0151 ± 7.8601	74.9471 ± 0.4817	380.5236 ± 7.7950	4.1375 ± 0.0700	21.8	0.059 ± 0.001	8.5	0.030 ± 0.007

Nucleogenic production ratios:

(^{36}Ar/^{37}Ar)$_{Ca}$ (2.642 ± 0.049) × 10^{-4}

(^{39}Ar/^{37}Ar)$_{Ca}$ (6.938 ± 0.409) × 10^{-4}

(^{40}Ar/^{39}Ar)$_{K}$ (4.288 ± 22.434) × 10^{-4}

(^{38}Ar/^{39}Ar)$_{K}$ (1.2017 ± 0.00272) × 10^{-2}

Decay constants from Steiger & Jäger (1977)

Age calculation:

Total Gas Age	0.07 ± 0.01 Ma		
Plateau Age (steps 5-6)	**0.03 ± 0.01 Ma**		
Normal isochron age (all steps)	0.03 ± 0.01 Ma	Initial ^{40}Ar/^{36}Ar:	299.1 ± 1.0 MSWD: 5.13
Inverse isochron age (all steps)	0.04 ± 0.00 Ma	Initial ^{40}Ar/^{36}Ar:	299.7 ± 1.0 MSWD: 5.35
Normal isochron age (steps 5-6)	0.03 ± 0.01 Ma	Initial ^{40}Ar/^{36}Ar:	295.9 ± 2.0 MSWD: n/a
Inverse isochron age (steps 5-6)	0.03 ± 0.01 Ma	Initial ^{40}Ar/^{36}Ar:	295.9 ± 2.0 MSWD: n/a

Sample S01-01 IGSN: IERIS0001 Lab ID: C16014 J value: (1.031 ± 0.004) ×10^{-3} total fusion of individual feldspar crystals in tephra sample

Meas. #	Lab ID#	Laser Output (%)	Relative Isotopic Abundances (×10^{-6} V) ^{40}Ar ±1σ	^{39}Ar ±1σ	^{38}Ar ±1σ	^{37}Ar ±1σ	^{36}Ar ±1σ	Ca/K ±1σ	%^{40}Ar*	Age (Ma) ±1σ
3	C1601403	6.4	587.7210 ± 1.5729	2302.1981 ± 8.3646	24.9156 ± 0.3064	680.1992 ± 8.6121	1.3122 ± 0.0636	0.296 ± 0.004	43.0	0.204 ± 0.016
4	C1601404	6.4	508.5050 ± 4.9977	2286.7001 ± 19.0453	26.3989 ± 0.4839	626.4340 ± 9.9817	1.1447 ± 0.0742	0.274 ± 0.005	43.0	0.177 ± 0.019
5	C1601405	4.6	243.0380 ± 2.0213	1361.1760 ± 6.8682	14.4831 ± 0.3206	24.3537 ± 2.8918	0.5581 ± 0.0579	0.018 ± 0.002	32.8	0.109 ± 0.024
6	C1601406	4.6	602.4960 ± 6.6014	3524.7559 ± 41.1885	38.8414 ± 0.5202	331.9124 ± 12.2220	1.3844 ± 0.0709	0.094 ± 0.004	36.2	0.115 ± 0.012
7	C1601407	4.6	454.9700 ± 1.3432	1394.7562 ± 4.0856	16.0235 ± 0.1607	35.4902 ± 2.8531	1.1751 ± 0.0593	0.025 ± 0.002	24.2	0.147 ± 0.024
8	C1601408	4.6	54930.5260 ± 539.0269	2112.2076 ± 23.2340	57.3253 ± 1.1290	60.1401 ± 5.3930	177.1104 ± 2.3724	0.028 ± 0.003	4.7	2.287 ± 0.779
9	C1601409	4.6	13526.4920 ± 15.0966	3374.4949 ± 4.1449	46.3610 ± 0.4563	91.7138 ± 2.4776	45.7077 ± 0.2334	0.027 ± 0.001	0.2	0.014 ± 0.039

Nucleogenic production ratios:

(^{36}Ar/^{37}Ar)$_{Ca}$ (2.642 ± 0.049) × 10^{-4}

(^{39}Ar/^{37}Ar)$_{Ca}$ (6.938 ± 0.409) × 10^{-4}

(^{40}Ar/^{39}Ar)$_{K}$ (4.288 ± 22.434) × 10^{-4}

(^{38}Ar/^{39}Ar)$_{K}$ (1.2017 ± 0.00272) × 10^{-2}

Decay constants from Steiger & Jäger (1977)

Age calculation:

Weighted average age (5,6,7) **0.12 ± 0.01 Ma**

Table A.2. ^{40}Ar/^{39}Ar – analytical results of the samples dated in chapter 2.

Table A.2 (previous page). $^{40}Ar/^{39}Ar$ – analytical results of the samples dated in chapter 2.
The lava samples S06-03 (groundmass), S07-01 (groundmass), S04-01 (feldspars) were dated using stepwise-heating analyses. The criteria for the age plateaus are described in Fleck et al. (1977). The tephra sample S01-01 was dated using seven total fusion analyses of individual feldspar crystals. The final age of S01-01 is a weighted average of the measurements that (i) agree within 2σ error, and (ii) have similar Ca/K ratios. All age calculations are based on the decay constants (of ^{40}K) and the atmospheric $^{40}Ar/^{36}Ar$ ratio from Steiger and Jäger (1977). All data from the radiometric dating is also available in the Geochron database at https://doi.org/10.26022/IEDA/111911 (Riedl et al., 2021c).

Appendix B

Supporting information for Chapter 3

This appendix contains the $^{40}Ar/^{39}Ar$ chronological data of sample KMM01 from Chapter 3, *"Continental rifting at magmatic centres: structural implications from the Late Quaternary Menengai Caldera, central Kenya Rift"*. This supporting information is also available online at https://doi.org/10.6084/m9.figshare.c.4647818

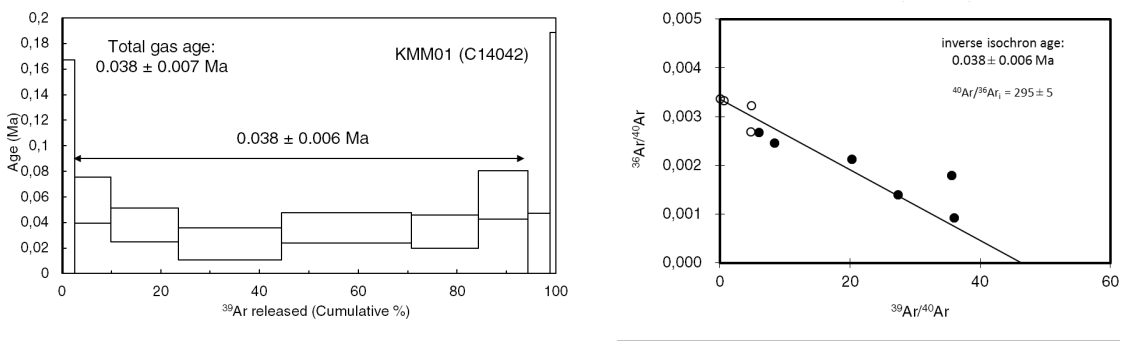

Figure B.1. Incremental heating results for sample KMM01

(Left panel) *age plateau. The sample processing follows the methodology of Uto et al. (1997). Multiple grains were incrementally heated using a 50 W CO_2 laser (10.6 μm wavelength). Isotope abundances were measured using a Micromass 5400 single detector noble gass mass spectrometer. All age calculations are based on decay constant values reported in Steiger & Jäger (1977). (left panel) Plateau age and age spectrum derived from incremental heating analysis. The plateau age was obtained from the weighted average of plateau steps in the stepwise-heating age-spectra diagrams according to the criteria outlined in Fleck et al. (1977): (1) two ages of the contiguous two steps in the "plateau" agree within 2 σ error excluding J value error; (2) the total fraction of the plateaucovers more than 50% of the total amount of analyzed ^{39}Ar; and (3) each plateau step has more than 3% of the total amount of analyzed ^{39}Ar. Given the young age of the sample, the following additional criteria were applied (4) the two ages at both ends of the plateau agree within a 2 σ error range; (5) the last step is not considered in the plateau age when the central value of the last step is beyond the 2 sigma range of the weighted average age of the remaining plateau steps; (6) the error of each "plateau" step is less than 0.1 Ma as well as the 1 σ error.* ***(Right panel)*** *inverse isochron plots ($^{36}Ar/^{40}Ar$ vs. $^{39}Ar/^{40}Ar$ isotope correlation diagrams). The age is derived from the x-axis intercept and shown with 1σ error.*

Laser output	$^{37}Ar/^{39}Ar$	$^{37}Ar/^{39}Ar$	$^{36}Ar/^{39}Ar$ $\times10^{-3}$	K/Ca	$^{40}Ar^*$	$^{39}Ar_K$	Fraction of released ^{39}Ar %	$^{40}Ar^*/^{39}Ar_K$	Age ± 1σ
1.4%	44.81 ± 0.27	0.135 ± 0.038	151.14 ± 2.73	4.37	0.36	0.17	0	0.16 ± 0.77	0.29 ± 1.38
1.8%	1.714 ± 0.018	0.073 ± 0.006	5.7 ± 0.2	8.04	1.43	2.40	2	0.02 ± 0.07	0.04 ± 0.12
2.0%	0.119 ± 0.006	0.062 ± 0.003	0.31 ± 0.03	9.54	27.06	7.28	7	0.032 ± 0.010	0.057 ± 0.018
2.2%	0.037 ± 0.006	0.0564 ± 0.0017	0.067 ± 0.014	10.43	58.50	13.72	14	0.021 ± 0.007	0.038 ± 0.013
2.4%	0.028 ± 0.006	0.0432 ± 0.0013	0.063 ± 0.011	13.60	46.72	20.86	21	0.013 ± 0.007	0.023 ± 0.013
2.8%	0.028 ± 0.006	0.0436 ± 0.0010	0.038 ± 0.008	13.50	72.50	26.38	26	0.020 ± 0.007	0.036 ± 0.012
3.2%	0.049 ± 0.006	0.088 ± 0.003	0.129 ± 0.013	6.71	37.10	13.46	13	0.018 ± 0.007	0.033 ± 0.013
3.8%	0.168 ± 0.006	0.198 ± 0.004	0.51 ± 0.03	2.97	20.56	10.07	10	0.034 ± 0.011	0.061 ± 0.019
4.4%	0.209 ± 0.007	0.215 ± 0.004	0.73 ± 0.05	2.73	4.55	4.55	5	0.010 ± 0.017	0.02 ± 0.03
5.0%	0.213 ± 0.009	0.119 ± 0.009	0.6 ± 0.2	4.96	20.33	1.12	1	0.04 ± 0.06	0.08 ± 0.11

Table B.1. Summary table of incremental heating analysis, sample KMM01

Summary of isotope fractions derived from incremental heating analysis. The abundances were corrected for background, mass discrimination, radioactive decay and interfering isotopes. Irradiation data is given in table B.2. Raw isotope abundances are given in table B.3, background abundances in table B.4.

Irradiation ID	J value $\times10^{-3}$	J value 1σ $\times10^{-3}$	$(^{40}Ar/^{36}Ar)_{air}$	$(^{39}Ar/^{37}Ar)_{Ca}$	± 1σ	$(^{36}Ar/^{37}Ar)_{Ca}$	± 1σ	$(^{40}Ar/^{39}Ar)_K$	± 1σ	$(^{38}Ar/^{39}Ar)_K$	± 1σ
PO-1	0.988	0.003952	287.36	0.00085669	0.00029115	0.00027508	3.2138E-06	0.00357045	0.0061842	0.01207061	4.3104E-05

Table B.2. Irradiation data and values for nuclear interference reactions

The sample was irradiated on 24 Feb 2014 at Oregon State University Reactor (OSTR). The Fish Canyon Tuff Sanidine (FC3S) was used as neutron flux monitor during irradiation. Alder Creek Sanidine (ACs-2) was co-irradiated to check the accuracy of the system. Crystals of K_2SO_4 and CaF_2 were co-irradiated to determine the values for nuclear interfering reactions during the irradiation. The analysis of the sample was done on 24 Aug 2014.

Lab ID#	Heating %	Laser Power (W)	^{40}Ar $\times10^{-3}$	$\pm 1\sigma$ $\times10^{-3}$	$^{39}Ar/^{40}Ar$	$\pm 1\sigma$	^{38}Ar $\times10^{-3}$	$\pm 1\sigma$ $\times10^{-3}$	^{37}Ar $\times10^{-3}$	$\pm 1\sigma$ $\times10^{-3}$	^{36}Ar $\times10^{-3}$	$\pm 1\sigma$ $\times10^{-3}$
C1404201	1.40%	0.7	2.0378	1.9	0.021956	0.0016583	54	0.00021509	130	0.0071837	15	0.0016583
C1404202	1.80%	0.9	1.1598	5.8	0.55758	0.0082807	26	0.0014619	79	0.0041905	35	0.0082807
C1404203	2.00%	1	0.29459	7.1	6.6425	0.02426	21	0.0035325	41	0.0010207	47	0.02426
C1404204	2.20%	1.1	0.21009	5.1	17.563	0.044427	14	0.0060186	25	0.00066633	37	0.044427
C1404205	2.40%	1.2	0.23958	7.5	23.413	0.066137	13	0.0069896	27	0.00077309	55	0.066137
C1404206	2.80%	1.4	0.27762	3.7	25.552	0.086927	11	0.0088558	21	0.00072348	75	0.086927
C1404207	3.20%	1.6	0.24716	3.8	14.647	0.046729	11	0.0090788	33	0.00092751	47	0.046729
C1404208	3.80%	1.9	0.51854	4.8	5.2225	0.036401	10	0.015207	19	0.0018538	36	0.036401
C1404209	4.40%	2.2	0.31613	6	3.8716	0.016485	23	0.0075271	15	0.0013737	37	0.016485
C1404210	5.00%	2.5	0.1224	12	2.4597	0.0042064	21	0.0011249	64	0.00064207	76	0.0042064

Table B.3. Relative isotope abundances of incremental heating analysis (raw values)

Isotope abundances of sample KMM01 determined during incremental-heating analysis. Given are the raw abundances before corrections were applied.

Lab ID#	Heating %	Laser Power (W)	$^{40}Ar_{blank}$ $\pm 1\sigma$ $\times10^{-3}$		$^{39}Ar_{blank}$ $\pm 1\sigma$ $\times10^{-3}$		$^{38}Ar_{blank}$ $\pm 1\sigma$ $\times10^{-3}$		$^{37}Ar_{blank}$ $\pm 1\sigma$ $\times10^{-3}$		$^{36}Ar_{blank}$ $\pm 1\sigma$ $\times10^{-3}$	
C1404201	1.40%	0.7	0.045657	13	0.000034247	1000	0.000084926	180	0.000044915	870	0.00027523	150
C1404202	1.80%	0.9	0.055861	16	0.00013255	180	0.000088677	390	0.00012525	70	0.00039847	51
C1404203	2.00%	1	0.055861	16	0.00013255	180	0.000088677	390	0.00012525	70	0.00039847	51
C1404204	2.20%	1.1	0.062815	7.2	0.00038778	310	0.000090345	490	0.00014894	480	0.00041403	110
C1404205	2.40%	1.2	0.062815	7.2	0.00038778	310	0.000090345	490	0.00014894	480	0.00041403	110
C1404206	2.80%	1.4	0.056434	14	0.00074496	120	0.000072996	610	0.00014466	330	0.00044893	29
C1404207	3.20%	1.6	0.056434	14	0.00074496	120	0.000072996	610	0.00014466	330	0.00044893	29
C1404208	3.80%	1.9	0.057623	7.8	0.00078358	120	0.00007835	280	0.00012317	240	0.00045542	86
C1404209	4.40%	2.2	0.057623	7.8	0.00078358	120	0.00007835	280	0.00012317	240	0.00045542	86
C1404210	5.00%	2.5	0.057623	7.8	0.00078358	120	0.00007835	280	0.00012317	240	0.00045542	86

Table B.4. Relative isotope abundances of blank measurements, used for correction

Isotope abundances of blank measurements during incremental-heating analysis. The given values were used to apply background correction on the analysis.

Appendix B: Supporting information for Chapter 3

Compound	SiO_2	TiO_2	Al_2O_3	FeO	MnO	MgO	CaO	Na_2O	K_2O	ZrO_2	
%	62.8	0.7	11.2	11.2	0.5	0.1	1.0	7.7	4.6	0.2	
Element	**Si**	**Ti**	**Al**	**Fe**	**Mn**	**Mg**	**Ca**	**Na**	**K**	**Zr**	**O**
Weight %	29.37	0.42	5.9	8.69	0.35	0.05	0.73	5.74	3.84	0.16	44.75
Weight % 1σ	0.24	0.1	0.12	0.28	0.14	0.06	0.09	0.13	0.12	0.2	0.31

***Table B.5**. Geochemistry of sample KMM01*
Sample geochemistry derived from EDX (Energy-dispersive X-ray spectroscopy) analysis.

Sample identifier	Dated unit	Location	Analysis identifier
KMM01	consolidated Menengai tuff mantling Athinai trachytes	0° 6.0326' S 36° 2.8787' E Emy quarry El Bonwala ridge N of Menengai	C14042

***Table B.6**. Location of sample KMM01*
Location data for the sample analysed by Ar-Ar geochonology.

Appendix C

Supporting information for Chapter 4

This appendix contains supporting information for Chapter 4, *"Increased ecological resource variability during a critical transition in hominin evolution"*. This includes supplementary text about the materials and methods (Text C.1 to C.3), as well as additional tables (Tables C.1 to C.2) and figures (Figs. C.1 to C.9).

Additional digital data (Excel files of the source data visualized in Figure 4.3) are available at the data repository of the original publication (Potts et al., 2020):
https://dx.doi.org/10.1126/sciadv.abc8975

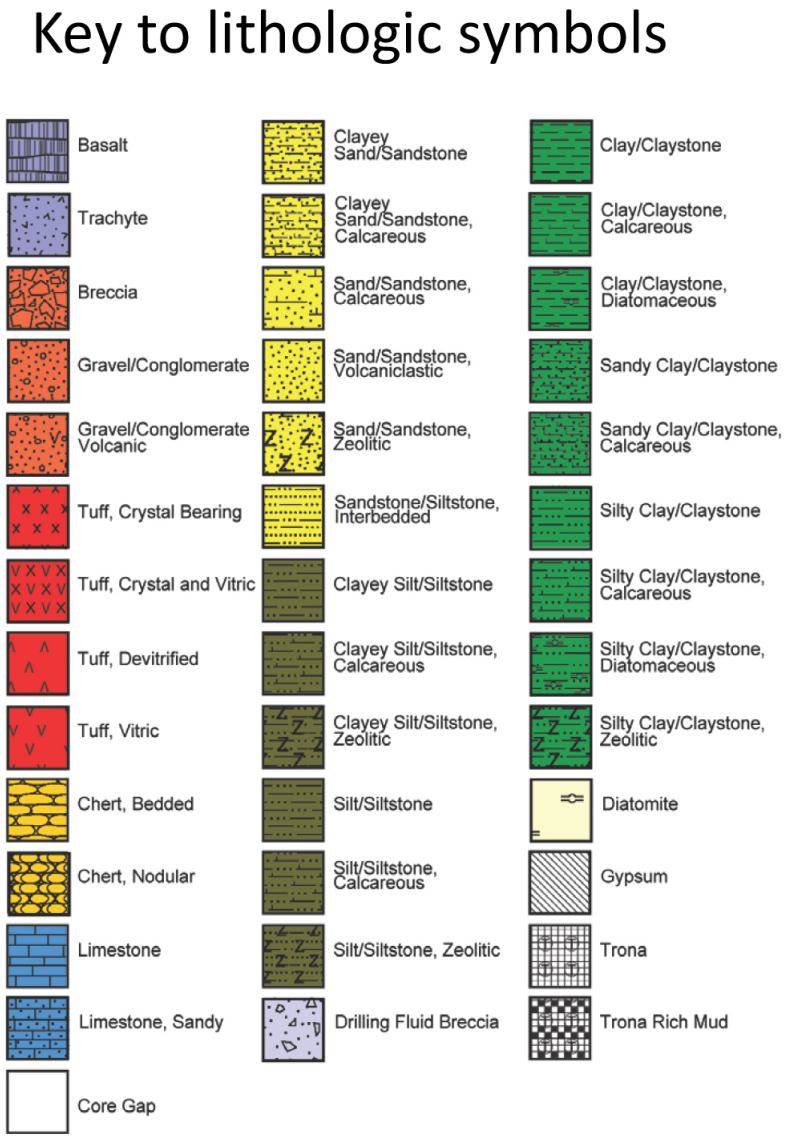

Figure C.1. Lithological key for Figs. 4.1E and 4.2A.

White indicates missing core (i.e. no recovery). Key from Cohen et al. (2016) and based on standardized lithological symbols for core description (https://csdco.umn.edu/resources/software/psicat).

A

Family	Olorgesailie Fm. Acheulean-associated fauna	Oltulelei Fm. MSA-associated fauna	Common name	Feeding strategy (diet)[1]	Body mass estimated average (kg)	Body size class[2]	Water Dependence[3]	References ecology/physiology
Bovidae		*Madoqua* sp.	dik dik	B	6	1b	N	*25,90*
		Antidorcas marsupialis	springbok	M	40	2	L	*90,91*
	Gazella sp.		gazelles	G	40	2	N/L	*90,91*
		Gazella thomsoni	Thompson gazelle	G	25	2	L	*25,90*
	Aepyceros sp.		impala	M	60	2	H	*90,92*
	Megalotragus sp.		large extinct Alcelaphin/hartebeest	G	400	4	Y[4]	
	Alcelaphin size 3a cf. *Alcelaphus*		hartebeest	G	175	3a	H	*25,90*
	Connochaetes sp.		wildebeest	G	250	3b	H	*25,90*
		Damaliscus hypsodon	extinct blesbok	G	70	2	Y[4]	
		Oryx cf. *O. beisa* - Hippotragin oryx size	Beisa oryx	G	200	3a	L	*90,91*
		Hippotragin - roan size	roan antelope	G	280	3b	?[5]	
	Taurotragus sp.		eland	B	600	4	N	*90*
		Taurotragus oryx	common eland	B	600	4	N	*90*
	Tragelaphus scriptus		bushbuck	M	50	2	L	*90*
		Tragelaphus strepsiceros	greater kudu	B	250	3b	L	*90*
		Tragelaphus cf. *T. imberbis*	lesser kudu	B	80	3a	N	*25,90*
	Syncerus (*Pelorovis*) cf. *S. antiquus*		extinct wild buffalo	G	900	5	Y[4]	
	Kobus cf. *K. kob*		kob	G	80	3a	H	*90*
	Redunca sp.		reedbuck	G	50	2	Y	*93*
Giraffidae	*Giraffa* sp.		giraffe	B	1500	5	L	*25,90,92*
Suidae	*Metridiochoerus* cf. *M. hopwood*i		extinct giant warthog genus	G	250	3b	Y[4]	
	Metridiochoerus cf. *M. compactus*		extinct giant warthog genus	G	150	3a	Y[4]	
	Kolpochoerus majus		extinct forest/riverhog genus	G/M	120	3a	Y[4]	
	Phacochoerus sp.		warthog	G	100	2	Y	*25,90*
		Phacochoerus sp.	warthog	G	100	2	Y	*25,90*
Hippopotamidae	*Hippopotamus* cf. *H. gorgops*		extinct hippopotamus	G	3000	6	Y[6]	
		Hippopotamus cf. *H. amphibious*	hippopotamus	G	1500	5	H	*90*
Equidae		*Equus* cf. *E. quagga*	Plains zebra	G	250	3b	H	*90*
	Equus cf. *E. grevyi*		Grevy's zebra	G	400	4	L	*90,92*
	Equus oldowayensis		extinct zebra/horse	G	450	4	Y[6]	
	Eurygnathohippus sp.		extinct horse	G	200	3a	Y[6]	
		Equus aff. *E. capensis*	extinct zebra	G	600	4	Y[6]	
Rhinoceratidae	*Ceratotherium simum*		white rhino	G	2500	5	H	*90*
	Diceros bicornis		black rhino	G	1100	5	H	*90*
		Diceros bicornis	black rhino	G	1100	5	H	*90*
Elephantidae	*Palaeoloxodon* (*Elephas*) *recki*		extinct elephant	G	8000	6	H[6]	
		Loxodonta africana	savanna elephant	M	4500	6	H	*25,90*
Rodentia		*Hystrix cristata*	crested porcupine	M	15	1c	N	*92*
		Pedetes sp.	springhare	G	3	1b	N	*94*
		Lepus sp.	hare	G	2	1b	N	*94*
Primates	*Theropithecus oswaldi*		extinct gelada monkey	G	200	3	Y[6]	

1. Diet: G=grazer B=browser M=mixed grazer/brows
2. Body size class: 0: indet 1: <23kg (1a: <1kg; 1b: 1-10kg; 1c:10-23kg) 2: 23-113kg 3: 113-340kg (3a: Topi size; 3b: Wildebeest/zebra size) 4: 340-900kg 5: 900-270
3. Water dependence: H=high L=low N=none Y=high or low ?=u
4. As a ruminant grazer, classified as water dependent (low or hi
5. Cannot classify indeterminate hippotragin; *Hippotragus* is highly water dependent but not *Oryx*.
6. Family/tribe-level physiological analogue

B

Geological Unit — Ecological characteristic

Body mass category

	Class 6	Class 5	Class 4	Class 3	Class 2	Class 1
Oltulelei Fm.	1	2	2	5	4	4
Olorgesailie Fm.	2	4	4	8	5	0

Water dependent?

	Yes	High	Low	No	Unknown
Oltulelei Fm.	3	4	4	6	1
Olorgesailie Fm.	11	7	4	1	0

Feeding strategy

	Megagrazer	Grazer	Mixed feeder	Browser
Oltulelei Fm.	2	9	3	4
Olorgesailie Fm.	5	14	2	2

Table C.1. Taxonomic composition of Acheulean- and MSA-associated mammalian faunas of the Olorgesailie basin.

Taxonomic composition categorized by body mass, water-dependence, and feeding strategy based on functional morphology and modern taxonomic analogues. ***(A)*** *Ecological characteristics for each taxon.* ***(B)*** *Summary counts of taxa attributed to ecological categories as shown in Fig. 4.1d pie charts comparing Oltulelei and Olorgesailie Fm. Faunas.*

Supplementary Text C.1. Geochronology and core stratigraphy

$^{40}Ar/^{39}Ar$ geochronology (A.L.D.)

Radiometric age control of the core was established by laser incremental heating $^{40}Ar/^{39}Ar$ dating of individual K-feldspar phenocrysts, extracted mainly from pumice lapilli from tephra horizons sampled opportunistically throughout the depth of the core, and from the basal trachyte flow. In total, 1579 incremental heating steps on 294 phenocrysts from 23 samples were analyzed. Based on observations of core lithostratigraphy and smear slide analysis, these samples date 22 distinct tephrostratigraphic units, representing typically discrete volcanic events, but in some cases recording tightly spaced, effectively continuous pulses of pyroclastic volcanism (Deino et al., 2019).

Magnetostratigraphy (J.K., C.W.H.)

A total of 21 discrete cube samples were taken between 152-162 MBS for paleomagnetic analyses in an attempt to identify the Brunhes/Matuyama Boundary (BMB, 0.781 Ma) (Ogg, 2012). The samples were analyzed using a 2-G® Enterprises small-access cryogenic magnetometer with an in-line alternating field (AF) demagnetization coil in the Paleomagnetics Laboratory at the Graduate School of Oceanography at the University of Rhode Island. The initial natural remanent magnetization (NRM) was measured and then the samples were subjected to 21 AF demagnetization and measurement steps starting at 2.5 mT and ending at 100 mT (the field was increased by 5 mT between 5 mT and 100 mT) in order to remove any unstable, viscous remanent magnetizations. Following measurement, the characteristic remanent magnetization (ChRM) declination and inclination values (Kirschvink, 1980) were calculated using the Demagnetization Analysis In Excel (DAIE) tool of Sagnotti (2013). In order to calculate the ChRM, we selected between 6-11 demagnetization steps between 5-80 mT and a least-squares fit was made to the selected data points. The fit was not anchored to the origin of the Zijderveld plot (Zijderveld, 1967) since the ChRMs generally trended towards the origin without forcing and we felt theunanchored option gave a better representation of the data quality demonstrated by the maximum angular deviation (MAD) calculated within the DAIE tool. The criteria for a “quality” ChRM value was that it be calculated from at least 3 consecutive demagnetization steps and the MAD values were less than 15° (Tauxe and Badgley, 1988). The ChRM declination, inclination, and MAD values were plotted versus depth in order to identify any possible reversal boundaries. The MAD values are all less than 10° (all but 3 are <7°) and, considered with the fact that a minimum of 6 demagnetization steps were used in the calculation of the ChRM, indicate that all of the samples produced quality ChRM directions. After ruling out declination changes related to core section breaks and potential coring-induced rotation, we identified a reversal boundary between 153.08-153.15 MBS. This reversal is characterized by an approximately 160° change in declination between the sample at 153.15 MBS and the 2 samples immediately above it (153.03 and 153.08 MBS). Considering the stratigraphic position of this reversal and other age constraints, we suggest that this reversal is the Brunhes-Matuyama Boundary (0.781 Ma).

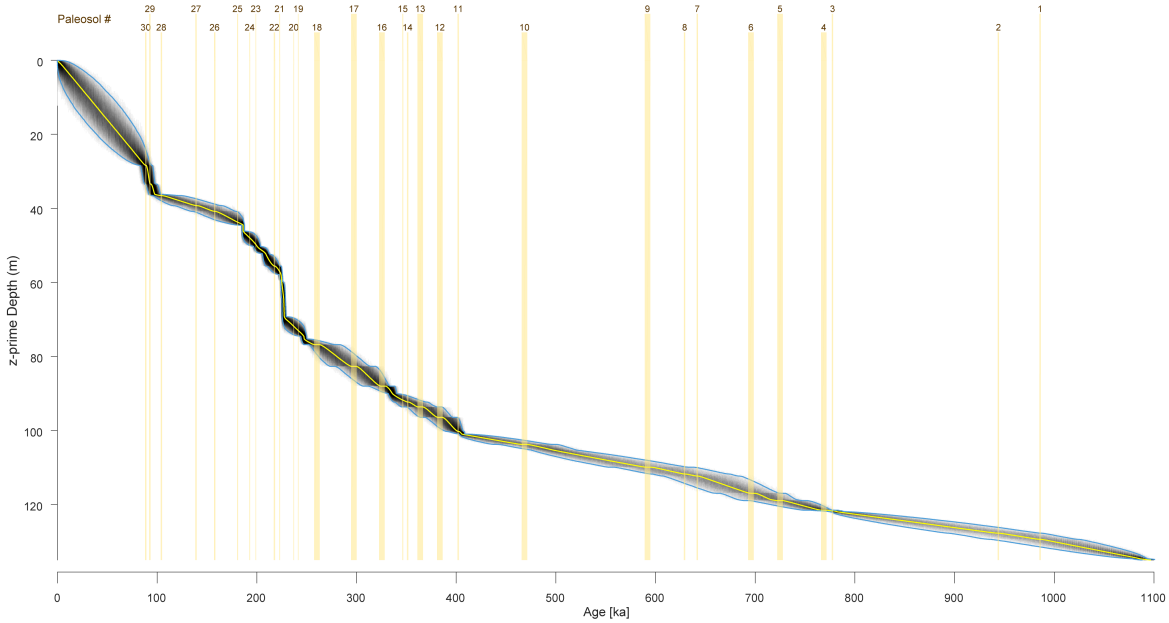

Figure C.2. Bayesian age model.

Bayesian age model for core OLO12-1A on the z-prime depth scale, (compressed depth scale corrected for rapid deposition) (Deino et al., 2019). Yellow line is median age, grey area represents age uncertainty and the blue lines mark the 95% confidence intervals. The age model is calculated at a vertical resolution of one centimeter. Vertical yellow bars represent paleosols and bar thickness indicates duration of stagnant phases. Periods of non-deposition (i.e., soil formation) are taken into account in the age model and represented by a slope of zero in the age model trajectory. Details on the age model are in Deino et al. (2019).

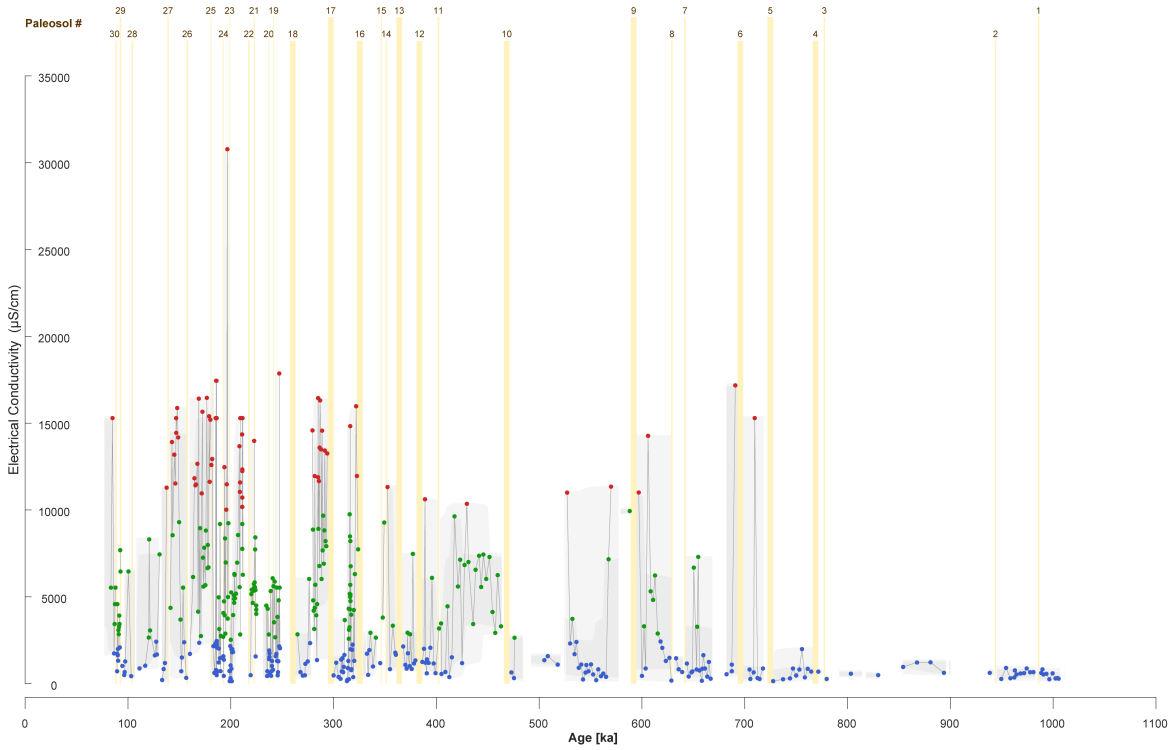

Figure C.3. Water potability.

Electrical Conductivity (EC) (n = 476) of paleolake waters derived from a transfer function approach based on diatom data (see main text: Materials and Methods). Blue, green, and red dots indicate fresh, brackish and saline conditions respectively (2500 µS/cm assumed as the limit of potable water for humans) (World Health Organisation, 2018). Extensive consumption of water values over 10000 µS/cm is harmful to various mammal species (Child et al., 1971). This figure exemplifies our approach of employing drill core data (in this case from diatom samples) to derive water salinity (EC), which is used to infer water potability, an aspect of landscape resource variability that affected mammalian, including hominin, adaptations.

Supplementary Text C.2. Terrestrial trace fossils and minimum water table depth (J.J.S.)

Terrestrial trace fossils were identified by comparison to modern trace fossils produced in Africa by termites and other air-breathing taxa (e.g., ants, beetles, spiders) and published examples from the rock record of Africa (Duringer et al., 2007; Genise, 2017; Roberts et al., 2016; Sands, 1987; Scott et al., 2009; Tschinkel, 2010). Diagnostic ichnotaxabases for termite traces include spreiten-like and meniscate tunnel backfill with sediment aggregates, meniscate-backfilled horizons (i.e. plates), as well as large excavated nests with sharp boundaries and active and/or passive fill with sediment aggregates and brecciated host material. Other terrestrial trace fossils not possible to attribute to particular producers or ichnotaxa were distinguished by sharp boundaries; passive brecciated fill and/or meniscate backfill; rounded margins and/or circular shape. Some have sediment fill different from that of host material and the same as pedogenically modified sediment within the stratigraphic unit.

Meniscate backfill with sediment aggregates was considered to be diagnostic for terrestrial traces in cases where burrows were associated with other features (i.e., vertical fracture networks) passively filled by brecciated sediment.

The minimum water table depth below each of the exposure surfaces (table C.2) was determined as the depth of terrestrial bioturbation observed below the top of the overlying paleosol (exposure surface, as identified by other characteristics, e.g., ped structure). Color, grain-size, and lithology of the burrow fill were used to identify the associated paleosol top in cases where the traces crosscut more than one exposure surface. The focus of this study was the stratigraphic interval with greatest abundance of termite bioturbation, indicating extreme fluctuations in lake-level/base-level/water-table depth in the OLO12-1A core. This interval was from 139.95 to 107.07 mbs, which encompasses paleosol #10 to paleosol #18.

Terrestrial bioturbation extends to as much as 5.18 m below the top of the corresponding overlying paleosol (e.g., paleosol #18; table C.2), which represents the land surface from which the burrows originated. In all cases in the OLO12-1A core, the deepest terrestrial traces present within each interval are attributed to termites. Although there is some variability in the depth of bioturbation between intervals, in almost all cases bioturbation crosscuts nearly the full thickness of the interval (from 74% to 96%), and extends up to as much as 2.91 m below the paleosol bottom depth (e.g., paleosol #18 bottom depth: 109.66 mbs; trace fossil bottom depth: 112.57 mbs). The interval capped by paleosol #13 is an anomaly in the pattern, with only 49% of the total depth of the sedimentary interval bioturbated by termite traces. This may be due to an artificial representation of the values for this interval, as core disturbance in section OLO12-1A-67Q-2-A did not allow for detailed observation.

Paleosol #	Age (ka)	Estimated duration (y)	Paleosol top depth (mbs)	Deepest terrestrial trace in interval (mbs)	Thickness of interval (m)	Minimum water table depth in interval (m)
18	262.91	5000	107.39	112.57	6.09	5.18
17	299.82	5000	113.48	118.21	5.35	4.73
16	328.93	5000	118.83	123.97	5.63	5.15*
15	346.94	250	122.64			
14	352.42	750	123.13			
13	367.21	5000	124.46	125.87	2.88	1.41**
12	386.72	5000	127.34	131	3.83	3.66
11	402.86	750	131.17	133.77	3.51	2.6
10	470.73	5000	134.67	139.37	6.21	4.7

Table C.2. Minimum water table depth.

Minimum water table depth below exposure surfaces (last column) by stratigraphic interval between 470.73 ka and 262.91 ka, represented by the depth to deepest terrestrial trace fossil below paleosol top within the core. See supplementary text C.2.

Supplementary Text C.3. Use of Si/K as an indicator of water availability (M.S., E.T.B.)
Variations in the biogenic silica content of lacustrine sedimentary archives are frequently interpreted as records of changing diatom productivity, and of lake productivity more generally. However, in highly alkaline saline waters such as Na_2CO_3 brines, diatoms are subject to dissolution so sedimentary records can also reflect water composition (Fritz et al., 2010). In saline systems variations in biogenic silica can be used as proxy of changes in paleosalinity with enhanced preservation at times of fresher waters.

Biogenic silica analyses by classic wet chemical methods are labor intensive and time consuming. Recently XRF scanning techniques have been utilized to provide a rapid and non-destructive approach to obtain high-resolution records that reflect changing BSi contents of lake sediment. In order to minimize Si variation due to dilution by biogenic material or carbonate minerals, XRF data are frequently reported as Si/Ti (Brown, 2015). Ti often serves as a proxy for silicate mineral content because XRF Al datasets are noisy due to the weak fluorescence from this light element. In the case of ODP-OLO12 drill cores, we found a good correspondence between XRF Si/K ratios and diatom counts, and determined that potassium is a better proxy for silicate minerals than Ti. ODP-OLO12 sediments are rich in volcanoclastic materials, and the Ti content of bulk silicates varies as a function of enrichment of sedimentary heavy minerals.

In general, higher Si/K ratios reflect lower salinity in ODP sediments. We note that Si/K can also be impacted by biogenic silica from other autochthonous sources (e.g., chrysophytes and sponges) and biogenic and non-biogenic allochthonous sources (e.g. grass phytoliths and quartz). However, the overall strong correspondence between Si/K and diatom counts indicates that diatom contents are the major source of variability in sedimentary Si content and gives us confidence in this high-resolution data set.

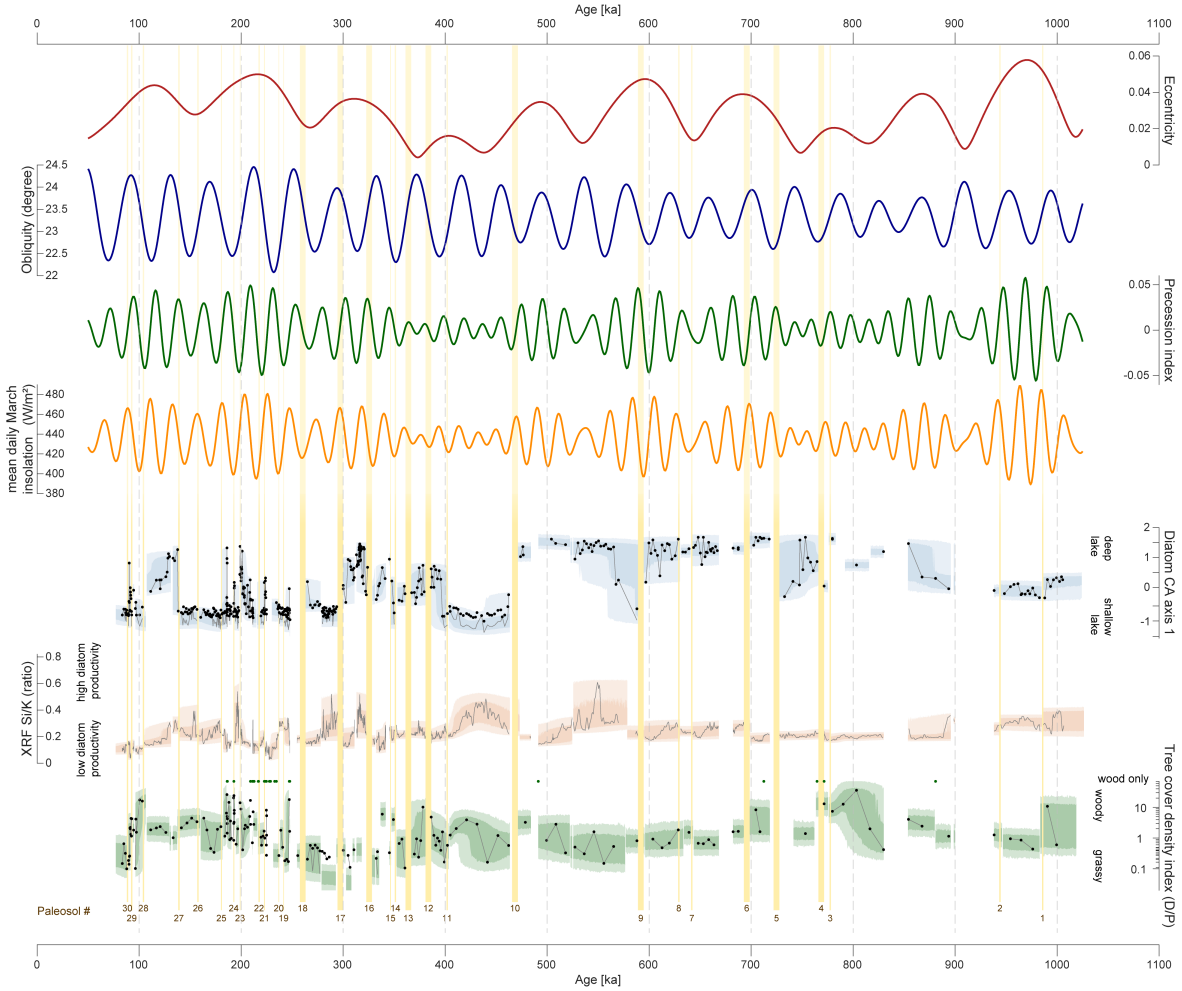

Figure C.4. Earth's orbital cycles in comparison to key data sets from core ODP-OLO12-1A.
Variation in orbital cycles of the past 1 Ma are shown in the top rows (Laskar et al., 2004). Curves show orbital eccentricity, obliquity (tilt) and precession, as well as resulting mean daily insolation for March at the latitude of the drilling location (1.8°S). Lower part shows selected paleoenvironmental data sets (diatom CA 1 axis indicating changes in lake depth, Si/K ratio indicating diatom productivity, phytolith D/P index indicating tree cover). Spectral analyses of these three indicator data sets are shown in Fig. 4.4. Vertical yellow bars denote paleosols shown centered on their median ages.

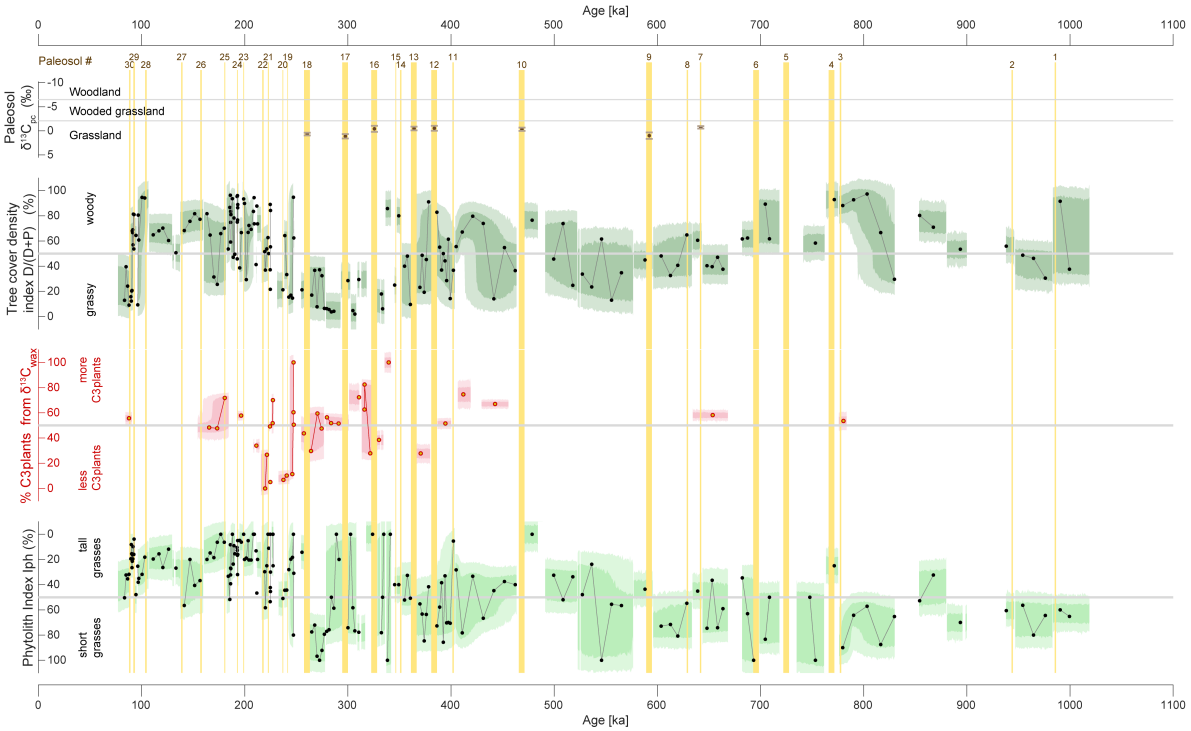

Figure C.5. Vegetation proxy results for core ODP-OLO12-1A.
Comparison between pedogenic carbonate δ 13C pc data, an alternative phytolith tree cover index, leaf wax δ13Cwax, and the phytolith Iph index. Stable carbon isotope values of carbonate nodules (δ 13C pc) from paleosols (n = 8); vegetation classes from Gasse (1986, 1980)*. The alternative phytolith tree cover index is based on equation D/(D+P)*100 and the same phytolith assemblage data (n = 218) as for the conventional D/P index shown in Fig. 4.3b. The alternative calculation integrates samples in which only wood phytoliths were present; higher values indicate denser woody cover. This percentage presentation is used to facilitate comparison with other vegetation signals. We note, however, that the percentage data are not reflecting the actual proportion of woody cover in a landscape and advise to use the conventional phytolith D/P index (Fig. 4.3b) which is widely used. Stable carbon isotope data of higher plant leaf waxes (δ 13C wax , n = 37) indicate the relative amount of C 3 vs. C 4 plants (see main text Materials and Methods). Phytolith index (Iph) from grass phytolith data indicate proportion of short (Chloridoideae) vs. tall (Panicoideae) grasses (n = 183) (Bremond et al., 2005b). All data sets are plotted at their corresponding median age. Dots denote single data points; lines connect single data points; envelopes reflect 68% (dark) and 95% (light) confidence intervals in the reconstructions, based on analytical and age model errors (Deino et al., 2019). Continuity of the data and the uncertainty envelopes are interrupted at hiatuses, non-recovery intervals, and proxy measurement gaps. Vertical yellow bars denote paleosols shown centered on their median ages.*

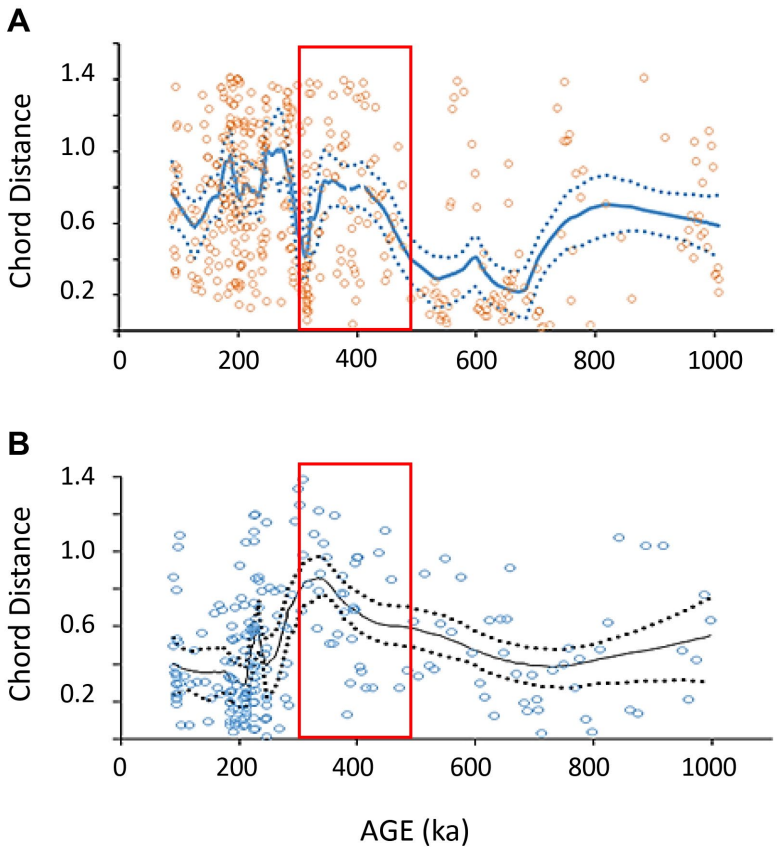

Figure C.6. Interassemblage variability in diatom taxa and phytolith morphotypes in samples through the ODP core OLO12-1A, from ~1.084 Ma to ~90 ka.

Chord distances (open circles) indicate change in assemblage composition through the sequence. High values represent more turnover; low values represent less turnover between stratigraphically adjacent assemblages. LOESS regression of chord distances minimizes variability between assemblages in order to highlight longer-term trends (dashed lines = 95% CI). Red rectangle indicates the window of evolutionary transition, 500-320 ka. ***(A)*** *For diatoms, interassemblage taxonomic variability rises above older regression values between ~425 and ~350 ka, during the interval when we infer the faunal turnover and the Acheulean-MSA transition occurred. Overall, interassemblage variability exhibits strong, rapid oscillations throughout the period from ~425 to 90 ka.* ***(B)*** *For phytoliths, interassemblage variability spikes between ~400 and ~350-300 ka, coinciding with the shifts in hominin and faunal adaptations, after which phytolith assemblages exhibit greater stability.*

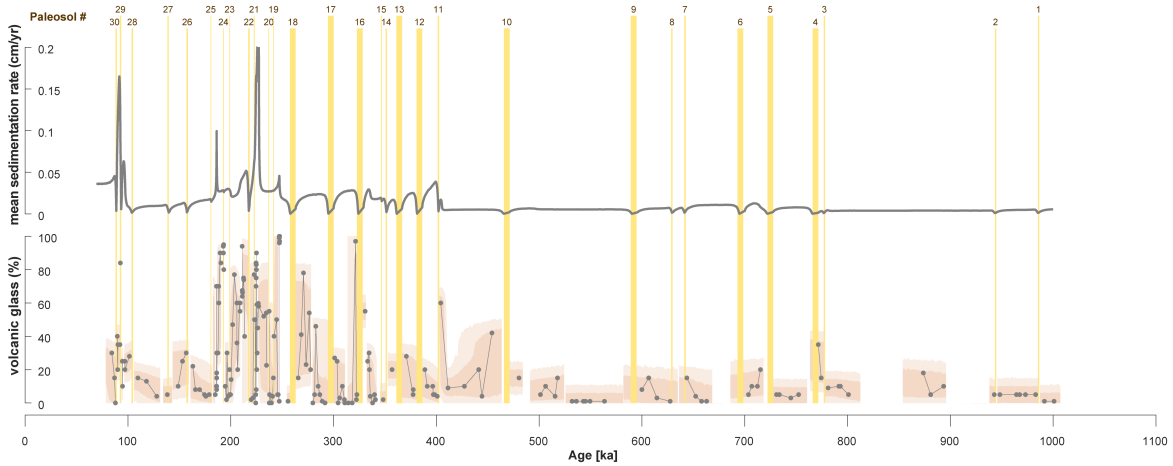

Figure C.7. Sedimentation rate and percentage of volcanic glass in core ODP-OLO12-1A.
Derived sedimentation rate (in cm/yr) and percentage of volcanic glass based on complete microscopic sediment composition. Sedimentation rate is derived from the median age output of the Bayesian age model and the z-prime depth scale (Deino et al., 2019). Vertical yellow bars represent paleosols; bar thickness represents the duration of stagnant phases.

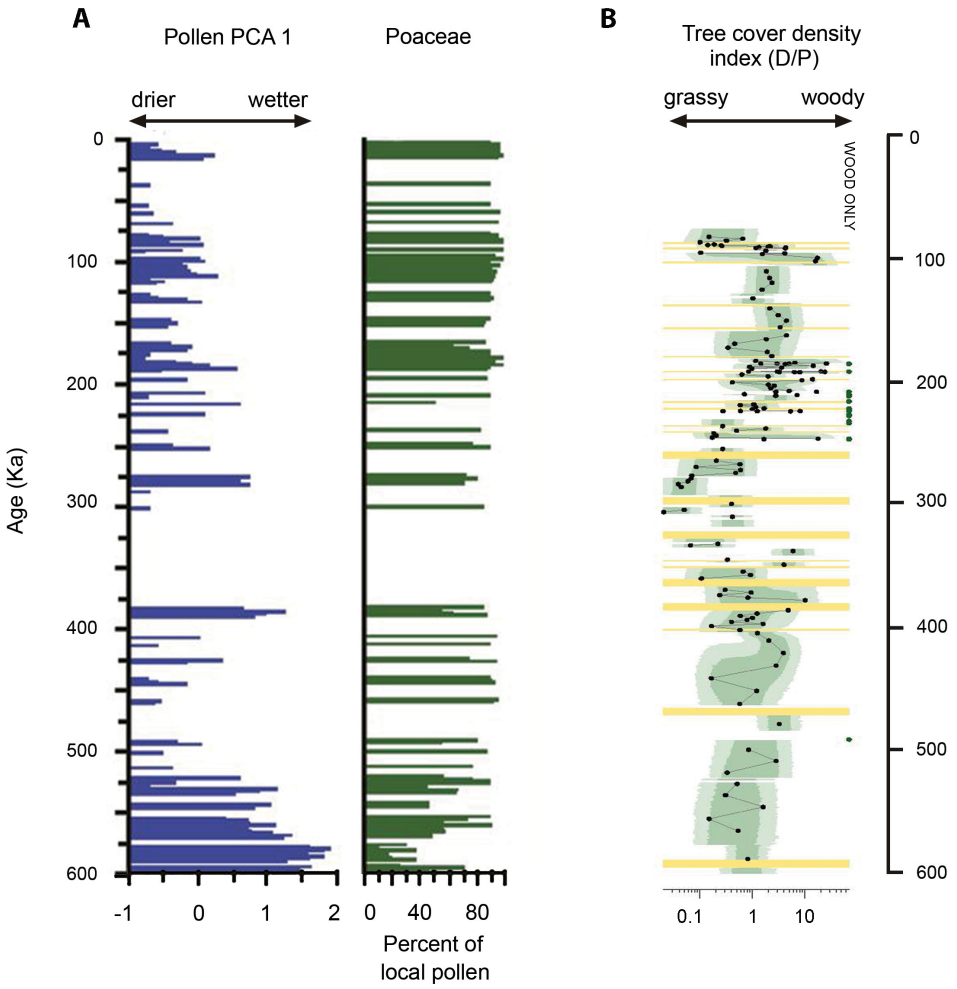

Figure C.8. Divergent vegetation signals evident in adjacent basins of the southern Kenya rift over the past 600,000 years.

(A) *Drill core data from the MAG14-2A Magadi basin pollen record (Owen et al., 2018), and* ***(B)*** *the ODP-OLO12-1A Koora basin phytolith woody cover density record (D/P index, Fig. 4.3b). Magadi pollen PCA 1 is interpreted to reflect an overall trend toward drier climate (progressive aridification (Owen et al., 2018)) from ~575 ka to ~50 ka. Percentage grass taxa (Poaceae) remains high throughout this interval of the Magadi record, but rises dramatically over time relative to other local taxa (wetland Cyperaceae). Coverage in the time window between ~400 to 300 ka is modest. By contrast, the Koora basin core exhibits evidence of strong fluctuation in woody-grassy vegetation, including times of predominantly woody vegetation (and predominantly tall grass; Iph index, Fig. 4.3B), with no overall vegetation trend toward drier conditions. $\delta^{13}C$ wax and $\delta^{13}C$ org also show strong shifts between grassy and wooded conditions (Fig. 4.3B), providing further support for different vegetation and water supply histories in the two basins over the past 600,000 years.*

A

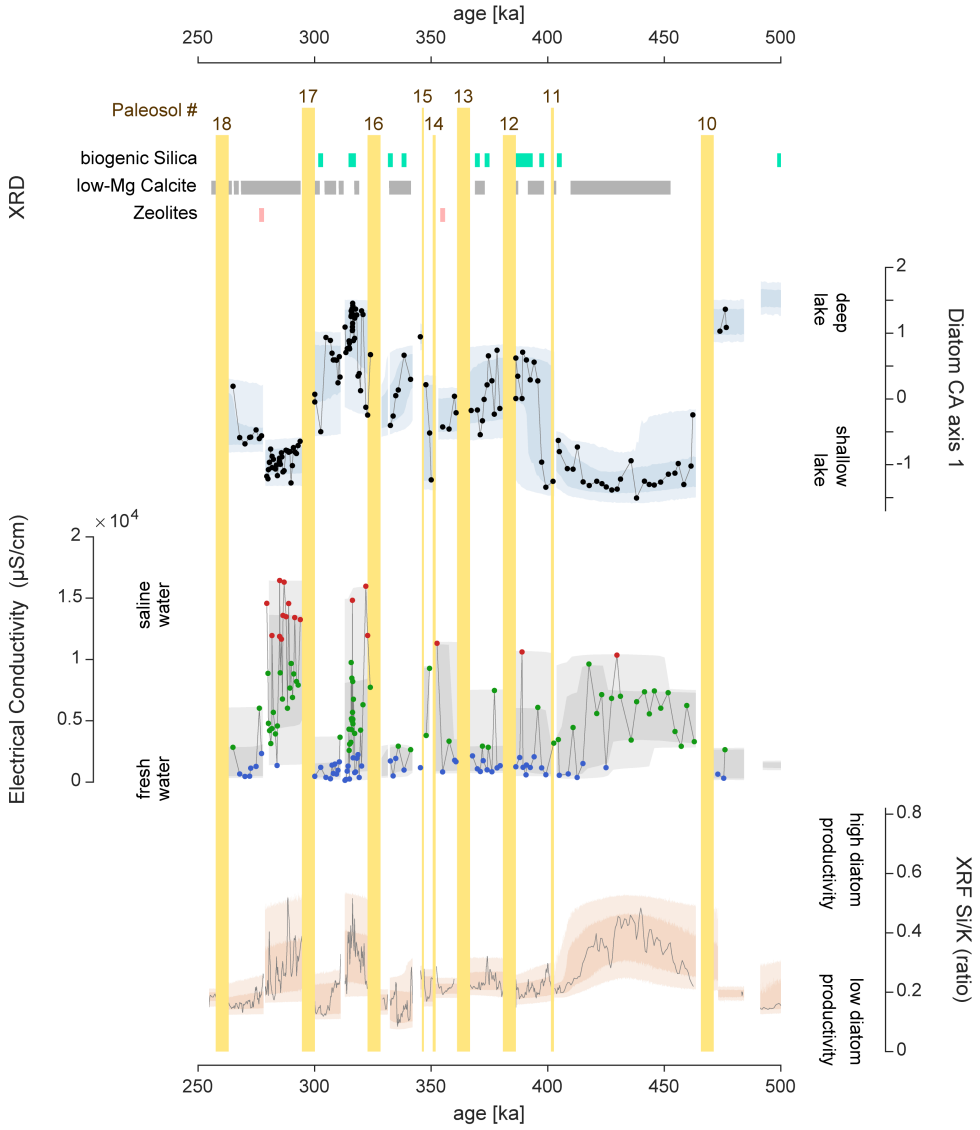

Figure C.9. Expanded data sets covering the critical window between 500 ka and 300 ka.
Expanded data sets covering the critical window between 500 ka and 300 ka. ***(A)*** *water availability, enlarged from main text Fig. 4.3a.*
(Figure continued on next page)

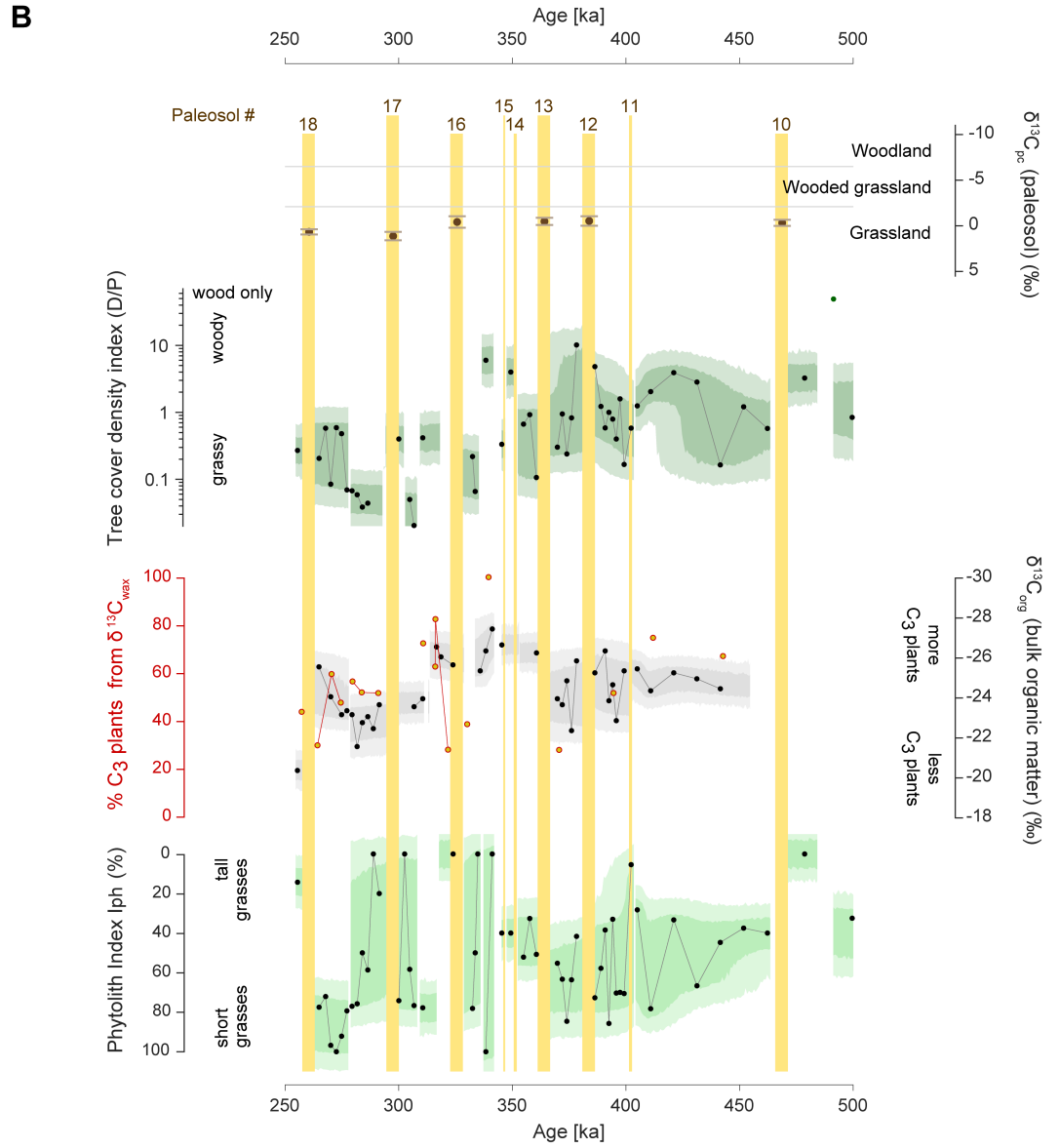

Figure C.9. (continued). Expanded data sets covering the critical window between 500 ka and 300 ka. *Expanded data sets covering the critical window between 500 ka and 300 ka.* ***(B)*** *vegetation dynamics, enlarged from main text Fig. 4.3b.*

Appendix D

Supporting information for Chapter 5

This appendix contains supporting information for Chapter 5, *"An early Holocene river system along the Kenya Rift valley and its influence on faunal exchange and longitudinal diversity gradients in East Africa"*. This includes a supporting discussion about the rainfall in Kenya, supplementary text about the methods (reservoir correction and radiocarbon age selection), as well as additional supporting figures (Figs. D.1 to D.9) and tables (D.1 to D.6).

Supporting Discussion: Past and present rainfall in Kenya

The topography of East Africa strongly modulates the amount and distribution of rainfall (Fig. D.1c–D.1d). Orographic precipitation is today prevalent across the central Kenya highlands (Nicholson, 2017), which receive mean annual rainfall of more than 2000 mm and have a positive moisture balance, in marked contrast to the adjacent semi-arid lowlands and the moisture-deficient rift valley (Bergner et al., 2009) (Fig. D.1d). The high rainfall at the 3000 and 4000 m high rift shoulders of the Mau Escarpment and the Aberdare Range generates runoff that today feeds into Lakes Naivasha, Nakuru, and Natron (Olaka et al., 2010). During the early Holocene a stronger monsoonal circulation produced about 20-30% more rainfall in East Africa than today in response to higher Northern Hemisphere summer insolation and increased greenhouse gas forcing (Kutzbach, 1981; Kutzbach and Street-Perrott, 1985; Otto-Bliesner et al., 2014). Orographic forcing by the central Kenyan highlands would therefore have generated even more precipitation and runoff over mountainous areas at this time, and the moisture supply to the Aberdare Range was indeed higher during the early Holocene than at present (Street-Perrott and Perrott, 1990). The abrupt increase in rainfall with the onset of the Holocene (Tierney et al., 2011; Verschuren et al., 2009) would have rapidly filled the headwater lake basins to their overflow levels, possibly within as little as 200 years according to lake-balance modeling (Bergner et al., 2003). Enhanced dry season rainfall during the early Holocene (Tierney et al., 2011) would have maintained river flow, in contrast to the present situation where flow in many Kenyan rivers is reduced or ceases during the biannual dry seasons (Olaka et al., 2016; Tarras-Wahlberg et al., 2002). Earlier cessation of overflow from Lake Nakuru-Elmentaita (by about 8.6 ka) than that of Lake Naivasha can be explained by the small catchment area of this basin as compared to the latter (Bergner et al., 2009) (Fig. D.1c).

Supplementary Methods: Radiocarbon reservoir correction

Previous studies have noted significant disagreement in the timing of highstands in East African lakes during the African Humid Period (e.g., Garcin et al., 2009; Tichy and Seegers, 1999; Tiercelin et al., 1981; Young and Renaut, 1979). We note that it was only possible to establish the synchronicity of overflow lake levels and the connectivity between all major lake basins by applying ^{14}C reservoir corrections to the chronologies of Lakes Magadi-Natron, Siriata, Baringo-Bogoria and Suguta. Reservoir-affected ^{14}C dates have significantly older ages of the order of 2000 – 4000 years than ages derived from reservoir-free ^{14}C dates, U/Th dates, or ^{137}Cs dates, which now constrain the reservoir effects for these basins (De Cort et al., 2013; Garcin et al., 2017). The source of depleted radiocarbon can be attributed to the continual release of mantle-derived CO_2 along faults and from hot springs in the tectonically active rift-floor area (Lee et al., 2016). Whether or not Nakuru-Elmenteita, Naivasha and Menengai sediments also contain this source of chronological error (which is apparently negligible in Lake Turkana; Garcin et al., 2012) remains to be investigated.

Lake Suguta

A reservoir effect of Lake Suguta was first investigated by Junginger et al. (2014), who derived a mean reservoir factor of 1900 ^{14}C years based on age offsets of four pairs of charcoal and carbonate dates (1570, 1940, 1970 and 2240 ^{14}C years). Garcin et al. (2017) showed that the mean reservoir effect has a large error (1σ= 275 ^{14}C years), indicating that the reservoir effect likely changed over time. Garcin et al. (2017) therefore established a reservoir model and applied following reservoir factors: 1570±80 ^{14}C years for dates ≥10930±50 ^{14}C BP, 2240±65 ^{14}C years for dates from 10795±50 to 10205±45 ^{14}C BP, 1970±70 ^{14}C years for dates from 10025±45 to 7850±50 ^{14}C BP and 1940±65 ^{14}C years for ages ≤6345±40 ^{14}C BP. We followed this approach for correcting carbonate-derived radiocarbon dates from Lake Suguta.

Lake Baringo-Bogoria

Both Lake Baringo and Lake Bogoria receive groundwater from on- and offshore hydrothermal springs, partly from deep sources (Dunkley et al., 1993; Renaut et al., 2017; Tarits et al., 2006). CO_2 is the dominating free-phase gas released by many of these springs that mixes with the lake water of Baringo. The CO_2 from hot springs of the northern Kenya Rift (including Lake Baringo) has a mean $\delta^{13}C$-CO_2 value of -9.2‰ (-5.4‰ to -14.6‰; n= 7; Dunkley et al., 1993), which is very similar to the carbon isotope composition of CO_2 of the Magadi-Natron springs (mean -8.0‰; Lee et al., 2016) and strongly indicates to be derived from the upper mantle (Darling et al., 1995). Hence a substantial ^{14}C reservoir effect for Lakes Baringo and Bogoria can be assumed and was already suspected by Young & Renaut (1979), Tiercelin et al. (1987, 1981) based on conspicuously old radiocarbon ages. An indication of a reservoir effect is given by two published ^{14}C dates obtained from the same interval (128-131 cm) of core Bogoria I for which bulk organic matter is dated to 4790±280 ^{14}C yr BP but the carbonate fraction to 10400±470 ^{14}C yr BP (difference of 5610 ^{14}C years) (Tiercelin et al., 1987). Because organic matter could also have been influenced by ^{14}C depleted carbon the age difference does not provide an unequivocal reservoir factor. De Cort et al. (2013) estimated the modern reservoir effect for Lake Bogoria from a ^{14}C date of 4160±35 ^{14}C yr BP at 40.5 cm depth and the ^{137}Cs activity (1964 peak at 35 cm) in core BOG01-1P. The ^{137}Cs-based extrapolated age at 40.5 cm is 1943 (or 182 ^{14}C yr BP) and the deduced ^{14}C reservoir effect is 3980 ^{14}C years (De Cort et al., 2013), which

we applied to all radiocarbon dates from Lakes Baringo and Bogoria (given the direct overflow of Lake Bogoria waters into Lake Baringo during the early Holocene).

Lake Siriata

We investigated the ^{14}C reservoir effect of Lake Siriata by comparing radiocarbon dates from three sample pairs consisting of charcoal and biogenic carbonates (i.e. *Corbicula* sp. shells); each pair collected from the same depth interval of lacustrine sediment deposits (Table D.3). Two shell dates (Poz-78499, Poz-78500) collected 20 cm apart from the same outcrop (KOO15-6B) are chronologically reversed (13600±70 ^{14}C BP vs. 13240±70 ^{14}C BP), while the corresponding charcoal dates (9220±100 ^{14}C BP vs. 9310±100 ^{14}C BP) are in chronological order resulting in significantly different reservoir effects (4380±120 ^{14}C years vs. 3930±120 ^{14}C years). These differences indicate that the reservoir effect was fluctuating on short (centennial) timescales, but the temporal overlap of the two charcoal dates precludes us from resolving the time when the reservoir effect had changed. A third reservoir factor has a comparable duration (3980±120 ^{14}C years) but was obtained from ca. 600-year younger sediments from a different outcrop (KOO15-3E). Given the consistent magnitudes of the age offsets we advocated to apply an average reservoir factor of 4095±180 ^{14}C years, which was subtracted from all carbonate ^{14}C dates (Table D.3). We also applied this reservoir effect to a ^{14}C date of fish bones (Poz-89660) from adjacent Lake Kwenia in the absence of a local reservoir factor (Table D.3).

Magadi-Natron

Both Lakes Magadi and Natron are fed by numerous hot springs, aligned along normal faults, from which mantle-derived CO_2 degasses (Lee et al., 2016). Given the deep and magmatic origin of this CO_2 it can be safely assumed to be depleted in ^{14}C ('dead carbon'). The constant recharge of fluids rich in mantle-derived CO_2 into Lakes Magadi and Natron necessitates the correction of radiocarbon dates by a local reservoir factor. However, for these lakes no parallel radiocarbon dates on lacustrine and terrestrial matter are available to infer a reservoir effect in the standard way. To establish a ^{14}C reservoir effect for the Magadi-Natron Basin we compared U/Th and ^{14}C dates from core NF1 from Lake Magadi published by Taieb et al. (1991) and Roberts et al. (1993). Two U/Th dates were obtained from the depth interval 148-168 cm of core NF1: 1) 10970±750 yr BP (range: 10220-11720 yr BP) on organo-phosphates and 2) 8500±2000 yr BP on sodium-silicates (Taieb et al., 1991). We discarded the second (younger) U/Th date because of its very large error, which would result in a highly uncertain temporal duration of the reservoir effect (~±2000 years).

The mean value of the 10970±750 yr BP U/Th date (= 10970 calendar years BP) is equivalent to 9560±16 ^{14}C yr BP on the IntCal13 radiocarbon calibration curve (Reimer et al., 2013). The lower bound U/Th date of 10220 BP equals 9031±14 ^{14}C yr BP and the upper bound U/Th date of 11720 BP equals 10102±20 ^{14}C yr BP on the IntCal13 curve. Incorporating all sigma ranges yields an equivalent radiocarbon age of 9560±550 ^{14}C yr BP for this U/Th date (for error propagation we calculated the square root of the sum of squares of both the ^{14}C error and the reservoir error).

Three radiocarbon dates were obtained by Taieb et al. (1991) and Roberts et al. (1993) on total organic matter from intervals adjacent to or partly overlapping with the U/Th sample of Magadi core NF1. The radiocarbon dates are 12200±357 ^{14}C yr BP from 168-178 cm (conventional date, sample no. NF173, lab no. LGQ 134; Taieb et al. 1991), 11110±110 ^{14}C yr BP from 139-140 cm (AMS date,

lab no. OxA-3284; Roberts et al. 1993) and 11420±110 ^{14}C yr BP from 167-168 cm (AMS date, lab no. OxA 3285; Roberts et al. 1993). Subtracting the ^{14}C age of 9560±550 BP from these three radiocarbon dates yields following ^{14}C reservoir factors:

a) 12200±357 ^{14}C yr BP - 9560±550 ^{14}C yr BP = 2640±655 ^{14}C years (0-10 cm below the U/Th date)

b) 11110±110 ^{14}C yr BP - 9560±550 ^{14}C yr BP = 1550±560 ^{14}C years (8-9 cm above U/Th date)

c) 11420±110 ^{14}C yr BP - 9560±550 ^{14}C yr BP = 1860±560 ^{14}C years (overlapping with the lowermost 1 cm of the U/Th date)

These three reservoir factors overlap from 1985 – 2110 ^{14}C years. The mean of this overlapping range is ~2050±63 ^{14}C years. We adopt this approximation of 2050±63 ^{14}C years for the reservoir correction of bulk and carbonate-based ^{14}C dates from Lake Magadi-Natron. We note that this reservoir factor is probably a conservative estimate as the second U/Th date from core NF1 would yield an average reservoir factor almost twice as large (~3870 ^{14}C years), which is similar to the 4095±180 ^{14}C year reservoir effect of the adjacent Lake Siriata.

Selection of radiocarbon dates for deriving overflow ages

All published radiocarbon dates used in this study are listed in Table D.2. In most cases, we reconstructed overflow conditions from radiocarbon samples that were deposited at overflow elevations. Our analysis therefore required good documentation of sample elevations of published radiocarbon dates. It is possible that nearly identical radiocarbon dates (overlapping sigma ranges) had been obtained from the same lake at both an overflow elevation (e.g. in a (near) shoreline setting) and an elevation below overflow level (indicating closed basin conditions). In such ambiguous case we gave priority to the higher-elevation sample as it is hard to explain how a sample could have been deposited above a paleo-lake surface, but conceivable that material could have concurrently been deposited below the lake surface (i.e. lake bottom) as well. We therefore attempted to restrict the selection of radiocarbon dated samples to those representing (near) shoreline conditions and wherever possible avoided samples collected from (thick) stratigraphic sections or sediment cores as these mostly stem from deposition under a deeper water column. However, if sediment proxies (e.g. diatoms) from such sections/cores clearly indicated open (overflow) conditions we considered them as well.

Lake Turkana

Garcin et al. (2012) provided a comprehensive and rigorous synthesis of published and new radiocarbon dates from the Lake Turkana Basin and established a robust lake level reconstruction with 105 ^{14}C dates and their corresponding sample elevations. Here we used only those dates (n=37) listed in Garcin et al. (2012) which were obtained from sample locations that were at or close to the former land-water-interface of Lake Turkana (near-shore/shoreline/beach deposits), thus clearly indicating former lake levels. We excluded dated samples from benthic sediments and those with equivocal sample context (e.g. sands, sandy silt, lacustrine deposition, archeological excavation). The reported elevations for the selected radiocarbon dates were used to determine the timing of overflow above the outlet sill located at an elevation of 457-460 m. However, it should be noted that extensional tectonism and associated normal faulting resulted in subsidence of the central Turkana Basin

floor and flexural uplift of the basin margins creating substantial relief differences over the Holocene and hence diverse elevations for the maximum highstand shorelines (MHS) across, at least, the southern Turkana Basin (Garcin et al., 2012; Melnick et al., 2012). Garcin et al. (2012) corrected their sample elevations for subsidence, which are used here. Further radiocarbon dated stratigraphic sections and sediment cores from Lake Turkana are published by e.g. Forman et al. (2014), Morrissey and Scholz (2014), Bloszies et al. (2015), and Beck et al. (2019b, 2019a). Yet these studies do not add definite evidence for additional overflow periods than those based on the Garcin et al. (2012) reconstruction and several of the dated samples remain uncertain in terms of their absolute elevations at the time of deposition due to the deformation of the Turkana Basin.

Lake Suguta

Lake level fluctuations of Lake Suguta were reconstructed by Bishop (1975), Truckle (1976), Casanova et al. (1988), Garcin et al. (2017, 2009) and Junginger et al. (2014), together reporting 68 radiocarbon dates from the Suguta valley. The reconstruction of past lake levels in the Suguta valley is complicated by Holocene crustal deformation (subsidence due to extension, normal faulting, tilting of blocks and isostatic rebound) which resulted in different absolute elevations of the maximum highstand shoreline (MHS) across the Suguta valley and in lower elevations of all MHS ($\leq$567 m) expressions than the present elevation of the outlet sill (581 m; Melnick et al., 2012). For reconstructing overflow conditions, we selected only dates (n=14) from Garcin et al. (2009) and Junginger et al. (2014) which indicated deposition close to the former land-water interface (shoreline). Various sample sites of the Suguta valley are steep-sided volcanic cones from which lake deposits could have been transported or eroded to lower elevations after deposition (especially with desiccation of the basin). We therefore followed a very conservative approach when selecting radiocarbon dated samples for this basin. We also did not include samples from (within) thick stratigraphic sections given the uncertainty of relating them to past lake surface elevations and avoided the use of published ^{14}C dates from older publications as these often lacked sufficient information regarding sample elevations. Yet, several ^{14}C dates from this earlier work (Bishop et al., 1975; Casanova et al., 1988; Truckle, 1976) with identified fossil fish (*Oreochromis*, *Lates* etc.) from stratigraphic sections were considered for the documentation of past fish dispersal.

Lakes Baringo and Bogoria

Lake Bogoria is surrounded by a series of shorelines (including stromatolitic deposits) between 990.7 m and 999 m (Tiercelin et al., 1981), which is 10 m above the modern lake level (989 m in 2003; De Cort et al., 2013) and represents the overflow elevation of this lake (Loboi Sill: drainage divide between Bogoria and Baringo). Due to its narrow half-graben-shape Lake Bogoria can fluctuate by several meters over subdecadal timescales (De Cort et al., 2013; Renaut, 1982). For example, it rose to up to 996 m around 1900, ~997 m in 1928, 994 m in 1979 (Renaut, 1982; Tiercelin et al., 1981) and to over 992 m in 2012 (De Cort et al., 2013). Therefore, paleo-shoreline indicators at these elevations could have been influenced by post-depositional alteration during the past few centuries. Stromatolites occur at 999 m (dated to 4140$\pm$60 ^{14}C BP) and at 995 m (dated to 3880$\pm$60 and 3750$\pm$180 ^{14}C BP; Tiercelin et al., 1981; Vincens et al., 1986). Given the substantial reservoir effect in Lake Bogoria the stromatolites could potentially have formed more recently than the derived Mid-Late Holocene ages or, alternatively, could have diagenetically incorporated younger carbon during subaerial exposure (Renaut, 1982). Because of these chronological uncertainties we avoided the use

of radiocarbon dated stromatolites from Lake Bogoria. Although sediment cores from Lakes Bogoria and Baringo indicate freshwater conditions for the early Holocene (e.g., Tiercelin et al., 1981), they either contain multiple age reversals likely related to the reservoir effect, lack sufficient age control or do not cover the entire Holocene (De Cort et al., 2013; Tiercelin et al., 1987, 1981). We therefore also omitted dated sediment cores from these lakes in this study. Consequently, we restricted the reconstruction of overflow to radiocarbon dated shells deposited on paleo-shorelines from Baringo, Bogoria and the intervening Loboi Plain.

Lake Menengai

Lake sediments deposited up to an elevation of 1860 m and thus indicating overflow are present in the eastern part of the Menengai Caldera (Leat, 1984), but this outcrop remains to be dated. We therefore used the only available radiocarbon dates from other lacustrine deposits inside the Menengai Caldera (Riedl et al., 2020; Chapter 3).

Lake Nakuru-Elmenteita

We used radiocarbon dates from sediment cores of modern Lakes Nakuru and Elmenteita, for which detailed diatom records indicate the sequence of open (overflow conditions) and closed basin conditions (Richardson, 1972; Richardson and Dussinger, 1986). We integrated the core dates with radiocarbon dates on former shorelines and dates from sediment strata from various archeological investigations in the basin that both constrain past lake level fluctuations given their elevations with respect to the overflow level.

Lake Naivasha

Shorelines of the Lake Naivasha Basin have not been dated yet and only one onshore date is available that directly indicates a past lake level (Protsch, 1976). We therefore relied on two dated sediment cores that cover the Holocene (Richardson and Dussinger, 1986; Richardson and Richardson, 1972). Detailed diatom records are available from these core studies, from which closed and open (fresh) conditions were reconstructed by Richardson and Richardson (1972) and Richardson and Dussinger (1986).

Lake Siriata

We dated lake sediments of Lake Siriata that in one case overlay a dated paleosol, which indicates dry conditions prior to the onset of the Holocene. The lake sediments preserve diatom assemblages which indicate open, fresh conditions (data unpublished) and all sediment packages can be related to a single shoreline at the overflow elevation directly dated by Ar-Ar of beach pumices to the early Holocene. The lack of regressive shorelines indicates the rapid desiccation of the lake basin.

Lake Magadi-Natron

Absolute lake levels were reconstructed by Hillaire-Marcel et al. (1986) from dated stromatolites surrounding the entire Magadi-Natron Basin, which was fully adopted here. We did not consider sediment core studies (e.g., Roberts et al., 1993; Taieb et al., 1991) due to uncertainties in translating sediment proxy data into absolute lake levels for this endorheic basin. The local reservoir effect also necessitates a reassessment of original core data interpretations such as the proxy-based lake level reconstruction by Roberts et al. (1993). Applying the reservoir effect of 2050 years to their recon-

struction would place the onset of maximum lake levels to the early Holocene instead of the originally proposed Late Glacial period (a similar temporal adjustment was made for the Suguta record of Garcin et al. (2009) with a ^{14}C reservoir-adjustment by Junginger et al. (2014) and Garcin et al. (2017)). This reservoir effect-corrected lake level reconstruction would then be synchronous with the highstand timing based on the stromatolites. We also incorporated radiocarbon dated layers of fossil fish from outcrop sections of the High Magadi Beds (e.g., Isaac et al., 1972) for the reconstruction of the Holocene fish fauna of this basin.

Supporting figures and tables

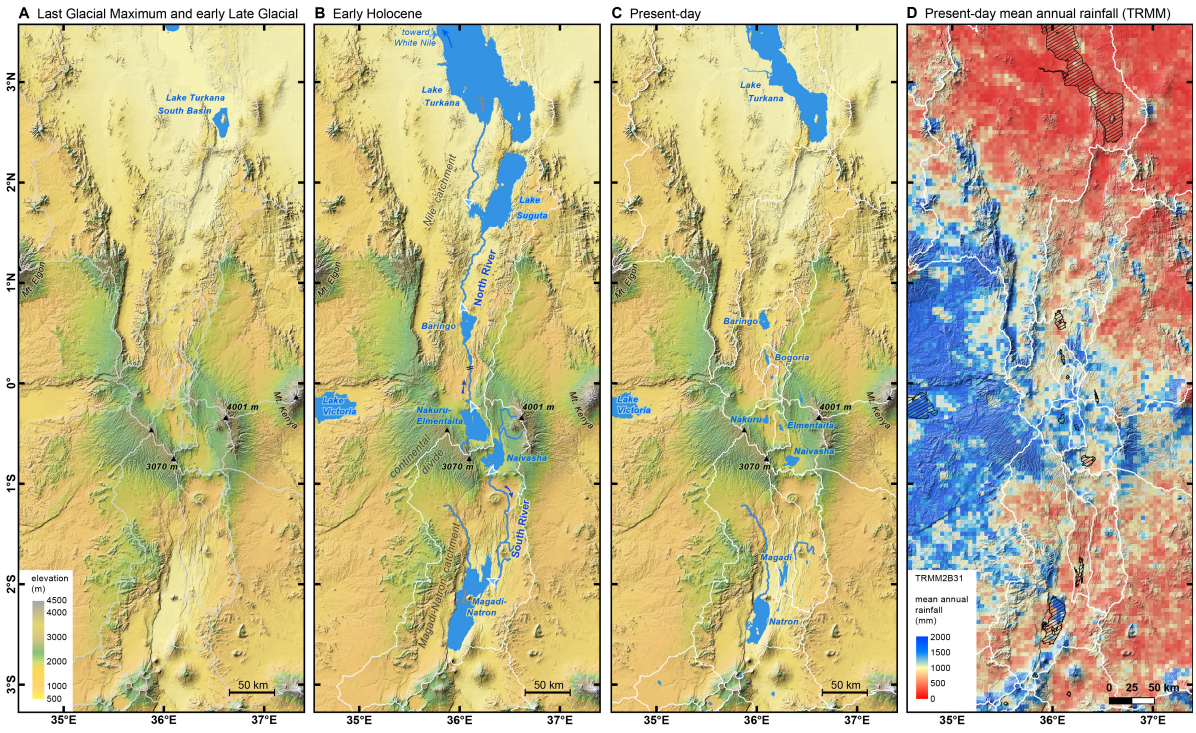

Figure D.1. Past and present drainage of the Kenya Rift valley.
(A) *lake occurrence and extent during the Last Glacial Maximum and early Late Glacial (24-16 ka),* ***(B)*** *lake occurrence and extent and extent of the river system during the early Holocene (AHP, 12-8 ka),* ***(C)*** *present-day lake occurrence and extent and extent of the river system, and* ***(D)*** *estimates of mean annual rainfall (mm/yr) for 1998-2010 from the Tropical Rainfall Measuring Mission (TRMM, 2011) satellite operation at a resolution of 5x5 km (based on TRMM 2B31 data product, compiled by B. Bookhagen).*

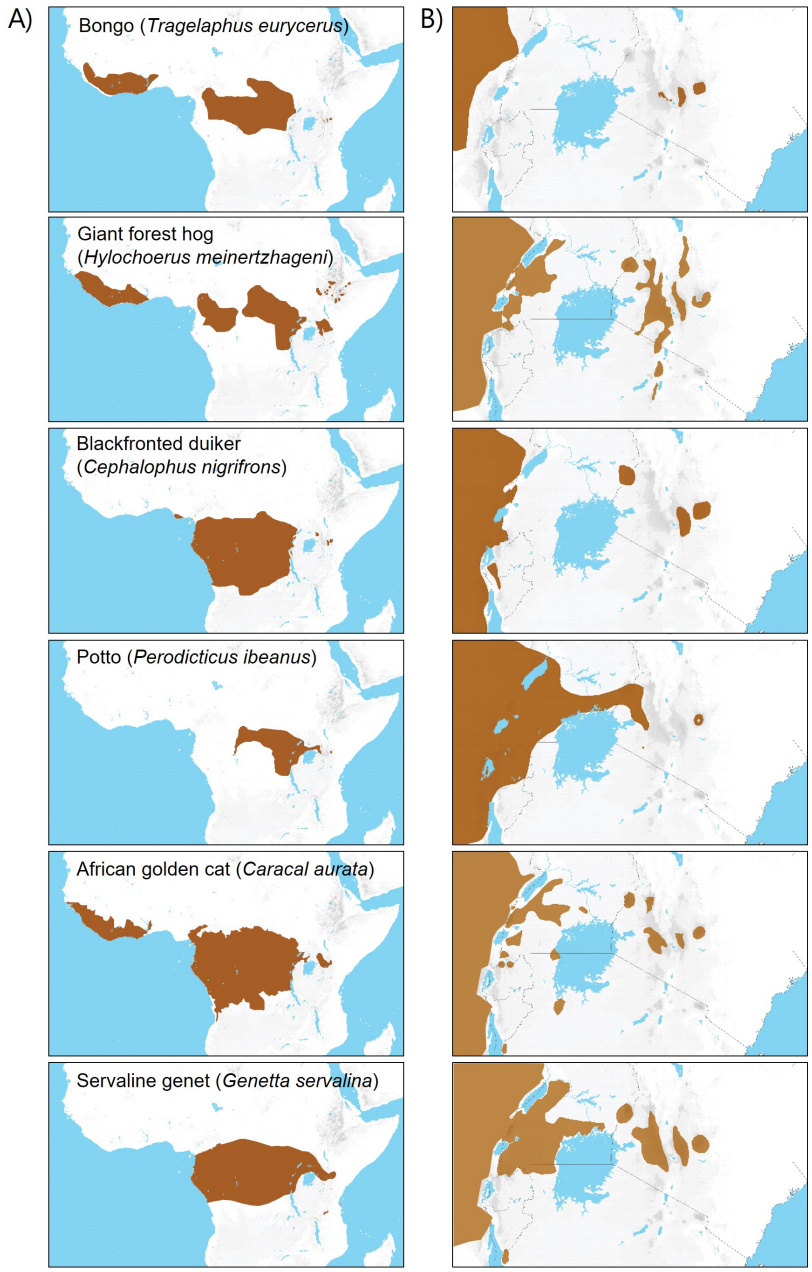

Figure D.2. Range maps of forest-dependent mammals with Guineo-Congolian distribution. ***(A)*** *Global distribution (Africa).* ***(B)*** *detailed distribution of the same species in East Africa. Maps in A) based on IUCN (2020) and in B) on IUCN (2020), Kingdon (1982, 1979, 1977, 1971).*

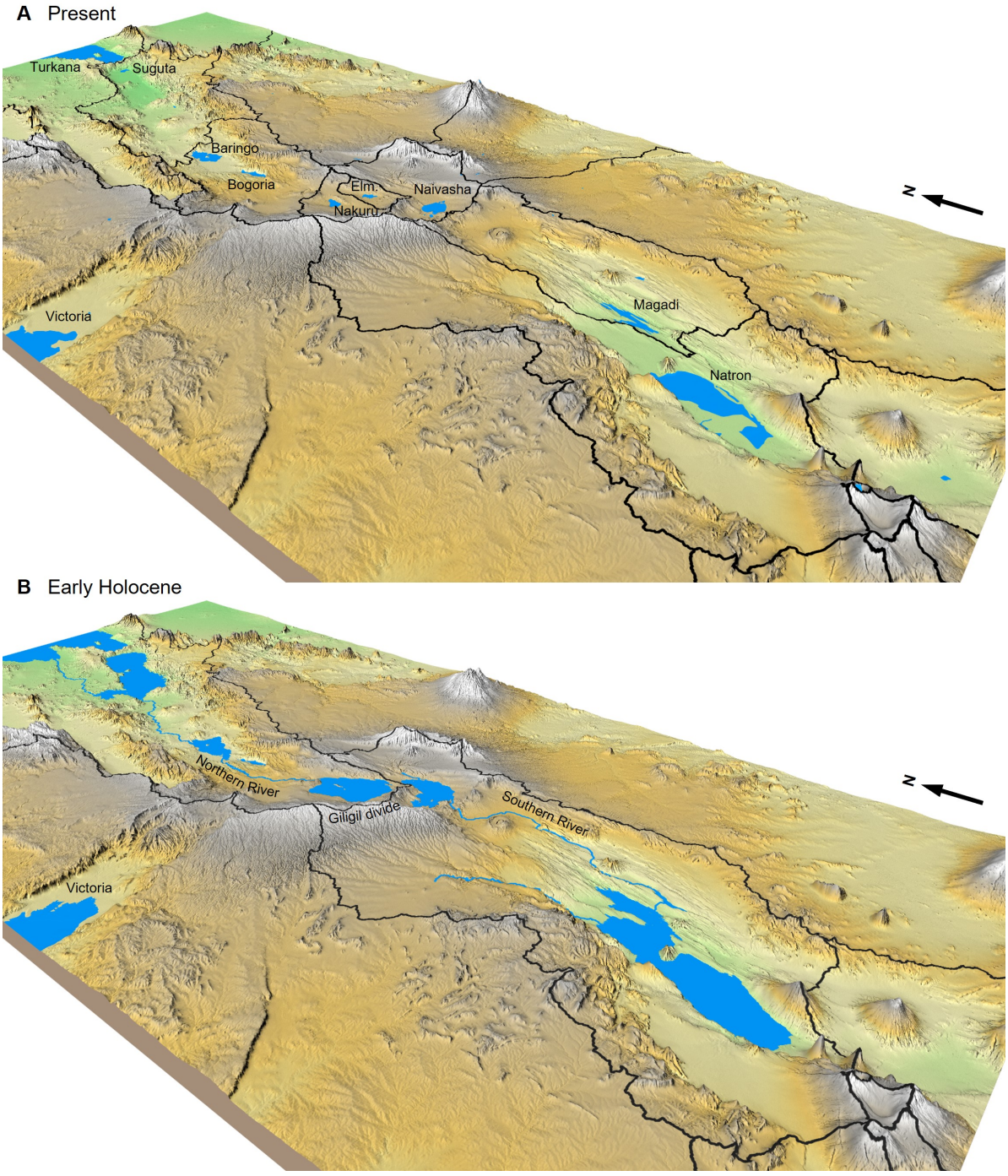

Figure D.3. Oblique views onto the Kenya Rift valley with its lakes and river systems.
(A) *present-day setting.* ***(B)*** *early Holocene setting. Catchment boundaries are outlined in black. Note the Gilgil divide as the highest area in the inner rift. Based on the TanDEM-X digital elevation model.*

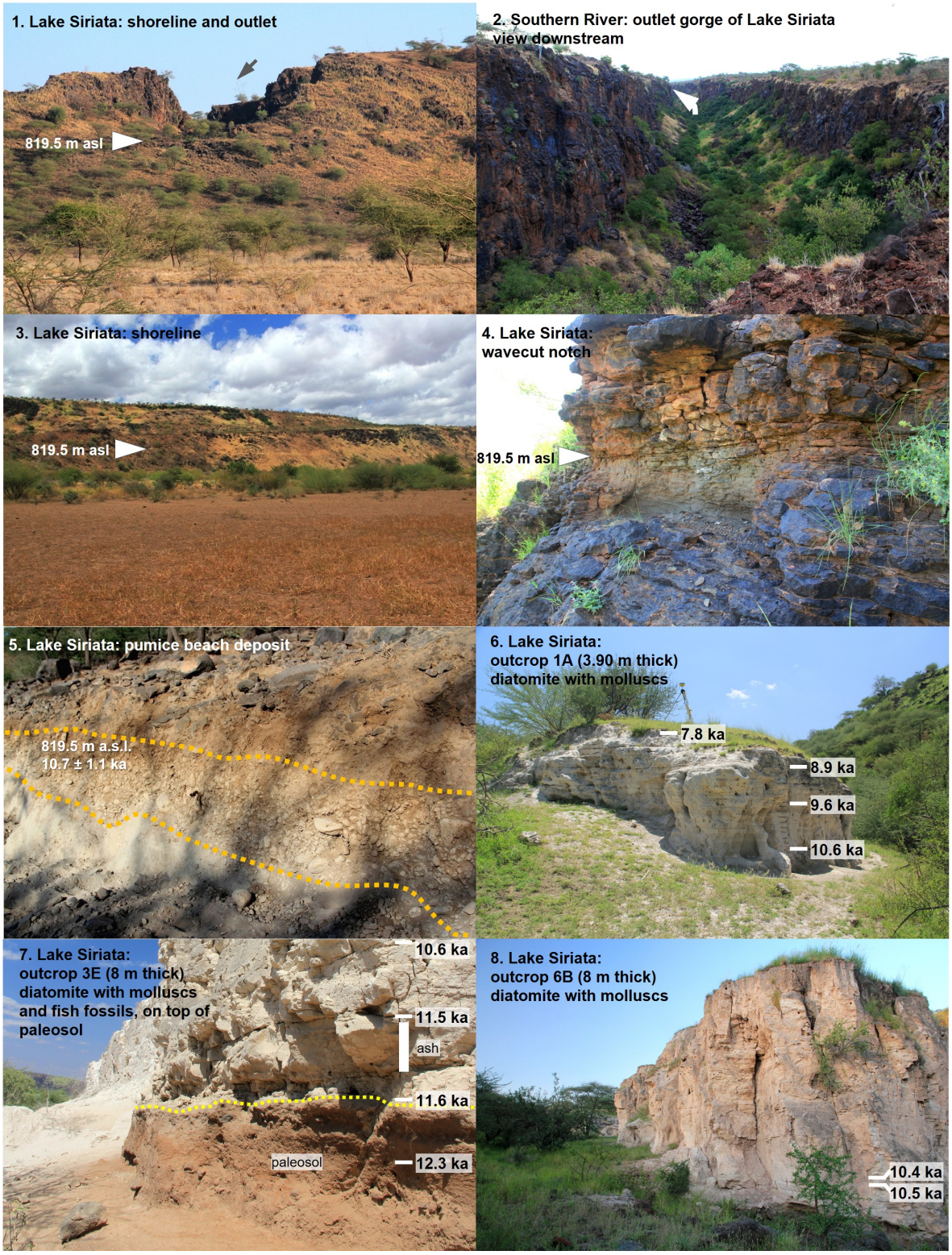

Figure D.4. Photos of study sites in the South and Central Kenya Rift

Photos show vestiges of past river activity and lacustrine deposition at overflow lake levels. White arrows indicate river flow directions, white triangles shorelines and white bars dated unites (with median ages). Photos 1-8 by R. Dommain.

(Part 1/3)

Figure D.4 (continued). Photos of study sites in the South and Central Kenya Rift

Photos show vestiges of past river activity and lacustrine deposition at overflow lake levels. White arrows indicate river flow directions, white triangles shorelines and white bars dated unites (with median ages). Photos 9-18 by R. Dommain.

(Part 2/3)

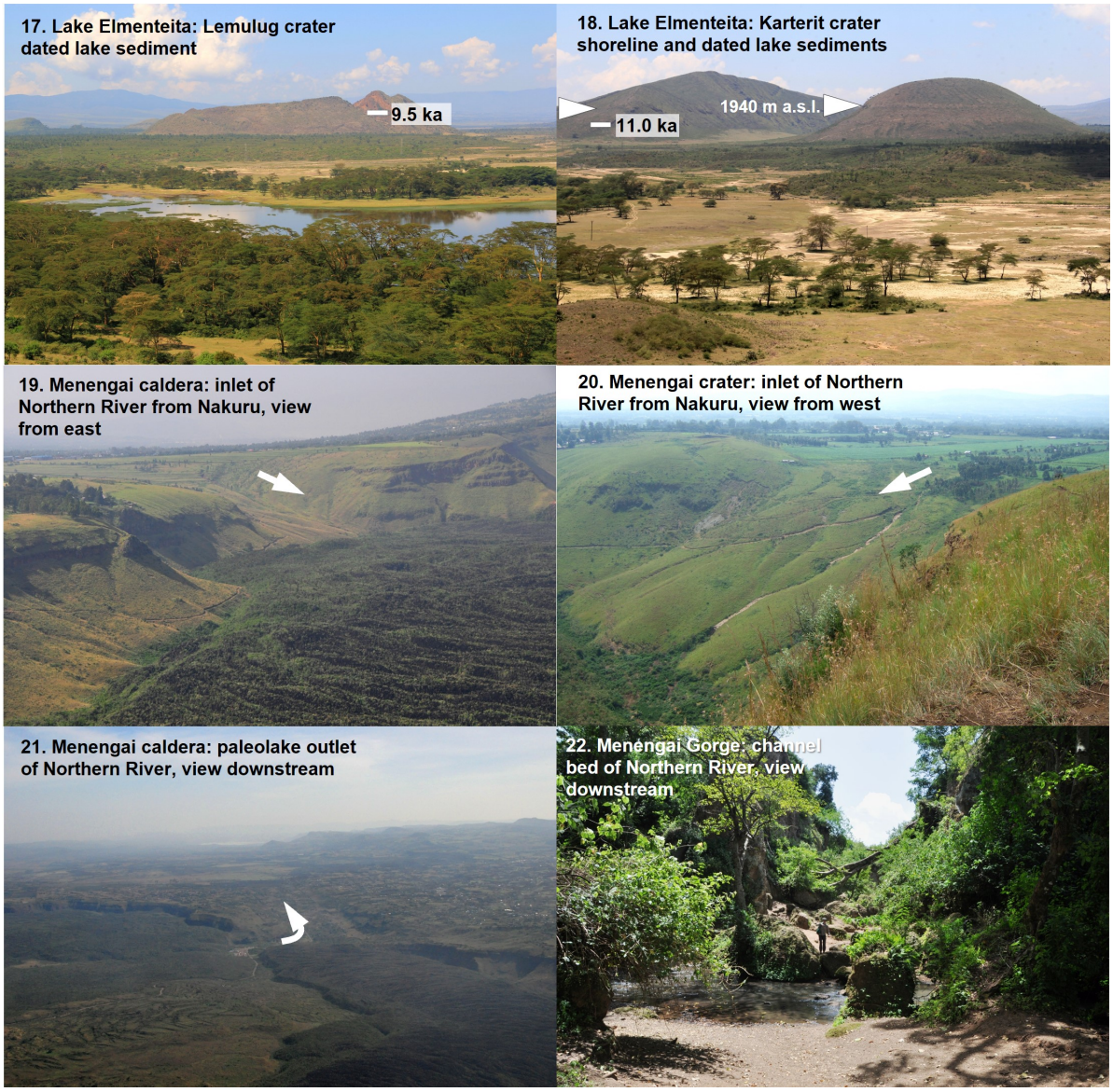

Figure D.4 (continued). Photos of study sites in the South and Central Kenya Rift

Photos show vestiges of past river activity and lacustrine deposition at overflow lake levels. White arrows indicate river flow directions, white triangles shorelines and white bars dated unites (with median ages). Photos 17-18 by R. Dommain, photos 19-22 by S. Riedl.

(Part 3/3)

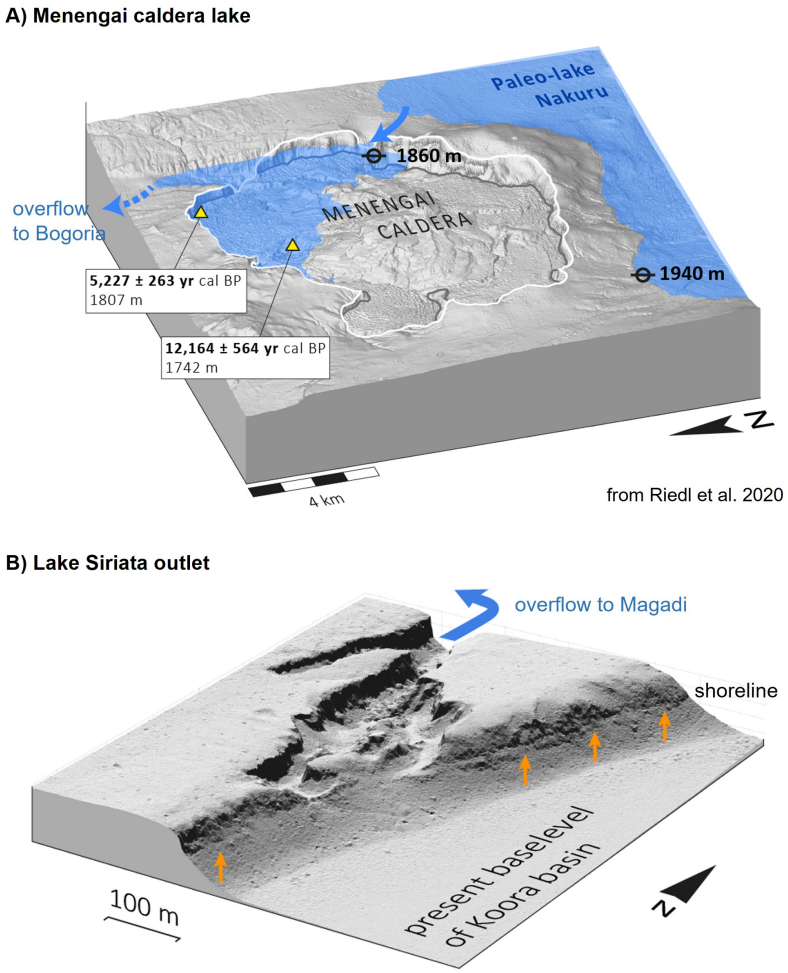

Figure D.5. Oblique views onto digital surface models (DSM) generated from Structure-from-Motion data.

(A) *shows the Holocene Menegai caldera lake with inlet from Lake Nakuru-Elmenteita and its outlet (DSM at 25 cm vertical resolution), from Riedl et al. (2020; Chapter 3).* ***(B)*** *shows the outlet gorge of Lake Siriata and part of the Siriata highstand shoreline indicated by orange arrows (DSM at 20 cm vertical resolution).*

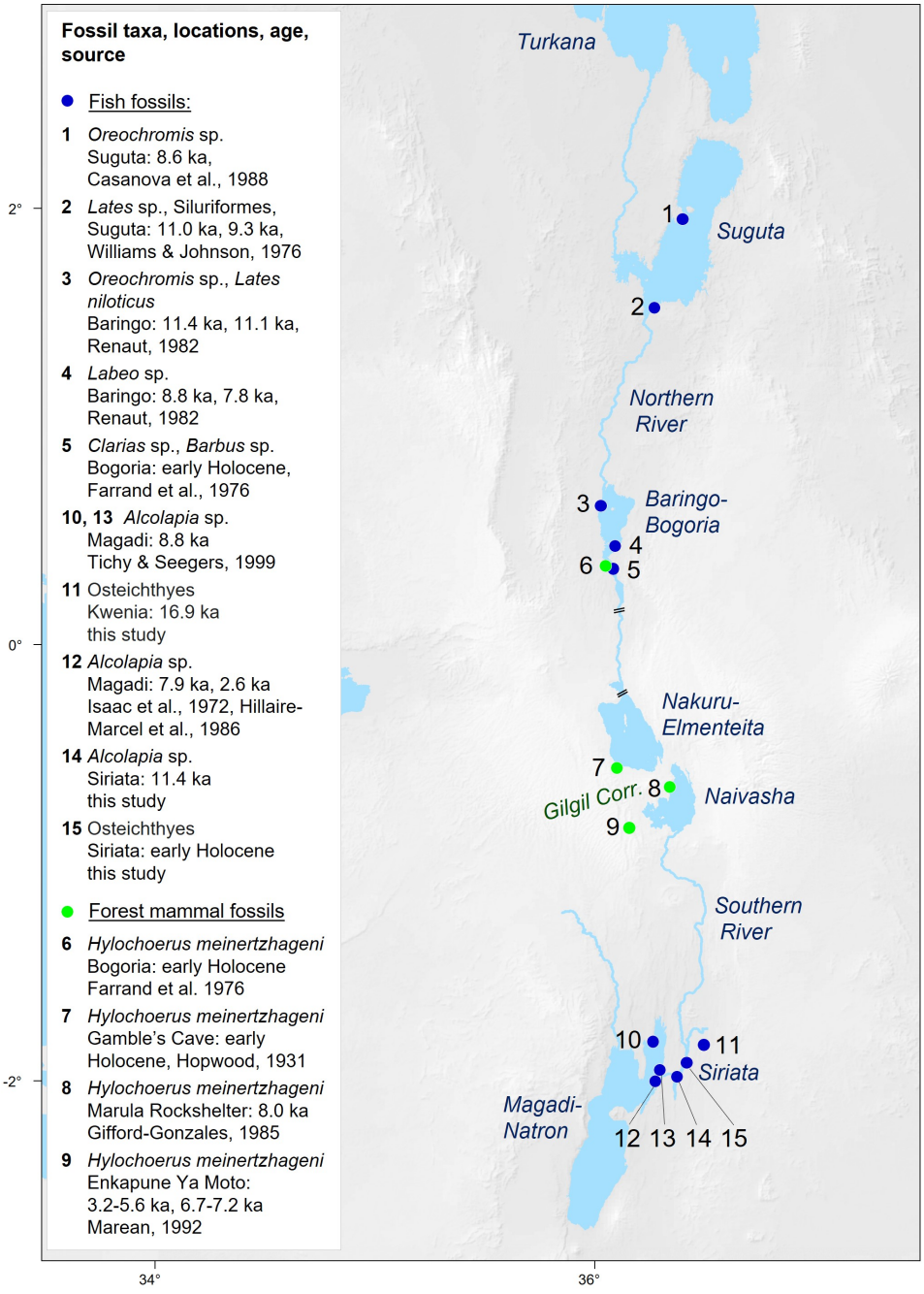

Figure D.6. Holocene fossil localities of freshwater fishes and forest mammals in the Kenya Rift valley. *Blue dots mark sites with fish fossils and green dots sites with mammal fossils. Lake extent and river system of the early Holocene shown for context. Legend lists taxa, locations, dates, and references for the sites.*

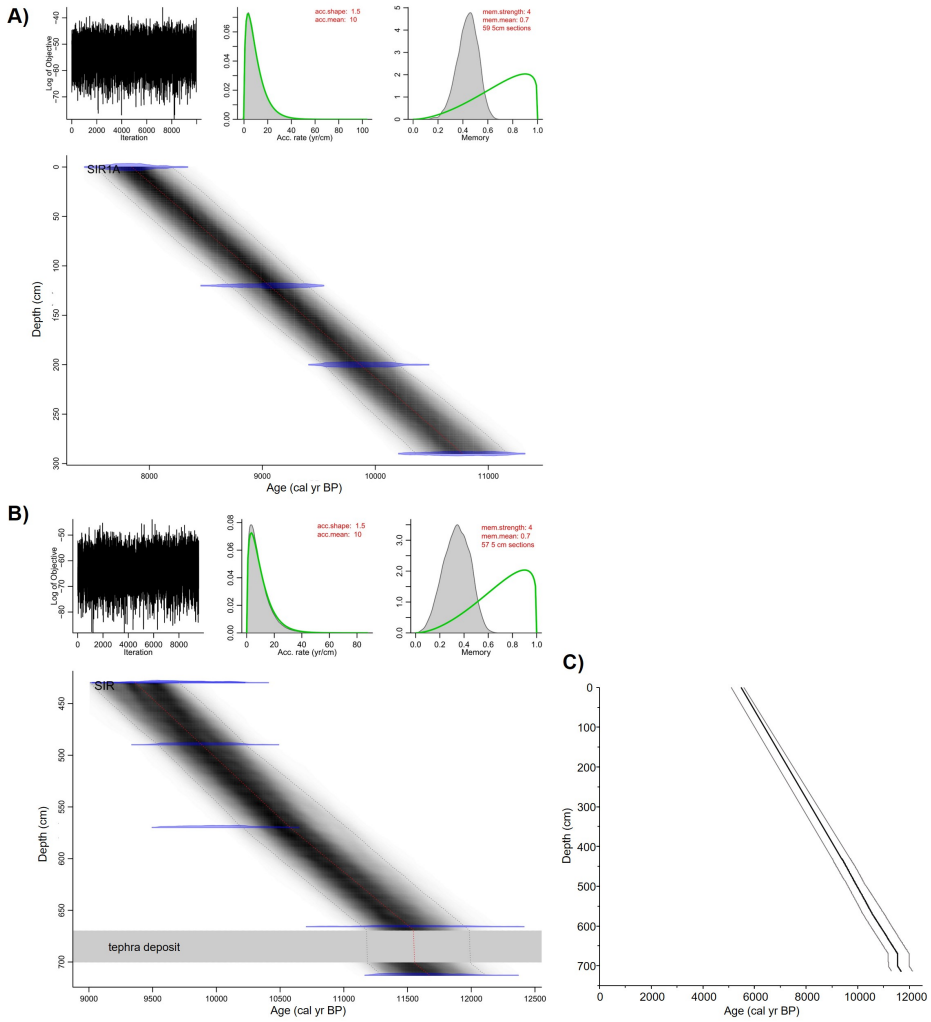

Figure D.7. Bayesian age models for Lake Siriata sediment outcrops.
Age model generated with the rbacon package 2.3.8. ***(A)*** *age model for 290-0 cm of outcrop 1A.* ***(B)*** *age model for the sediment package from 713-430 cm below surface, including an instantanous deposit (tephra: 700-670 cm) of outcrop 3E.* ***(C)*** *age model for outcrop 3E extrapolated from 430 cm to 0 cm with same sedimentation rate as in between the uppermost two radiocarbon dates of B) and the same age uncertainties as in B).*

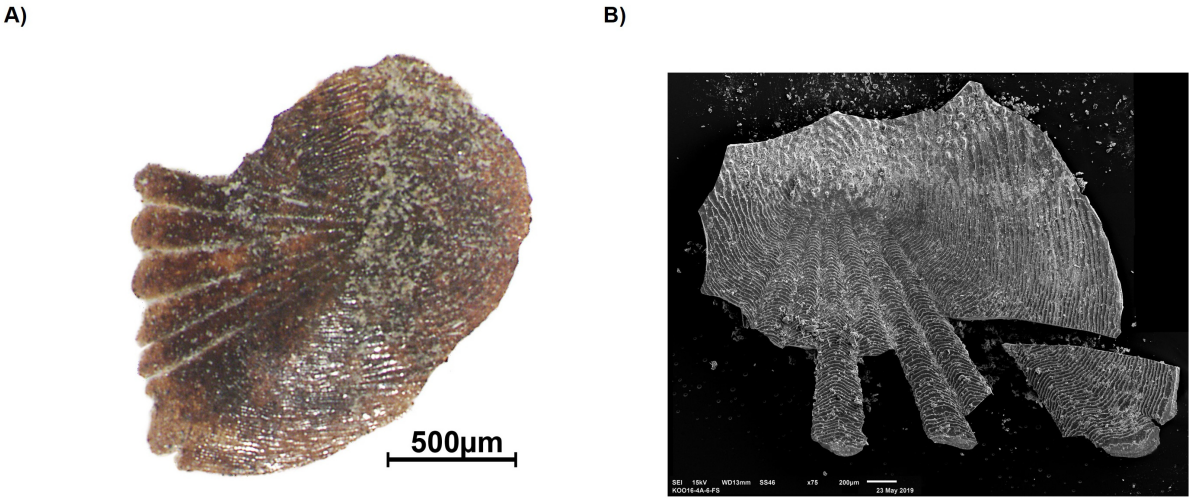

Figure D.8. Fish scale of Alcolapia sp. from Lake Siriata early Holocene sediments.
(A) *Color photo,* ***(B)*** *SEM photo of the same scale with broken edges. The scale was retrieved from a bulk sediment sample from 650-670 cm below the top of outcrop 3E and dates to between 11.0 and 12.0 ka with a median age of 11.4 ka according to the BACON age model in Fig. D.7b.*

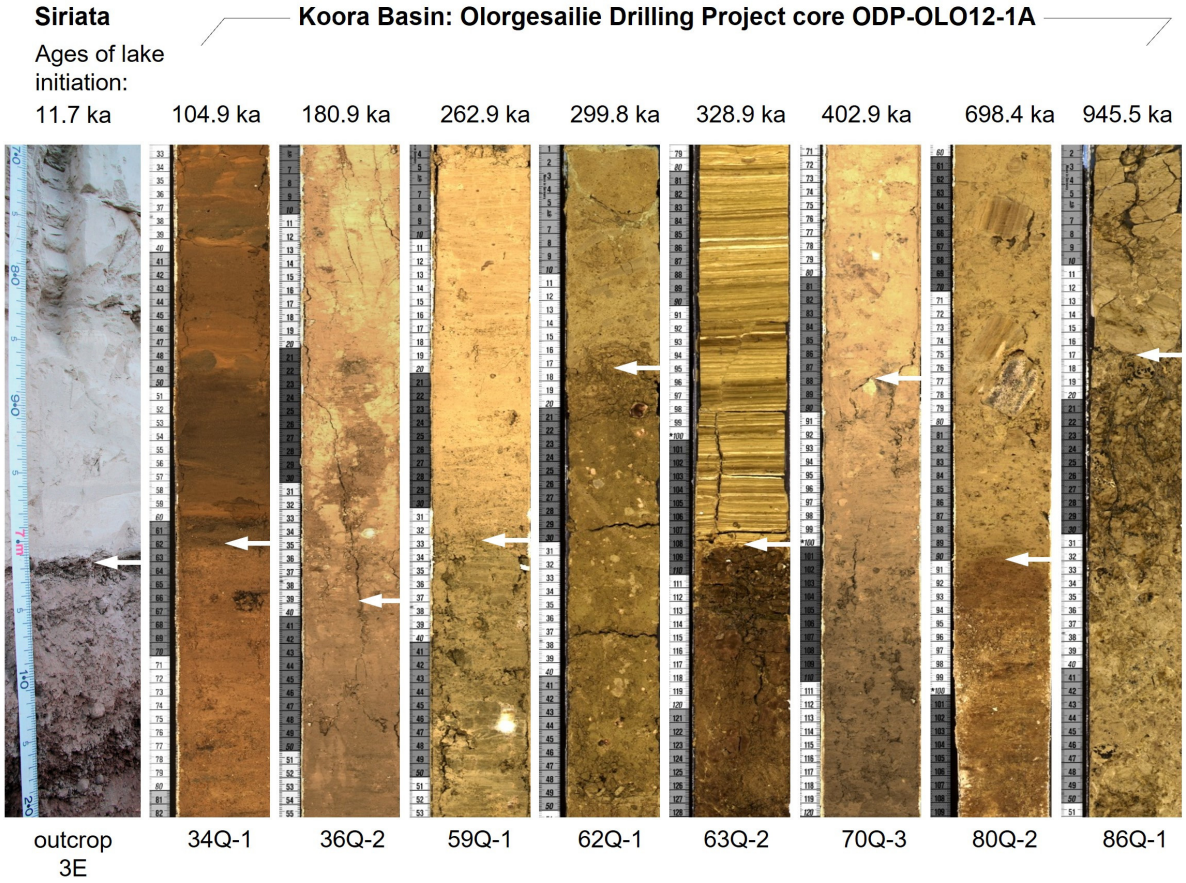

Figure D.9. Comparison of transitions from paleosols to lake sediments between Siriata outcrop 3E and the Koora basin drill core OLO12-1A record.

White arrows show approximate locations of lithological change from paleosol to overlying lake sediment, which indicate shifts from dry land to lake conditions, possible related to flooding from upstream sources. Ages at the top refer to these transitions (ages from Deino et al., 2019). Numbers at the bottom are core section IDs.

List of fish species present in East African rift lakes

Species	Family	Distribution[1]	Natron	Magadi	Naiv.	Nak.	Elm.	Bogoria	Baringo	Suguta	Turkana	Albert	Edward[2]	George[2]	References
Alestes baremoze	Alestidae	NS									1	1			Seegers et al. (2003), Wandera & Balirwa (2010)
Alestes dentex	Alestidae	NS									1	1			Seegers et al. (2003), Wandera & Balirwa (2010)
Brycinus ferox	Alestidae	e									1				Seegers et al. (2003)
Brycinus macrolepidotus	Alestidae	NS, CB									1	1			Wandera & Balirwa (2010), Lévêque et al. (1991)
Brycinus minutus	Alestidae	e									1				Seegers et al. (2003)
Brycinus nurse	Alestidae	NS										1			Wandera & Balirwa (2010)
Brycinus nurse nana	Alestidae	e / NS									1				Seegers et al. (2003)
Hydrocynus forskahlii	Alestidae	NS									1	1			Seegers et al. (2003), Wandera & Balirwa (2010)
Hydrocynus vittatus	Alestidae	NS, CB, Z									1	1			Seegers et al. (2003), Wandera & Balirwa (2010)
Micralestes aff. *elongatus*	Alestidae	NS									1				Seegers et al. (2003)
Ctenopoma muriei	Anabantidae	NS?										1	1	1	Decru et al. (2020), fishbase.se, GBIF (2021)
Bagrus bajad	Bagridae	NS									1	1			Seegers et al. (2003), Wandera & Balirwa (2010)
Bagrus docmak	Bagridae	NS									1	1	1	1	Seegers et al. (2003), Wandera & Balirwa (2010) Decru et al(2020)
Alcolapia alcalicus	Cichlidae	e	1												Seegers et al. (2003), Seegers & Tichy (1999)
Alcolapia grahami	Cichlidae	e		1											Seegers et al. (2003), Seegers & Tichy (1999)
Alcolapia latilabris	Cichlidae	e	1												Seegers & Tichy (1999)
Alcolapia ndalalani	Cichlidae	e	1												Seegers & Tichy (1999)
Astatoreochromis alluaudi	Cichlidae	LVB											1	1	Greenwood (1973)
Haplochromis aeneocolor	Cichlidae	e												1	Greenwood (1973)
Haplochromis akika	Cichlidae	e												1	Lippitsch (2003) fishbase.se
Haplochromis (*Thorachochromis*) *albertianus*	Cichlidae	e										1			Wandera & Balirwa (2010)
Haplochromis angustifrons	Cichlidae	e											1	1	Greenwood (1973), Decru et al. (2020)
Haplochromis (*Thorachochromis*) *avium*	Cichlidae	e										1			Wandera & Balirwa (2010)
Haplochromis (*Thorachochromis*) *bullatus*	Cichlidae	e										1			Wandera & Balirwa (2010)
Haplochromis concilians	Cichlidae	e											1		Vranken et al. (2020b)
Haplochromis eduardianus	Cichlidae	e											1	1	Greenwood (1973)
Haplochromis eduardii	Cichlidae	e											1		Greenwood (1973), Greenwood (1980)
Haplochromis elegans	Cichlidae	e											1	1	Greenwood (1973)
Haplochromis engystoma	Cichlidae	e											1		Greenwood (1973)

[1] species distribution based on listed references and information retrieved from www.fishbase.se (Froese and Pauly, 2021). Abbreviations: AN = Albert Nile, AR = Albertine Rift, CB = Congo Basin, e = endemic, EC = East Coast, LA = Lake Albert, LK = Lake Kyoga, LT = Lake Tanganyika, LV = Lake Victoria, LVB = Lake Victoria Basin, N = Nile, NS = Nilo-Sudan, VN = Victoria Nile, Z = Zambezi.

[2] total number of fish species for Lakes Edward and George remains unknown, because many endemic cichlid species have not been formally described (Decru et al., 2020).

Table D.1. List of fish species present in East African rift lakes.

(part 1/5)

Species	Family	Distribution[1]	Natron	Magadi	Naiv.	Nak.	Elm.	Bogoria	Baringo	Suguta	Turkana	Albert	Edward[2]	George[2]	References
Haplochromis erutus	Cichlidae	e											1		Vranken et al. (2020b)
Haplochromis fuscus	Cichlidae	e											1		Vranken et al. (2020a) fishbase.se
Haplochromis gracilifur	Cichlidae	e											1		Vrancken et al. (2019)
Haplochromis labiatus	Cichlidae	e											1	1	Greenwood (1973)
Haplochromis limax	Cichlidae	e											1	1	Greenwood (1973)
Haplochromis (*Thoracochromis*) *loati*	Cichlidae	N, LA										1			Wandera & Balirwa (2010)
Haplochromis lobatus	Cichlidae	e											1		Vranken et al. (2020c)
Haplochromis (*Thoracochromis*) *macconneli*	Cichlidae	e									1				Seegers et al. (2003)
Haplochromis macropsoides	Cichlidae	e											1	1	Greenwood (1973), Decru et al. (2020)
Haplochromis (*Thoracochromis*) *mahagiensis*	Cichlidae	e										1			Wandera & Balirwa (2010)
Haplochromis mentatus	Cichlidae	e											1		fishbase.se
Haplochromis molossus	Cichlidae	e											1	1	Vrancken et al. (2019)
Haplochromis mylodon	Cichlidae	e											1	1	Greenwood (1973)
Haplochromis nigripinnis	Cichlidae	e											1	1	Greenwood (1973), Decru et al. (2020)
Haplochromis nubilus	Cichlidae	LVB											1	1	Greenwood (1973), Decru et al. (2020)
Haplochromis oregosoma	Cichlidae	e												1	Greenwood (1973)
Haplochromis pappenheimi	Cichlidae	e											1	1	Greenwood (1973)
Haplochromis paradoxus	Cichlidae	e											1		Vrancken et al. (2019)
Haplochromis pharyngalis (syn. *H. petronius*)	Cichlidae	e											1	1	Greenwood (1973), Vranken et al. (2020a)
Haplochromis planus	Cichlidae	e											1		Vranken et al. (2020b)
Haplochromis relictidens	Cichlidae	e											1		Vrancken et al. (2019)
Haplochromis (*Thoracochromis*) *rudolfianus*	Cichlidae	e									1				Seegers et al. (2003)
Haplochromis schubotzi	Cichlidae	e											1	1	Greenwood (1973)
Haplochromis schubotziellus	Cichlidae	e											1	1	Greenwood (1973)
Haplochromis serridens	Cichlidae	e											1		fishbase.se
Haplochromis squamipinnis	Cichlidae	e											1	1	Greenwood (1973)
Haplochromis taurinus	Cichlidae	e											1	1	Vrancken et al. (2019), Decru et al. (2020)
Haplochromis (*Thoracochromis*) *turkanae*	Cichlidae	e									1				Seegers et al. (2003)
Haplochromis vicarius	Cichlidae	e											1	1	fishbase.se
Haplochromis (*Thoracochromis*) *wingatii*	Cichlidae	AN, LA										1			Greenwood (1973)
Hemichromis exsul	Cichlidae	e									1				Seegers et al. (2003)
Neochromis "nigricans"	Cichlidae	?										1			Wandera & Balirwa (2010)

[1] species distribution based on listed references and information retrieved from www.fishbase.se (Froese and Pauly, 2021). Abbreviations: AN = Albert Nile, AR = Albertine Rift, CB = Congo Basin, e = endemic, EC = East Coast, LA = Lake Albert, LK = Lake Kyoga, LT = Lake Tanganyika, LV = Lake Victoria, LVB = Lake Victoria Basin, N = Nile, NS = Nilo-Sudan, VN = Victoria Nile, Z = Zambezi.

[2] total number of fish species for Lakes Edward and George remains unknown, because many endemic cichlid species have not been formally described (Decru et al. 2020).

Table D.1. (continued). *List of fish species present in East African rift lakes.*
(part 2/5)

Species	Family	Distribution[1]	Natron	Magadi	Naiv.	Nak.	Elm.	Bogoria	Baringo	Suguta	Turkana	Albert	Edward[2]	George[2]	References
Neochromis "zebra"	Cichlidae	?										1			Wandera & Balirwa (2010)
Oreochromis leucosticus	Cichlidae	AR										1	1	1	Decru et al. (2020), Wandera & Balirwa (2010)
Oreochromis niloticus baringoensis	Cichlidae	e							1						Seegers et al. (2003)
Oreochromis niloticus eduardianus	Cichlidae	AR										1	1	1	Decru et al. (2020), Wandera & Balirwa (2010)
Oreochromis niloticus ssp "Bogoria?"	Cichlidae	e						1							Ndiwa et al. (2014) Ford et al. (2019)
Oreochromis niloticus sugutae	Cichlidae	e								1					Seegers et al. (2003)
Oreochromis niloticus vulcani	Cichlidae	e									1				Seegers et al. (2003)
Pseudocrenilabrus multicolor	Cichlidae	LVB, N										1		1	Greenwood (1973), fishbase.se
Sarotherodon galilaeus	Cichlidae	NS, CB									1	1			Seegers et al. (2003)
Tilapia (*Coptodon*) *zillii*	Cichlidae	NS, CB									1	1			Seegers et al. (2003), Decru et al. (2020)
Citharinus citharus	Citharinidae	NS									1	1		1	Seegers et al. (2003), Wandera & Balirwa (2010), GBIF (2021)
Citharinus latus	Citharinidae	NS										1			Wandera & Balirwa (2010)
Clarias alluaudi	Clariidae	LVB, AR										1	1		Wandera & Balirwa (2010), fishbase.se
Clarias gariepinus	Clariidae	pan-Africa						1	1	1	1	1	1	1	Seegers et al. (2003), Wandera & Balirwa (2010), Decru et al. (2020)
Clarias hilli	Clariidae	CB										1			Lévêque et al. (1991)
Clarias liocephalus	Clariidae	LVB, AR, CB										1	1	1	Wandera & Balirwa (2010), fishbase.se
Heterobranchus longifilis	Clariidae	NS, CB, Z									1				Seegers et al. (2003)
Auchenoglanis biscutatus	Claroteidae	NS									1				Wakjira & Getahun (2017)
Auchenoglanis occidentalis	Claroteidae	NS, CB									1	1			Seegers et al. (2003), Wandera & Balirwa (2010)
Chrysichthys turkana	Claroteidae	e									1				Hardman (2008)
Barbus spec. "Baringo"	Cyprinidae	e						1	1						Seegers et al. (2003)
Barbus turkanae	Cyprinidae	e									1				Seegers et al. (2003)
Barilius niloticus (syn. *Leptocypris niloticus*)	Cyprinidae	NS										1			Wandera & Balirwa (2010)
Chelaethiops bibie	Cyprinidae	NS									1				Seegers et al. (2003)
Enteromius (*Barbus*) *neglectus*	Cyprinidae	N										1			Wandera & Balirwa (2010)
Enteromius (*Barbus*) *neumayeri*	Cyprinidae	LVB, LT						1			1	1			Seegers et al. (2003), Greenwood (1962)
Enteromius (*Barbus*) *perince*	Cyprinidae	NS										1			Wandera & Balirwa (2010)
Enteromius (*Barbus*) *stigmatopygus*	Cyprinidae	NS									1				Seegers et al. (2003)
Enteromius cf. *mimus*	Cyprinidae	EC											1	1	Maetens et al. (2020)

[1] species distribution based on listed references and information retrieved from www.fishbase.se (Froese and Pauly, 2021). Abbreviations: AN = Albert Nile, AR = Albertine Rift, CB = Congo Basin, e = endemic, EC = East Coast, LA = Lake Albert, LK = Lake Kyoga, LT = Lake Tanganyika, LV = Lake Victoria, LVB = Lake Victoria Basin, N = Nile, NS = Nilo-Sudan, VN = Victoria Nile, Z = Zambezi.

[2] total number of fish species for Lakes Edward and George remains unknown, because many endemic cichlid species have not been formally described (Decru et al. 2020).

Table D.1. (continued). *List of fish species present in East African rift lakes.*
(part 3/5)

Species	Family	Distribution[1]	Natron	Magadi	Naiv.	Nak.	Elm.	Bogoria	Baringo	Suguta	Turkana	Albert	Edward[2]	George[2]	References
Enteromius kerstenii	Cyprinidae	Z, LVB, EC											1	1	Decru et al. (2020)
Enteromius alberti	Cyprinidae	LVB											1	1	Maetens et al. (2020)
Enteromius apleurogramma	Cyprinidae	LVB											1	1	Daget (1984)
Labeo coubie	Cyprinidae	NS									1	1			Wandera & Balirwa (2010), Wakjira & Getahun (2017)
Labeo cylindricus	Cyprinidae	Z, EC, CB						1	1	1	1				Seegers et al. (2003)
Labeo forskalii	Cyprinidae	N											1		fishbase.se
Labeo horie	Cyprinidae	N									1	1			Seegers et al. (2003), Wandera & Balirwa (2010)
Labeo niloticus	Cyprinidae	NS									1				Seegers et al. (2003)
Labeobarbus altianalis	Cyprinidae	LVB, AR											1	1	Decru et al. (2020)
Labeobarbus bynni	Cyprinidae	NS									1	1			Seegers et al. (2003), Wandera & Balirwa (2010)
Labeobarbus intermedius	Cyprinidae	NS						1	1	1	1				Seegers et al. (2003)
Leptocypris niloticus	Cyprinidae	N									1				Seegers et al. (2003)
Neobola (*Engraulicypris*) *bredoi*	Cyprinidae	e										1			Wandera & Balirwa (2010)
Neobola stellae	Cyprinidae	e									1				Seegers et al. (2003)
Raiamas senegalensis	Cyprinidae	NS									1				Seegers et al. (2003)
Distichodus nefasch (syn. *D. niloticus*)	Distichodontidae	N									1	1			Seegers et al. (2003), Wandera & Balirwa (2010)
Distichodus rostratus	Distichodontidae	NS										1			Wandera & Balirwa (2010)
Gymnarchus niloticus	Gymnarchidae	NS									1				Seegers et al. (2003)
Lates longispinis	Latidae	e									1				Seegers et al. (2003)
Lates macrophthalmus	Latidae	e										1			Wandera & Balirwa (2010)
Lates niloticus	Latidae	NS									1	1			Seegers et al. (2003), Wandera & Balirwa (2010)
Malapterurus electricus	Malapteruridae	NS									1	1			Seegers et al. (2003), Wandera & Balirwa (2010)
Mochokus niloticus	Mochokidae	NS									1				Seegers et al. (2003)
Synodontis filamentosus	Mochokidae	NS									1				Wakjira & Getahun (2017)
Synodontis frontosus	Mochokidae	N									1	1			Seegers et al. (2003), Wandera & Balirwa (2010)
Synodontis nigrita	Mochokidae	NS										1			Wandera & Balirwa (2010)
Synodontis schall	Mochokidae	NS									1	1			Seegers et al. (2003), Wandera & Balirwa (2010)
Gnathonemus cyprinoides	Mormyridae	NS										1			Wandera & Balirwa (2010)

[1] species distribution based on listed references and information retrieved from www.fishbase.se (Froese and Pauly, 2021). Abbreviations: AN = Albert Nile, AR = Albertine Rift, CB = Congo Basin, e = endemic, EC = East Coast, LA = Lake Albert, LK = Lake Kyoga, LT = Lake Tanganyika, LV = Lake Victoria, LVB = Lake Victoria Basin, N = Nile, NS = Nilo-Sudan, VN = Victoria Nile, Z = Zambezi.

[2] total number of fish species for Lakes Edward and George remains unknown, because many endemic cichlid species have not been formally described (Decru et al. 2020).

Table D.1. (continued). *List of fish species present in East African rift lakes.*
(part 4/5)

Species	Family	Distribution[1]	Natron	Magadi	Naiv.	Nak.	Elm.	Bogoria	Baringo	Suguta	Turkana	Albert	Edward[2]	George[2]	References
Hyperopisus bebe	Mormyridae	NS									1	1			Seegers et al. (2003), Wandera & Balirwa (2010)
Marcusenius petherici	Mormyridae	N										1			Wandera & Balirwa (2010)
Mormyrops anguilloides	Mormyridae	NS, CB, Z										1			Wandera & Balirwa (2010)
Mormyrus caschive	Mormyridae	N									1	1			Wandera & Balirwa (2010), Wakjira & Getahun (2017)
Mormyrus kannume	Mormyridae	N, LVB									1	1	1	1	Wakjira & Getahun (2017)
Mormyrus macrocephalus	Mormyridae	VN, LK										1			Wandera & Balirwa (2010)
Mormyrus niloticus	Mormyridae	N										1			Wandera & Balirwa (2010)
Pollimyrus (*Marcusenius*) *nigricans*	Mormyridae	LVB, AR										1		1	Wandera & Balirwa (2010), GBIF (2021)
Nothobranchius albertinensis	Notobranchiidae	e										1			Nagy et al. (2020)
Nothobranchius ugandensis	Notobranchiidae	LVB, LA										1			Nagy & Watters (2018)
Heterotis niloticus	Osteoglossidae	NS, CB									1				Seegers et al. (2003)
Polypterus bichir	Polypteridae	NS									1				Seegers et al. (2003)
Polypterus senegalus	Polypteridae	NS									1	1			Seegers et al. (2003), Wandera & Balirwa (2010)
Aplocheilichthys jeanneli (syn. *Lacustricola jeanneli*)	Procatopodidae	e									1				Seegers et al. (2003)
Aplocheilichthys magieinsis	Procatopodidae	?										1			Wandera & Balirwa (2010)
Aplocheilichthys rudolfianus	Procatopodidae	e									1				Seegers et al. (2003)
Aplocheilichthys spec. "Baringo"	Procatopodidae	possibly e							1						Seegers et al. (2003)
Aplocheilichthys spec. "Naivasha"	Procatopodidae	e			1										Seegers et al. (2003)
Laciris pelagica	Procatopodidae	e											1		Decru et al. (2020)
Lacustricola bukobanus	Procatopodidae	AR, LV											1	1	Decru et al. (2020)
Lacustricola kassenjiensis	Procatopodidae	AR										1			Wandera & Balirwa (2010)
Lacustricola vitschumbaensis	Procatopodidae	AR, LV											1	1	Decru et al. (2020)
Protopterus aethiopicus	Protopteridae	N, CB									1	1	1	1	Seegers et al. (2003), Wandera & Balirwa (2010), Decru et al. (2020)
Schilbe intermedius	Schilbeidae	NS, CB, Z, EC										1			Wandera & Balirwa (2010)
Schilbe mystus (syn. *Eutropius niloticus*)	Schilbeidae	NS										1			Wandera & Balirwa (2010)
Schilbe uranoscopus	Schilbeidae	NS									1				Seegers et al. (2003)
Tetraodon lineatus	Tetraodontidae	NS									1				Seegers et al. (2003)
		Sum species	3	1	1	0	0	6	6	4	57	62	48	39	
		Endemic spp.	3	1	1	0	0	2	3	1	14	7	29	19	

[1] species distribution based on listed references and information retrieved from www.fishbase.se (Froese and Pauly, 2021). Abbreviations: AN = Albert Nile, AR = Albertine Rift, CB = Congo Basin, e = endemic, EC = East Coast, LA = Lake Albert, LK = Lake Kyoga, LT = Lake Tanganyika, LV = Lake Victoria, LVB = Lake Victoria Basin, N = Nile, NS = Nilo-Sudan, VN = Victoria Nile, Z = Zambezi.

[2] total number of fish species for Lakes Edward and George remains unknown, because many endemic cichlid species have not been formally described (Decru et al. 2020).

Table D.1. (continued). *List of fish species present in East African rift lakes.*
(part 5/5)

Annotated list of published radiocarbon dates used in Chapter 5.

#	Lab ID	^{14}C date (BP)	Reservoir corrected ^{14}C date (BP)	Calibrated median age (cal. BP)	Dated material	Sample location	Published elevation (m)	Additional published information	Interpretation	Published Location*	Reference
Turkana											
1	Gx-4642-I-A	3405±130		3667	Bone apatite	Koobi Fora	416	Beach sand	Closed basin	3.94°N?, 36.2°E?	Owen et al. (1982) Garcin et al. (2012)
2	L-1203-H	3650±150		3987	mixed shell	Kibish	443	Beach ridge	Closed basin	5.3167°N, 35.926°E	Butzer & Thurber (1969), Butzer et al. (1972), Garcin et al. (2012)
3	SUA-637	3945±135		4392	Charcoal	Koobi Fora	416	Beach sand	Closed basin	3.94°N?, 36.2°E?	Owen et al. (1982), Garcin et al. (2012)
4	P-2610	3960±60		4418	Charcoal	Koobi Fora	416	Beach sand	Closed basin	3.94°N?, 36.2°E?	Owen et al. (1982), Garcin et al. (2012)
5	P-2609	3970±60		4434	Charcoal	Koobi Fora	412	Beach sand	Closed basin	3.92°N?, 36.225°E?	Owen et al. (1982), Garcin et al. (2012)
6	SUA-637-b	4100±125		4616	Humic acid	Koobi Fora	416	Beach sand	Closed basin	3.94°N?, 36.2°E?	Owen et al. (1982), Garcin et al. (2012)
7	SUA-634	4160±110		4679	Charcoal	Koobi Fora	412	Beach sand	Closed basin	3.92°N?, 36.225°E?	Owen et al. (1982), Garcin et al. (2012)
8	KIA36859	4330±30		4891	*Melanoides tuberculata*	Lake Turkana South Island	427	Beach ridge	Closed basin	2.6261°N, 36.5712°E	Garcin et al. (2012)
9	KIA36861	4370±35		4931	*Melanoides tuberculata*	Lake Turkana South Island	410	Beach ridge	Closed basin	2.6247°N, 36.5715°E	Garcin et al. (2012)
10	Gx-5475-A	4560±185		5212	Bone apatite	Koobi Fora	417	Beach sand	Closed basin	3.95°N?, 36.25°E?	Owen et al. (1982), Garcin et al. (2012)
11	Gx-4642-II-A	4580±170		5238	Bone apatite	Koobi Fora	416	Beach sand	Closed basin	3.94°N?, 36.2°E?	Owen et al. (1982), Garcin et al. (2012)
12	KIA36858	4645±35		5406	*Melanoides tuberculata*	Lake Turkana South Island	438	Beach ridge	Closed basin	2.6272°N, 36.572°E	Garcin et al. (2012)
13	KIA36860	4680±35		5400	*Melanoides tuberculata*	Lake Turkana South Island	418	Beach ridge	Closed basin	2.6255°N, 36.5716°E	Garcin et al. (2012)
14	KIA 36865	4695±35		5403	*Melanoides tuberculata*	Lake Turkana South Island	393	Beach ridge	Closed basin	2.6192°N, 36.5711°E	Garcin et al. (2012)
15	n.a.	4800±100		5520	*Etheria*	Eliye Springs (Turkana)	439	Beach ridge	Closed basin	3.12°N, 35.98°E	Robbins (1972), Thomson (1966), Garcin et al. (2012)
16	Y-1575	4880±100		5624	*Etheria elliptica*	Eliye Springs (Turkana)	427	Beach ridge	Closed basin	3°N, 36°E	Stuiver (1969), Garcin et al. (2012)
17	KIA 36862	4910±35		5635	Bivalve Shell	Lake Turkana South Island	405	Beach ridge	Closed basin	2.6237°N, 36.5713°E	Garcin et al. (2012)
18	Birm-540	4940±230		5682	*Etheria elliptica*	Koobi Fora	429	Beach ridge	Closed basin	3.9667°N?, 36.2°E	Owen et al. (1982), Williams & Johnson (1976), Garcin et al. (2012)
19	L-1303-A	5550±350		6353	mixed shell	Kibish	440	Beach ridge	Closed basin	5.1667°N, 35.5863°E	Butzer et al. (1972), Garcin et al. (2012)
20	N-1101	6010±160		6869	Shell	Lothagam	463	Shell beds	Overflow	2.8°N?, 36°E?	Robbins (1972), Garcin et al. (2012)
21	N-812	6200±130		7089	Charcoal	Lothagam	430	Beach sands	Closed basin	2.8°N?, 36°E?	Butzer et al. (1972), Yamasaki et al. (1974), Garcin et al. (2012)
22	L-1303-D	7000±150		7831	mixed shell	Kibish	366	Transgressive sandstone	Closed basin	4.4667°N, 36.9403°E	Butzer et al. (1972), Garcin et al. (2012)

*) ? at geographic coordinates denotes uncertain location for Lake Turkana region as given in Garcin et al. (2012).

Table D.2. Annotated list of published radiocarbon dates used to reconstruct lake overflow and closed lake conditions.
(part 1/10)

#	Lab ID	^{14}C date (BP)	Reservoir corrected ^{14}C date (BP)	Calibrated median age (cal. BP)	Dated material	Sample location	Published elevation (m)	Additional published information	Interpretation	Published Location*	Reference
23	Gx-5476-A	7855±160		8713	Bone apatite	Koobi Fora	436	Sand bar	Closed basin	3.956°N, 36.375°E	Owen et al. (1982), Garcin et al. (2012)
24	N-813	7960±140		8823	Shell	Lothagam	463	Shell beds	Overflow	2.839°N?, 35.9641°E ?	Robbins (1972), Garcin et al. (2012)
25	KIA 36856	8180±45		9123	*Melanoides tuberculata*	Lake Turkana South Island	454	Abrasion platform, interpreted as end of overflow	Overflow	2.6611°N, 36.5879°E	Garcin et al. (2012)
26	N-1102	8230±180		9180	Shell	Lothagam	456	Dark organic sediment	Overflow	2.8421°N?, 36.0206°E ?	Robbins (1972), Garcin et al. (2012)
27	Gx-5480-A	8355±235		9306	Bone apatite	Koobi Fora	457	Sand spits	Overflow	4.077°N?, 36.347°E?	Owen et al. (1982), Garcin et al. (2012)
28	Gx-5481-A	8395±270		9356	Bone apatite	Koobi Fora	457	Sand spits	Overflow	4.077°N?, 36.347°E?	Owen et al. (1982), Garcin et al. (2012)
29	N-1100	8420±170		9386	Shell	Lothagam	463	Sands	Overflow	2.8°N?, 36°E?	Yamasaki et al. (1974), Garcin et al. (2012)
30	Hel-1276	8920±130		9995	Shell	Koobi Fora	436	Sand bar	Interruption of Overflow	3.956°N?, 36.375°E?	Owen et al. (1982), Garcin et al. (2012)
31	Hel-1277	9110±130		10290	*Etheria*	Koobi Fora	436	Sand bar	Interruption of Overflow	3.956°N?, 36.375°E?	Owen et al. (1982), Garcin et al. (2012)
32	SUA-635	9315±140		10527	Shell	Koobi Fora	412	Beach sand	Interruption of Overflow	3.92°N?, 36.225°E?	Owen et al. (1982), Garcin et al. (2012)
33	Gx-5479	9660±235		11005	Shell	Koobi Fora	457	Sand spits	Overflow	4.077°N?, 36.347°E?	Owen et al. (1982), Garcin et al. (2012)
34	KIA36857	9740±50		11182	*Etheria elliptica*	Lake Turkana South Island	459	Abrasion platform	Overflow	2.6611°N, 36.5879°E	Garcin et al. (2012)
35	RI-954	9940±260		11502	Shell	Koobi Fora	457	Sand spits	Overflow	4.077°N?, 36.347°E?	Owen et al. (1982), Garcin et al. (2012)
36	KIA 36864	10025±55		11524	*Melanoides tuberculata*	South Island	414	Beach ridge	Lowstand, but nearly identical onset of Overflow	2.6221°N, 36.5708°E	Garcin et al. (2012)
37	SUA-638	10720±150		12630	Shell	Koobi Fora	416	Beach sand	Closed basin	3.94°N?, 36.2°E?	Owen et al. (1982), Garcin et al. (2012)
Suguta											
38	KIA35809	6345±40	4405±75	5018	ostracods	SE of Namarunu, central Suguta valley	312	240 m below overflow level.	Closed basin, lowstand	1.9128 N, 36.4651 E	Garcin et al. (2009), Garcin et al. (2017)
39	KIA36873	7850±50	5880±85	6700	*Melanoides tuberculata*	N flank of Emuru-angogolak volcanic center, S edge of Suguta valley	565	Maximum highstand shoreline (overflow level).	Overflow	1.5608 N, 36.3342 E	Garcin et al. (2009), Garcin et al. (2017)
40	KIA36866	8510±60	6540±95	7449	*Melanoides tuberculata*	Baragoi River mouth, S edge of Suguta valley	557	Maximum highstand shoreline (overflow level).	Overflow	1.61890 N, 36.4609 E	Garcin et al. (2009), Garcin et al. (2017)
41	KIA33903	9365±50	7395±85	8222	*Melanoides tuberculata*	"SANC" cinder cone, N edge of Suguta valley	533	Several shorelines from 492-560 m (560 m = maximum highstand). Carbonate-rich layer with snails and reworked material from 520-536 m.	Closed basin	2.2725 N, 36.5782 E	Garcin et al. (2009), Garcin et al. (2017)

*) ? at geographic coordinates denotes uncertain location for Lake Turkana region as given in Garcin et al. (2012).

Table D.2 (continued). Annotated list of published radiocarbon dates used to reconstruct lake overflow and closed lake conditions.

(part 2/10)

#	Lab ID	^{14}C date (BP)	Reservoir corrected ^{14}C date (BP)	Calibrated median age (cal. BP)	Dated material	Sample location	Published elevation (m)	Additional published information	Interpretation	Published Location	Reference
42	KIA33909	9775±45	7805±85	8601	*Melanoides tuberculata*	Losetum cinder cone, S edge of Suguta valley	519	Wave-cut notch at 561 m represents maximum highstand shoreline and discontinuous carbonate-rich layers from 500-550 m.	Closed basin?	1.5755 N, 36.3728 E	Garcin et al. (2009), Garcin et al. (2017)
43	KIA33901	9840±45	7870±85	8709	*Melanoides tuberculata*	"SANC" cinder cone, N edge of Suguta valley	481	Several shorelines from 492-560 m (560 m = maximum highstand). Date from a carbonate-rich layer with snails and reworked material at the bottom of the cinder cone.	Closed basin?	2.2724 N, 36.5781 E	Garcin et al. (2009), Garcin et al. (2017)
44	KIA33916	9970±45	8000±85	8854	*Melanoides tuberculata*	Nakitoekirion, W edge of Suguta valley	507	Site shows a series of terraces from 490 m to maximum highstand level at reached at 570 m. Isolated lacustrine nearshore deposits probably contemporenous to maximum highstand shoreline.	Contemporenous to overflow	1.9498 N, 36.3805 E	Garcin et al. (2009), Garcin et al. (2017)
45	KIA36872	9980±55	8010±90	8865	*Melanoides tuberculata*	S of Tirr Tirr Plateau, E edge of Suguta valley	559	Maximum highstand shoreline (overflow level), expressed as terrace reaching 566 m.	Overflow	1.7897 N, 36.5153 E	Garcin et al. (2009), Garcin et al. (2017)
46	KIA33917	10025±45	8055±85	8928	*Melanoides tuberculata*	S of Namarunu volcanic center, W edge of Suguta valley	564	Maximum highstand shoreline (overflow level).	Overflow	1.9555 N, 36.4156 E	Garcin et al. (2009), Garcin et al. (2017)
47	KIA33918	10750±50	8510±80	9503	*Melanoides tuberculata*	S of Namarunu volcanic center, W edge of Suguta valley	564	Maximum highstand shoreline (overflow level).	Overflow	1.9555 N, 36.4156 E	Garcin et al. (2009), Garcin et al. (2017)
48	KIA33913	10760±50	8520±80	9509	*Melanoides tuberculata*	Namurinyang cinder cone, N edge of Suguta valley	556	Shallow lacustrine deposits (partly reworked) below maximum highstand shoreline expressed as a wavecut notch at 570 m on a steep-sided cinder cone.	Contemporenous to Overflow	2.2479 N, 36.6137 E	Garcin et al. (2009), Garcin et al. (2017)
49	KIA37060	11495±60	9925±100	11409	*Etheria elliptica*	Namruy area, SW edge of Suguta valley	561	Shell found on top of Namruy (LN08) section, likely reworked from maximum highstand shoreline elevation.	Overflow	1.5378 N, 36.2251 E	Junginger et al. (2014), Garcin et al. (2017)
50	KIA33910	13725±60	12155±100	14031	*Melanoides tuberculata*	Namruy area, SW edge of Suguta valley	532	Up to 60-m-thick deltaic deposits indicative of near- to offshore environments. Upper units at 564 m (maximum highstand), lower unites at 500 m. Fossil snails and fish throughout the deposit.	Closed basin	1.5373 N, 36.2256 E	Garcin et al. (2009), Garcin et al. (2017)
51	KIA33907	13900±60	12330±100	14378	*Etheria elliptica*	Namruy area, SW edge of Suguta valley	530	Up to 60-m-thick deltaic deposits indicative of near- to offshore environments. Upper units at 564 m (maximum highstand), lower unites at 500 m. Fossil snails and fish throughout the deposit.	Closed basin	1.5373 N, 36.2256 E	Garcin et al. (2009), Garcin et al. (2017)

Table D.2 (continued). Annotated list of published radiocarbon dates used to reconstruct lake overflow and closed lake conditions.

(part 3/10)

#	Lab ID	^{14}C date (BP)	Reservoir corrected ^{14}C date (BP)	Calibrated median age (cal. BP)	Dated material	Sample location	Published elevation (m)	Additional published information	Interpretation	Published Location	Reference
52	UQ1017	9300±400	7680±405	8558	*Melanoides tuberculata*	Rupa, W-central Suguta Valley	484	^{14}C date normalized with -25‰ to 9650±400 yr BP. Diatomites rich in fossil *Tilapia* sp. (=*Oreochromis* sp.).	Approximate age of fish fossils	1.937 N, 36.395 E	Casanova et al. (1988)
53	Birm-585 a	11250±220	9680±235	11030	*Etheria elliptica*	Naserkalia, close to Suguta River, south of Suguta Valley	n.a.	Coarse gravel of beach deposit rich in catfish and perch overlying diatomaceous sediments. (catfish = Siluriformes; perch = *Lates* sp.).	Age of fish fossils	1.5333 N, 36.2666 E	Bishop (1975), Williams & Johnson (1976)
54	Birm-585 b	10570±300	8330±305	9272	*Etheria elliptica*	Naserkalia, close to Suguta River, south of Suguta Valley	n.a.	Coarse gravel of beach deposit rich in catfish and perch overlying diatomaceous sediments. (catfish = Siluriformes; perch = *Lates* sp.).	Age of fish fossils	1.5333 N, 36.2666 E	Bishop (1975), Williams & Johnson (1976)
Baringo-Bogoria											
55	Birm-883 a	10560±170	6580±170	7470	*Melanoides tuberculata* inner shell	NW shore of Lake Bogoria	992.6	Sample 2.95-3.10 m above 1976 Bogoria lake level.	No overflow (Lake Bogoria Closed/isolated)	0.300 N, 36.078 E	Young & Renaut (1979)
56	Birm-883 b	10320±150	6340±150	7245	*Melanoides tuberculata* middle shell	NW shore of Lake Bogoria	992.6	Sample 2.95-3.10 m above 1976 Bogoria lake level.	No overflow (Lake Bogoria Closed/isolated)	0.300 N, 36.078 E	Young & Renaut (1979)
57	Birm-542 a	13850±430	9870±430	11397	*Melanoides tuberculata* middle shell	W shore Lake Baringo, Kobwob Murren	987	Beach/near-shore deposit 15.85 m above 1969/1973 Baringo lake level, maximum shoreline. Sediments contain fossil *Tilapia* (*Oreochromis*) sp. and *Lates niloticus*.	Overflow of Baringo (connected Lake Baringo Bogoria), Age of fish fossils	0.633 N, 36.016 E	Williams & Johnson (1976), Young & Renaut (1979), Renaut (1982)
58	Birm-542 b	13670±320	9690±320	11087	*Melanoides tuberculata* inner shell	W shore Lake Baringo, Kobwob Murren	987	Beach/near-shore deposit 15.85 m above 1969/1973 Baringo lake level, maximum shoreline. Sediments contain fossil *Tilapia* (*Oreochromis*) sp. and *Lates niloticus*.	Overflow of Baringo (connected Lake Baringo Bogoria), Age of fish fossils	0.633 N, 36.016 E	Williams & Johnson (1976), Young & Renaut (1979), Renaut (1982)
59	Birm-541 a	11870±310	7890±310	8783	*Melanoides tuberculata* inner shell	Logumukum (Loboi Plain), halfway between Lakes Bogoria and Baringo	987	Emerged beach 15.85 m above 1969/1973 Baringo lake level, maximum shoreline. Sediments contain fossil *Labeo* sp.	Overflow of Bogoria and Baringo (connected Lake Baringo-Bogoria), Age of fish fossils	0.450 N, 36.083 E	Williams & Johnson (1976), Young & Renaut (1979), Renaut (1982)
60	Birm-541 b	10860±280	6880±280	7742	*Melanoides tuberculata* middle shell	Logumukum (Loboi Plain), halfway between Lakes Bogoria and Baringo	987	Emerged beach 15.85 m above 1969/1973 Baringo lake level, maximum shoreline. Sediments contain fossil *Labeo* sp.	Overflow of Bogoria and Baringo (connected Lake Baringo-Bogoria), Age of fish fossils	0.450 N, 36.083 E	Williams & Johnson (1976), Young & Renaut (1979), Renaut (1982)
61	Birm-544 a	12260±280	8280±280	9213	*Melanoides tuberculata* inner shell	W of Lake Baringo	ca. 986.5	Silt 15.54 m above 1969/1973 Baringo lake level.	Overflow of Baringo (connected Lake Baringo Bogoria)	0.583 N, 36.000 E	Williams & Johnson (1976), Young & Renaut (1979)
62	Birm-544 b	12600±280	8620±280	9676	*Melanoides tuberculata* middle shell	W of Lake Baringo	ca. 986.5	Silt 15.54 m above 1969/1973 Baringo lake level.	Overflow of Baringo (connected Lake Baringo Bogoria)	0.583 N, 36.000 E	Williams & Johnson (1976), Young & Renaut (1979)

Table D.2 (continued). Annotated list of published radiocarbon dates used to reconstruct lake overflow and closed lake conditions.
(part 4/10)

#	Lab ID	^{14}C date (BP)	Reservoir corrected ^{14}C date (BP)	Calibrated median age (cal. BP)	Dated material	Sample location	Published elevation (m)	Additional published information	Interpretation	Published Location	Reference
63	Birm-545 a	9940±250	5960±250	6813	*Melanoides tuberculata* inner shell	W of Lake Baringo	ca. 981	Intermediate shoreline 10.06 m above 1969/1973 Baringo lake level.	Overflow of Baringo	0.592 N, 36.000 E	Williams & Johnson (1976), Young & Renaut (1979)
64	Birm-545 b	10810±270	6830±270	7696	*Melanoides tuberculata* middle shell	W of Lake Baringo	ca. 981	Intermediate shoreline 10.06 m above 1969/1973 Baringo lake level.	Overflow of Baringo	0.592 N, 36.000 E	Williams & Johnson (1976), Young & Renaut (1979)
65	Birm-543 a	7620±180	3640±180	3978	*Unio* sp. & *Viviparus*? sp. inner shells	W of Lake Baringo	ca. 975	Beach/near-shore deposit 3.66 m above 1969/1973 Baringo lake level.	No overflow (Lake Baringo Closed/isolated)	0.603 N, 36.014 E	Williams & Johnson (1976)
66	Birm-543 b	8460±180	4480±180	5127	*Unio* sp. & *Viviparus*? sp. middle shells	W of Lake Baringo	ca. 975	Beach/near-shore deposit 3.66 m above 1969/1973 Baringo lake level.	No overflow (Lake Baringo Closed/isolated)	0.603 N, 36.014 E	Williams & Johnson (1976)
Menengai											
67	KIA28136	4555±146		5207	Charcoal in diatomite	Menengai caldera	1807	Sediments partly laminated, indicating deep lake.	Minimum age of overflow	0.1631 S, 36.0960 E	Riedl et al. (2020)
68	Poz-59047	10440±210		12249	Plant remains in basal lake sediments (diatomite)	Menengai caldera	1742	Caldera lake coeval with phreatomagmatic "Ruplax tuff", indicating water-filled caldera.	Possible onset of overflow	0.1816 S, 36.0735 E	Riedl et al. (2020), Leat (1983)
Nakuru-Elmenteita											
69	GX-4320	1370±140		1282	n.a.	Nderit Drift, Fm. 4	n.a. (~1830-1850)	Incision and filling of Nderit River Gorge into L. Nakuru basin floor (alluvial canyon fillings); post high lake stage.	Closed basin(s), likely separate lakes	0.5191 S, 36.1038 E	Bower et al. (1977)
70	GX-4419	3135±155		3332	n.a.	Nderit Drift, Fm. 4	n.a. (~1830-1850)	Incision and filling of Nderit River Gorge into L. Nakuru basin floor (alluvial canyon fillings); post high lake stage.	Closed basin(s), likely separate lakes	0.5191 S, 36.1038 E	Bower et al. (1977)
71	N-821	3540±120		3832	charcoal	Nderit Drift, Fm. 4	n.a. (~1830-1850)	Brown, alluvial silts, upper member of formation. Lake Nakuru below +50 m lake level.	Closed basin(s), likely separate lakes	0.5191 S, 36.1038 E	Butzer et al. (1972), Isaac et al. (1972)
72	n.a.	3735±255		4113	bulk sediment	Lake Nakuru core	n.a.	Lake Nakuru moderately fresh and probably confined to its own basin (same with L. Elmenteita). Mostly a dry lake during this time.	Closed basin(s), likely separate lakes	0.3701 S, 36.0895 E	Richardson (1972)
73	GX-4470	4040±140		4535	n.a.	Nderit Drift, Fm. 4	n.a. (~1830-1850)	Incision and filling of Nderit River Gorge into L. Nakuru basin floor (alluvial canyon fillings); post high lake stage.	Closed basin(s), likely separate lakes	0.5191 S, 36.1038 E	Bower et al. (1977); Bower & Nelson (1978)
74	I-5554	6490±125		7394	bulk sediment	Lake Elmenteita core	n.a.	Lake Elmenteita was moderately alkaline, its level at the time above the modern lake level, but no overflow. Marks beginning of rapidly declining lake levels.	Closed basin	0.4424 S, 36.2439 E	Richardson (1972)
75	GX-4317	7005±175		7839	charcoal	Nderit Drift, Fm. 3, Mbr. 8	n.a. (~1830-1850)	Incision and filling of Nderit River Gorge into L. Nakuru basin floor asscoiated with intermediate level of Lake Nakuru.	Closed basin	0.5191 S, 36.1038 E	Bower et al. (1977); Bower & Nelson (1978)
76	GX-4215	7105±180		7932	charcoal	Nderit Drift, Fm. 3, Mbr. 8	n.a. (~1830-1850)	Incision and filling of Nderit River Gorge into L. Nakuru basin floor asscoiated with intermediate level of Lake Nakuru.	Closed basin	0.5191 S, 36.1038 E	Bower et al. (1977); Bower & Nelson (1978)

Table D.2 (continued). Annotated list of published radiocarbon dates used to reconstruct lake overflow and closed lake conditions.

(part 5/10)

#	Lab ID	^{14}C date (BP)	Reservoir corrected ^{14}C date (BP)	Calibrated median age (cal. BP)	Dated material	Sample location	Published elevation (m)	Additional published information	Interpretation	Published Location	Reference
77	UCLA-1757	7410±160		8216	buried hominin	Bromhead's Site	1867	104 m above present level of Lake Nakuru. Post overflow highstand.	Closed basin	0.4910 S, 36.0827 E	Protsch (1978), Berger & Protsch (1989)
78	GX-0290	8095±190		9005	charcoal	Gamble's Cave, Layer 4	~1934	Excavation directly above beach deposits from last phase of overflow of L. Nakuru, indicate stable lake level. (Comment: otherwise the charcoal should have been deposited at lower elevation)	Overflow (merged lakes)	0.5513 S, 36.0915 E	Bower et al. (1977)
79	GX-0289	8245±175		9198	charcoal	Gamble's Cave, Layer 4	~1934	Excavation directly above beach deposits from last phase of overflow of L. Nakuru, indicate stable lake level. (Comment: otherwise the charcoal should have been deposited at lower elevation)	Overflow (merged lakes)	0.5513 S, 36.0915 E	Bower et al. (1977)
80	KIA13109	8440±40		9474	snail shells	Lemulug Volcano	1932	Highest outcrops of early Holocene lacustrine sediments corresponding to maximum highstand shoreline at Katerit Volcano.	Overflow (merged lakes)	0.5005 S, 36.2436 E	Dühnforth et al. (2006)
81	GX-0288	8510±180		9508	charcoal	Gamble's Cave, Layer 4	~1934	Excavation directly above beach deposits from last phase of overflow of L. Nakuru, indicate stable lake level. (Comment: otherwise the charcoal should have been deposited at lower elevation)	Overflow (merged lakes)	0.5513 S, 36.0915 E	Bower et al. (1977)
82	n.a.	8640±215		9703	organic mud	Lake Nakuru core	n.a.	Open, merged freshwater lake. Dominance of *Stephanodiscus rotula*, indicating deep, (seasonally) stratified lake. Probably surface outlet to the north.	Overflow (merged lakes)	0.3701 S, 36.0895 E	Richardson (1972), Richardson & Dussinger (1986)
83	I-5179	8740±190		9815	organic mud	Lake Elmenteita core	n.a.	Enlarged, very fresh lake. Dominance of *Stephanodiscus rotula*, indicating a deep, (seasonally) stratified lake. Probably surface outlet to the north. Open merged freshwater lake.	Overflow (merged lakes)	0.4424 S, 36.2439 E	Richardson (1972), Butzer et al. (1972), Richardson & Dussinger (1986)
84	L-1201	9650±250		10997	mixed shells	Katerit Volcano	1888	Radiocarbon date of shell layer at 1888 m associated with maximum highstand shoreline at 1943 m present on the same volcano (180 m above present lake level (= overflow level).	Overflow (merged lakes)	0.5074 S, 36.2700 E	Washbourn-Kamau (1970), Butzer et al. (1972)
85	n.a.	10340±150		12154	organic mud	Lake Nakuru core	n.a.	Beginning of Lake Nakuru's major freshening phase and merging of Lakes Nakuru and Elmenteita. Very fresh, start of Gamble's Cave shoreline. Open, merged freshwater lake.	Overflow (merged lakes)	0.3701 S, 36.0895 E	Richardson (1972), Richardson & Dussinger (1986)

Table D.2 (continued). Annotated list of published radiocarbon dates used to reconstruct lake overflow and closed lake conditions.

(part 6/10)

#	Lab ID	^{14}C date (BP)	Reservoir corrected ^{14}C date (BP)	Calibrated median age (cal. BP)	Dated material	Sample location	Published elevation (m)	Additional published information	Interpretation	Published Location	Reference
86	KIA13108	10390±45		12267	snail shells	E of Lake Elmenteita	1894	Near shoreline deposit (beach gravel) dated at 2.5 m below surface.	Closed basin(s)	0.4270 S, 36.2629 E	Dühnforth et al. (2006)
87	GX-4214	10685±270		12523	n.a.	Nderit drift, Fm 3, Member 7	n.a. (~1830-1850)	Incising of the of Nderit River Gorge into the Lake Nakuru basin floor, accompanied by deposition of alluvial sediments. Preceding L. Nakuru overflow phase.	Closed basin(s)	0.5191 S, 36.1038 E	Bower et al. (1977)
88	N-822-3	12000±215		13893	charcoal	Nderit drift Unit b	n.a. (~1830-1850)	Ponded valley and deltaic deposits, indicating a transgressive phase of ca. 60 m above modern level of Lake Nakuru.	Closed basin(s)	0.5191 S, 36.1038 E	Butzer et al. (1972), Isaac et al. (1972), Yamasaki et al. (1972)
89	GX-4215	12065±365		14089	n.a.	Nderit drift, Fm 3, Member 7	n.a. (~1830-1850)	Incising of the of Nderit River Gorge into the Lake Nakuru basin floor, accompanied by deposition of alluvial sediments. Preceding L. Nakuru overflow phase.	Closed basin(s)	0.5191 S, 36.1038 E	Bower et al. (1977)
90	I-5062	12160±170		14091	charcoal	Nderit drift Unit b	n.a. (~1830-1850)	Ponded valley and deltaic deposits, indicating a transgressive phase of ca. 60 m above modern level of Lake Nakuru.	Closed basin(s)	0.5191 S, 36.1038 E	Butzer et al. (1972), Isaac et al. (1972)
91	I-5178	12200±180		14176	organic mud	Lake Elmenteita core	n.a.	Early weak phase of freshening of Lake Elmenteita, before receding again. Lakes remains closed.	Closed basin(s)	0.4424 S, 36.2439 E	Richardson (1972)
92	N-822-2	12200±220		14210	charcoal	Nderit drift Unit b	n.a. (~1830-1850)	Ponded valley and deltaic deposits, indicating a transgressive phase of ca. 60 m above modern level of Lake Nakuru.	Closed basin(s)	0.5191 S, 36.1038 E	Butzer et al. (1972), Isaac et al. (1972), Yamasaki et al. (1972)
93	N-822-1	12300±220		14391	charcoal	Nderit drift Unit b	n.a. (~1830-1850)	Ponded valley and deltaic deposits, indicating a transgressive phase of ca. 60 m above modern level of Lake Nakuru.	Closed basin(s)	0.5191 S, 36.1038 E	Butzer et al. (1972), Isaac et al. (1972), Yamasaki et al. (1972)
94	n.a.	12850±190		15333	bulk sediment	Nakuru core	n.a.	Diatom assemblages indicate brief shift from low lake level and high alkalinity to more dilute conditions and higher lake level followed by return to lower levels until ~10500 ^{14}C BP.	Closed basin(s)	0.3701 S, 36.0895 E	Richardson (1972), Richardson & Dussinger (1986)
Marula Rockshelter											
95	GX-6763-A	7195±260		8026	n.a.	Marula Rock Shelter	~2000	Dated deposit from which a rich fauna, including one lower 2nd molar from *Hylochoerus meinertzhageni* was recovered.	Date of fossil fauna	0.6505 S, 36.3388 E	Gifford-Gonzalez (1998, 1985), Ambrose (1985)

Table D.2 (continued). Annotated list of published radiocarbon dates used to reconstruct lake overflow and closed lake conditions.

(part 7/10)

#	Lab ID	^{14}C date (BP)	Reservoir corrected ^{14}C date (BP)	Calibrated median age (cal. BP)	Dated material	Sample location	Published elevation (m)	Additional published information	Interpretation	Published Location	Reference
Naivasha											
96	n.a.	1740±95		1660	bulk sediment	Lake Naivasha main basin core	n.a.	Lowstand. Beginning of modern lake character.	Closed basin	0.7757 S, 36.3538 E	Richardson & Dussinger (1986)
97	Y-1436	3000±60		3183	bulk sediment	Crescent Island Crater core	n.a.	Date from above dessication layer. Lake probably dried out completely for a short time.	Closed basin	0.7643 S, 36.4097 E	Richardson (1966), Butzer et al. (1972), Richardson & Richardson (1972)
98	Y-1769	3040±60		3240	bulk sediment	Crescent Island Crater core	n.a.	Date from above dessication layer. Lake probably dried out completely for a short time.	Closed basin	0.7643 S, 36.4097 E	Butzer et al. (1972), Richardson & Richardson (1972)
99	n.a.	4145±100		4668	bulk sediment	Lake Naivasha main basin core	n.a.	Shallow conditions after rapid lake level decline.	Closed basin	0.7757 S, 36.3538 E	Richardson & Dussinger (1986)
100	Y-1339	5650±120		6452	bulk sediment	Crescent Island Crater core	n.a.	The date marks the termination of enlarged, deep lake phase with an active surface outlet. Deep-lake diatom indicators decline/dissapaer after this time, while organic matter content increases.	Overflow	0.7643 S, 36.4097 E	Richardson (1966), Butzer et al. (1972), Richardson & Richardson (1972)
101	I-1340	9200±160		10399	bulk sediment	Crescent Island Crater core	n.a.	Fairly stable, enlarged and deep freshwater lake which was overflowing through its surface outlet the Ol Njorowa gorge. Occurrence of *Stephanodiscus* in the diatom assemblage indicates a deep, possibly stratified lake .	Overflow	0.7643 S, 36.4097 E	Richardson (1966), Butzer et al. (1972), Richardson & Richardson (1972)
102	n.a.	9670±160		10996	bulk sediment	Lake Naivasha main basin core	n.a.	Begin highstand phase with continuously high water levels. Diatom assemblages dominated by *Melosira agassizii*.	Overflow	0.7757 S, 36.3538 E	Richardson & Dussinger (1986)
103	UCLA-1741	10850±330		12748	hominin bones	Prehistoric site close to Naivasha town.	n.a.	Drowned hominin found in bottom of lacustrine silt layer close to (former) lake shore. Skeleton located 10 m below highest Naivasha lake level.	Closed basin	0.7333 S, 36.4333 E	Protsch (1976), Berger & Protsch (1989)
104	n.a.	12270±180		14318	bulk sediment	Lake Naivasha main basin core	n.a.	Diatom assemblages indicate low lake level (below and close to modern level) and relatively fresh to more alkaline conditions.	Closed basin	0.7757 S, 36.3538 E	Richardson & Dussinger (1986)
Magadi-Natron											
105	UQ938	7000±100	4950±120	5703	stromatolite	Magadi-Natron basin	n.a.	Regressive shoreline	Two separate lakes	n.a.	Hillaire-Marcel et al. (1986)
106	UQ982	7880±450	5830±455	6662	stromatolite	Magadi-Natron basin	n.a.	Regressive shoreline	Two separate lakes	n.a.	Hillaire-Marcel et al. (1986)
107	UQ959	8100±200	6050±210	6914	stromatolite	Magadi-Natron basin	n.a.	Regressive shoreline	Two separate lakes	n.a.	Hillaire-Marcel et al. (1986)
108	UQ920	8500±100	6450±120	7360	stromatolite	Magadi-Natron basin	n.a.	Regressive shoreline	Two separate lakes	n.a.	Hillaire-Marcel et al. (1986)
109	UQ936	9650±100	7600±120	8406	stromatolite	NW of L. Magadi	650	Highstand shoreline	Single merged lake	1.770 S, 36.245 E	Hillaire-Marcel et al. (1986)
110	UQ907	9650±200	7600±210	8420	stromatolite	Magadi-Natron basin	645-656	Highstand shoreline	Single merged lake	n.a.	Hillaire-Marcel et al. (1986)

Table D.2 (continued). Annotated list of published radiocarbon dates used to reconstruct lake overflow and closed lake conditions.

(part 8/10)

#	Lab ID	^{14}C date (BP)	Reservoir corrected ^{14}C date (BP)	Cali-brated median age (cal. BP)	Dated material	Sample location	Pub-lished elevation (m)	Additional published information	Interpretation	Published Location	Reference
111	UQ904	9700±200	7650±210	8481	stromatolite	NE of L. Natron	656	Highstand shoreline	Single merged lake	2.215 S, 36.153 E	Hillaire-Marcel et al. (1986)
112	UQ953	9710±100	7660±120	8469	stromatolite	Magadi-Natron basin	645-656	Highstand shoreline. Compan-ion sample to UQ951: top of stromatolite	Single merged lake	n.a.	Hillaire-Marcel et al. (1986)
113	UQ910	9800±100	7750±120	8557	stromatolite	W of L. Magadi	656	Highstand shoreline	Single merged lake	1.804 S, 36.261 E	Hillaire-Marcel et al. (1986)
114	UQ932	9800±200	7750±210	8599	stromatolite	N of L. Natron	656	Highstand shoreline	Single merged lake	1.997 S, 36.049 E	Hillaire-Marcel et al. (1986)
115	UQ894	9850±100	7800±120	8621	stromatolite	NE of L. Natron	656	Highstand shoreline	Single merged lake	2.172 S, 36.103 E	Hillaire-Marcel et al. (1986)
116	UQ951	9860±150	7810±165	8660	stromatolite	Magadi-Natron basin	645-656	Highstand shoreline. Compan-ion sample to UQ953: bottom of stromatolite	Single merged lake	n.a.	Hillaire-Marcel et al. (1986)
117	UQ673	9900±150	7850±165	8709	stromatolite	SW of L. Natron	645	Highstand shoreline	Single merged lake	2.543 S, 35.891 E	Hillaire-Marcel et al. (1986)
118	UQ943	10090±140	8040±155	8919	stromatolite	Magadi-Natron basin	645-656	Highstand shoreline	Single merged lake	n.a.	Hillaire-Marcel et al. (1986)
119	UQ614	10250±110	8200±125	9171	stromatolite	Magadi-Natron basin	645-656	Highstand shoreline	Single merged lake	n.a.	Hillaire-Marcel et al. (1986)
120	UQ659	10300±105	8250±120	9227	stromatolite	Magadi-Natron basin	645-656	Highstand shoreline	Single merged lake	n.a.	Hillaire-Marcel et al. (1986)
121	UQ627	10300±115	8250±130	9224	stromatolite	Magadi-Natron basin	645-656	Highstand shoreline	Single merged lake	n.a.	Hillaire-Marcel et al. (1986)
122	UQ652	10300±130	8250±145	9218	stromatolite	NW of L. Natron	656	Highstand shoreline	Single merged lake	2.221 S, 35.968 E	Hillaire-Marcel et al. (1986)
123	UQ899	10300±200	8250±210	9190	stromatolite	NE of L. Magadi	656	Highstand shoreline	Single merged lake	1.806 S, 36.322 E	Hillaire-Marcel et al. (1986)
124	UQ564	10360±160	8310±170	9270	stromatolite	W of L. Natron	645	Highstand shoreline	Single merged lake	2.308 S, 35.956 E	Hillaire-Marcel et al. (1986)
125	UQ877	10460±120	8410±135	9381	stromatolite	NE of L. Natron	656	Highstand shoreline	Single merged lake	2.138 S, 36.060 E	Hillaire-Marcel et al. (1986)
126	UQ661	10560±125	8510±140	9502	stromatolite	Magadi-Natron basin	645-656	Highstand shoreline	Single merged lake	n.a.	Hillaire-Marcel et al. (1986)
127	UQ933	10650±100	8600±120	9617	stromatolite	Magadi-Natron basin	645-656	Highstand shoreline	Single merged lake	n.a.	Hillaire-Marcel et al. (1986)
128	UQ669	10660±115	8610±130	9636	stromatolite	Magadi-Natron basin	645-656	Highstand shoreline	Single merged lake	n.a.	Hillaire-Marcel et al. (1986)
129	UQ911	10750±200	8700±210	9775	stromatolite	W of L. Magadi	650	Highstand shoreline	Single merged lake	1.926 S, 36.183 E	Hillaire-Marcel et al. (1986)
130	UQ886	10850±300	8800±305	9887	stromatolite	Magadi-Natron basin	645-656	Highstand shoreline	Single merged lake	n.a.	Hillaire-Marcel et al. (1986)
131	UQ888	10950±200	8900±210	9975	stromatolite	Magadi-Natron basin	645-656	Highstand shoreline	Single merged lake	n.a.	Hillaire-Marcel et al. (1986)
132	UQ909	11350±200	9300±210	10536	stromatolite	W of L. Magadi	656	Highstand shoreline	Single merged lake	1.804 S, 36.261 E	Hillaire-Marcel et al. (1986)
133	UQ618	11375±140	9325±155	10551	stromatolite	NW of L. Natron	645-656	Highstand shoreline	Single merged lake	2.157 S, 35.980 E	Hillaire-Marcel et al. (1986)
134	UQ917	11500±100	9450±120	10732	stromatolite	N of L. Natron	656	Highstand shoreline	Single merged lake	1.997 S, 36.049 E	Hillaire-Marcel et al. (1986)
135	UQ587	11640±100	9590±120	10928	stromatolite	SW of L. Natron	650	Highstand shoreline	Single merged lake	2.518 S, 35.903 E	Hillaire-Marcel et al. (1986)
136	UQ636	11950±115	9900±130	11399	stromatolite	Magadi-Natron basin	645-656	Highstand shoreline	Single merged lake	n.a.	Hillaire-Marcel et al. (1986)

Table D.2 (continued). Annotated list of published radiocarbon dates used to reconstruct lake overflow and closed lake conditions.

(part 9/10)

#	Lab ID	^{14}C date (BP)	Reservoir corrected ^{14}C date (BP)	Calibrated median age (cal. BP)	Dated material	Sample location	Published elevation (m)	Additional published information	Interpretation	Published Location	Reference
137	UQ767	12025±175	9975±185	11540	stromatolite	Magadi-Natron basin	645-656	Highstand shoreline	single merged lake	n.a.	Hillaire-Marcel et al. (1986)
138	UQ930	12450±100	10400±120	12262	stromatolite	S of L. Magadi	645	Highstand shoreline	Single merged lake	1.995 S, 36.266 E	Hillaire-Marcel et al. (1986)
139	UQ927	4560±400	2510±405	2581	*Alcolapia* fish bone	SE of Lake Magadi	605	High Magadi beds	Age of fish fossils, two separate lakes	1.94 S, 36.29 E	Hillaire-Marcel et al. (1986)
140	N-862	9120±170	7070±180	7897	Organic fraction of carbonaceous fish fossil lamina (*Alcolapia*)	Dry Lagoon SE of Lake Magadi	n.a.	High Magadi Beds: a few meters above 604 m lake level	Age of fish fossils, two separate lakes	1.9833 S, 36.2666 E	Isaac et al. (1972), Butzer et al. (1972), Yamasaki et al. (1972)
141	n.a.	10000 ±200†	7950±210	8830	*Alcolapia* fish bone	SE and NW side of Lake Magadi	ca. 624 and 629	20 and 25 m above 1996 Magadi lake level	Age of fish fossils, single merged lake	1.9883 S, 36.2686 E; 1.8087 S, 36.2594 E	Tichy & Seegers (1999), H. Tichy pers. communication

†) sigma range assumed (not reported in original paper)

Table D.2 (continued). Annotated list of published radiocarbon dates used to reconstruct lake overflow and closed lake conditions.

(part 10/10)

New radiocarbon dates from the study sites in the Southern Kenya Rift.

Site	Lab ID	Outcrop ID	Depth below top of outcrop (cm)	Depositional environment	Dated material	^{14}C date (yr BP)	Reservoir effect (yr ± 1σ)[1]	Reservoir corrected ^{14}C date (yr BP)[1, 2]	Calibrated median age (cal. yr BP)	Calibrated age 2σ error bounds (cal. yr BP)	Geographic coordinates (°)	Elevation (m)
Siriata	Poz-78488	KOO15-1A[3]	0	lacustrine	*Corbicula* sp.	11080 ± 60		6985 ± 190	7824	7495 - 8179	1.99588 S 36.35392 E	809.1
Siriata	Poz-78489	KOO15-1A	100	lacustrine	*Corbicula* sp.	12210 ± 60		8155 ± 190	9086	8598 - 9493	1.99588 S 36.35392 E	808.1
Siriata	Poz-75380	KOO15-1A	180	lacustrine	*Melanoides tuberculata*	12890 ± 60		8795 ± 190	9868	9453 - 10291	1.99588 S 36.35392 E	807.3
Siriata	Poz-78491	KOO15-1A	270	lacustrine	*Corbicula* sp.	13580 ± 110		9485 ± 210	10788	10233 - 11259	1.99588 S 36.35392 E	806.4
Siriata	Poz-89468	KOO15-3E[4]	430	lacustrine	charcoal	8680 ± 250		-	9753	9034 - 10370	1.96413 S 36.36753 E	806.7
Siriata	Poz-78492	KOO15-3E	430	lacustrine	*Corbicula* sp.	12660 ± 70	3980 ± 260	8565 ± 195	9596	9128 - 10169	1.96413 S 36.36753 E	806.7
Siriata	Poz-78493	KOO15-3E	490	lacustrine	*Corbicula* sp.	12900 ± 90		8805 ± 200	9879	9456 - 10381	1.96413 S 36.36753 E	806.1
Siriata	Poz-78495	KOO15-3E	570	lacustrine	*Melanoides tuberculata*	13040 ± 70		8945 ± 195	10019	9544 - 10501	1.96413 S 36.36753 E	805.3
Siriata	Poz-78423	KOO15-3E	666	lacustrine	*Melanoides* fragments	14060 ± 180		9965 ± 255	11541	10735 - 12396	1.96413 S 36.36753 E	804.3
Siriata	Poz-78442	KOO15-3E	700	tephra	Charcoal	7540 ± 50		-	8361	8205 - 8421	1.96413 S 36.36753 E	804.0
Siriata	Poz-89664	KOO15-3E	713	lacustrine	Charcoal	10030 ± 150		-	11595	11194 - 12112	1.96413 S 36.36753 E	803.9
Siriata	Poz-78390	KOO15-3E	750	silicious paleosol	Charcoal	10440 ± 100		-	12320	12005 - 12628	1.96413 S 36.36753 E	803.5
Siriata	Poz-78496	KOO15-3D	22-23.5	lacustrine	*Corbicula* sp.	12770 ± 70		8675 ± 195	9745	9302 - 10225	1.96375 S 36.36785 E	812.9
Siriata	Poz-78497	KOO15-3D	40-44	lacustrine	*Corbicula* sp.	12670 ± 60		8575 ± 190	9610	9136 - 10166	1.96375 S 36.36785 E	812.7
Siriata	Poz-78498	KOO15-6B[5]	575	lacustrine	*Corbicula* sp.	13710 ± 70		9615 ± 195	10939	10300 - 11600	2.03814 S 36.36776 E	809.6
Siriata	Poz-78499	KOO15-6B	630	lacustrine	*Corbicula* sp.	13600 ± 70	4380 ± 120	9505 ± 195	10815	10267 - 11239	2.03814 S 36.36776 E	809.0
Siriata	Poz-78392	KOO15-6B	630	lacustrine	Charcoal	9220 ± 100		-	10403	10217 - 10655	2.03814 S 36.36776 E	809.0
Siriata	Poz-78500	KOO15-6B	650	lacustrine	*Corbicula* sp.	13240 ± 70	3930 ± 120	9145 ± 195	10327	9682 - 11065	2.03814 S 36.36776 E	808.8
Siriata	Poz-78391	KOO15-6B	650	lacustrine	Charcoal	9310 ± 100		-	10505	10244 - 10745	2.03814 S 36.36776 E	808.8
Kwenia	Poz-89660	KWE16-1C[6]	ca. 15	lacustrine	Fish bone	18030 ± 100		13935 ± 205	16889	16289 - 17478	1.83197 S 36.49121 E	1093.1
Ol Keju Nyiro River	Poz-89658	RI[7]	580	fluvial / alluvial	Bulk sediment	6130 ± 40		-	7025	6912 - 7160	1.59300 S 36.40646 E	921.3
Ol Keju Nyiro River	Poz-89659	RII[7]	180	fluvial / alluvial	Bulk sediment	3770 ± 40		-	4139	3986 - 4282	1.59297 S 36.40684 E	925.3

[1] sigma range calculated by root mean square and rounded to nearest 5.

[2] reservoir correction to all carbonate-derived ^{14}C dates by subtraction of 4095±180 ^{14}C years.

[3] see photo 6 in Fig. D.4. [4] see photo 7 in Fig. D.4. [5] see photo 8 in Fig. D.4. [6] see photo 9 in Fig. D.4. [7] see photo 10 in Fig. D.4.

Table D.3. *Radiocarbon dates from the study sites in the Southern Kenya Rift.*

Cumulative probability distributions for the time and duration of overflow and closed basin conditions of Kenya Rift lakes

River	Lake Basin	Age ranges as Cumulative Probability Distributions (CPD) in years cal. BP (probability)*		
		mid-late Holocene closed-lake basin level	**early Holocene overflow-lake level**	**late Pleistocene closed-lake basin level**
Northern River	Nakuru-Elmenteita	*One Sigma Ranges*: 1181 – 1380 (0.085651) 3279 – 3280 (0.000346) 3345 – 3404 (0.021324) 3428 – 3442 (0.004892) 3634 – 4085 (0.212959) 4298 – 4328 (0.010201) 4353 – 4370 (0.005998) 4384 – 4585 (0.080385) 4597 – 4611 (0.00493) 4767 – 4782 (0.005428) 7271 – 7516 (0.122416) 7537 – 7562 (0.009146) 7664 – 8369 (0.436325) *Two Sigma Ranges*: 1058 – 1524 (0.103493) 3070 – 4836 (0.448508) 7180 – 7196 (0.0018) 7243 – 8418 (0.446199)	*One Sigma Ranges*: 8784 – 8831 (0.016846) 8863 – 8888 (0.009005) 8892 – 8918 (0.008841) 8954 – 8962 (0.002627) 8969 – 10160 (0.962681) *Two Sigma Ranges*: 8592 – 10237 (0.775591) 10572 – 11356 (0.095099) 11378 – 11387 (0.000668) 11623 – 11677 (0.004142) 11692 – 12548 (0.124501)	*One Sigma Ranges*: 12121 – 12406 (0.173455) 13608 – 13684 (0.031648) 13696 – 14756 (0.794897) *Two Sigma Ranges*: 12014 – 12869 (0.206384) 13436 – 15728 (0.793616)
	Menengai	*no lake/no dates*	*One Sigma Ranges:* 4965 – 5469 (0.578404) 5564 – 5565 (0.000722) 12073 – 12564 (0.420873) *Two Sigma Ranges:* 4840 – 5593 (0.511361) 11620 – 11683 (0.009513) 11686 – 12719 (0.479127)	*no lake/no dates*
	Baringo-Bogoria	*One Sigma Ranges*: 3851 – 4085 (0.090095) 4974 – 5018 (0.016382) 5030 – 5298 (0.102728) 6790 – 7843 (0.790795) *Two Sigma Ranges*: 3575 – 4417 (0.161979) 4727 – 4751 (0.001705) 4819 – 5486 (0.149733) 5508 – 5581 (0.006504) 6322 – 6371 (0.003697) 6392 – 8051 (0.674339) 8095 – 8105 (0.0008) 8122 – 8130 (0.000582) 8142 – 8151 (0.000661)	*One Sigma Ranges*: 7510 – 7544 (0.009181) 7555 – 7966 (0.146254) 8460 – 8468 (0.002357) 8475 – 8497 (0.005584) 8511 – 9911 (0.603144) 10708 – 11407 (0.217683) 11450 – 11472 (0.005516) 11557 – 11597 (0.010282) *Two Sigma Ranges*: 7343 – 7346 (0.000255) 7417 – 12089 (0.999745)	*no dates*

* CPDs based on ^{14}C dates listed in Tables D.2 and D.3.

Table D.4. *Cumulative probability distributions for the time and duration of overflow and closed basin conditions of Kenya Rift lakes.*
(Part 1/3)

River	Lake Basin	Age ranges as Cumulative Probability Distributions (CPD) in years cal. BP (probability)*		
		mid-late Holocene closed-lake basin level	**early Holocene overflow-lake level**	**late Pleistocene closed-lake basin level**
Northern River (continued)	Suguta	*One Sigma Ranges*: 4871 – 5045 (0.098026) 8163 – 8334 (0.115458) 8455 – 8503 (0.489169) 9439 – 9554 (0.134765) *Two Sigma Ranges*: 4847 – 5289 (0.127685) 8022 – 8380 (0.127339) 8416 – 9028 (0.383551) 9333 – 9338 (0.000563) 9405 – 9631 (0.116378) 9647 – 9655 (0.000896)	*One Sigma Ranges*: 6634 – 6790 (0.134967) 7326 – 7399 (0.051313) 7410 – 7525 (0.119973) 7527 – 7565 (0.029519) 8654 – 8671 (0.010704) 8699 – 9034 (0.365062) 9050 – 9085 (0.022831) 9433 – 9552 (0.185197) 11249 – 11358 (0.070677) 11375 – 11390 (0.009757) *Two Sigma Ranges*: 6492 – 6895 (0.164983) 7266 – 7588 (0.168263) 8600 – 9144 (0.331329) 9169 – 9250 (0.010714) 9311 – 9359 (0.007005) 9397 – 9631 (0.155636) 9647 – 9655 (0.000781) 11199 – 11719 (0.160296) 11737 – 11747 (0.000992)	*One Sigma Ranges*: 13983 – 14221 (0.13715) *Two Sigma Ranges*: 13776 – 14687 (0.243588)
	Turkana	*One Sigma Ranges*: 3639 – 3837 (0.034644) 4158 – 4174 (0.002662) 4176 – 4203 (0.005202) 4224 – 5754 (0.866892) 5826 – 5878 (0.009566) 9968 – 9982 (0.002543) 10155 – 10518 (0.078491) *Two Sigma Ranges*: 3450 – 6324 (0.741544) 6329 – 6348 (0.000817) 6368 – 6394 (0.001123) 6793 – 7290 (0.040704) 7621 – 8011 (0.034587) 8443 – 8994 (0.034554) 9707 – 9718 (0.000485) 9733 – 10721 (0.109791) 11320 – 11723 (0.035663) 11733 – 11749 (0.000731)	*One Sigma Ranges*: 6802 – 6814 (0.003189) 6847 – 6863 (0.004349) 6869 – 6882 (0.003766) 8607 – 9604 (0.785724) 10875 – 10942 (0.024026) 11077 – 11252 (0.178945) *Two Sigma Ranges*: 6535 – 7179 (0.093926) 7213 – 7240 (0.001631) 8465 – 8465 (0.000055) 8478 – 8495 (0.001018) 8513 – 9916 (0.611416) 10098 – 10111 (0.000738) 10564 – 12015 (0.291216)	*One Sigma Ranges*: 12431 – 2471 (0.083021) 12522 – 12763 (0.916979) *Two Sigma Ranges*: 12161 – 12207 (0.014779) 12231 – 12353 (0.045286) 12371 – 12975 (0.939935)

* CPDs based on ^{14}C dates listed in Tables D.2 and D.3.

***Table D.4 (continued)**. Cumulative probability distributions for the time and duration of overflow and closed basin conditions of Kenya Rift lakes.*
(Part 2/3)

River	Lake Basin	Age ranges as Cumulative Probability Distributions (CPD) in years cal. BP (probability)*		
		mid-late Holocene closed-lake basin level	**early Holocene overflow-lake level**	**late Pleistocene closed-lake basin level**
Southern River	Naivasha	*One Sigma Ranges*: 1558 – 1722 (0.197652) 3067 – 3360 (0.664182) 4589 – 4591 (0.001961) 4614 – 4709 (0.095148) 4754 – 4766 (0.010991) 4784 – 4814 (0.030065) *Two Sigma Ranges*: 1417 – 1459 (0.010186) 1517 – 1868 (0.230346) 2996 – 3381 (0.513014) 4429 – 4855 (0.246455)	*One Sigma Ranges*: 6297 – 6633 (0.409336) 10236 – 10569 (0.321667) 10793 – 10964 (0.140759) 11005 – 11023 (0.014298) 11065 – 11197 (0.113939) *Two Sigma Ranges*: 6207 – 6737 (0.337962) 9939 – 9992 (0.007035) 10008 – 10030 (0.002562) 10035 – 10062 (0.003387) 10127 – 11356 (0.647936) 11378 – 11388 (0.001118)	*One Sigma Ranges*: 12418 – 13085 (0.467764) 13946 – 14715 (0.532236) *Two Sigma Ranges*: 11831 – 11884 (0.004877) 11937 – 13362 (0.483944) 13742 – 15091 (0.511179)
	Siriata	*no lake/no dates*	*One Sigma Ranges*: 8325 – 8407 (0.058948) 9426 – 10874 (0.89379) 10945 – 11075 (0.047262) *Two Sigma Ranges*: 7610 – 8010 (0.044789) 8204 – 8264 (0.007156) 8285 – 8421 (0.049488) 8815 – 8823 (0.000544) 8875 – 8875 (0.000067) 8979 – 11997 (0.897957)	*One Sigma Ranges*: 12155 – 12438 (0.810331) 12461 – 12527 (0.189669) Two Sigma Ranges: 12005 – 12628 (1.0)
	Magadi-Natron	*One Sigma Ranges*: 5589 – 5762 (0.194649) 5809 – 5888 (0.070305) 6749 – 6769 (0.015671) 6771 – 7480 (0.719375) *Two Sigma Ranges*: 5340 – 5340 (0.000133) 5467 – 5991 (0.270677) 6209 – 6254 (0.006523) 6259 – 7578 (0.722667)	*One Sigma Ranges*: 8219 – 8238 (0.005786) 8307 – 9888 (0.994214) *Two Sigma Ranges*: 8166 – 11709 (0.990765) 12174 – 12209 (0.00231) 12236 – 12239 (0.000271) 12271 – 12354 (0.005635) 12369 – 12383 (0.001019)	*no shoreline dates*

* CPDs based on ^{14}C dates listed in Tables D.2 and D.3.

Table D.4 (continued). *Cumulative probability distributions for the time and duration of overflow and closed basin conditions of Kenya Rift lakes.*
(Part 3/3)

Oxygen isotope data from Siriata lake sediment outcrops

#	Outcrop ID	Depth below top (cm)	Analyzed material	$\delta^{18}O$ (‰)	Uncorrected shell ^{14}C-date (yr BP)	Median age (yr cal BP)*
1	KOO15-1A	0	*Corbicula*	-2.334	11080 ± 60	7844
2	KOO15-1A	0	*Corbicula*	-0.275	11080 ± 60	7844
3	KOO15-1A	0	*Corbicula*	-0.370	11080 ± 60	7844
4	KOO15-1A	0	*Corbicula*	-0.476	11080 ± 60	7844
5	KOO15-1A	10	*Corbicula*	-0.130		7944
6	KOO15-1A	10	*Corbicula*	-0.962		7944
7	KOO15-1A	10	*Corbicula*	0.214		7944
8	KOO15-1A	10	*Corbicula*	0.318		7944
9	KOO15-1A	30	*Corbicula*	-0.326		8151
10	KOO15-1A	30	*Corbicula*	-0.786		8151
11	KOO15-1A	40	*Corbicula*	-1.527		8252
12	KOO15-1A	40	*Corbicula*	-0.034		8252
13	KOO15-1A	40	*Corbicula*	-0.891		8252
14	KOO15-1A	40	*Corbicula*	-1.030		8252
15	KOO15-1A	50	*Corbicula*	0.367		8355
16	KOO15-1A	50	*Corbicula*	-2.174		8355
17	KOO15-1A	50	*Corbicula*	1.406		8355
18	KOO15-1A	50	*Corbicula*	1.943		8355
19	KOO15-1A	60	*Corbicula*	-0.347		8454
20	KOO15-1A	60	*Corbicula*	-0.667		8454
21	KOO15-1A	60	*Corbicula*	-2.816		8454
22	KOO15-1A	60	*Corbicula*	-1.335		8454
23	KOO15-1A	70	*Corbicula*	1.443		8557
24	KOO15-1A	70	*Corbicula*	-0.506		8557
25	KOO15-1A	100	*Corbicula*	-1.302	12210 ± 60	8862
26	KOO15-1A	100	*Corbicula*	-1.075	12210 ± 60	8862
27	KOO15-1A	100	*Corbicula*	-0.592	12210 ± 60	8862
28	KOO15-1A	100	*Corbicula*	-0.376	12210 ± 60	8862
29	KOO15-1A	110	*Corbicula*	-0.654		8966
30	KOO15-1A	110	*Corbicula*	-0.644		8966
31	KOO15-1A	110	*Melanoides*	-0.830		8966
32	KOO15-1A	110	*Melanoides*	-0.240		8966
33	KOO15-1A	180	*Corbicula*	-0.458	12890 ± 60	9661
34	KOO15-1A	180	*Corbicula*	0.245	12890 ± 60	9661
35	KOO15-1A	180	*Melanoides*	0.062	12890 ± 60	9661
36	KOO15-1A	180	*Melanoides*	0.696	12890 ± 60	9661
37	KOO15-1A	190	*Corbicula*	-0.204		9762
38	KOO15-1A	190	*Corbicula*	-0.414		9762
39	KOO15-1A	190	*Melanoides*	0.109		9762
40	KOO15-1A	200	*Corbicula*	-0.273		9862
41	KOO15-1A	200	*Corbicula*	0.775		9862
42	KOO15-1A	200	*Melanoides*	0.289		9862
43	KOO15-1A	200	*Melanoides*	0.691		9862
44	KOO15-1A	230	*Corbicula*	0.682		10158
45	KOO15-1A	230	*Corbicula*	-1.185		10158
46	KOO15-1A	230	*Corbicula*	0.770		10158
47	KOO15-1A	230	*Corbicula*	0.877		10158
48	KOO15-1A	270	*Corbicula*	-0.824	13580 ± 110	10567
49	KOO15-1A	270	*Corbicula*	-0.530	13580 ± 110	10567
50	KOO15-1A	270	*Corbicula*	0.016	123580 ± 110	10567
51	KOO15-1A	270	*Corbicula*	0.326	123580 ± 110	10567

***Table D.5**. Oxygen isotope measurements on mollusk shells from Siriata lake sediment outcrops. (Part 1/2)*

#	Outcrop ID	Depth below top (cm)	Analyzed material	$\delta^{18}O$ (‰)	Uncorrected shell ^{14}C-date (yr BP)	Median age (yr cal BP)*
52	KOO15-3E	430	*Corbicula*	-0.987	12660 ± 70	9379
53	KOO15-3E	430	*Corbicula*	-1.052	12660 ± 70	9379
54	KOO15-3E	430	*Melanoides*	-0.360	12660 ± 70	9379
55	KOO15-3E	430	*Melanoides*	0.202	12660 ± 70	9379
56	KOO15-3E	475	*Corbicula*	-0.832		9763
57	KOO15-3E	475	*Corbicula*	-0.648		9763
58	KOO15-3E	475	*Corbicula*	-0.637		9763
59	KOO15-3E	475	*Corbicula*	-0.468		9763
60	KOO15-3E	490	*Corbicula*	-1.100	12900 ± 90	9890
61	KOO15-3E	490	*Corbicula*	-1.107	12900 ± 90	9890
62	KOO15-3E	490	*Melanoides*	-0.949	12900 ± 90	9890
63	KOO15-3E	490	*Melanoides*	-1.001	12900 ± 90	9890
64	KOO15-3E	525	*Corbicula*	-1.362		10190
65	KOO15-3E	525	*Melanoides*	-0.338		10190
66	KOO15-3E	525	*Melanoides*	-0.226		10190
67	KOO15-3E	570	*Corbicula*	-0.785	13040 ± 70	10569
68	KOO15-3E	570	*Corbicula*	0.400	13040 ± 70	10569
69	KOO15-3E	570	*Melanoides*	-0.021	13040 ± 70	10569
70	KOO15-3E	570	*Melanoides*	0.001	13040 ± 70	10569
71	KOO15-3E	600	*Corbicula*	0.336		10863
72	KOO15-3E	600	*Corbicula*	0.620		10863
73	KOO15-3E	600	*Melanoides*	-0.137		10863
74	KOO15-3E	600	*Melanoides*	0.239		10863
75	KOO15-3E	630	*Corbicula*	-0.290		11158
76	KOO15-3E	630	*Corbicula*	-1.065		11158
77	KOO15-3E	630	*Melanoides*	-0.501		11158
78	KOO15-3E	630	*Melanoides*	-0.496		11158
79	KOO15-3E	650	*Corbicula*	-0.071		11353
80	KOO15-3E	650	*Corbicula*	-0.135		11353
81	KOO15-3E	650	*Melanoides*	0.007		11353
82	KOO15-3E	650	*Melanoides*	0.123		11353
83	KOO15-3E	660	*Corbicula*	-0.810		11452
84	KOO15-3E	660	*Corbicula*	-0.559		11452
85	KOO15-3E	660	*Melanoides*	0.742		11452
86	KOO15-3E	660	*Melanoides*	0.729		11452
87	KOO15-3E	666	*Melanoides*	-0.368	14060 ± 180	11508
88	KOO15-3E	666	*Melanoides*	-0.971	14060 ± 180	11508
89	KOO15-3E	666	*Melanoides*	-0.610	14060 ± 180	11508
90	KOO15-3E	666	*Melanoides*	-0.734	14060 ± 180	11508

Table D.5 (continued). *Oxygen isotope measurements on mollusk shells from Siriata lake sediment outcrops. (Part 2/2)*

Late Glacial-Holocene pollen records from East African lakes

Sediment core location	**Periods of forest expansion(ka BP)**	**Dominating woody plant taxa during periods of forest expansion**	**Reference**
Lake Albert	1) 14.0-13.2 2) 11.3-6.0	1) & 2) Moraceae, *Olea welwitschia*, *Celtis*, *Macaranga*, *Alchornea*	Beuning et al. (1997)
Lake Victoria	1) 13.9-12.8 2) 10.8-2.0	1) Oleaceae, *Macaranga*, *Trema* 2) Moraceae, *Celtis*, *Alchornea*, Oleaceae	Kendall (1969)
Mount Elgon	1) 12.6-4.0	1) *Hagenia*, *Olea*, *Podocarpus*, *Rapanea*, *Macaranga kilimandscharica*	Hamilton (1982)
Lake Naivasha	1) 14.4-7.3	1) *Olea*, *Rapanea*, *Celtis*, *Myrica*, *Pygeum* (=*Prunus*)	Maitima (1991)
Lake Emakat (Ngorongoro Highlands)	1) 14.5-9.9	1) *Hagenia abyssinica*, *Nuxia congesta*, *Olea*, *Juniperus*, *Podocarpus*	Ryner et al. (2006)

***Table D.6**. Late Glacial-Holocene pollen records from East African lakes.*